Electron Ptychographic Imaging of Polymer and Macromolecular Ordering



Botao Hao

St Cross College

University of Oxford

A thesis submitted for the degree of

Doctor of Philosophy

April 2023

Table of Contents

Chapter 1. General Introduction to Electron Ptychography 1

1.1 Aims of Projects and the Thesis Structure 1

1.1.1 Aims of Using Electron Ptychography in This Thesis 1

1.1.2 Thesis Structure 2

1.2 Basics of Transmission Election Microscopy and Its Applications in Imaging Polymers and Macromolecules 5

1.2.1 General Introduction 5

1.2.2 Aberration Correction and High-resolution Imaging 8

1.2.3 Challenges of Imaging Polymers and Macromolecules 10

1.2.3.1 Beam Damage 10

1.2.3.2 Image Contrast 10

1.3 Conventional Techniques to Image Polymers and Macromolecules and Their Insufficiencies 12

1.3.1 High-resolution Transmission Electron Microscopy 12

1.3.1.1 General Introduction 12

1.3.1.2 Insufficiencies of Imaging Polymers and Macromolecules 13

1.3.2 Scanning Transmission Electron Microscopy 14

1.3.2.1 General Introduction 14

1.3.2.2 Insufficiencies of Imaging Polymers and Macromolecules 16

1.4 Electron Ptychography 18

1.4.1 General Introduction of Ptychography 18

1.4.2 Electron Ptychography in Scanning Transmission Electron Microscopy and Its Advantages of Imaging Polymers and Macromolecules 20

1.5 Multislice Image Simulation 23

1.6 Project Design and New Science 24
1.7 References 25
Chapter 2. Introduction to Polyvinyl Alcohol 31
2.1 General Introduction 31
2.1.1 Preparation of Polyvinyl Alcohol 31
2.1.2 Properties of Polyvinyl Alcohol 33
2.1.2.1 Physical Properties of Polyvinyl Alcohol 33
2.1.2.2 Chemical Properties of Polyvinyl Alcohol 34
2.1.2.3 Tacticity of Polyvinyl Alcohol 35
2.1.2.4 Crystallinity of Polyvinyl Alcohol 36
2.2 Polyvinyl Alcohol Hydrogels 39
2.3 Applications of Polyvinyl Alcohol 42
2.3.1 General Commercial Applications 42
2.3.2 Biomedical Applications 42
2.3.3 Pharmaceutical Applications 43
2.4 Why Studying Crystallinity of Polyvinyl Alcohol Matters 45
2.4.1 Improving PVA Products 45
2.4.2 Tackling Environmental Threat 45
2.5 Design of Using Electron Ptychography to Image Polyvinyl Alcohol 47
2.6 References 49
Chapter 3. Introduction to Peptide Amphiphiles 57
3.1 General Introduction 57
3.1.1 Amino Acids 57
3.1.2 Peptide, Peptide Amphiphiles and Protein 57
3.1.3 Four Levels of Structures of Amino Acids, Peptides and Proteins 59
3.1.4 Amino Acids and Peptide Amphiphiles in This Work 61

3.2 Secondary Structures of Peptides and Proteins 63
3.2.1 Alpha-helix 63
3.2.2 Beta-sheet 65
3.2.3 Beta-Turn and Beta-Hairpin 69
3.2.4 Random Coils 70
3.3 Self-assembling Peptide-Amphiphile Fibres and Hydrogels 71
3.3.1 General Introduction to the Self-assembly of Peptide Amphiphiles 71
3.3.2 Different Systems of Self-assembling Peptide-Amphiphile Fibres 74
3.3.2.1 Surfactant Systems 74
3.3.2.2 Coiled-coil Systems 76
3.3.2.3 π-π stacking Systems 77
3.3.3 Parameters Influencing the Self-assembly 79
3.3.3.1 Amino Acid Sequence 79
3.3.3.2 Peptide Concentration 81
3.3.3.3 pH 84
3.3.3.4 Other Parameters 86
3.4 Main Applications of Peptide Amphiphiles 87
3.4.1 Tissue Engineering 87
3.4.2 Drug Delivery 88
3.4.3 Other Applications 89
3.5 Why Studying Crystallinity of Peptide Amphiphiles Matters 90
3.6 Design of Using Electron Ptychography to Image Peptide Amphiphiles 91
3.7 References 93
Chapter 4. Materials and Methods 110
4.1 Materials 110
4.2 Preparing Polyvinyl Alcohol and Peptide Solutions 111

4.3 Sample Preparation Methods 112
4.3.1 Spin-coating 112
4.3.2 Dip-casting 112
4.3.3 Drop-casting 112
4.4 Increasing Crystallinity of Samples 113
4.4.1 Freeze-thawing 113
4.4.2 Annealing 113
4.5 Transmission Electron Microscopy 114
4.5.1 Experimental Procedures and Fibre Width Measurement Using Line Profiles 114
4.5.2 High-resolution Transmission Electron Microscopy 115
4.5.3 Fast Fourier Transform Analysis 117
4.6 Fourier Transform Infrared Spectroscopy 120
4.7 Atomic Force Microscopy 121
4.8 X-ray Diffraction 122
4.9 Scanning Transmission Electron Microscopy and Electron Ptychography 123
4.9.1 Experimental Procedures and Parameters Used for Images 123
4.9.2 Dose and Beam Damage 124
4.10 Model Modification and Image Simulation 126
4.11 References 127
Chapter 5. Morphological Study of Peptide Amphiphiles 130
5.1 Introduction 130
5.2 Results 131
5.2.1 Transmission Electron Microscopic Images of Samples Prepared by Different Methods 131
5.2.2 Study on Critical pH Values for Peptide Fibres 133

5.2.3 Microscopic Images of F8 138
5.2.3.1 Transmission Electron Microscopic Images of Samples with Different Peptide Concentration 138
5.2.3.2 Transmission Electron Microscopic Images of Samples with Different pH 140
5.2.3.3 Atomic Force Microscopic Images 142
5.2.4 Microscopic Images of F9 144
5.2.4.1 Transmission Electron Microscopic Images of Samples with Different Peptide Concentration 144
5.2.4.2 Transmission Electron Microscopic Images of Samples with Different pH 145
5.2.4.3 Atomic Force Microscopic Images 147
5.2.5 Microscopic Images of FP 149
5.2.5.1 Transmission Electron Microscopic Images of Samples with Different Peptide Concentration 149
5.2.5.2 Transmission Electron Microscopic Images of Samples with Different pH 150
5.2.5.3 Atomic Force Microscopic Images 151
5.2.5.4 High-magnification Atomic Force Microscopic Images of Twisting Fibres 153
5.2.6 High-resolution Transmission Electron Microscopic Images of Peptide Fibres ..155
5.3 Discussion 157
5.3.1 Methods of Sample Preparation 157
5.3.2 Differences between Transmission Electron Microscopic and Atomic Force Microscopic Images 157
5.3.3 Twisting Fibres of FP 159
5.3.4 How Different Factors Influence PA Morphologies 162
5.3.4.1 Peptide Sequence 162
5.3.4.2 Peptide Concentration 164
5.3.4.3 pH 164
5.3.5 Relationship Between Peptide Morphology and Peptide Crystallisation 166

5.4 Conclusions....168
5.5 References....171
Chapter 6. Basic Structural and Crystallographic Study on Polyvinyl Alcohol and Peptide Amphiphiles....174
6.1 Introduction....174
6.2 Results and Discussion....175
6.2.1 Fourier-transform Infrared Spectroscopy....175
6.2.1.1 β-sheet Peptide Amphiphiles....175
6.2.1.2 Polyvinyl Alcohol....176
6.2.2 X-ray Thin-film Diffraction....177
6.2.2.1 β-sheet Peptide Amphiphiles....177
6.2.2.2 Polyvinyl Alcohol....179
6.2.3 High-resolution Transmission Electron Microscopy....180
6.2.3.1 Polyvinyl Alcohol....180
6.2.3.2 β-sheet Peptide Amphiphiles....182
6.2.3.3 Potential α-helix Peptide Amphiphiles....183
6.3 Unassigned d-spacings of the Above Materials....186
6.4 Conclusions....192
6.5 References....195
Chapter 7. Electron Ptychographic Imaging of Peptide Amphiphiles....197
7.1 Introduction....197
7.2 Results....198
7.2.1 Beam Damage Study on Peptides....198
7.2.2 High-angle Annular Dark Field-Scanning Transmission Electron Microscopy and Electron Ptychography....201
7.3 Discussion....204

7.3.1 β-sheet Structural Study 204
7.3.2 Repeat Distance Study and New Understandings of Peptide Amphiphilic β-sheet Crystals 204
7.3.3 Symmetrical Differences Between Three Peptide Amphiphiles 209
7.3.4 Possible Interpretation of the Contrast in the Electron Ptychographic Images 213
7.4 Unassigned d-spacings of the Above Materials 218
7.5 Conclusions 222
7.6 References 224
Chapter 8. Electron Ptychographic Imaging of Polyvinyl Alcohol 226
8.1 Introduction 226
8.2 Results 227
8.2.1 Beam Damage Study on Polyvinyl Alcohol 227
8.2.2 High-angle Annular Dark Field-Scanning Transmission Electron Microscopy and Electron Ptychography 228
8.3 Discussion 233
8.3.1 d-spacings Acquired from Electron Ptychographic Images 233
8.3.2 Patterns Acquired from the Electron Ptychographic Images 234
8.4 PVA Model Modification 237
8.5 Image Simulation 242
8.6 Conclusions 246
8.7 References 248
Chapter 9. General Conclusions and Future Work 249
Appendix 252
A.1 Line Profiles of High-resolution Transmission Electron Microscopy Images 252

A.2 Line Profiles of Fast Fourier Transform Images of High-resolution Transmission Electron Microscopy 260

A.3 Line Profiles of High-angle Annular Dark Field-Scanning Transmission Electron Microscopy and Electron Ptychography Images 262

List of Figures

Figure 1.1 Diagrammatic explanation of numerical aperture. 6

Figure 1.2 Schematic of transmission electron microscope (TEM). 7

Figure 1.3 Schematic of spherical aberration. 9

Figure 1.4 A TEM image of a β-sheet peptide sample with a weak image contrast. 11

Figure 1.5 Schematic ray diagrams of TEM and STEM. 15

Figure 1.6 Schematic of the collection process of a four-dimensional ptychographic imaging dataset. 19

Figure 1.7 Scheme of electron ptychography in HAADF-STEM. 20

Figure 2.1 Chemical structure of polyvinyl alcohol. 31

Figure 2.2 The main route of polyvinyl alcohol preparation. 32

Figure 2.3 Chemical structure of poly (vinyl alcohol-co-vinyl acetate). 32

Figure 2.4 Schematic presentation of PVA molecules in (a) isotactic, (b) syndiotactic and (c) atactic configurations. 35

Figure 2.5 Previous diffraction-derived PVA models viewed along the [010] direction (along the molecular axis). Hydrogen bonding in the figure is indicative. (a) Bunn's model. (b) Sakurada's model. 37

Figure 2.6 Structure of hydrogels. (a) A general hydrogel. (b) A semi-crystalline PVA hydrogel. 40

Figure 3.1 General structure of an amino acid. 57

Figure 3.2 Formation of a peptide from amino acids. 58

Figure 3.3 Schematic illustrations of four levels of protein structures. 59

Figure 3.4 Structures of amino acids and peptides used in this project. 62

Figure 3.5 Schematics of α-helix in peptides and proteins. 64

Figure 3.6 Generalised parallel and anti-parallel β-sheet structures and the hydrogen bonding distribution in each structure. 67
Figure 3.7 A 3D molecular model of F8 single molecule. (a) View from the [100] direction. (b) View from the [010] direction. (c) View from the [001] direction. 68
Figure 3.8 (a) Schematic of two types of beta turns. (b) A beta hairpin unit, consisting of two anti-parallel beta strands with a beta turn. 69
Figure 3.9 A tertiary structure composed of different types of secondary structures, including α-helix, β-sheet, terminal arms, and loops. 70
Figure 3.10 Schematic of typical peptide self-assembly into hydrogels. 73
Figure 3.11 Schematic of surfactant compositions. 74
Figure 3.12 Structures of a surfactant self-assembling system designed by Stupp's group. ...75
Figure 3.13 Schematic of a coiled-coil self-assembling system. 77
Figure 3.14 Schematic of a π-π stacking self-assembling system. 78
Figure 3.15 Previous peptide fibre models developed by Smith *et al.*, in view of π-π stacking systems. 79
Figure 3.16 Structure and self-assembling morphologies of EAK16-II and EAK16-IV. 81
Figure 3.17 AFM images of EAK16-II in pure water at various peptide concentrations. 82
Figure 3.18 AFM images of EAK16-I assemblies at various peptide concentrations. 83
Figure 3.19 AFM images of EAK16-IV at various pH values. 85
Figure 4.1 Schematic of the measurement of the peptide fibre width using line profiles in a TEM image. 115
Figure 4.2 Schematic of the measurement of a d-spacing using line profiles in a HRTEM image. 117
Figure 4.3 Schematic of the measurement of a d-spacing using line profiles in the FFT of Figure 4.1(a). 119

Figure 4.4 Schematic of the measurement of the peptide fibre width using line profiles in an AFM image.. 121

Figure 5.1 TEM images of spin-coated F8 samples (pH=7, 0.5 mg/mL). (a) Spinning at1500 rpm for 60 seconds. (b) Spinning at 2500 rpm for 60 seconds. (c) Spinning at1500 rpm for 30 seconds. (d) Spinning at 2500 rpm for 30 seconds. 132

Figure 5.2 TEM images of F8 samples (pH=7, 0.5 mg/mL) by different sample preparation methods. (a) Spin-coating. (b) Drop-casting. (c) Dip-casting. 133

Figure 5.3 TEM images of peptide samples at critical pH values with no fibres (a) F8 at pH = 2. (b) F8 at pH = 12. (c) F9 at pH = 3. (d) F9 at pH = 13. (e) FP at pH = 3. (f) FP at pH = 12. 135

Figure 5.4 AFM images of peptide samples at critical pH values with no fibres (a) F8 at pH = 2. (b) F8 at pH = 12. (c) F9 at pH = 3. (d) F9 at pH = 13. (e) FP at pH = 3. (f) FP at pH = 12. 137

Figure 5.5 TEM images of F8 samples at pH=7, with different peptide concentrations. (a) 0.5 mg/mL. (b) 1 mg/mL. (c) 2 mg/mL. (d) 5 mg/mL. (e) 10 mg/mL. (f) 20 mg/mL.....139

Figure 5.6 TEM images of F8 samples at 0.5 mg/mL, with different pH values. (a) pH=3. (b) pH=4. (c) pH=5. (d) (b) pH=6. (e) pH=7, isoelectric point of F8. (f) pH=8. (g) pH=9. (h) pH=10. (i) pH=11.....141

Figure 5.7 AFM images of F8 samples. (a) pH=4, 0.5 mg/mL. (b) pH=7, 0.5 mg/mL. (c) pH=10, 0.5 mg/mL. (d) pH=7, 20 mg/mL. 143

Figure 5.8 TEM images of F9 samples at pH=9.5, with different peptide concentrations. (a) 0.5 mg/mL. (b) 1 mg/mL. (c) 2 mg/mL. (d) 5 mg/mL. (e) 10 mg/mL. (f) 20 mg/mL.....144

Figure 5.9 TEM images of F9 samples at 0.5 mg/mL, with different pH values. (a) pH=4. (b) pH=5. (c) pH=6. (d) (b) pH=7. (e) pH=8. (f) pH=9.5, isoelectric point of F8. (g) pH=10. (h) pH=11. (i) pH=12. 146

Figure 5.10 AFM images of F9 samples. (a) pH=6, 0.5 mg/mL. (b) pH=9.5, 0.5 mg/mL. (c) pH=12, 0.5 mg/mL. (d) pH=9.5, 20 mg/mL. (e) Magnified image of the area in the blue square in (d).....148

Figure 5.11 TEM images of FP samples at pH=7, with different peptide concentrations. (a) 0.5 mg/mL. (b) 2 mg/mL. (c) 5 mg/mL. (d) 20 mg/mL.....150

Figure 5.12 TEM images of FP samples at 0.5 mg/mL, with different pH values. (a) pH=5. (b) pH=7, isoelectric point of FP. (c) pH=9. (d) pH=11.....151

Figure 5.13 AFM images of FP samples. (a) pH=5, 0.5 mg/mL. (b) pH=7, 0.5 mg/mL. (c) pH=9, 0.5 mg/mL. (d) pH=11, 0.5 mg/mL. (e) pH=7, 20 mg/mL. (f) Magnified image of the area in the blue square in (e).....152

Figure 5.14 AFM images of FP twisting fibres at high magnification at 0.5 mg/mL, with different pH values. (a) pH=5. (b) pH=7. (c) pH=9. (d) Scheme of a twisting fibre. R stands for the unit repeat distance of the twist along the fibre axis. D represents the diameter of the fibre. The ratio of R over D can reflex the level of twisting, where the level increases with the ratio decreases. (e) Summary of R/D ratios of (a), (b) and (c).....154

Figure 5.15 HRTEM and FFT images of peptide fibres. (a) F8 fibres. (b) Magnified image of the area in the red square in (a). (c) Magnified image of the area in the blue square in (a). (d) F9 fibres. (e) Magnified image of the area in the green square in (d). (f) FP fibres. (g) SAED of (f). 156

Figure 5.16 Explanation of AFM size errors resulted from the radius of the AFM probes. Proposed by Sherratt *et al*. [21]. W_m is the measured width of the cylindrical sample, and W_t is the true width of the cylindrical sample.....158

Figure 5.17 Previous peptide fibre models developed by Smith *et al.* [22]. Duplicate of Figure 3.15 for data interpretation in this section. (a) A self-assembling pair of molecules. Presented as the “sawtooth” structure. (b) A fibre consisting of self-assembling molecules. 160

Figure 5.18 FP models constructed following the model shown in Figure 5.18(b). (a) FP at its isoelectric point, no ions in the system. The spacing “a” represents the distance of adjacent molecules along the fibre length direction. (b) FP not at its isoelectric point, ions are involved in the system. The spacing “b” represents the distance of adjacent molecules along the fibre length direction. Spacings comparison, a > b. 161
Figure 5.19 Peptide models (a) F8. (b) F9. (c) FP. 163
Figure 5.20 F8 models. (a) F8 at its isoelectric point, no ions in the system. The spacing “a” represents the distance of adjacent molecules along the chain axis (the fibre width direction). (b) F8 not at its isoelectric point, ions are involved in the system. The spacing “b” represents the distance of adjacent molecules along the chain axis (the fibre width direction). Spacings comparison, a > b. 165
Figure 6.1 FTIR spectrum of peptides. (a) F8. (b) F9. (c) FP. 176
Figure 6.2 FTIR analysis of PVA. (a) FTIR spectrum of PVA. (b) Interpretation of (a) based on the information from the previous study by Mansur *et al*. 177
Figure 6.3 XRD patterns of peptide thin-film samples showing in each case the trace from: the Si substrate material (lower), as-cast peptide on Si (middle), and freeze-thawed peptide on Si (upper trace). (a) F8. (b) F9. (c) FP. (d) Summary of the crystal peak of the three peptides. The large peaks at around 29 degrees 2θ are due to signal from the underlying Si substrate, as can be seen from the Si background traces. 178
Figure 6.4 XRD patterns of PVA thin-film samples including unprocessed one, freeze-thawed one and a series of samples after annealing at temperatures between 160 ℃ and 250 ℃ for 20min. 180
Figure 6.5 Electron microscopic images of a single-crystal PVA thin-film sample. (a) HRTEM. (b) FFT of (a). 181

Figure 6.6 Electron microscopic images another single-crystal PVA thin-film sample. (a) HRTEM. (b) FFT of (a). (c) Line profile of the d-spacing marked in (a). 182
Figure 6.7 HRTEM images of freeze-thawed single-crystal peptide thin-film samples. Peptide concentration is 20 mg/mL, and pH are at their corresponding isoelectric points for each sample. (a) F8. (b) F9. (c) FP. 183
Figure 6.8 Electron microscopic images of a F2A2 thin-film sample, pH=7, 20 mg/mL. (a) HRTEM. (b) Magnified image of the area in the red square in (a). (c) Magnified image of the area in the blue square in (a). 185
Figure 6.9 Electron microscopic images of a FAFA thin-film sample, pH=7, 20 mg/mL. (a) HRTEM. (b) Magnified image of the area in the red square in (a). (c) Magnified image of the area in the blue square in (a). 185
Figure 6.10 Electron microscopic images of a F8 thin-film sample, pH=7, 20 mg/mL. (a) HRTEM. (b) Magnified image of the area in the red square in (a). (c) Magnified image of the area in the blue square in (a). 186
Figure 6.11 Electron microscopic images of a F8 thin-film sample, pH=7, 20 mg/mL. (a) HRTEM. (b) Magnified image of the area in the red square in (a). (c) Magnified image of the area in the blue square in (a). 187
Figure 6.12 Electron microscopic images of a F9 thin-film sample, pH=9.5, 20 mg/mL. (a) HRTEM. (b) Magnified image of the area in the red square in (a). (c) Magnified image of the area in the blue square in (a). (d) Magnified image of the area in the blue square in (a). 188
Figure 6.13 Electron microscopic images of a F9 thin-film sample, pH=9.5, 20 mg/mL. (a) HRTEM. (b) Magnified image of the area in the red square in (a). (c) Magnified image of the area in the blue square in (a). (d) Magnified image of the area in the blue square in (a). 189

Figure 6.14 Electron microscopic images of a F9 thin-film sample, pH=9.5, 20 mg/mL. (a) HRTEM. (b) Magnified image of the area in the red square in (a). (c) Magnified image of the area in the blue square in (a). 190
Figure 6.15 Electron microscopic images of a FP thin-film sample, pH=7, 20 mg/mL. (a) HRTEM. (b) Magnified image of the area in the red square in (a). 190
Figure 7.1 Two sequential SSB scans of the F8 sample. (a) First scan of the F8 sample. (b) Enlargement of the area in the red square in (a). (c) Second scan of the F8 sample with the same crystal of a, with a larger magnification. 199
Figure 7.2 Two sequential SSB scans of the F9 sample. (a) First scan of the F9 sample. (b) Second scan of the F9 sample with the same crystal of a, with the magnification and dose.200
Figure 7.3 Two sequential SSB scans of the FP sample. (a) First scan of the FP sample. (b) Second scan of the FP sample with the same crystal of a, with the magnification and dose.200
Figure 7.4 HAADF-STEM images of the same crystallite of an F9 before and after the high-resolution HAADF-STEM and electron ptychography work. (a) Before HAADF-STEM and electron ptychography acquisitions. (b) After HAADF-STEM and electron ptychography acquisitions. 200
Figure 7.5 Electron microscopic images of peptides. (a) HAADF-STEM image of F8. (b) Electron ptychography SSB phase image of F8. (c) Enlarged SSB phase image of the marked area in (b), with marked spacings and an angle. (d) HAADF-STEM image of F9. (e) Electron ptychography SSB phase image of F9. (f) Enlarged SSB phase image of the marked area in (e), with marked spacings and an angle. (g) HAADF-STEM image of FP. (h) Electron ptychography SSB phase image of FP. (i) Enlarged SSB phase image of the marked area in (h), with marked spacings and an angle. (j) Summary of spacings and angles acquired from above electron ptychographic images. 202

Figure 7.6 Schematic of PA self-assembly due to the hydrophobicity, taking F8 molecules as the example. (a) A F8 single molecule. (b) A pair of self-assembling F8 molecules.....205
Figure 7.7 Schematic of two F8 crystal models in the yz plane. (a) Models built based on information taken from references [x] and [y], with no "sawtooth" structure involved. Scientists treat the length between two adjacent same side groups (d_3) as the repeat distance. (b) Models built with the consideration of the "sawtooth" structure. According to the periodicity of the molecules, the repeat distance is 0.5 d_3 in this model. 206
Figure 7.8 (a) A F8 crystal model in the yz plane, with all the chain ends aligning with one another along the [010] direction. A notable repeat distance at 4.5 d_3 is expected. (b) A F8 crystal model in the yz plane, with and the chain ends are rather randomly distributed in the [001] direction. No repeat distance at 4.5 d_3 is expected. 208
Figure 7.9 An F9 crystal model in the yz plane, with two K groups locate adjacently at the end of each F9 molecule and two K groups face one to another at the chain ends and outsets of neighbouring chains. 210
Figure 7.10 Parallel and anti-parallel F8 and FP models in the xz plane. (a) Parallel FP model, with no chain offset. (b) Parallel F8 model, with a 0.13 nm offset along the molecular axis between neighbouring molecular chains, forming a 74° angle between adjacent chains. (c) Anti-parallel FP model, with no chain offset. (d) Anti-parallel F8 model, with a 0.13 nm offset along the molecular axis between neighbouring molecular chains, forming a 74° angle between adjacent chains. 211
Figure 7.11 Parallel and anti-parallel F8 and FP models overlaying in their electron ptychographic images. (a) Parallel FP model on its electron ptychographic image. (b) Anti-parallel FP model on its electron ptychographic image. (c) Parallel F8 model on its electron ptychographic image. (b) Anti-parallel F8 model on its electron ptychographic image. 212

Figure 7.12 Multilayer parallel and anti-parallel F8 and FP models. Based on the models shown in Figure 7.7(b), another layer is added along the y axis onto the single-layer models shown in Figure 7.11. (a) View of the self-assembling “sawtooth” structure shown in Figure 7.7(b) in the [010] direction. (b) Multilayer parallel FP model. (c) Multilayer anti-parallel FP model. (d) Multilayer parallel F8 model. (e) Multilayer anti-parallel F8 model.....214
Figure 7.13 Modified multilayer F8 models. (a) Modified multilayer parallel F8 model. (b) Modified multilayer anti-parallel F8 model.....215
Figure 7.14 Modified multilayer parallel and anti-parallel FP models overlaying in its electron ptychographic images. (a) Modified multilayer parallel FP model on its electron ptychographic image. (b) Modified multilayer anti-parallel FP model on its electron ptychographic image. 216
Figure 7.15 Modified multilayer parallel and anti-parallel F8 models overlaying in its electron ptychographic images. (a) Modified multilayer parallel F8 model on its electron ptychographic image. (b) Modified multilayer anti-parallel F8 model on its electron ptychographic image. 216
Figure 7.16 Electron microscopic images of F8 in an unassigned viewing direction. (a) HAADF-STEM image. (b) Simultaneous electron ptychography SSB phase image. (c) FFT of (b).....219
Figure 7.17 Electron microscopic images of F9 in an unassigned viewing direction. (a) HAADF-STEM image. (b) Simultaneous electron ptychography SSB phase image. (c) FFT of (b).....219
Figure 7.18 Electron microscopic images of F9 in an unassigned viewing direction. (a) HAADF-STEM image. (b) Simultaneous electron ptychography SSB phase image. (c) FFT of (b).....220

Figure 7.19 Electron microscopic images of FP in an unassigned viewing direction. (a) HAADF-STEM image. (b) Simultaneous electron ptychography SSB phase image. (c) FFT of (b).....221
Figure 8.1 Second WDD acquisition with a slight sample move on the PVA sample.....228
Figure 8.2 HAADF-STEM images of a PVA crystallite after HAADF-STEM and electron ptychography work. (a) A PVA crystallite. (b) Magnified image of the area in the green square in (a). Holes in red circles suggest mass loss of the sample after image acquisitions.....228
Figure 8.3 Electron microscopic and simulated images of PVA orientated in the [010] viewing direction. (a) HAADF-STEM image. (b) Simultaneous electron ptychography WDD phase image. (c) FFT of (a). (d) FFT of (b). (e) Simulated single-crystal electron diffraction pattern of Bunn's model. (f) Comparison between electron ptychographic data and Bunn's model. 230
Figure 8.4 Electron microscopic images of PVA orientated in the [$\bar{1}$10] viewing direction. (a) HAADF-STEM image. (b) Simultaneous electron ptychography WDD phase image. (c) FFT of b. (d) Simulated single-crystal electron diffraction pattern of Bunn's model. (e) Comparison between experimental data and Bunn's model. 232
Figure 8.5 Enlarged WDD phase image superposed with previous models orientated in the [010] viewing direction. (a) WDD phase image with Bunn's model. (b) WDD phase image with Sakurada's model.....235
Figure 8.6 Enlarged WDD phase image superposed with previous model orientated in the [$\bar{1}$10] viewing direction. (a) WDD phase image with Bunn's model. (b) WDD phase image with Sakurada's model.....236
Figure 8.7 Schematic illustration of the model modification process as observed in the [010] viewing direction (all oxygen sites represent half the occupancy of oxygen atoms). (a) The whole process of PVA model modification includes three steps. Note that the carbon (and

oxygen) atoms shown in this viewing direction show the possible locations of carbon (and oxygen) they do not represent the position of atoms in every unit cell repeat. However, all such locations will be represented in the projection of many unit cells along this axis. (b) Explanation of the third step, viewing from the [001] direction. 240
Figure 8.8 Experimental and simulated images of PVA in the [010] viewing direction. (a) Experimental HAADF-STEM image. (b) Experimental electron ptychography WDD phase image. (c) The modified PVA structure by the method elaborated in Figure 8.7 (all oxygen sites represent half the occupancy of oxygen atoms). (d) Simulated flat HAADF image. (e) Simulated electron ptychographic WDD-phase image. 242
Figure 8.9 Experimental and simulated images of PVA in the [$\bar{1}$10] viewing direction. (a) Experimental HAADF image. (b) Experimental electron ptychography WDD phase image. (c) The modified PVA structure by the method elaborated in Figure 8.7 (all oxygen sites represent half the occupancy of oxygen atoms). (d) Simulated flat HAADF image. (e) Simulated electron ptychographic WDD-phase image. 243
Figure 8.10 PVA model models viewed from the [010] direction (all oxygen sites represent half the occupancy of oxygen atoms). (a) Bunn's model. (b) Sakurada's model. (c) The modified PVA structure by the method elaborated in Figure 8.7. 245

List of Tables

Table 2.1 Some physical properties of polyvinyl alcohol. 33

Table 2.2 Some chemical properties of polyvinyl alcohol. 34

Table 2.3 Different methods of preparation to produce atactic, isotactic and syndiotactic polyvinyl alcohol. 36

Table 5.1 Summary of fibre information from F8 TEM images at pH 7 with different peptide concentrations. 139

Table 5.2 Summary of fibre information from F8 TEM images at 0.5 mg/mL with different pH values. 142

Table 5.3 Summary of fibre information from F8 AFM images shown in Figure 5.7. 143

Table 5.4 Summary of fibre information from F9 TEM images at pH 9.5 with different peptide concentrations. 145

Table 5.5 Summary of fibre information from F9 TEM images at 0.5 mg/mL with different pH values. 147

Table 5.6 Summary of fibre information from F9 AFM images shown in Figure 5.10. 148

Table 5.7 Summary of fibre information from FP TEM images at pH 7 with different peptide concentrations. 150

Table 5.8 Summary of fibre information from FP TEM images at 0.5 mg/mL with different pH values. 151

Table 5.9 Summary of fibre information from FP AFM images shown in Figure 5.13. 153

Table 5.10 Summary of fibre information from F8 TEM images and calibrated AFM images. 158

Table 5.11 Summary of fibre information from F9 TEM images and calibrated AFM images. 158

Table 5.12 Summary of fibre information of three peptides acquired from TEM images. ...162

Table 6.1 Summary of all d-spacings of F8, F9 and FP acquired from HRTEM. 191

Table 7.1 Summary of all potential d_1-equivalent d-spacings acquired from XRD, HRTEM and HAADF-STEM/electron ptychography. 204

Table 7.2 Summary of all d-spacings of F8, F9 and FP acquired from HAADF-STEM/electron ptychography.....221

Table 8.1 Summary of d-spacings acquired from XRD, HAADF and electron ptychography. 234

List of Abbreviations

Abbreviated title	Full title	Type
TEM	Transmission electron microscopy	Characterisation techniques
SEM	Scanning electron microscopy	
CTEM	Conventional transmission electron microscopy	
HRTEM	High-resolution transmission electron microscopy	
STEM	Scanning transmission electron microscopy	
ACTEM	Aberration-corrected transmission electron microscopy	
BF	Bright-field	
ADF	Annular dark-field	
HAADF	High-angle Annular Dark Field	
AFM	Atomic force microscopy	
FTIR	Fourier-transform infrared spectroscopy	
XRD	X-ray Diffraction	
FFT	Fast Fourier transform	Data processing methods
SSB	Single-side band	
WDD	Wigner distribution deconvolution	
PVA	Polyvinyl alcohol	Materials - polymers
F	Phenylalanine	Materials - amino acids
E	Glutamic acid	
K	Lysine	
P	Proline	
A	Alanine	
F8	FEFKFEFK	Materials - peptides
F9	FEFKFEFKK	
FP	FEFEPKFKF	
FAFA	FEAKFEAK	
F2A2	FEFKAEAK	
NaOH	Sodium hydroxide	Materials - others
HCl	Hydrochloric acid	
DI water	Deionised water	

Abstract

Polymers and macromolecules are widely used in the medical and pharmaceutical fields due to their outstanding biocompatibility, low density, and relatively low cost. However, the lack of microstructural study on these materials limits the ability to tailor them for broader and deeper applications.

As important methods for microstructural research, electron microscopic techniques have the potential to image polymers and macromolecules, but these materials are challenging for conventional electron microscopies because of their low crystallinity, poor contrast and severe beam damage. Therefore, an electron microscopic technique that uses reduced dose and also has higher contrast from light elements is required for the microstructural study.

Electron ptychography is an electron efficient imaging mode that offers phase contrast for light element detection. After the acquisition, a 4D dataset comprising the intensity in the STEM detector plane recorded as a function of each probe position can be reconstructed to give a phase image. Hence, electron ptychography has lower sample damage and better phase contrast compared to traditional techniques, which is helpful to overcome the existing challenges.

In this work, electron ptychography has been applied to explore the fine structures, particularly how light atoms order, in polyvinyl alcohol (PVA, a polymer) and some peptide amphiphiles (macromolecules). In the future, it is expected that the methodology can be expanded to other polymeric and macromolecular systems, and thus, better microstructural understanding could contribute, for example, to better medical and pharmaceutical applications of polymers and macromolecules.

Declaration

The work in this thesis is conducted by the author at the Department of Materials, University of Oxford, from 2018 to 20213, supervised by Professor Hazel Assender and Professor Peter Nellist. No portion of the work referred to in the thesis has been submitted in support of an application for another degree or qualification at this or any other university or institute of learning. Some parts of this thesis are under the progress of publications.

Atomic-scale imaging of polyvinyl alcohol crystallinity using electron ptychography – Chapters 6 & 8.

Direct visualisation of peptide amphiphile β-sheet crystals using electron ptychography – Chapters 6 & 7.

Acknowledgements

I would like to express my sincere thanks to all those who have lent me hands throughout my DPhil. My deepest gratitude goes foremost to Prof. Hazel Assender and Prof. Peter Nellist, my supervisors, for their constant encouragement, support, and guidance. Without their support, the whole DPhil project and this thesis would not be possible.

I would also like to express my heartfelt gratitude to Prof. Alberto Saiani and his student Ding Cong from the University of Manchester, for sharing their invaluable experience and knowledge, and for providing the peptides used in this project.

My sincere gratitude is extended to Richard Turner, for his technical help throughout my DPhil; Dr. Neil Young and Dr. Ian Griffiths, for their guidance in the use of equipment in the David Cockayne Centre for Electron Microscopy; Dr. Colin Johnston and Nicola Flanagan, for their patience and advice on using equipment in the Oxford Materials Characterisation Service.

I also owe my sincere gratitude to all peers in Polymers and STEM Research Groups, and other Department cohorts. Particular mentions must go to Dr. Xudong Tao, Dr. Kai Zhang, Justin Limkaichong, Zhiyuan Ding, Dr. Weixin Song, Dr. Xiaonan Luo, Dr. Ali Mostaed, Dr. Chen Gong, Dr. Peng Tang, Zheng Zhang, Donghao Liu and Tongshan Liu, who gave me their help and time in listening to me and helping me work out my problems during the difficult course of the experiment.

Finally, my thanks would go to my beloved family for their love and support.

Dedication

To Mum and Dad.

Chapter 1. General Introduction to Electron Ptychography

1.1 Aims of Projects and the Thesis Structure

1.1.1 Aims of Using Electron Ptychography in This Thesis

The crystallinity of polymers and macromolecules are fundamental to many key properties, including strength, transparency, and gas barrier properties [1][2]. Though their overall degree of crystallinity arose from the long-range order can be studied by conventional methods, for example, X-ray diffraction (XRD), but the local crystal information (influenced by the short-range variation due to diverse causes, for instance, the rotation of polymer chains along covalent bonds [3]) of plenty of polymer and macromolecular structures have not been well established due to the lack of direct observation methods [4].

Transmission electron microscopy (TEM) can potentially image local areas within polymer and macromolecular crystals, but it is still extremely challenging for conventional transmission electron microscopy (CTEM), mainly due to the weak image contrast and the severe beam sensitiveness of polymers and macromolecules [4][5]. Electron ptychography is an electron efficient imaging mode that offers image contrast for light element detection, and this advanced microscopic technique can potentially overcome the existing challenges on imaging polymer and macromolecular crystals. Two intriguing systems, polyvinyl alcohol (PVA) and peptide amphiphiles (PAs), are selected for the study.

1.1.2 Thesis Structure

This chapter introduces the TEM-related techniques used to characterise polymers and macromolecules. As the work in this thesis is about applying electron microscopic techniques instead of developing those techniques, the mathematical principles of TEM, STEM, electron ptychography and multislice simulations will be briefly introduced, and more details of these techniques can be found in references [11],[31],[33],[42], [44], [45] and [53]-[55].

Chapters 2 and 3 are literature reviews of the polymer system (PVA) and the macromolecular system (PAs). In Chapter 2, preparation and properties of PVA are firstly introduced, where two extant models of the PVA crystals are also elaborated. After that, applications of PVA hydrogels are reviewed, and followed by the discussion of the importance of studying PVA crystal structure. At the end of Chapter, the design of the project of using electron ptychography to image PVA crystals is presented.

Chapter 3 follows the similar structure as Chapter 2 to introduce the PA system, comprising six areas: an introduction to amino acids, peptides and proteins; secondary structures of peptides and proteins, including the extant crystallographic understanding of PA crystals; different self-assembling systems of PAs; applications of PAs; the importance of the crystallographic study on PA β-sheet crystals; and the design of the project on using electron ptychography to image PA β-sheet crystals.

In Chapter 4, materials and the experimental procedures used in this thesis are introduced.

In Chapter 5, the morphologies of three kinds of PA (FEFKFEFK (F8), FEFKFEFKK (F9) and FEFEPKFKF (FP), whose structure are shown in Figure 3.4) fibres are investigated. The morphologies of these peptide fibres have been studied as a function of concentration and pH. The research shown in Chapter 5 aims to provide a systematic study of the effect of peptide concentration and pH on fibre morphology, and the correlation between fibre morphology and PA β-sheet crystals.

The basic crystallographic studies on both PVA and PAs are conducted in Chapter 6. By using Fourier-transform Infrared Spectroscopy (FTIR), X-ray diffraction (XRD) and high-resolution transmission electron microscopy (HRTEM), some key features of PVA and PAs have been confirmed.

Chapters 7 and 8 present electron ptychographic images of PVA and PAs. The use of electron ptychography has shown more information than high-angle annular dark field - scanning transmission electron microscopy (HAADF-STEM) images. In Chapter 7, based on electron ptychographic images, analysis on the β-sheet crystal structure, including d-spacings, repeat distances, symmetric differences between three PAs and possible interpretation of the contrast in images are conducted.

The model modification of PVA crystal is operated in Chapter 8 based on PVA electron ptychographic images. The PVA crystal has shown variations locally due to the influence of different factors, such as various hydrogen bonding directions and the rotation of the polymer backbone. The multislice image simulation of the new model is also operated in Chapter 8, and the simulation results has supported the new PVA model.

Finally, Chapter 9 presents the general conclusions from the study, along with recommendations for future work.

1.2 Basics of Transmission Election Microscopy and Its Applications in Imaging Polymers and Macromolecules

1.2.1 General Introduction

Transmission electron microscopy (TEM) is a microscopy technique in which an image is formed by transmitting electron beams through a specimen [6]. Owing to a number of fundamental studies by Ernst Abbe [7], Köhler and Rohr [8], Hans Busch [9], *etc*., the first TEM was demonstrated by Max Knoll and Ernst Ruska in 1931 [10], and the first commercial TEM was then produced in 1939 [11]. With the improvements of TEM in nearly a century, this equipment has been widely used in cancer research, virology, materials science, nanotechnology, and semiconductor research [12].

Theoretically, as equation 1.1 shows, the highest resolution, *d*, that a light microscope may achieve is restricted by the wavelength of the photons (λ) used to probe the sample and the numerical aperture *NA* of the system [6][12][13]. Figure 1.1 gives the diagrammatic explanation of *NA*, where *n* is the index of refraction of the medium in which the lens operates and α is the greatest half-angle of the light cone that may enter the lens.

$$d = \frac{\lambda}{2n\sin\alpha} \approx \frac{\lambda}{2\,\mathrm{NA}} \qquad (1.1)$$

In the early 20th century, scientists proposed using electrons with short wavelength to replace visible light with large wavelength for a higher resolution.

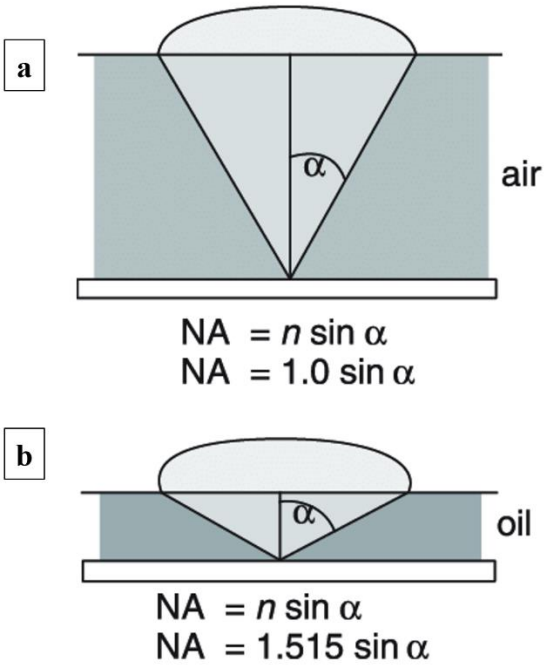


Figure 1.1 Diagrammatic explanation of numerical aperture, where *n* is the index of refraction of the medium in which the lens is working (1.0 for air in (a), and typically 1.515 for immersion oil in (b)), *α* is the half-angle of the maximum cone of light that can enter or exit the lens. Reproduced from reference [13].

The equation below [6][11] states how the wavelength of electrons is related to other parameters, where, h is Planck's constant, m_0 is the rest mass of an electron and E is the kinetic energy of the accelerated electron. Hence, the higher the kinetic energy, the smaller the wavelength, which leads to a better resolution.

$$\lambda_e = \frac{h}{\sqrt{2m_0E\left(1+\frac{E}{2m_0c^2}\right)}} \tag{1.2}$$

To achieve this, electrons generated by thermionic emission or field electron emission are accelerated by an electric potential (measured in volts) and focused by electrostatic and electromagnetic lenses onto the sample. The transmitted beam containing information about electron density, phase and periodicity is finally used to form an image [11][14].

Figure 1.2 briefly illustrates the process of using TEM to image samples. From the top down, the electrons are emitted from the electron gun and then focused into a thin parallel beam with the condenser lenses and the condenser aperture. The beam then irradiates the sample, and some transmitted electrons are focused by the objective lens to generate an image. After that, the image is enlarged by intermediate and projector lenses and projected onto a fluorescent screen. The image is finally recorded by a camera for further post processing and analysis.

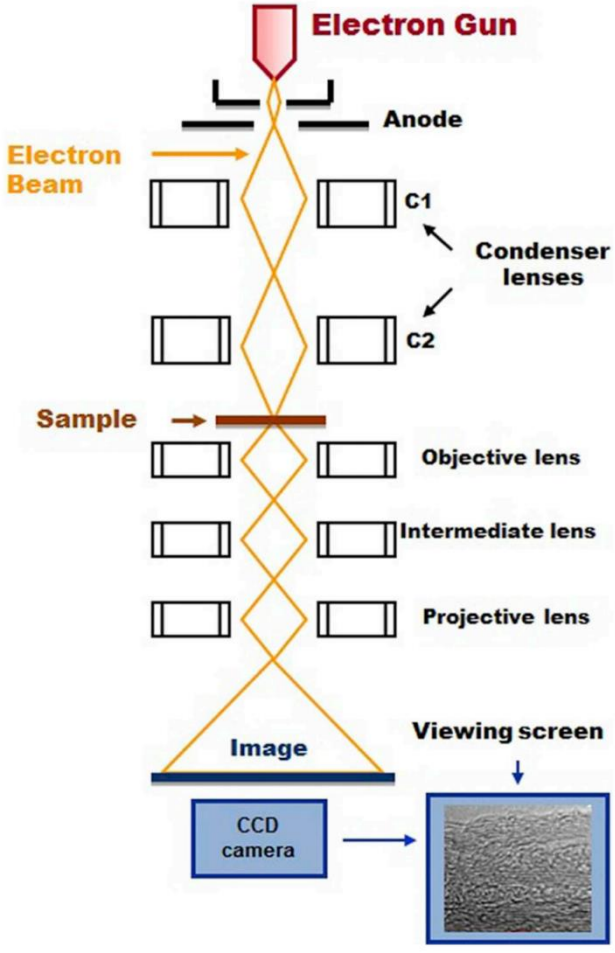


Figure 1.2 Schematic of transmission electron microscope (TEM). Reproduced from reference [15].

1.2.2 Aberration Correction and High-resolution Imaging

As introduced in Section 1.1.1, the aim of projects in this thesis is to study the local order of polymer and macromolecular samples, and high-resolution imaging techniques are required for the study of local detailed structures.

The theoretical resolution of a TEM can be approximated by the equation below [11], where r_{th} is the theoretical resolution, λ is the wavelength of electrons, and α is the semi-angle of collection.

$$r_{\mathrm{th}} = 0.61\frac{\lambda}{\alpha} \tag{1.3}$$

However, the performance of a (S)TEM is restricted by various lens defects [11]. And the most important defect that restricts the resolution of a (S)TEM is spherical aberration [11]. As shown in Figure 1.3(b), spherical aberration occurs when the outer parts of a lens do not focus light rays in the same way that the central part does [16], and various rays do not meet after the lens in a single focal point [16][17]. A point object can be imaged as a point when using a perfect lens. In contrast, with spherical aberration, a point object is imaged as a disk of finite size [11]. This limits the ability to magnify, because details of structures can be degraded due to spherical aberration. After considering spherical aberration, the practical resolution is summarised by the below equation, where r_{sph} is the spherical aberration error, which limits the resolution of the microscope.

$$r = \left(r_{\mathrm{th}}^2 + r_{\mathrm{sph}}^2\right)^{1/2} \tag{1.4}$$

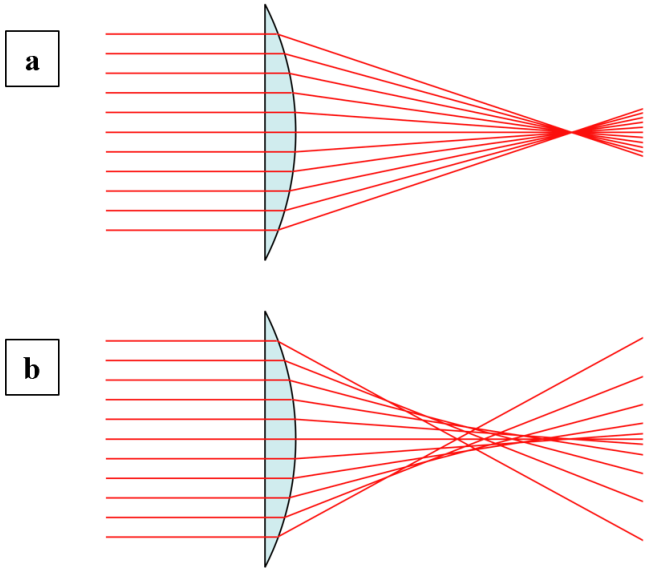


Figure 1.3 Schematic of spherical aberration. Reproduced from reference [17]. (a) A perfect lens with no spherical aberrations, where all incoming rays are focused on the focal point. (b) A real lens with spherical surfaces that causes spherical aberration, where various rays do not meet after the lens in a single focal point.

To minimise spherical aberration, aberration correctors have been designed. They create a diverging surface that can spread out the off-axis beams, such that these beams re-converge to the focal point [11]. The aberration-correction process is achieved by complex and computer-controlled set of quadrupoles and hexapoles or octupoles [11][18]. With the aid of aberration corrector, high-resolution imaging has been enabled to acquire detailed information about the sample [15]. Two commonly used high-resolution imaging techniques, high-resolution transmission electron microscopy (HRTEM) and scanning transmission electron microscopy (STEM) are introduced in Section 1.3.

1.2.3 Challenges of Imaging Polymers and Macromolecules

1.2.3.1 Beam Damage

The damage of (S)TEM arises from both elastic and inelastic scattering of incident electrons [19]. The former represents electrostatic deflection generated by the electrostatic field of atomic nuclei, which causes atomic displacement and the formation of defects in crystals (also known as knock-on damage) [19][20]. The latter refers to the interaction of incoming electrons with the atomic electrons that surround each nucleus, producing radiolysis effects, causing structural change or mass loss of the specimen [19][20].

Polymers and macromolecules are particularly sensitive to radiolysis effects, and there are two major ways of the beam damage of polymers and macromolecules [11]. First, incident electrons can break polymer and macromolecular backbones, leading to structural change [11]. Then, electrons break side groups of polymers and macromolecules, generating reactive free radicals that can form crosslinked new structures [4][11]. The beam damage usually exhibits as mass loss of the sample and loss of crystallinity in the crystalline part of the sample [4][11]. Therefore, a dose-efficient imaging technique is required for this study in order to minimise the beam damage of polymer and macromolecular samples in this thesis.

1.2.3.2 Image Contrast

Image contrast arises from wave amplitude and phase shifts in the electron beam passing through a specimen [11], while for polymer and macromolecular samples, phase shift is the dominant effect [5]. Both shifts can be attributed to the scattering of the incident beam by the

specimen [11]. The mass of atoms in the specimen is correlated to the intensity of the scattering [11][21][22]. Most polymers and macromolecules consist of light atoms, for instance, carbon, nitrogen and oxygen. These atoms only weakly scatter the electrons, resulting in a small shift in wave amplitude and phase [21]. This can give rise to the low contrast of polymer and macromolecular samples. An example is shown in Figure 1.4, where the TEM image contrast of a β-sheet peptide (the same type of material that is studied in this thesis) sample was very weak.

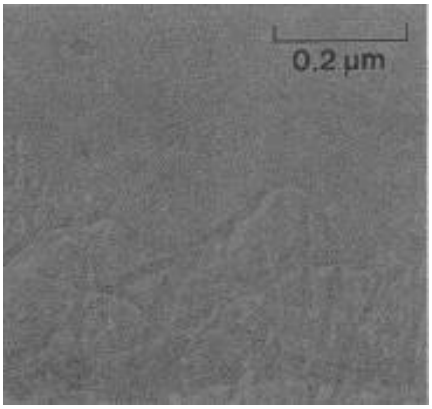


Figure 1.4 A TEM image of a β-sheet peptide sample with a weak image contrast. Reprinted from reference [23].

Considering samples in this thesis are very thin, these samples can be defined as weak-phase objects (WPO). This means that the specimen can be regarded as objects that do not change the amplitude of the incident electron wave but slightly changes the phase of the wave [24]. Phase-contrast should be exploited for imaging polymers and macromolecules, but it should be noted that beam damage (as introduced in Section 1.2.3.1) needs to be considered for selecting imaging methods. Some phase-contrast imaging techniques will be introduced in the next section.

1.3 Conventional Techniques to Image Polymers and Macromolecules and Their Insufficiencies

1.3.1 High-resolution Transmission Electron Microscopy

1.3.1.1 General Introduction

The most common phase-contrast imaging method is high-resolution transmission electron microscopy (HRTEM), which is an imaging mode that creates contrast through the interference of diffracted beams [25]. Compared to analytical TEMs that were introduced in Section 1.2.1, a large diameter objective aperture is used in HRTEM imaging to select multiple beams for a higher phase contrast to form an image that can reveal information about the atomic structure of the sample [26].

Lattice fringes result from the interference between two or more diffracted beams from a crystalline material [27]. The finest spacings of the lattice fringes visible in high-resolution images from a specific HRTEM are referred to as lattice-fringe resolution. For many years, the lattice-fringe resolution was widely regarded as the pinnacle of HRTEM merit [27]. However, lattice fringes with very fine spacings rarely provide useful information about local atomic arrangements [27].

As introduced in Section 1.2.1.2, advances in spherical aberration correction have enabled a new generation of HRTEMs to reach the atomic resolution once thought impossible [26][27]. To date, HRTEM has become a powerful tool for studying atomic-scale properties of materials such as semiconductors, metals and nanoparticles [25].

For the HRTEM data, using the fast Fourier transform (FFT) algorithm can represent the crystal in the reciprocal space [11][28][29]. In the reciprocal space, each point of the reciprocal lattice is indexed, and the inter-planar spacing can be calculated by measuring the reciprocal of relevant reciprocal vector magnitude [28][29]. This is important to understand the crystal structure of the sample.

1.3.1.2 Insufficiencies of Imaging Polymers and Macromolecules

Although HRTEM has been widely used as a phase-contrast method for direct imaging of the atomic structure of the sample, there are still some issues with using HRTEM to image polymers and macromolecules.

Firstly, HRTEM needs to introduce aberrations to introduce phase differences in the diffracted beams [25][30]. This is typically performed with a combination of defocus and spherical aberration [25][30]. As a result, the performance of HRTEM can be sacrificed in order to optimise contrast.

In addition, HRTEM occurs the contrast reversal problem with the thickness and focus [11][31]. This makes data interpretation and quantitative measurements difficult. The beam damage problem remains for imaging polymers and macromolecules [4][5]. The comparison of the dose-efficiency between HRTEM and the electron ptychography (the technique used in this thesis) will be introduced in Section 1.4.2.

To summarise, HRTEM is a phase-imaging method that can potentially be used for the atomic-resolution imaging of polymers and macromolecules, but the insufficiencies in lens aberrations, data interpretation and beam damage hinder the performance of HRTEM to image polymers and macromolecules.

1.3.2 Scanning Transmission Electron Microscopy

1.3.2.1 General Introduction

With suitable optics and when combined with suitable detectors, a TEM can be converted into a scanning transmission electron microscope (STEM) by adding a system that scans a convergent beam across the sample to form the image [14][32]. As shown in Figure 1.5, In contrast to conventional TEM (CTEM), the electron beam of STEM with a convergence angle (α) is focused to a small spot and then scanned across the specimen in a raster pattern. Scattered electrons are then detected, and their intensity plotted as a function of probe position to form an image [32][33].

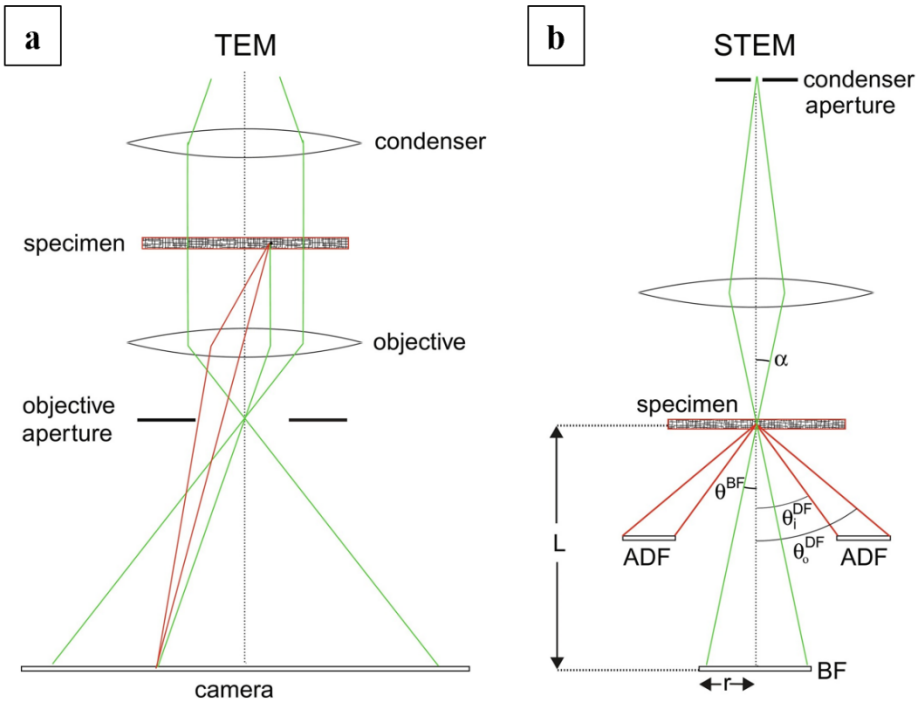


Figure 1.5 Schematic ray diagrams of TEM and STEM. Reprinted from reference [34].

In the STEM mode, probe sizes below the interatomic spacings in a number of materials can also be possible. Therefore, after the probe scans over a region of interest, atomic-resolution images can be readily formed for this region [31][33]. For the high-resolution imaging of radiation-sensitive polymers and macromolecules, STEM allows better damage control than HRTEM, because STEM only irradiates the scanned- and thus imaged-area of the specimen by using small-probe scanning. On the contrary, applying parallel beams, it is difficult to limit irradiation of adjacent areas in HRTEM [5]. Furthermore, previous results [35][36] also suggest that STEM permits a higher electron dose than CTEM without causing significant damage to the sample. As a result, STEM can outperform CTEM in terms of beam damage control on polymer and macromolecular samples.

Two common detectors and imaging modes used in STEM are bright-field (BF) and annular dark-field (ADF) [31]-[33]. High-angle annular dark-field imaging (HAADF) is a STEM method

that produces an annular dark field image formed by very high angles in the ADF mode [31]-[33]. Both detectors generate images by summing the electron intensity over a region of the far field beyond the sample and displaying the result as a function of probe position [31][22]. As shown in Figure 1.5(b), the BF detector collects over a disc of scattering angles centred on the optic axis of the microscope, while the ADF detector collects over an annulus at higher angle where only scattered electrons are detected [31][33].

The mechanism of BF-STEM image acquisition is similar to that of CTEM, and in both cases, coherent scattering and the principle of reciprocity are used for imaging [31][33], while ADF imaging makes use of incoherent scattering [31][33]. The difference between coherent and incoherent imaging is that coherent imaging has a fixed phase relationship between electrons emerging from different parts of the object under study, while incoherent imaging is the opposite of this [37]. And the incoherent imaging provides ADF-STEM a strong sensitivity to atomic number, allowing different elements to show up with different intensities in the image [31][33]. As this thesis is not about STEM technique development, the details of coherent and incoherent imaging will not be further introduced. More information about this field can be found in references [31], [33] and [37].

1.3.2.2 Insufficiencies of Imaging Polymers and Macromolecules

Although BF-STEM has been used for imaging light atoms [22][38][39], this method has the similar problem with the HRTEM. Although a scanning beam enables the precise control of the irradiated region of the specimen, only a fraction of the scattered electrons at low angles is collected and applied for generating the contrast of image [11]. In other words, BF-STEM is not

a dose-efficient method, and the intense dose used for high-resolution imaging can damage the fragile sample [32], such as polymers and macromolecules.

Similarly to HRTEM, BF-STEM also has the contrast reversal problem [11][31], making data interpretation and quantitative measurements challenging. On the other hand, as an incoherent imaging method, ADF-STEM does not reverse contrast with thickness or focus [31]. Instead, ADF-STEM mainly generates image contrast via Z-contrast [11][31][33]. Although it is very sensitive to heavy elements with large atomic number (Z) [11][40], imaging light atoms with low atomic number (Z) is still changing for this technique because of the contrast issue [41]. Moreover, ADF-STEM also has the same issue in dose efficiency, where only electrons at higher angles are collected and used.

Accordingly, an advanced microscopic technique is required for the direct imaging of polymer and macromolecule ordering. In the following section, electron ptychography will be introduced as a potential solution.

1.4 Electron Ptychography

1.4.1 General Introduction of Ptychography

The word “ptychography” roots from the Greek word “ptycho”, which means “fold”. In the field of microscopic science, ptychography refers to a computational method of microscopic imaging [42]. Generally, ptychography generates images by processing a series of coherent interference (mostly diffraction) [42] patterns.

Figure 1.6 shows the collection process of a ptychographic dataset. It is notable that there is an overlapping area of adjacent spots, and this overlap produces the coherent interference [33][42]. The interference between direct (illumination) beam and diffracted discs contains phase contrast information [42]. The phase contrast information in the disc overlap regions depends on the probe position, and the intensity changes can be recorded as the probe moves. As shown in Figure 6.1, an incident illumination locally irradiates a small area of the sample, and the interference pattern is recorded by a detector. With shifts in the specimen, the information of interference pattern from different positions can also be recorded. Two indexes of the diffraction pattern (recorded on the pixelated detector as shown in Figure 1.7) and two indexes of the illumination position are used for recording the ptychographic data. Therefore, these four indexes make up the four-dimensional (4D) dataset in ptychography [42][43].

Abundant in information, the 4D data set can then be reconstructed and analysed by computer algorithms. Two commonly used methods for the reconstruction are Single-Side Band (SSB) or Wigner Distribution Deconvolution (WDD) methods [44]-[47]. As this project is not

developing ptychographic methodologies, algorithms of reconstruction methods will not be further introduced. More information can be found in references [42] and [44]-[48].

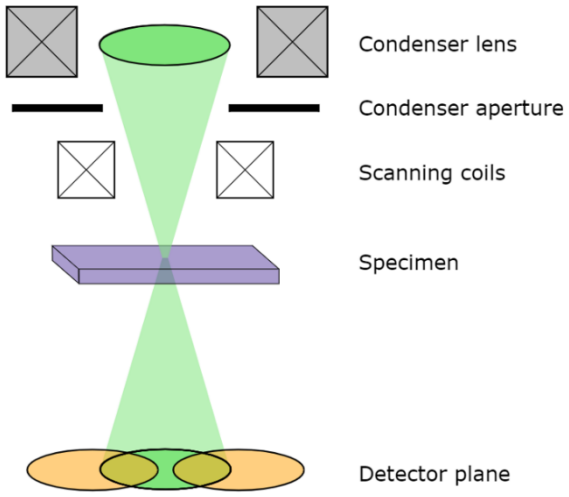


Figure 1.6 Schematic of the collection process of a four-dimensional ptychographic imaging dataset. Reproduced from reference [46].

1.4.2 Electron Ptychography in Scanning Transmission Electron Microscopy and Its Advantages of Imaging Polymers and Macromolecules

The use of electron ptychography in STEM has been proven to be an effective phase-retrieval method for imaging light atoms [21][44][49][50]. Figure 1.7 shows how electron ptychography is used in STEM. Compared to the original HAADF-STEM imaging, an extra fast pixelated detector [51][52] is required to collect convergent beam electron diffractions at a high speed at each probe pixel [45][46][51][52]. This enables that ptychographic dataset consists of the full convergent beam electron diffraction pattern for each probe position that is scanned over the sample and contains most of the scattering information generated by the electron-sample interaction in the STEM experiment [21][45][46][49][50].

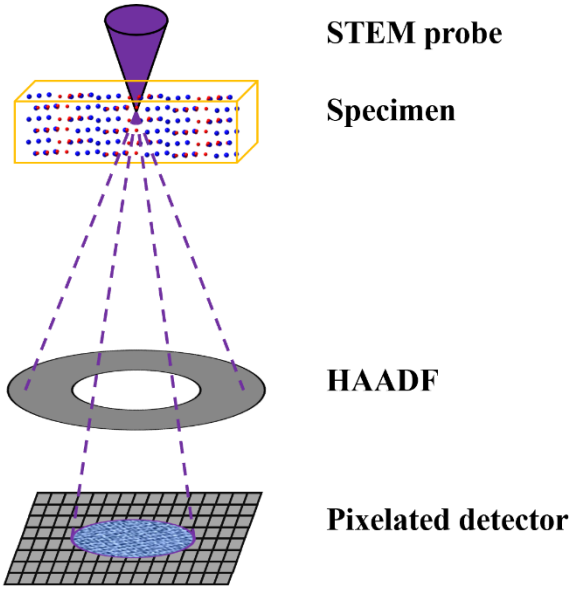


Figure 1.7 Scheme of electron ptychography in HAADF-STEM.

Moreover, HAADF can be recorded simultaneously because electron ptychography does not require lens aberration to form contrast compared to HRTEM [21][45][46][51][52]. As a result, the

phase information recorded from electron ptychography, and the simultaneous Z-contrast imaging form HAADF-STEM can be used for a full analysis [45][46][49]. After reconstruction of the above abundant information by SSB or WDD methods [42],[44]-[48], electron ptychography phase images can present structural information on light atoms at atomic level [21][44][49][50].

Turning to another challenge in imaging materials in this thesis, beam damage can also be mitigated by using electron ptychography. This is because electron ptychography collects and uses most of electrons which contain phase-contrast information to generate images [44][45][49][51][52], leading to a high dose-efficiency. By contrast, ADF-STEM only uses signals in dark field, which means the raw signal intensity is much lower than that used by electron ptychography. Therefore, a relatively low beam current can be used for this technique to image polymers and macromolecules, lowering beam damage on the sample.

Compared to another phase-contrast imaging method HRTEM, Pennycook *et al.* [30] suggested that electron ptychography provides images at twice the resolution of HRTEM images under equivalent conditions. For weakly scattering specimens, for instance, polymers and macromolecules, ptychographic electron imaging can provide superior dose efficiency to HRTEM [30].

Accordingly, electron ptychography can be a dose-efficient phase-contrast method for imaging polymers and macromolecules. Several previous studies have proven that ptychographic phase images retrieved from the 4D datasets can generate phase contrast to light atoms in beam-sensitive samples, where carbon [21][49], oxygen [21][50] and even lithium atoms [49][50] can be viewed in reconstructed images. The advantages mentioned above of electron ptychography

discussed above can also be helpful in revealing the precise structure of the PVA and PA crystals.

1.5 Multislice Image Simulation

The multislice algorithm is a method for simulating the elastic interaction of an electron beam with matter, including all multiple scattering effects [53]. Most simulation packages use a basic multislice approach that involves sectioning the specimen into many slices that are normal to the incident beam. There are various methods for performing the multislice calculation, each developed for a different reason. Some attempt to optimise the use of available hardware, while others aim to provide convenient methods for performing different simulation tasks with the same programme [11]. The package used in this thesis is MULTEM [54], and this package can provide accurate simulations for STEM and electron ptychography at much higher calculation speeds than with a conventional CPU [54]. Customising the MULTEM codes to conduct image simulations was beyond the scope of this thesis, and all image simulation work in this thesis was performed by Zhiyuan Ding in our group.

The theory of above methods is elaborated in references [53]-[55], but as explained in Section above, those contents are beyond the scope of this thesis.

1.6 Project Design and New Science

This thesis contains two projects, the use of electron ptychography in imaging polymer (PVA system) and macromolecular (the self-assembling PA system) ordering. The preliminary steps focus on investigating the overall crystallinity of materials and potential methods to increase their crystallinities. These contents are discussed in Chapters 5 and 6. Appropriate PVA and PA samples are then studied by electron ptychography. The detailed design for PVA and PAs can be found at the end of their Sections 2.5 and 3.6, respectively. Chapters 7 and 8 present the new findings in PVA and PA crystals by using electron ptychography.

The impact of the thesis is evaluated by scientific novelty and potential applications. First, because the understanding of the polymer and macromolecular crystals has been hindered by the lack of direct imaging techniques in the past, applying the novel advanced technique, electron ptychography, to image these materials provides a precise understanding of local ordering, which has never been studied before. The methodology used in this thesis can therefore be regarded as a novel scientific endeavour. In the future, the methodology used in this thesis can be expanded to other polymer and macromolecular systems. Better structural understanding of these materials will upgrade the product qualities and cut down the fabrication costs.

1.7 References

[1] Mileva, D., Tranchida, D., & Gahleitner, M. (2018). Designing polymer crystallinity: An industrial perspective. *Polymer Crystallization*, *1*(2), e10009.

[2] Flory, P. J. (1981). Structural regularity and crystallinity in macromolecules. In *Structural Order in Polymers* (pp. 3-9). Pergamon.

[3] Tsvetkov, V. N. (1963). Flexibility and Shape of Macromolecules. *Rubber Chemistry and Technology*, *36*(2), 337-350.

[4] Drummy, L. F., & Kübel, C. (2010). Polymer microscopy: Current challenges. *Polymer Reviews*, *50*(3), 231-234.

[5] Sawyer, L., Grubb, D. T., & Meyers, G. F. (2008). *Polymer microscopy*. Springer Science & Business Media.

[6] Tang, C. Y., & Yang, Z. (2017). Transmission electron microscopy (TEM). In *Membrane characterization* (pp. 145-159). Elsevier.

[7] Davidson, M. W. (2009). Pioneers in Optics: Ernst Abbe (1840-1905). *Microscopy Today*, *17*(1), 38-41.

[8] Davidson, M. W. (2013). Pioneers in Optics: James Bradley and August Köhler. *Microscopy Today*, *21*(5), 50-52.

[9] Busch, H. (1926). Berechnung der Bahn von Kathodenstrahlen im axialsymmetrischen elektromagnetischen Felde. *Annalen der Physik*, *386*(25), 974-993.

[10] Ruska, E., & Knoll, M. (1931). Die magnetische Sammelspule für schnelle Elektronenstrahlen. *The magnetic concentrating coil for fast electron beams.) Z. techn. Physik*, *12*, 389-400.

[11] Williams, D. B., & Carter, C. B. (1996). *The transmission electron microscope* (pp. 3-17). Springer Us.

[12] Conduct Science.

https://conductscience.com/transmission-electron-microscopy-tem/.

Accessed March 5, 2023.

[13] McNamara, G., Difilippantonio, M., Ried, T., & Bieber, F. R. (2017). Microscopy and image analysis. *Current Protocols in Human Genetics*, *94*(1), 4-4.

[14] Wikipedia _ Transmission electron microscopy.

https://en.wikipedia.org/wiki/Transmission_electron_microscopy.

Accessed March 5, 2023.

[15] Kwiecińska, B., Pusz, S., & Valentine, B. J. (2019). Application of electron microscopy TEM and SEM for analysis of coals, organic-rich shales and carbonaceous matter. *International Journal of Coal Geology*, *211*, 103203.

[16] Sivak, J. G., & Kreuzer, R. O. (1983). Spherical aberration of the crystalline lens. *Vision Research*, *23*(1), 59-70.

[17] Wikipedia _ Spherical aberration.

https://en.wikipedia.org/wiki/Spherical_aberration.

Accessed March 28, 2023.

[18] Hetherington, C. (2004). Aberration correction for TEM. *Materials Today*, *7*(12), 50-55.

[19] Egerton, R. F. (2013). Control of radiation damage in the TEM. *Ultramicroscopy*, *127*, 100-108.

[20] Egerton, R. F., Li, P., & Malac, M. (2004). Radiation damage in the TEM and SEM. *Micron*, *35*(6), 399-409.

[21] Yang, H., Rutte, R. N., Jones, L., Simson, M., Sagawa, R., Ryll, H., Huth, M., Pennycook, T. J., Green, M.L.H., Soltau, H., Kondo, Y., Davis, B. G., & Nellist, P. D. (2016). Simultaneous atomic-resolution electron ptychography and Z-contrast imaging of light and heavy elements in complex nanostructures. *Nature Communications*, *7*(1), 12532.

[22] Findlay, S. D., Shibata, N., Sawada, H., Okunishi, E., Kondo, Y., Yamamoto, T., & Ikuhara, Y. (2009). Robust atomic resolution imaging of light elements using scanning transmission electron microscopy. *Applied Physics Letters*, *95*(19), 191913.

[23] Krejchi, M. T., Atkins, E. D., Waddon, A. J., Fournier, M. J., Mason, T. L., & Tirrell, D. A. (1994). Chemical sequence control of β-sheet assembly in macromolecular crystals of periodic polypeptides. *Science*, 1427-1432.

[24] Fejes, P. L. (1977). Approximations for the calculation of high-resolution electron-microscope images of thin films. *Acta Crystallographica Section A: Crystal Physics, Diffraction, Theoretical and General Crystallography*, *33*(1), 109-113.

[25] Spence, J. C., & Crewe, A. V. (1981). Experimental high-resolution electron microscopy. *Physics Today*, *34*(9), 90.

[26] Buseck, P., Cowley, J., & Eyring, L. (Eds.). (1989). *High-resolution transmission electron microscopy: and associated techniques*. Oxford University Press.

[27] Smith, D. J. (2005). High resolution transmission electron microscopy. *Handbook of microscopy for nanotechnology*, 427-453.

[28] Zhang, Q., Bai, R., Peng, B., Wang, Z., & Liu, Y. (2023). FFT pattern recognition of crystal HRTEM image with deep learning. *Micron*, *166*, 103402.

[29] Glaeser, R. M. (2008). Retrospective: radiation damage and its associated "information limitations". *Journal of structural biology*, *163*(3), 271-276.

[30] Pennycook, T. J., Martinez, G. T., Nellist, P. D., & Meyer, J. C. (2019). High dose efficiency atomic resolution imaging via electron ptychography. *Ultramicroscopy*, *196*, 131-135.

[31] Pennycook, S. J., & Nellist, P. D. (Eds.). (2011). *Scanning transmission electron microscopy: imaging and analysis*. Springer Science & Business Media.

[32] Keyse, R. (2018). *Introduction to scanning transmission electron microscopy*. Routledge.

[33] Nellist, P. D. (2019). Scanning transmission electron microscopy. In *Springer Handbook of Microscopy* (pp. 49-99). Cham: Springer International Publishing.

[34] Wolf, S. G., & Elbaum, M. (2019). CryoSTEM tomography in biology. *Methods in cell biology*, *152*, 197-215.

[35] Jones, L., Varambhia, A., Beanland, R., Kepaptsoglou, D., Griffiths, I., Ishizuka, A., Azough, F., Freer, R., Ishizuka, K., Cherns, D., Ramasse, Q. M., Lozano-Perez, S., & Nellist, P. D. (2018). Managing dose-, damage-and data-rates in multi-frame spectrum-imaging. *Microscopy*, *67*(suppl_1), i98-i113.

[36] Ilett, M., Brydson, R., Brown, A., & Hondow, N. (2019). Cryo-analytical STEM of frozen, aqueous dispersions of nanoparticles. *Micron*, *120*, 35-42.

[37] Van Aert, S., Van Dyck, D., & den Dekker, A. J. (2006). Resolution of coherent and incoherent imaging systems reconsidered-Classical criteria and a statistical alternative. *Optics express*, *14*(9), 3830-3839.

[38] Okunishi, E., Ishikawa, I., Sawada, H., Hosokawa, F., Hori, M., & Kondo, Y. (2009). Visualization of light elements at ultrahigh resolution by STEM annular bright field microscopy. *Microscopy and Microanalysis*, *15*(S2), 164-165.

[39] Ishikawa, R., Okunishi, E., Sawada, H., Kondo, Y., Hosokawa, F., & Abe, E. (2011). Direct imaging of hydrogen-atom columns in a crystal by annular bright-field electron microscopy. *Nature materials*, *10*(4), 278-281.

[40] Pennycook, S. J., & Jesson, D. E. (1991). High-resolution Z-contrast imaging of crystals. *Ultramicroscopy*, *37*(1-4), 14-38.

[41] Yücelen, E., Lazić, I., & Bosch, E. G. (2018). Phase contrast scanning transmission electron microscopy imaging of light and heavy atoms at the limit of contrast and resolution. *Scientific Reports*, *8*(1), 1-10.

[42] Rodenburg, J., & Maiden, A. (2019). Ptychography. In *Springer Handbook of Lasers and Optics* (pp. 819–904). Springer Handbook of Lasers and Optics.

[43] Yang, H., Jones, L., Ryll, H., Simson, M., Soltau, H., Kondo, Y., Sagawa, R., Banba, H., MacLaren, I., & Nellist, P. D. (2015). 4D STEM: High efficiency phase contrast imaging using a fast pixelated detector. In *Journal of Physics: Conference Series* (Vol. 644, No. 1, p. 012032). IOP Publishing.

[44] Yang, H., MacLaren, I., Jones, L., Martinez, G. T., Simson, M., Huth, M., Ryll, H., Soltau, H., Sagawa, R., Kondo, Y., Ophus, C., Ercius, P., Jin, L., Kovács, A., & Nellist, P. D. (2017). Electron ptychographic phase imaging of light elements in crystalline materials using Wigner distribution deconvolution. *Ultramicroscopy*, 180, 173-179.

[45] Pennycook, T. J., Lupini, A. R., Yang, H., Murfitt, M. F., Jones, L., & Nellist, P. D. (2015). Efficient phase contrast imaging in STEM using a pixelated detector. Part 1: Experimental demonstration at atomic resolution. *Ultramicroscopy*, 151, 160-167.

[46] Yang, H., Pennycook, T. J., & Nellist, P. D. (2015). Efficient phase contrast imaging in STEM using a pixelated detector. Part II: Optimisation of imaging conditions. *Ultramicroscopy*, 151, 232-239.

[47] Rodenburg, J. M. (2008). Ptychography and related diffractive imaging methods. *Advances in imaging and electron physics*, *150*, 87-184.

[48] O'Leary, C. M., Martinez, G. T., Liberti, E., Humphry, M. J., Kirkland, A. I., & Nellist, P. D. (2021). Contrast transfer and noise considerations in focused-probe electron ptychography. *Ultramicroscopy*, *221*, 113189.

[49] Lozano, J. G., Martinez, G. T., Jin, L., Nellist, P. D., & Bruce, P. G. (2018). Low-dose aberration-free imaging of Li-rich cathode materials at various states of charge using electron ptychography. *Nano letters*, *18*(11), 6850-6855.

[50] Song, W., Pérez-Osorio, M. A., Marie, J. J., Liberti, E., Luo, X., O'Leary, C., House, R. A., Bruce, P. G., & Nellist, P. D. (2022). Direct imaging of oxygen shifts associated with the oxygen redox of Li-rich layered oxides. *Joule*, *6*(5), 1049-1065.

[51] Huth, M., Simson, M., Ritz, R., Ryll, H., Martinez, G. T., Lozano, J., Bruce, P.G., Nellist, P.D., Sagawa, R., Kondo, Y., & Soltau, H. (2018). 4D Analytical STEM with the pnCCD. *Microscopy and Microanalysis*, *24*(S1), 220-221.

[52] Ryll, H., Simson, M., Hartmann, R., Holl, P., Huth, M., Ihle, S., Kondo, Y., Kotula, P., Liebel, A., Müller-Caspary, K., Rosenauer, A., Sagawa, R., Schmidt, J., Soltau, H., & Strüder, L. (2016). A pnCCD-based, fast direct single electron imaging camera for TEM and STEM. *Journal of Instrumentation*, *11*(04), P04006.

[53] Kirkland, E. J. (1998). *Advanced computing in electron microscopy* (Vol. 12). New York: Plenum Press.

[54] Lobato, I., & Van Dyck, D. (2015). MULTEM: A new multislice program to perform accurate and fast electron diffraction and imaging simulations using Graphics Processing Units with CUDA. *Ultramicroscopy*, 156, 9-17.

[55] Cowley, J. M., & Moodie, A. F. (1957). The scattering of electrons by atoms and crystals. I. A new theoretical approach. *Acta Crystallographica*, *10*(10), 609-619.

Chapter 2. Introduction to Polyvinyl Alcohol

2.1 General Introduction

2.1.1 Preparation of Polyvinyl Alcohol

Polyvinyl alcohol (often abbreviated as PVA) is a water-soluble polymer, with hydroxy side groups attaching on the carbon backbone (chemical structure shown in Figure 2.1). It was firstly prepared by Hermann and Haehnel in 1924 via saponification of polyvinyl ester in sodium hydroxide solution [1]. Because vinyl alcohol is unstable and tautomerizes quickly into acetaldehyde, PVA is not produced through the polymerization of the corresponding monomer [2]. Instead, the main route to prepare PVA is hydrolysis of polyvinyl acetate (PVAc) following a two-step process shown in Figure 2.2. Starting from vinyl acetate, PVAc is firstly prepared via free radical polymerization. PVA is then produced by hydrolysis of PVAc [3]. In the second step, PVAc can be either completely or partially hydrolysed [4][5]. As a result, the PVA product could be either a homopolymer as shown in Figure 2.1 or a copolymer as illustrated in Figure 2.3. To avoid the influence of PVAc for a more precise study on the pure PVA structure, the degree of hydrolysis of PVA used in this project is 99%, so the PVA structure in this project can be viewed as the one shown in Figure 2.1.

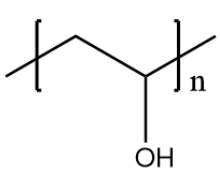


Figure 2.1 Chemical structure of polyvinyl alcohol.

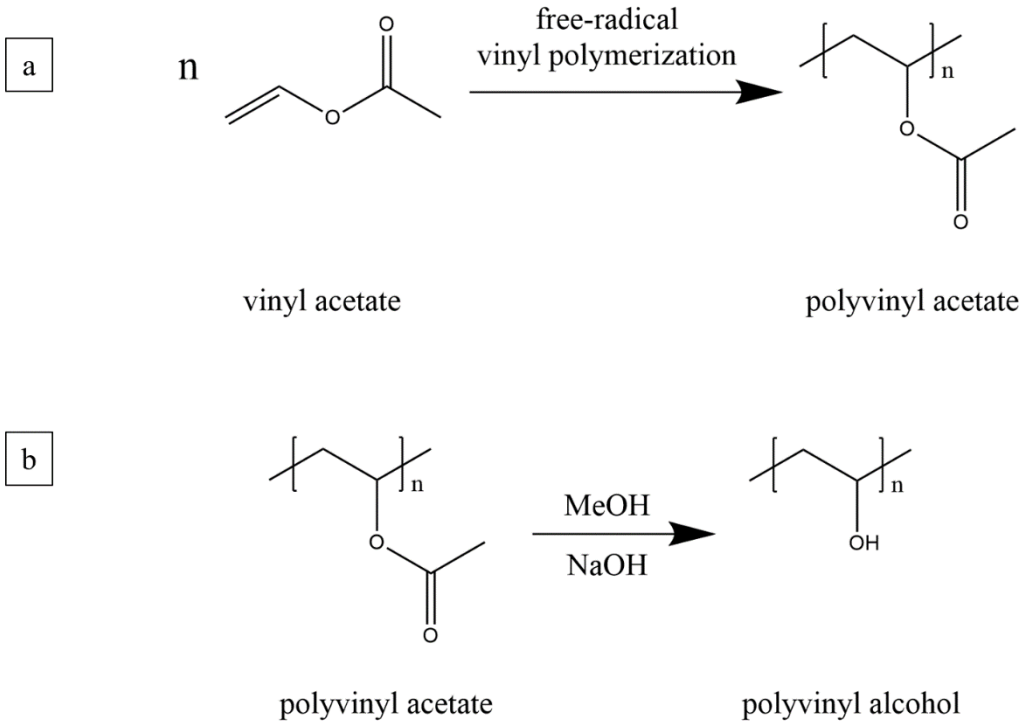


Figure 2.2 The main route of polyvinyl alcohol preparation. (a) Polymerisation of polyvinyl acetate. (b) Hydrolysis of polyvinyl acetate.

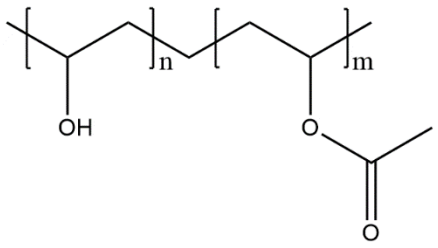


Figure 2.3 Chemical structure of poly (vinyl alcohol-*co*-vinyl acetate).

2.1.2 Properties of Polyvinyl Alcohol

2.1.2.1 Physical Properties of Polyvinyl Alcohol

Generally, commercial PVA is a tasteless, odourless, nontoxic, creamy or whitish granular polymer powder [6]-[8]. According to Gaaz *et al.* [9] and Matsumura [10], the degree of hydrolysis affects some key properties of PVA, such as density, solubility, glass transition and melting temperatures. As for PVA solutions, Marten [11] suggests that some other physical properties, for instance, viscosity and adhesive strength, depend on the degree of hydrolysis as well as molecular weight of PVA. Besides, the crystallinity of PVA also plays a significant role in determining the physical properties of PVA [13]-[15]. The crystallinity of PVA will be discussed in Section 2.1.2.3. Some physical properties of PVA are listed in Table 2.1.

Table 2.1 Some physical properties of polyvinyl alcohol. Reproduced from information in references [13] and [16].

Physical Properties	Descriptions
Appearance	Creamy or whitish granular powder
Bulk density	641 kg·s/m^3
Density	1.19 to 1.31 g/cm^3
Storage stability	When protected from moisture, indefinite
Flammability	Flammable, burns similarly to paper
Stability to sunlight	Excellent
Glass transition temperature (Tg)	75 to 85 °C
Specific heat	1.5 J/(g·K)
Melting point	230 °C for fully hydrolysed PVA; 180 to 190 °C for partially hydrolysed PVA

2.1.2.2 Chemical Properties of Polyvinyl Alcohol

Chemical properties are always attributed to the chemical structure of materials. For PVA, the quantity of hydroxyl groups mostly governs its chemical properties [17]. As PVA is prepared by hydrolysis of PVAc, it also means that chemical properties of PVA are dominated by the degree of hydrolysis [13][17]. Therefore, the primary property to discuss in this section is the degree of hydrolysis of PVA. Commercial PVA products can be classified as partially hydrolysed, moderately hydrolysed and completely hydrolysed. Their degrees of hydrolysis range from 84.2% to 89.0%, 92.2% to 96.5% and over 98%, respectively [8]. As for the solubility, PVA is basically soluble in water, but insoluble in aliphatic and aromatic hydrocarbons, ketones and esters [18]. Turning to the molecular weight, Halima [18] concludes that commercial PVA is typically between 20000 to 400000 g/mol. The above properties are summarised in Table 2.2.

Table 2.2 Some chemical properties of polyvinyl alcohol. Reproduced with information from references [8], [18] and [19].

Chemical Properties	Descriptions
Molecular weight	20000 to 400000 g/mol
Solubility	Soluble in water; Insoluble in aliphatic and aromatic hydrocarbons, ketones and esters
Degree of hydrolysis	84.2% to 89.0% for partially hydrolysed PVA; 92.2% to 96.5% for moderately hydrolysed PVA; Over 98.0% for completely hydrolysed PVA

Additionally, in a similar way to other polyhydric alcohols, PVA can undergo esterification reactions with inorganic and organic acids [14], form cyclic esters with borax [14][20]. and react with sulphur trioxide, alkane sulfonyl chlorides, titanium lactate, and titanium sulphate [11][14].

2.1.2.3 Tacticity of Polyvinyl Alcohol

Tacticity refers to the relative stereochemistry of adjacent chiral centres within a macromolecule or polymer [21]. The tacticity of the polymer is a significant factor that influences some properties of the polymer, for instance, the melting temperature, the solubility in a solvent or some mechanical properties [21]. Meanwhile, tacticity of the polymer also plays an important role in the crystallinity by affecting the long-range order of the polymer [21].

Figure 2.4 shows three forms of PVA with different tacticity, namely, isotactic (all hydroxyl substituents are located on the same side of the backbone), syndiotactic (hydroxyl substituents have alternate positions along the chain), and atactic (hydroxyl substituents are placed randomly along the chain) [22][23]. Polymer scientists have a consensus that isotactic polymers tend to have the highest degree of crystallinity as their molecular structures are the most ordered. On the contrary, atactic polymers are more likely to be amorphous due to their random structural arrangements [21].

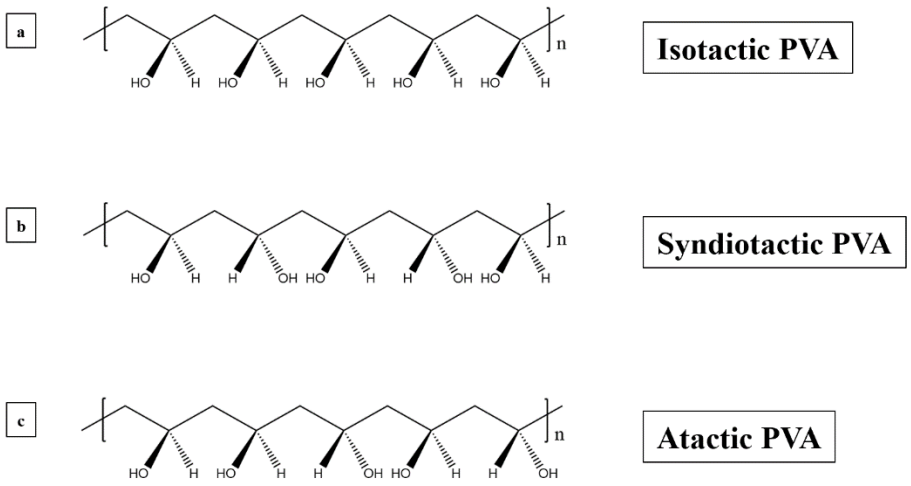


Figure 2.4 Schematic presentation of PVA molecules in (a) isotactic, (b) syndiotactic and (c) atactic configurations.

PVA is atactic in nature for commercially available grades (produced by the method introduced in Sector 2.1.1), but some methods can be used for preparing isotactic and syndiotactic PVA products [15][22][23]. Those methods are summarised in Table 2.3. It should be noted that PVA used and studied in this project are commercially atactic PVA.

Table 2.3 Different methods of preparation to produce atactic, isotactic and syndiotactic polyvinyl alcohol. Reproduced from information in Reference [15].

Methods of preparation	Tacticity of PVA products
Hydrolysis of polyvinyl acetate	Atactic
Polymerisation of vinyl tert-butyl ether in toluene	Isotactic
Polymerisation of vinyl tert-butyl ether in methylene chloride	Slightly syndiotactic
Polymerisation of vinyl trimethylsilyl ether in nitroethane	Highly syndiotactic

2.1.2.4 Crystallinity of Polyvinyl Alcohol

Study of the crystallinity of PVA can be dated back to the 1940s'. By using X-ray diffraction, Mooney [24] concluded in 1941 that PVA has a semi-crystalline pseudo-orthorhombic structure with cell parameters at a = 0.782 nm, b = 0.252 nm, c = 0.560 nm. Mooney [24] also concluded that PVA has a crystalline structure owing to the stereochemical regularity of PVA molecules. To be more specific, the polymer chain has a planar zigzag conformation and the hydroxyl groups of PVA are on the same side of the plane [20].

Based on Mooney's study, Bunn [25] updated the study of PVA crystallinity in 1948. Bunn suggested that crystalline PVA should be regarded as a layered structure held together by hydroxyl bonds and van der Waals force rather than molecular stereochemical regularity [21]. Besides, the hydroxyl bonds have minor influence on PVA crystals, due to the possible random distribution of hydroxyl groups [25]. As introduced in the last section, this is consistent with the

atactic structure of commercial PVA products. By using X-ray diffraction, the new PVA crystal is monoclinic (a = 0.781 nm, b = 0.252 nm, c = 0.551 nm, α = γ = 90°, β = 91.7 °) [25]. As shown in Figure 2.4(a), Bunn's model is one of the generally accepted PVA crystal models.

Another well-supported model was proposed by Sakurada *et al.* in 1950 [26]. They suggested a different PVA crystal model (Sakurada's model is shown in Figure 2.4(b)) also by using X-ray diffraction [26]. The discrepancy between two models comes from the way they arrange intermolecular hydrogen bonding. Following the primitive monoclinic crystal system, Sakurada *et al*. made a tweak in cell parameters to a = 0.783 nm, b = 0.252 nm, c = 0.553 nm, α = γ = 90°, β = 87.0 ° [26]. To date, these two possible crystal structures are still mooted.

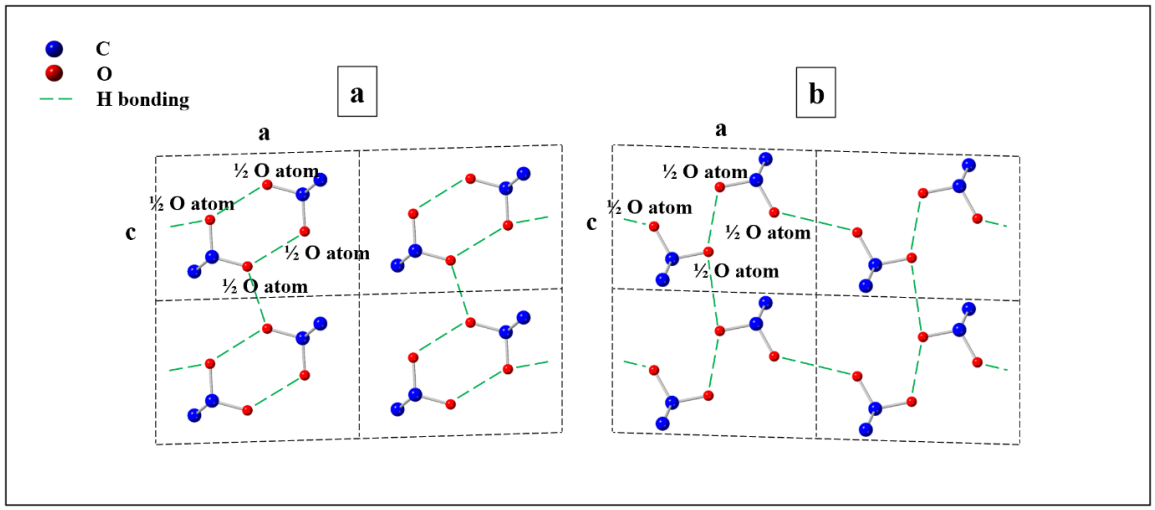


Figure 2.5 Previous diffraction-derived PVA models viewed along the [010] direction (along the molecular axis). Hydrogen bonding in the figure is indicative. (a) Bunn's model. (b) Sakurada's model.

As the degree of crystallinity can be very low for raw PVA samples, increasing the crystallinity is important for the study of PVA crystal structures. Bolto *et al.* [27] and Hickey *et al.* [28] manged to form new crystalline PVA regions by the freezing and thawing cycles on PVA. Moreover,

Assender and Windle [29] found that annealing can be another effective way to further crystallise PVA. Freeze-thawing and annealing, therefore, are regarded as two effective methods to prepare highly crystalline PVA samples. These two methods (which will be elaborated in Chapter 4) were used to prepare PVA samples in this work.

2.2 Polyvinyl Alcohol Hydrogels

In many cases, PVA is used in the form of hydrogels. Hydrogels are water-insoluble, three-dimensional crosslinked networks of polymer chains capable of holding large amounts of water [30][31]. Figure 2.5 (a) presents the structure of hydrogels, which contain water, polymer chains, and the most important part to form the hydrogel, crosslinks. The crosslinks that connect the polymers in a hydrogel classify the hydrogels into two types: physical hydrogels and chemical hydrogels. Covalent cross-links exist in chemical hydrogels, while non-covalent linkages are present in physical hydrogels [32]. Because of covalent bonding, chemical hydrogels are generally chemically stable [33]. However, with some covalent links that are active to be untied and retied by chemical reactions, some reversible chemical hydrogels have been widely used in a variety of therapeutic products [34][35]. Physical hydrogels are typically biocompatible and non-toxic [32]. They are readily reversible and typically more responsive than chemical hydrogels. Linked by hydrogen bonds, hydrophobic interactions and chain entanglements, physical hydrogels can be tuned by adjusting an external stimulus such as pH, ion concentration, and temperature [36][37]. According to Omidian and Park, the quantity of absorbed water varies depending on the type of crosslinks (chemical or physical) and the degree of chemical or physical cross linking [30][31].

According to Muppalaneni and Omidian [14], PVA hydrogels have generally low swelling abilities because of their susceptibility to hydrogen bonding and crystallisation. Chemical PVA hydrogels are not widely used at the moment as PVA cannot be readily crosslinked by intramolecular reactions. Chemicals, such as formaldehyde, glutaraldehyde, and ketones, have potentials to form the chemical crosslinks for PVA hydrogels. However, these chemicals are

toxic, and it is difficult to control the residual cross linker left in the final polymer in an acceptable and safe range in concentration [38].

Physical methods are preferred to prepare PVA hydrogels with different desirable functions [14]. Wong and Parasrampuria [39] suggest that production of PVA hydrogels is usually accompanied by the increase of the degree of crystallinity of PVA, as stable crystals can act as firm physical crosslinks. Figure 2.5 (b) shows the structure of crystalline PVA hydrogels. Freeze-thawing is the most common way to prepare PVA hydrogels [40][41]. Lozinsky and Plieva [41] propose that hydroxyl groups of the adjacent PVA chains tend to form weak intra and intermolecular hydrogen bonds during the freeze-thawing process, leading to the formation of PVA crystallites and PVA hydrogels.

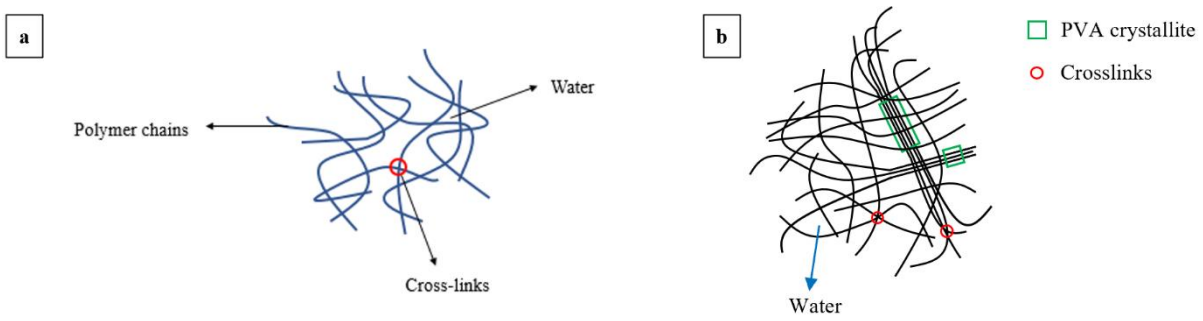


Figure 2.6 Structure of hydrogels. (a) A general hydrogel. (b) A semi-crystalline PVA hydrogel.

Elastic, viscous and viscoelastic properties of PVA hydrogels with water are dependent on the concentration of PVA aqueous solutions. For example, hydrogels prepared at low water concentrations tend to have higher mechanical properties, for instance they would exhibit reasonable elastic properties. On the contrary, viscous properties would be favoured under reverse conditions of high water-content [14]. The composition of a PVA can be tuned during a

freeze-thawing process by controlling parameters such as, freeze-thawing temperatures, number of freezing and thawing cycles and rate of freezing [42]. Therefore, theoretically, the PVA hydrogels can be modulated to obtain desirable viscoelastic properties [14]. However, this has not been achieved yet, and the study of PVA structure can be helpful to accomplish the modulation.

2.3 Applications of Polyvinyl Alcohol

2.3.1 General Commercial Applications

Owing to its low manufacturing cost and high chemical stability, PVA is now widely used in a variety of industries, including textile, paper, binding and coating, adhesives, and food packaging [43][44]. PVA is also a well-known water-soluble polymer with high strength and optical transparency in water [45][46]. Therefore, PVA is used in packaging and as an optical polarizer due to its desirable properties [47]. In addition, PVA hydrogels are used as disposable contact lenses due to their optical clarity as well as other advantages such as, their high moisture retention and great softness [45][46]. Other industries that can benefit from this polymer include water treatment, eyedrops and laundry detergents [48]-[50].

2.3.2 Biomedical Applications

Compared to other materials used in biomedical and pharmaceutical fields, PVA hydrogels have relatively low cost. Also, properties such as high water-solubility, biocompatibility and drug compatibility make PVA hydrogels a potential candidate as biomedical and pharmaceutical materials [14].

As for biomedical applications, according to Hassan and Peppas [51], PVA hydrogels have been investigated for use as artificial heart linings, artificial cartilages, catheters, skin, and pancreas membranes since the last century. For instance, PVA hydrogels were used as artificial cartilages. Based on Noguchi *et al.*'s research [52], there was only minor swelling of PVA after two weeks when PVA artificial cartilages were implanted in a rabbit knee joint. They therefore

concluded that this PVA material possessed exceptional bio-adhesive properties [52]. Moreover, PVA hydrogels have also been studied for usages including artificial kidney membranes for dialysis [53], intervertebral disc nuclei [54], and bioprosthetic heart valves [55].

Mechanical properties of PVA hydrogels play an important role in the above-mentioned applications. In Kobayashi *et al.*'s papers [56][57], PVA hydrogels were prepared by freeze-thawing after annealing, and these materials were explored for use as an artificial meniscus. As a result, the implanted PVA meniscus retained excellent mechanical properties, with no apparent signs of wear or distortion [56][57]. Besides, the fine structure of PVA articular cartilages were studied using microscopy. It is also found that their mechanical properties are related to the morphology of PVA hydrogels [58]. However, there are no publications yet that study how the crystal structure and morphology of PVA can potentially influence their biomedical applications.

2.3.3 Pharmaceutical Applications

PVA hydrogels have been investigated as drug delivery methods through oral, buccal, intramuscular, transdermal, and rectal routes [14]. To date, PVA drug carriers have been studied to load insulin [59], fluconazole [60], bovine serum albumin [61], *etc*. Mallapragada and McCarthy-Schroeder [62] found that crystallinity of PVA has a strong effect on modulating drug diffusion from hydrogels, and it may influence the drug release performances. For example, based on Mongia *et al.*'s [63] study on applying PVA hydrogels in wound healing system, the increase of cycles of freezing and thawing when preparing PVA hydrogels could bring better adhesive properties. Hence, the drug release process can be slowed down. Mallapragada and McCarthy-Schroeder [62] suggest that adhesion/release process of the PVA hydrogels in Mongia *et al.*'s

study is theoretically controlled by altering the crystallinity of PVA during the freezing and thawing process. Therefore, understanding the crystallinity of PVA can facilitate PVA hydrogels in pharmaceutical applications.

2.4 Why Studying Crystallinity of Polyvinyl Alcohol Matters

2.4.1 Improving PVA Products

Crystallisation is related to mechanical properties of materials, particularly for organics [64], as well as other physical properties such as solubility and diffusion coefficients, density, and tribological and optical properties [651][66]. As introduced in Section 2.1.2.3, the crystal structure of PVA is not well-established, and therefore, studying the precise crystal structure is helpful for tailoring PVA for broader and deeper applications.

Taking PVA hydrogels in biomedical and pharmaceutical areas as examples, mentioned in the last section, both applications have a strong correlation to the PVA crystallinity. In the biomedical field, a better understanding of PVA crystal structure could contribute to a more efficient way to form PVA crystals, leading to better mechanical properties for PVA products, for example, PVA artificial cartilages. Turning to the pharmaceutical applications, understanding PVA crystal structure is crucial for modulating the PVA crystallinity, and also for further controlling the properties of PVA drug carriers.

In addition, general commercial products can also be improved. For instance, the viscosity and the adhesive abilities of PVA glues can be improved by tuning the PVA crystal structures. To sum up, studying the PVA crystallinity is helpful to improve existing and developing PVA products.

2.4.2 Tackling Environmental Threat

Plastic pollution has become one of the most pressing environmental issues, as the rapidly increasing production of disposable plastic products overwhelms the world's ability to deal with them. It has deleterious effects on the environment, terrestrial and freshwater ecosystems, wildlife and human beings. Improper disposal and inefficient recycling of plastic packages are deemed as part of the biggest culprits causing plastic pollution [67][68].

Due to the advantages such as water-solubility and low toxicity, PVA can be a potential material for plastic packaging to help solve the above-mentioned issue. Nigro *et al*. [69] demonstrated that standard PVA powder and commercial PVA-based bags are ecotoxicologically safe. Although some scientists fear that processing effluents can introduce pollution to the environment [70], some papers [71][72] reported eco-friendly methods to degrade PVA by using the UV light and hydrogen peroxide (H_2O_2). Overall, PVA can be a future candidate to replace hard-to-degrade polyethylene (PE) and polypropylene (PP) bags.

However, PVA packages are not widely used in daily life. The main challenge is that the price of PVA packages is high, which comes from expensive additives used in PVA packaging materials. Additives including chitosan [73] and starch [74] are commonly used to achieve relatively desirable properties. Herein, some properties, for instance, gas barrier properties, are dominated by the crystallinity of PVA. Therefore, a better understanding of the crystal structure of PVA packing products can be helpful to develop stronger and more durable raw PVA packages, or at least, reduce the use of additives, and further reduce the price of PVA packages. The improvement in structural understanding may propel a generation of PVA packings, and hence, facilitate solving the plastic pollution problem.

2.5 Design of Using Electron Ptychography to Image Polyvinyl Alcohol

As introduced in the last chapter, electron ptychography can be a potential method to characterise PVA crystals at the molecular level even at the atomic scale. One of the areas of study in this thesis is to use electron ptychography to image and study PVA crystals.

As hydrogen bonding plays a significant part in the formation of PVA crystallites, the first step in this project is to use Fourier-transform infrared spectroscopy (FTIR) to characterise hydrogen bonding in PVA samples. After that, as discussed in Section 2.1.2.4, the next challenge in this project is that original PVA samples can have very low crystallinity, increasing the difficulty of the study. Based on previous research, freeze-thawing and annealing methods are applied for a more crystalline PVA sample. The overall crystallinity of freeze-thawed and annealed samples is then detected by X-ray diffraction (XRD).

Due to the lack of microscopic data from previous publications, PVA crystals are firstly imaged using high-resolution transmission electron microscopy (HRTEM) for basic local information of PVA crystals. Then, scanning transmission electron microscopy (STEM) and electron ptychography are applied for a more informative and detailed characterisation of PVA crystals.

According to microscopic data, it is expected to have a better understanding of PVA crystals, and some modifications based on old PVA models may be operated at this stage. Finally, simulations on STEM and electron ptychographic images of the new PVA model are conducted to further provide evidence for a modified the PVA crystal model.

To conclude, this project aims to use electron ptychography to study the local structures inside the PVA crystal. The findings of the electron ptychographic study are anticipated to improve the understanding of PVA crystals.

2.6 References

[1] Herrmann, W. O., & Haehnel, W. (1924). *Chem. Forschungsgemeinschaft*; DE-OS 450 286.

[2] James, K. (2016). Fabrication of polyvinyl alcohol/chitosan/bidens pilosa composite electrospun nanofibers and their enhanced antibacterial activities.

[3] Nawaz, A., & Hümmelgen, I. A. (2019). Poly (vinyl alcohol) gate dielectric in organic field-effect transistors. *Journal of Materials Science: Materials in Electronics*, *30*(6), 5299-5326.

[4] Squillace, O., Fong, R., Shepherd, O., Hind, J., Tellam, J., Steinke, N. J., & Thompson, R. L. (2020). Influence of PVAc/PVA hydrolysis on additive surface activity. *Polymers*, *12*(1), 205.

[5] Hedayati, H. R., Khorasani, M., Ahmadi, M., & Ballard, N. (2022). Preparation of well-defined Poly (Vinyl alcohol) by hydrolysis of Poly (Vinyl acetate) synthesized by RAFT suspension polymerization. *Polymer*, *246*, 124674.

[6] Abdullah, Z. W., Dong, Y., Davies, I. J., & Barbhuiya, S. (2017). PVA, PVA blends, and their nanocomposites for biodegradable packaging application. *Polymer-Plastics Technology and Engineering*, *56*(12), 1307-1344.

[7] Ye, M., Mohanty, P., & Ghosh, G. (2014). Morphology and properties of poly vinyl alcohol (PVA) scaffolds: impact of process variables. *Materials Science and Engineering: C*, *42*, 289-294.

[8] DeMerlis, C. C., & Schoneker, D. R. (2003). Review of the oral toxicity of polyvinyl alcohol (PVA). *Food and chemical Toxicology*, *41*(3), 319-326.

[9] Gaaz, T. S., Sulong, A. B., Akhtar, M. N., Kadhum, A. A. H., Mohamad, A. B., & Al-Amiery, A. A. (2015). Properties and applications of polyvinyl alcohol, halloysite nanotubes and their nanocomposites. *Molecules*, *20*(12), 22833-22847.

[10] Matsumura, S. (2005). Biodegradation of poly (vinyl alcohol) and its copolymers. *Biopolymers Online: Biology• Chemistry• Biotechnology• Applications*, *9*.

[11] Marten, F. L. (2002). Vinyl alcohol polymers. *Encyclopedia of polymer science and technology*.

[12] Peng, Z., Kong, L. X., Li, S. D., & Spiridonov, P. (2006). Poly (vinyl alcohol)/silica nanocomposites: morphology and thermal degradation kinetics. *Journal of nanoscience and nanotechnology*, *6*(12), 3934-3938.

[13] Aslam, M., Kalyar, M. A., & Raza, Z. A. (2018). Polyvinyl alcohol: A review of research status and use of polyvinyl alcohol-based nanocomposites. *Polymer Engineering & Science*, *58*(12), 2119-2132.

[14] Muppalaneni, S., & Omidian, H. (2013). Polyvinyl alcohol in medicine and pharmacy: a perspective. *J. Dev. Drugs*, *2*(3), 1-5.

[15] Nagarkar, R., & Patel, J. (2019). Polyvinyl alcohol: A comprehensive study. *Acta Sci. Pharm. Sci*, *3*(4), 34-44.

[16] Sekisui Specialty Chemicals.

https://www.sekisui-sc.com/products/polyvinyl-alcohol/.

Accessed January 30, 2023.

[17] Tubbs, R. K. (1966). Sequence distribution of partially hydrolyzed poly (vinyl acetate). *Journal of Polymer Science Part A-1: Polymer Chemistry*, *4*(3), 623-629.

[18] Marín Cardona, E. S., Rojas Camargo, J., & Ciro Monsalve, Y. A. (2014). A review of polyvinyl alcohol derivatives: promising materials for pharmaceutical & biomedical applications.

[19] Halima, N. B. (2016). Poly (vinyl alcohol): review of its promising applications and insights into biodegradation. *RSC advances*, *6*(46), 39823-39832.

[20] Wise, E. T., & Weber, S. G. (1995). A simple partitioning model for reversibly crosslinked polymers and application to the poly (vinyl alcohol)/borate system (" slime"). *Macromolecules*, *28*(24), 8321-8327.

[21] Young, R. J., & Lovell, P. A. (2011). *Introduction to polymers*. CRC press.

[22] Carrasco-Correa, E. J., Beneito-Cambra, M., Herrero-Martínez, J. M., & Ramis-Ramos, G. (2011). Evaluation of molecular mass and tacticity of polyvinyl alcohol by non-equilibrium capillary electrophoresis of equilibrium mixtures of a polymer and a dye. *Journal of Chromatography A, 1218*(16), 2334-2341.

[23] Moritani, T., Kuruma, I., Shibatani, K., & Fujiwara, Y. (1972). Tacticity of poly (vinyl alcohol) studied by nuclear magnetic resonance of hydroxyl protons. *Macromolecules*, *5*(5), 577-580.

[24] Mooney, R. C. (1941). An X-ray study of the structure of polyvinyl alcohol. *Journal of the American Chemical Society*, *63*(10), 2828-2832.

[25] Bunn, C. W. (1948). Crystal structure of polyvinyl alcohol. *Nature*, *161*(4102), 929-930.

[26] Sakurada, I., Fuchino, K., & Okada, N. (1950). Crystal structure of polyvinyl alcohol. *Bull. Inst. Chem. Res., Kyoto Univ.*, 1950, 23, 78-79.

[27] Bolto, B., Tran, T., Hoang, M., & Xie, Z. (2009). Crosslinked poly (vinyl alcohol) membranes. *Progress in polymer science*, *34*(9), 969-981.

[28] Hickey, A. S., & Peppas, N. A. (1995). Mesh size and diffusive characteristics of semicrystalline poly (vinyl alcohol) membranes prepared by freezing/thawing techniques. *Journal of membrane science*, *107*(3), 229-237.

[29] Assender, H. E., & Windle, A. H. (1998). Crystallinity in poly (vinyl alcohol). 1. An X-ray diffraction study of atactic PVOH. *Polymer*, 39(18), 4295-4302.

[30] Omidian, H., & Park, K. (2010). Introduction to hydrogels. *Biomedical applications of hydrogels handbook*, 1-16.

[31] Omidian, H., & Park, K. (2012). Hydrogels. *Fundamentals and applications of controlled release drug delivery*, 75-105.

[32] Gulrez, S. K., Al-Assaf, S., & Phillips, G. O. (2011). Hydrogels: methods of preparation, characterisation and applications. *Progress in molecular and environmental bioengineering-from analysis and modeling to technology applications*, *117150*.

[33] Nikolić, L. B., Zdravković, A. S., Nikolić, V. D., & Ilić-Stojanović, S. S. (2019). Synthetic hydrogels and their impact on health and environment. *Cellulose-Based Superabsorbent Hydrogels*, 1-29.

[34] Federer, C., Kurpiers, M., & Bernkop-Schnürch, A. (2020). Thiolated chitosans: A multi-talented class of polymers for various applications. *Biomacromolecules*, *22*(1), 24-56.

[35] Leichner, C., Jelkmann, M., & Bernkop-Schnürch, A. (2019). Thiolated polymers: Bioinspired polymers utilizing one of the most important bridging structures in nature. *Advanced Drug Delivery Reviews*, *151*, 191-221.

[36] Jeong, B., Kim, S. W., & Bae, Y. H. (2012). Thermosensitive sol–gel reversible hydrogels. *Advanced drug delivery reviews*, *64*, 154-162.

[37] Yan, Y., Xu, S., Liu, H., Cui, X., Shao, J., Yao, P., Huang, J., Qiu, X., & Huang, C. (2020). A multi-functional reversible hydrogel adhesive. *Colloids and Surfaces A: Physicochemical and Engineering Aspects*, *593*, 124622.

[38] Mallapragada, S. K., & McCarthy-Schroeder, S. (2000). Poly (vinyl alcohol) as a drug delivery carrier. In *Handbook of pharmaceutical controlled release technology* (pp. 31-46). Marcel Dekker.

[39] Wong, D., & Parasrampuria, J. (1996). Polyvinyl alcohol. In *Analytical profiles of drug substances and excipients* (Vol. 24, pp. 397-441). Academic press.

[40] Lozinsky, V. I. (1998). Cryotropic gelation of poly (vinyl alcohol) solutions. *Russian Chemical Reviews*, *67*(7), 573-586.

[41] Lozinsky V.I., Plieva F.M. (1998) Poly (vinyl alcohol) cryogels employed as matrices for cell immobilization. 3. Overview of recent research and developments. Enzyme and Microbial Technology 23: 227-242.

[42] Lozinsky, V. I., Vainerman, E. S., Domotenko, L. V., Mamtsis, A. M., Titova, E. F., Belavtseva, E. M., & Rogozhin, S. V. (1986). Study of cryostructurization of polymer systems VII. Structure formation under freezing of poly (vinyl alcohol) aqueous solutions. *Colloid and Polymer Science*, *264*, 19-24.

[43] Song, K., Zhang, Y., Meng, J., Green, E. C., Tajaddod, N., Li, H., & Minus, M. L. (2013). Structural polymer-based carbon nanotube composite fibers: Understanding the processing–structure–performance relationship. *Materials*, *6*(6), 2543-2577.

[44] Tan, C. J., & Tong, Y. W. (2007). The effect of protein structural conformation on nanoparticle molecular imprinting of ribonuclease a using miniemulsion polymerization. *Langmuir*, *23*(5), 2722-2730.

[45] Finch, C. A. (1983). Some properties of polyvinyl alcohol and their possible applications. *Chemistry and Technology of Water-Soluble Polymers*, 287-306.

[46] Finch, C. A. (Ed.). (1973). *Polyvinyl alcohol; properties and applications*. John Wiley & Sons.

[47] Ng, K. W., Wanivenhaus, F., Chen, T., Hsu, H. C., Allon, A. A., Abrams, V. D., Torzilli, P. A., Warren, R. F., & Maher, S. A. (2012). A novel macroporous polyvinyl alcohol scaffold promotes chondrocyte migration and interface formation in an in vitro cartilage defect model. *Tissue Engineering Part A*, *18*(11-12), 1273-1281.

[48] Schonberger, H., Baumann, A., Keller, W., & Pogopetris, P. (1997). Study of microbial degradation of polyvinyl alcohol (PVA) in wastewater treatment plants. *American Dyestuff Reporter*, *86*(8), 9-18.

[49] Soe, H. M. S. H., Kerdpol, K., Rungrotmongkol, T., Pruksakorn, P., Autthateinchai, R., Wet-Osot, S., Loftsson, & T., Jansook, P. (2023). Voriconazole Eye Drops: Enhanced Solubility and Stability through Ternary Voriconazole/Sulfobutyl Ether β-Cyclodextrin/Polyvinyl Alcohol Complexes. *International Journal of Molecular Sciences*, *24*(3), 2343.

[50] Byrne, D., Boeije, G., Croft, I., Hüttmann, G., Luijkx, G., Meier, F., Parulekar, Y., & Stijntjes, G. (2021). Biodegradability of polyvinyl alcohol-based film used for liquid detergent capsules. *Tenside Surfactants Detergents*, *58*(2), 88-96.

[51] Hassan, C. M., & Peppas, N. A. (2000). Structure and applications of poly (vinyl alcohol) hydrogels produced by conventional crosslinking or by freezing/thawing methods. *Biopolymers· PVA hydrogels, anionic polymerisation nanocomposites*, 37-65.

[52] Noguchi, T., Yamamuro, T., Oka, M., Kumar, P., Kotoura, Y., Hyonyt, S. H., & Ikadat, Y. (1991). Poly (vinyl alcohol) hydrogel as an artificial articular cartilage: evaluation of biocompatibility. *Journal of Applied Biomaterials*, *2*(2), 101-107.

[53] Paul, W., & Sharma, C. P. (1995). Polyacrylonitrile-reinforced poly (vinyl alcohol) membranes: Mechanical and dialysis performance. *Journal of applied polymer science*, *57*(12), 1447-1454.

[54] Bao, Q. B., & Yuan, H. A. (2000). Artificial disc technology. *Neurosurgical focus*, *9*(4), 1-7.

[55] Wan, W. K., Campbell, G., Zhang, Z. F., Hui, A. J., & Boughner, D. R. (2002). Optimizing the tensile properties of polyvinyl alcohol hydrogel for the construction of a bioprosthetic heart valve stent. *Journal of Biomedical Materials Research: An Official Journal of the Society for Biomaterials, the Japanese Society for Biomaterials, and the Australian Society for Biomaterials and the Korean Society for Biomaterials*, *63*(6), 854-861.

[56] Kobayashi, M. (2004). A study of polyvinyl alcohol-hydrogel (PVA-H) artificial meniscus in vivo. *Bio-medical materials and engineering*, *14*(4), 505-515.

[57] Kobayashi, M., Chang, Y. S., & Oka, M. (2005). A two-year in vivo study of polyvinyl alcohol-hydrogel (PVA-H) artificial meniscus. *Biomaterials*, *26*(16), 3243-3248.

[58] Gu, Z. Q., Xiao, J. M., & Zhang, X. H. (1998). The development of artificial articular cartilage–PVA-hydrogel. *Bio-medical materials and engineering*, *8*(2), 75-81.

[59] Kimura, T., Sato, K., Sugimoto, K., Tao, R., Murakami, T., Kurosaki, Y., & Nakayama, T. (1996). Oral administration of insulin as poly (vinyl alcohol)-gel spheres in diabetic rats. *Biological and Pharmaceutical Bulletin*, *19*(6), 897-900.

[60] Hassan, C. M., Stewart, J. E., & Peppas, N. A. (2000). Diffusional characteristics of freeze/thawed poly (vinyl alcohol) hydrogels: applications to protein-controlled release from multilaminate devices. *European Journal of Pharmaceutics and Biopharmaceutics*, *49*(2), 161-165.

[61] Pruyn, S. A., Rajabi, M., Adeyeye, M., & Mousa, S. A. (2019). Pharmaceutical applications of water-soluble polymers in nanomedicine and drug delivery. In *The Road from Nanomedicine to Precision Medicine* (pp. 299-334). Jenny Stanford Publishing.

[62] Mallapragada, S. K., & McCarthy-Schroeder, S. (2000). Poly (vinyl alcohol) as a drug delivery carrier. In *Handbook of pharmaceutical controlled release technology* (pp. 31-46). Marcel Dekker.

[63] Mongia, N. K., Anseth, K. S., & Peppas, N. A. (1996). Mucoadhesive poly (vinyl alcohol) hydrogels produced by freezing/thawing processes: applications in the development of wound healing systems. *Journal of Biomaterials Science, Polymer Edition*, *7*(12), 1055-1064.

[64] Saha, S., Mishra, M. K., Reddy, C. M., & Desiraju, G. R. (2018). From molecules to interactions to crystal engineering: mechanical properties of organic solids. *Accounts of chemical research*, 51(11), 2957-2967.

[65] Mileva, D., Tranchida, D., & Gahleitner, M. (2018). Designing polymer crystallinity: An industrial perspective. *Polymer Crystallization*, 1(2), e10009.

[66] Mark, J. E. (Ed.). (2007). *Physical properties of polymers handbook* (Vol. 1076, p. 825). New York: Springer.

[67] Ritchie, H., & Roser, M. (2018). Plastic pollution. *Our World in Data*.

[68] MacLeod, M., Arp, H. P. H., Tekman, M. B., & Jahnke, A. (2021). The global threat from plastic pollution. *Science*, *373*(6550), 61-65.

[69] Nigro, L., Magni, S., Ortenzi, M. A., Gazzotti, S., Della Torre, C., & Binelli, A. (2022). Are "liquid plastics" a new environmental threat? The case of polyvinyl alcohol. Aquatic Toxicology, 248, 106200.

[70] Giroto, J. A., Guardani, R., Teixeira, A. C. S., & Nascimento, C. A. O. D. (2006). Study on the photo-Fenton degradation of polyvinyl alcohol in aqueous solution. *Chemical Engineering and Processing: Process Intensification*, *45*(7), 523-532.

[71] Sun, W., Chen, L., & Wang, J. (2017). Degradation of PVA (polyvinyl alcohol) in wastewater by advanced oxidation processes. *Journal of Advanced Oxidation Technologies*, *20*(2).

[72] Hamad, D., Mehrvar, M., & Dhib, R. (2014). Experimental study of polyvinyl alcohol degradation in aqueous solution by UV/H2O2 process. *Polymer Degradation and Stability*, *103*, 75-82.

[73] Yu, Z., Li, B., Chu, J., & Zhang, P. (2018). Silica in situ enhanced PVA/chitosan biodegradable films for food packages. *Carbohydrate polymers*, *184*, 214-220.

[74] Ismail, H., & Zaaba, N. F. (2011). Effect of additives on properties of polyvinyl alcohol (PVA)/tapioca starch biodegradable films. *Polymer-Plastics Technology and Engineering*, *50*(12), 1214-1219.

Chapter 3. Introduction to Peptide Amphiphiles

3.1 General Introduction

3.1.1 Amino Acids

Amino acids are defined as organic compounds with both amino and carboxylic acid functional groups [1]. Figure 3.1 shows the general structure of an amino acid. The side group R here differentiates various types of amino acids with different physical and chemical properties. According to their chemical compositions, side groups can be categorised into different groups, such as hydrophobic and hydrophilic; aliphatic and aromatic; neutral, positively and negatively charged [2].

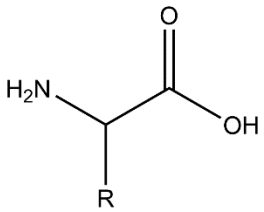


Figure 3.1 General structure of an amino acid.

Although there are hundreds of amino acids existing in nature, only 20 types of amino acids are found in human bodies [3]. Only less than water, amino acids (mainly in the form of proteins) are the second-largest component of human muscles and other tissues [4]. Some reports [5][6] also demonstrate that amino acids can be crucial to the life emergence on the earth.

3.1.2 Peptide, Peptide Amphiphiles and Protein

Peptides are oligomers consisting of several amino acids linked by chemical bonds [7]. Figure 3.2 shows the formation of a dipeptide from two amino acids. The chemical bond in the red square is the peptide bond, formed with the condensation reaction [7]. The repeating -N-C-C- unit shown in the green zigzag in Figure 3.2 is known as the peptide backbone, and distinctive side groups shown in the blue square contributes to a great diversity of peptides.

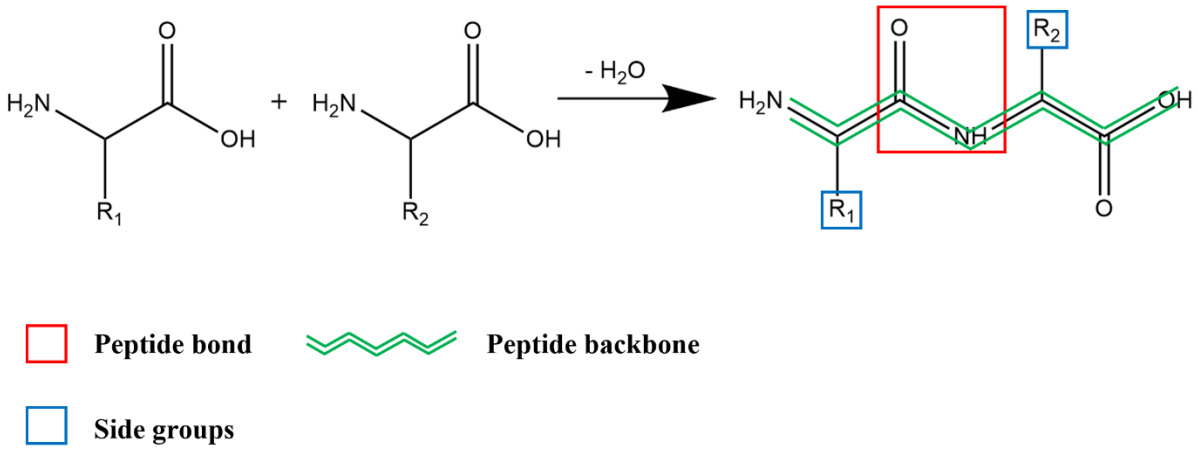


Figure 3.2 Formation of a peptide from amino acids. A peptide bond, a peptide backbone and two side groups are illustrated in the product.

Peptide amphiphiles (in abbreviation, PA, also known as amphiphilic peptides) is a certain type of peptide made up of amino acids with both hydrophobic and hydrophilic side groups, or hydrophilic amino acids attached to a lipid tail [8]. This kind of materials was firstly designed by Stupp's lab [9][10] with a self-assembling core-shell, where several different self-assembling systems based on PAs were developed later. Those systems will be discussed in Section 3.3.1 later. The self-assembly of PAs are also linked to the secondary structures of peptides, which will be introduced in Section 3.2.

A peptide with a short molecular length is called oligopeptides, whereas polypeptides have a longer peptide chain. With the increase of the length of molecular chain, proteins are composed of a single polypeptide with more than 50 amino acids [11] or several polypeptides arranged in a biologically functional way [12]. The four-tier structures of peptides and proteins will be introduced in the next section, but as this work are studying material structures at the peptide level, other backgrounds of proteins will not be mentioned further.

3.1.3 Four Levels of Structures of Amino Acids, Peptides and Proteins

To understand the structures ranging from an amino acid to a peptide, to large proteins, biologists distinguish four levels of organisation [13]. The structure of each level is presented in Figure 3.3 [14].

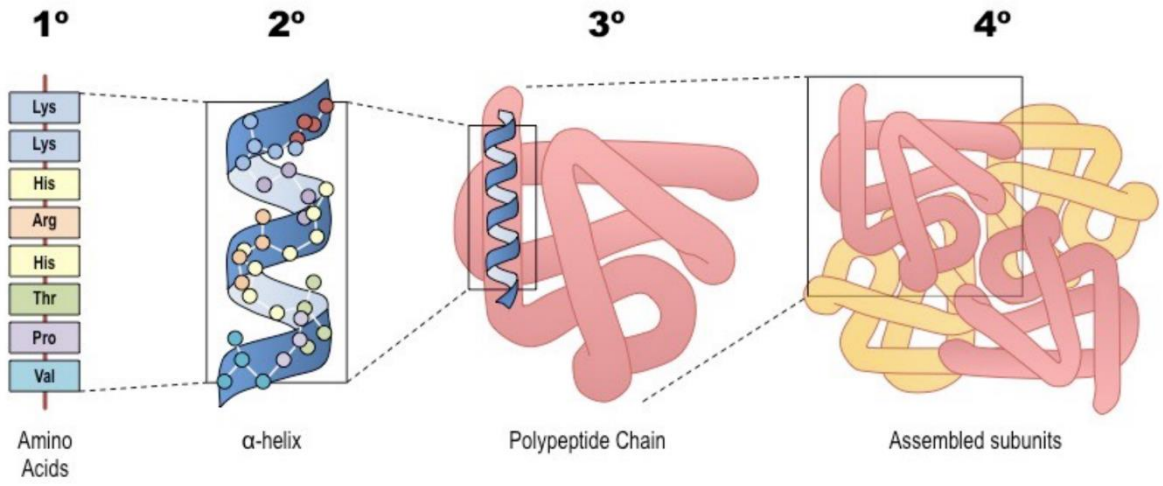


Figure 3.3 Schematic illustrations of four levels of protein structures. Reproduced from Reference [14].

The primary structure is defined as the sequence of amino acids in a polypeptide chain [15]. Taking F8 (a PA used in this work, and its structure is shown in Figure 3.4) as an example, the

primary structure of PA is FEFKFEFK. The primary structures of natural proteins *in vivo* are determined by cellular genetic codes, and even a single amino acid change causes a gene mutation, which almost always results in a non-functional protein [16]. By contrast, proteins and peptides *in vitro* can have designed primary structures for various desirable applications [17][18]. Because it determines the nature of interactions between side groups of different amino acids, primary structure governs all subsequent levels of protein organisation [15][19][20].

Secondary structures refer to the local folded structures that exist within a peptide as a consequence of interactions between backbone atoms [21]. These interactions are mainly inter-chain hydrogen bonding between the amine and carboxyl groups [22][23]. Because of the intimate involvement of hydrogen bonding, secondary structures also provide a certain of mechanical stability to the peptide chain [24]. The two most common formations of secondary structures are the α-helix and the β-sheet [20][21], but there are also other elements such as β-turn and random coils occurring in some systems [25]-[27].

The tertiary structure of a protein or a peptide stands for the three-dimensional shape of a molecule as a whole [28]. The tertiary structure of a protein is formed with joint influences, including hydrogen bonding between side groups, electrostatic forces, hydrophobicity, disulphide linkages, and van der Waals forces [28]-[30].

Several tertiary structures of polypeptides (also referred to as subunits)) then can form a quaternary structure, which normally perform as form a biologically active protein [31][32]. Unlike the previous three levels of protein structure, quaternary structure does not exist in all proteins since some proteins are composed of a single peptide chain [31][32].

Although the factors that influence protein crystallisation are poorly understood, some researchers believe that secondary structures play crucial roles in forming peptide and protein crystals [33]-[35]. As this project is to use a new microscopic technique to refine understanding of peptide crystals, details of secondary structures will therefore be elaborated in Section 3.2.

3.1.4 Amino Acids and Peptide Amphiphiles in This Work

Figure 3.4 shows the structure of peptides and amino acids used in this work. F8 and F9 have most publications among these five types. According to previous studies on F8 and F9 [36]-[40], they tend to form the β-sheet secondary structure and fibrous tertiary structure. This work is to apply microscopic techniques to study F8 and F9 fibres and their β-sheet crystal structures.

The proline (P) group is designed to, and functions as, a secondary-structural disruptor to impede peptides from conforming to an α-helix or β-sheet conformation [41][42]. Proline also works on the tertiary structure of some peptides by kinking or twisting peptide fibres mainly via the steric effect [43]. Although FP is also mainly made up of the phenylalanine (F), glutamic acid (E) and lysin (K) amino acids that constitute F8 & F9, in this case a proline is located at the middle of the molecule. This work will investigate the influence of the proline (P) group on both tertiary structure and secondary structure of FP.

Substituting two phenylalanine (F) with two alanine (A) at different positions, both FAFA and F2A2 are found to have coexisting α-helix and β-sheet secondary structures [39]. This work will also use microscopic methods to prove the coexistence of them.

The details of the experimental design in this work can be found in Section 3.6.

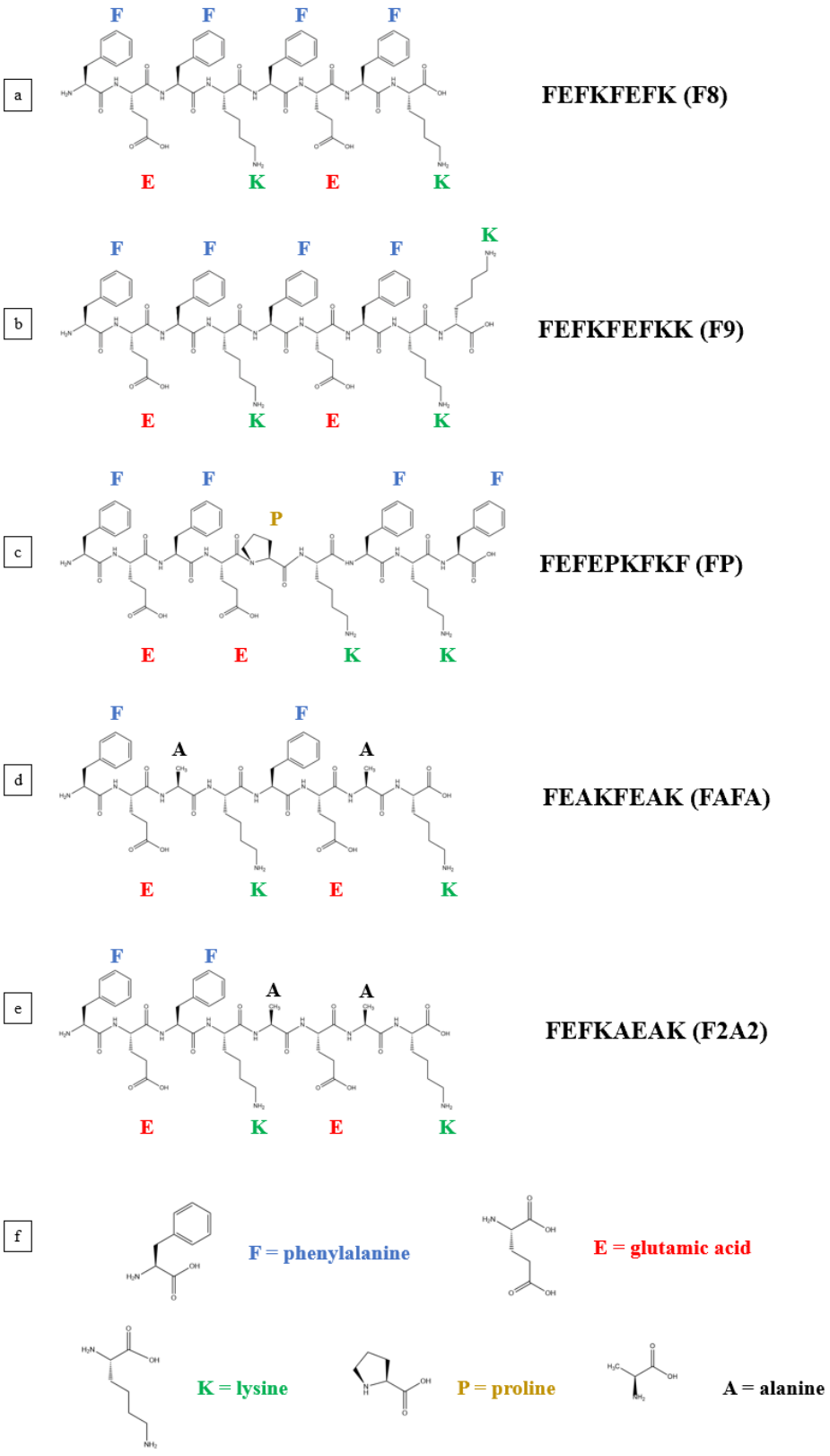


Figure 3.4 Structures of amino acids and peptides used in this project.

3.2 Secondary Structures of Peptides and Proteins

3.2.1 Alpha-helix

The alpha helix (α-helix) is a common right-hand helix motif in the secondary structure of peptides and proteins [44][45]. It was discovered by Linus Pauling, Robert Corey and Herman Branson in the early 1950s. In 1950 and 1951, they published two papers [46][47] to introduce their models of polypeptide chains with the spiral and helical configurations. Pauling therefore received his first Nobel Prize in 1954 "for his study into the nature of the chemical bond and its application to the understanding of the structure of complex molecules", which included the discovery of the α-helix structure. Furthermore, according to Egli and Zhang [44], the α-helix model also inspired Watson and Crick to propose the double helix terminology for the structure of DNA.

The well-acknowledged α-helix model is shown in Figure 3.5. Within an α-helix, each amino acid residue corresponds to a 100° turn, and therefore, a helix has the non-integral, 3.6 residues per turn [48][49]. As the Pauling-Corey-Branson models [46][47] suggest each amino acid projects to 0.15 nm along the helical axis (which was also supported by Max Perutz in his *Nature* paper published 1951 [50]), the pitch of the alpha-helix (the vertical distance between consecutive turns of the helix) is 0.54 nm, which is the product of 1.5 and 3.6 [46][47][49]. The most important feature of an α-helix is that the N-H group of an amino acid forms a hydrogen bond with the C=O group of the amino acid four residues earlier. For instance, as shown in Figure 3.5(d), in an α-helix consisting of five amino acids, hydrogen bonding forms between the C=O group of amino acid No.1 to the N-H group of amino acid No.5 [51]. This repeated “i+4 towards i” hydrogen bonding is the most prominent feature of an α-helix [49].

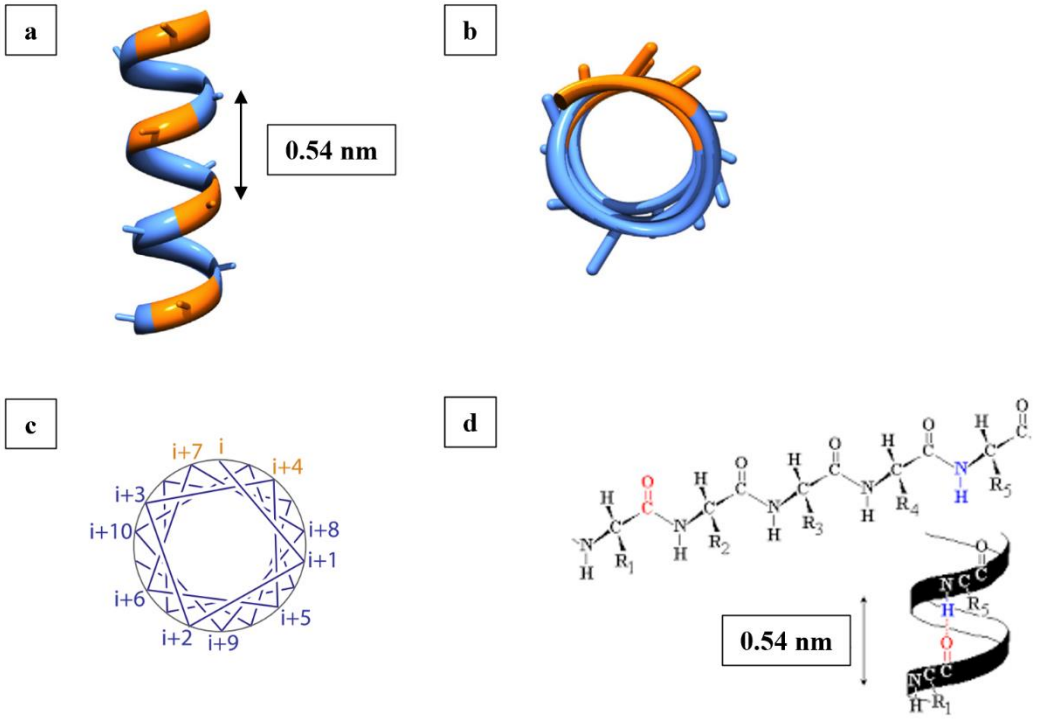


Figure 3.5 Schematics of α-helix in peptides and proteins. Reproduced from references [48] and [51]. (a) The side-view of the α-helix model, with i, i + 4, i + 7 and i + 11 residues displayed on the same side. (b) The top-down view of the α-helix model. (c) The geometric model of the α-helical wheel. (d) An α-helix consisting of five amino acids. Hydrogen bonding forms between the C=O group of amino acid No.1 to the N-H group of amino acid No.5.

Pace and Scholtz [52] also found that different amino acids have varying propensities to form an α-helix structure. For the amino acids used in this project, alanine (A) is extremely favourable to form the α-helix structure. Glutamic acid (E) and lysine (K) have relatively high helix-forming propensities, whereas phenylalanine (F) and proline (P) have poor helix-forming propensities [52]. According to Botwright's FTIR results [39], α-helix forms an element of FAFA and F2A2's secondary structures with the coexistence of β-sheet structures, but no α-helix structures were found in F8, F9 and FP.

The crystallography of α-helix peptides or proteins have not been well established. Electron ptychography introduced in Chapter 1 can be a potential method for the crystallographic study on α-helix crystals. Unfortunately, in this work, no appropriate α-helix FAFA or F2A2 crystals were found (as will be shown in Chapter 6) for the electron ptychographic imaging, but a methodology based on this technique will be introduced as a part of future work in Chapter 9.

3.2.2 Beta-sheet

Another common type of secondary structure of peptides and proteins are beta-sheet (β-sheet), which is also known as β-pleated or β-pleated sheet. Beta sheets are made up of beta strands (β-strands) that are connected laterally by hydrogen bonds, resulting in a pleated sheet [53]. The β-sheet structure was discovered in keratin fibres by William Astbury for the first time in 1933 [54]. X-ray analysis of these fibres revealed that they are composed of parallel or antiparallel extended β-strands. Based on Astbury's results, Pauling and Corey (discoverers of the α-helix structure) [55] suggest refined structures for both parallel and antiparallel sheets. Their parallel and antiparallel models are still the most accepted ones for the β-sheet structure to date.

The generalised β-sheet models (made by F8 molecules) are shown in Figure 3.6, where side groups are removed for clarity, and only backbones of F8 are shown here as the example. The arrangement of the side groups arrangement is not very well studied, as shown in Figure 3.7, according to previous studies [56][57], side groups can obliquely locate inter-sheet in a direction with a y axis (will be elaborated later) component.

Two typical arrangements, namely parallel and anti-parallel β-sheet structures are shown in Figure 3.6(b) and 3.6(c). The difference between parallel and anti-parallel structures is determined by how the end groups align in the β-sheet plane [58][59]. This contributes to their different orientations of hydrogen bonding, where hydrogen bonds of parallel sheets are slanted in alternate directions, rather than perpendicular to the strands, as seen in antiparallel sheets.

Following that, some crystallographic and computational studies have improved the understanding of the β-sheet structure. According to Maji *et al.*'s [60] and Serpell's [61] papers, β-sheet peptide crystals follow the orthorhombic crystal system. The lattice directions have not been well defined, but to make the crystal information clear, the principal lattice directions are made and shown in Figure 3.6. The molecular-chain axis is the z axis, the β-sheet structure, with the intermolecular hydrogen bonding lies in the xz plane, and layers of beta sheets are arranged along the y axis. As for the spacings marked in Figure 3.6, d_1 is the spacing between the adjacent strands within the β-sheet plane (will be called the β-sheet spacing in the rest of thesis), and d_2 refers to the inter-sheet spacing along the y axis, while d_3 represents the repeat distance along the chain axis. Many previous studies suggest that d_1 ranges from 0.44 to 0.47 nm [62]-[64], and this inter-strand d-spacing is the sign for peptide samples to suggest their β-sheet secondary structure [64]. The repeat distance along the molecular axis is around 0.70 nm [62][65], which is twice that of a single amino-acid length along the molecular axis [66][67]. d_2 varies significantly from peptide to peptide, but this study will focus on images taken along the [010] direction, so this spacing is less relevant to later results. As a reference to build peptide models, this work uses 1.07 nm from Serpell's paper [61] for the length of d_2.

All suggested spacings above were determined by XRD and molecular calculation methods, which cannot provide direct information to understand the full structure. Electron

ptychography will be used for the direct observation of the PA β-sheet crystal information in Chapter 7.

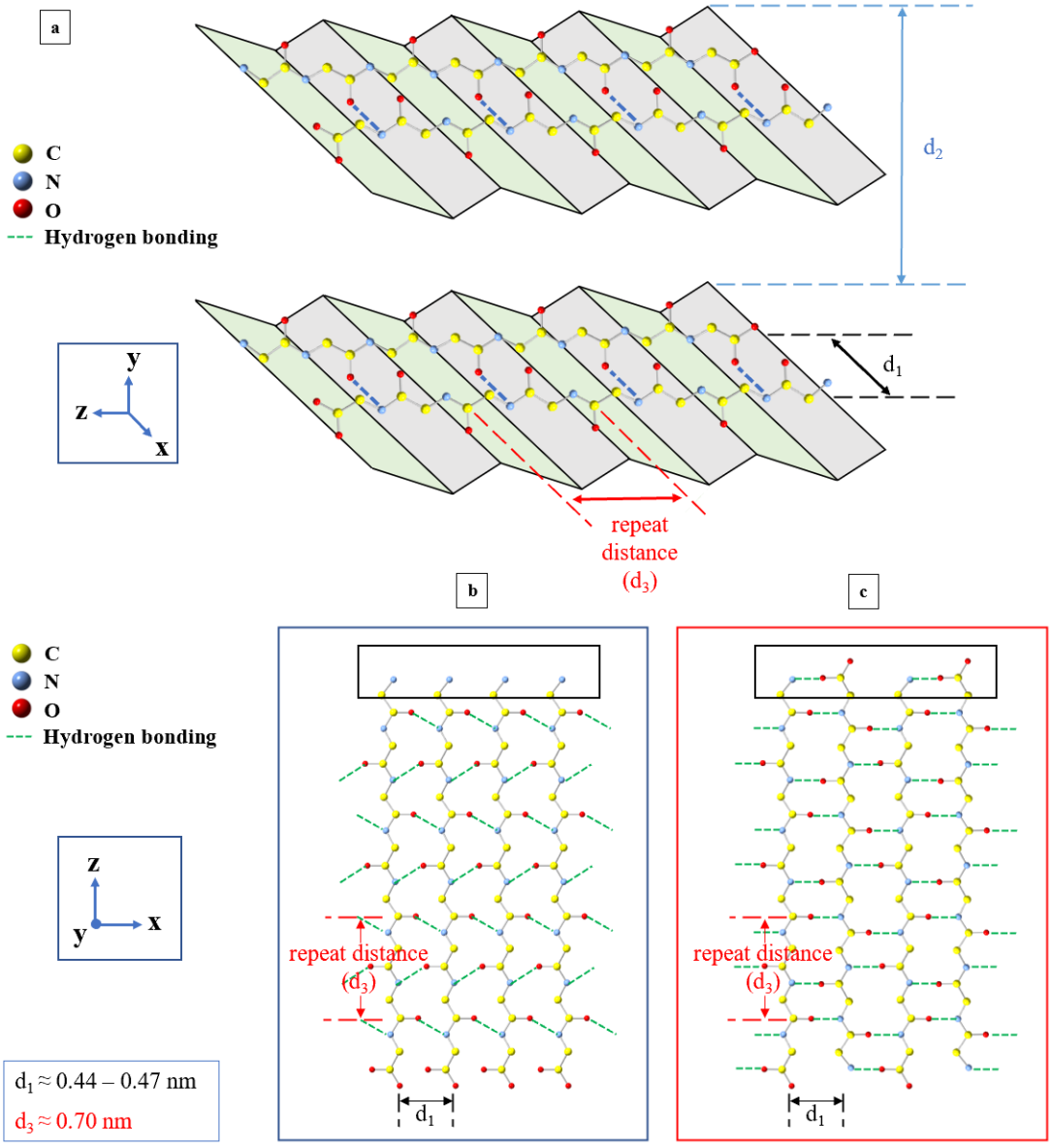


Figure 3.6 Generalised parallel and anti-parallel β-sheet structures and the hydrogen bonding distribution in each structure. In all cases, the z axis is defined as the molecular axis, with the β-sheet lying in the xz plane. (a) A 3D model of anti-parallel β-sheet structure showing the key repeat distances: d_1: the β-sheet spacing, d_2: the inter-sheet spacing, repeat distance: the amino acid repeat distance (along the chain axis). (b) A 2D

model of one sheet of parallel β-sheet structure. (c) A 2D model of one sheet of anti-parallel β-sheet structure.

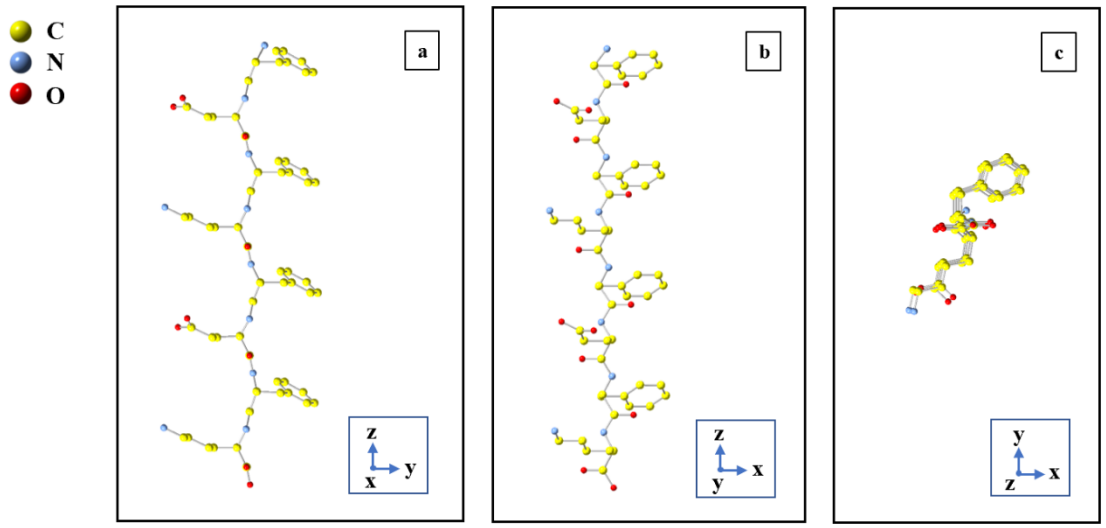


Figure 3.7 A 3D molecular model of F8 single molecule. (a) View from the [100] direction. (b) View from the [010] direction. (c) View from the [001] direction.

Turing to PAs used in this work, previous studies on F8 and F9 by our group [39][40] and Saiani's group [36][38],[68]-[71] demonstrate that they tend to form the β-sheet secondary structure, but it is still not clear whether the structure is parallel, antiparallel, or a mixture of both. Electron ptychography will be used in Chapter 7 to explore the formations of β-sheet structures of F8 and F9. Although FP has a slightly different nature of amino acids, it is also mainly made up by phenylalanine (F), glutamic acid (E) and lysine (K). Additionally, as introduced in the last section, proline (P) has poor propensities to form another main secondary structure, α-helix [52], it is therefore expected that FP are more likely to form β-sheet structure, and this work will also investigate the influence of the proline group on the secondary structure of FP.

3.2.3 Beta-Turn and Beta-Hairpin

Besides the two most common secondary structural elements, alpha helices and beta sheets, a secondary structure in the form of beta turns occurs as well.

A beta turn (β-turn) is a sort of secondary structure in proteins that causes the polypeptide chain to reverse orientation in the space of four residues [72][73]. As shown in Figure 3.8(a), the β-turn structure can be formed in two ways which are different due to the conformational isomerism. However, in both cases, hydrogen bonding forms between the C=O group of amino acid No.1 to the N-H group of amino acid No.4 [72][74]. In addition, the common beta-hairpin (β-hairpin, and some research classify it as an individual secondary structure) structure consists of two anti-parallel beta strands and a beta turn (shown in Figure 3.8(b)) [75][76].

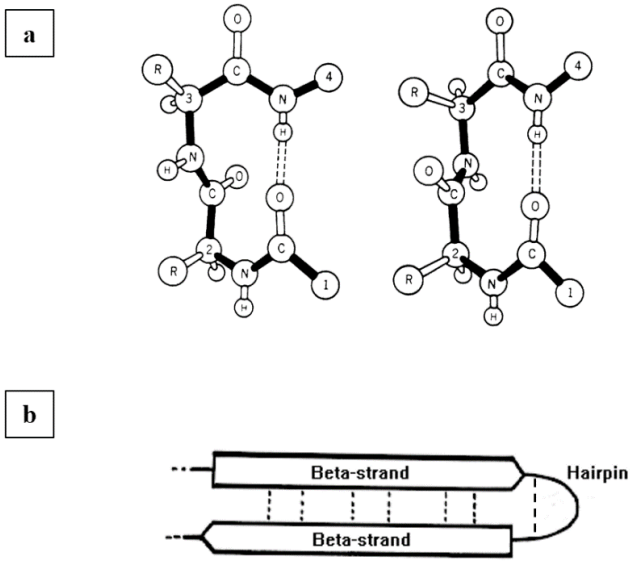


Figure 3.8 (a) Schematic of two types of beta turns. Reproduced from reference [74]. (b) A beta hairpin unit, consisting of two anti-parallel beta strands with a beta turn. Reproduced from reference [75].

3.2.4 Random Coils

Certain sections of the protein and peptide chains lack regular secondary structures shown in the last three sections and are devoid of a regular hydrogen bonding pattern [76][77]. They are known as random coils. Their constituents are terminal arms (including N-terminus and the C-terminus) and loops (connecting regular secondary structure elements). As shown in Figure 3.9, random coils together with above regular secondary structures build up tertiary structures of proteins and peptides [28][78].

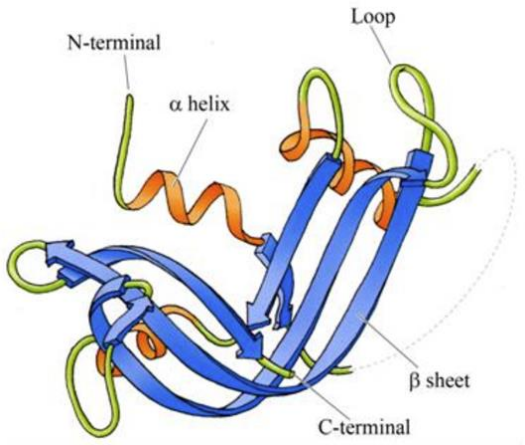


Figure 3.9 A tertiary structure composed of different types of secondary structures, including α-helix, β-sheet, terminal arms, and loops. Reproduced from reference [78].

3.3 Self-assembling Peptide-Amphiphile Fibres and Hydrogels

3.3.1 General Introduction to the Self-assembly of Peptide Amphiphiles

The capacity of molecules to link through noncovalent interactions into organised 3D structures via a bottom-up strategy is referred to as self-assembly [79]. Peptide amphiphiles self-assemble in aqueous solutions, dictated by the interactions of the hydrophobic and hydrophilic amino acid residues with water [2][39]. Figure 3.10 presents the self-assembly process from the peptide primary structure to peptide fibres and hydrogels. The figure is made with the aid of a number of references [2],[39],[40],[53],[80]-[89].

As introduced in the last section, the first stage is the self-assembly of peptides to secondary structures owing to intra-molecular hydrogen bonding. Following that, different peptides with different amino acid sequences and natures can form various peptide protofibrils out of interactions including inter-molecular hydrogen bonding, hydrophobicity, ionic interaction, π-π stacking, van der Waal force, *etc*. Herein, hydrophobicity is the main driving force for PAs with β-sheet conformations, and π-π stacking also plays a significant role for PAs with aromatic groups [39][90][91].

On the next stage, protofibrils in filament (straight and helical) forms can then grow to become peptide fibrils. Meanwhile, the nucleation and agglomeration of some globular protofibrils generate crosslinked fibrils. Besides the formation of fibrils, other globules aggregate to peptide micelles [89][92]. Finally, peptide hydrogels are constructed when the peptide concentration exceeds the critical gelation concentration (CGC) by peptide fibre entanglement and agglomeration [39]. The formation methods determine that most peptide hydrogels are

physical hydrogels [39][40] (which was elaborated in Section 2.2. Briefly speaking, physical hydrogels are made of non-covalent linkages). Peptide hydrogels have great potential to be used in tissue engineering and drug delivery, and their applications will be further introduced in Section 3.4.

As shown in Figure 3.10 and introduced above, there are various routes for the peptide self-assembly into fibres and hydrogels. A number of self-assembling peptide systems have been designed and studied, and the following section will detail three major systems.

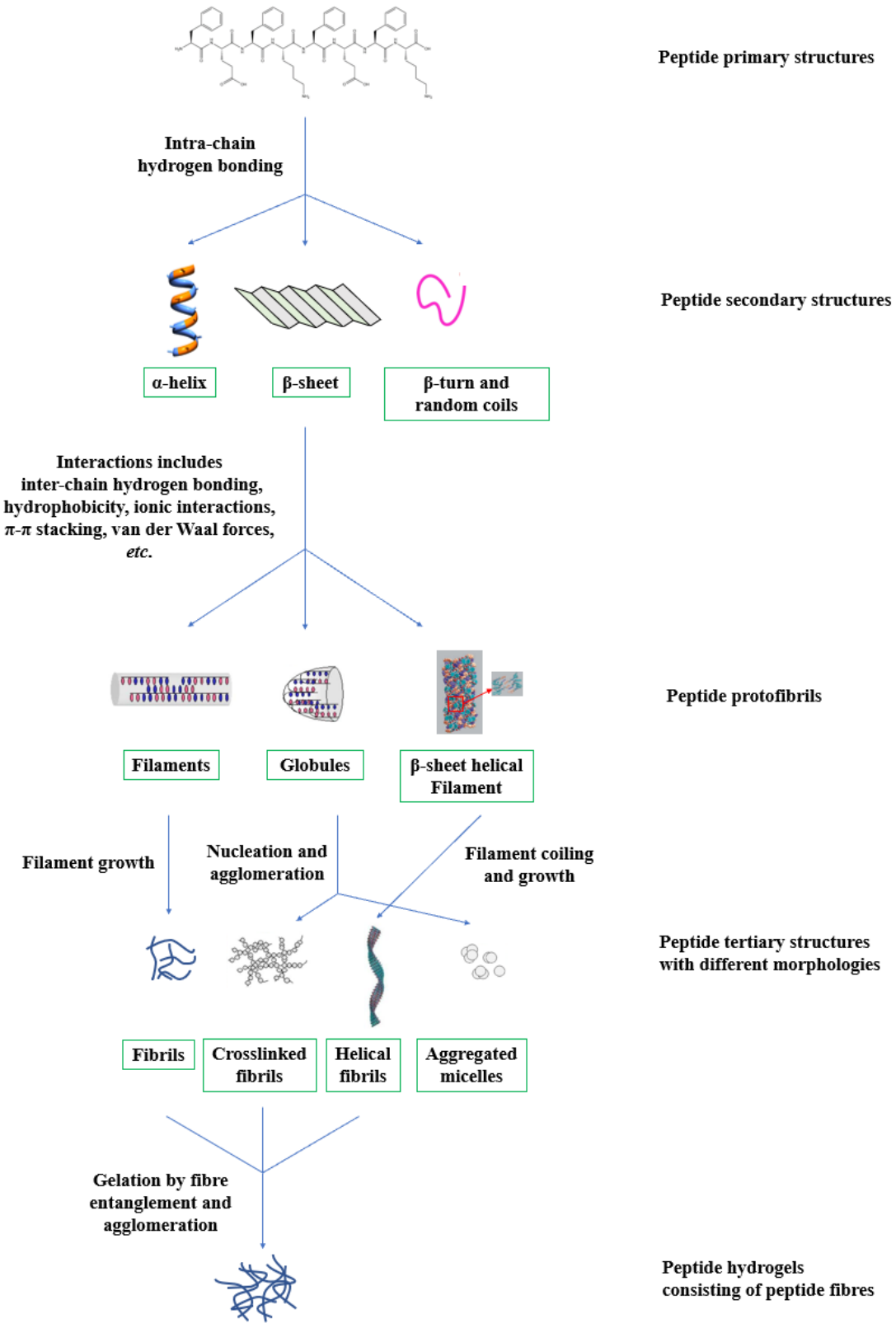


Figure 3.10 Schematic of typical peptide self-assembly into hydrogels, recreated from a variety of sources [2],[39],[40],[53],[80]-[89].

3.3.2 Different Systems of Self-assembling Peptide-Amphiphile Fibres

3.3.2.1 Surfactant Systems

Surfactants are chemical compounds that reduce the surface tension or interfacial tension between two liquids, a liquid and a gas, or a liquid and a solid [93]. As shown in Figure 3.11, surfactants are amphiphilic, which means that each molecule has both a hydrophilic "water-seeking" head and a hydrophobic "water-avoiding" tail [94]. The first PA self-assembling system was designed by Stupp's group in 2001 [9], as the self-assembling PA has a similar structure of the surfactants, so that this system is called a surfactant system.

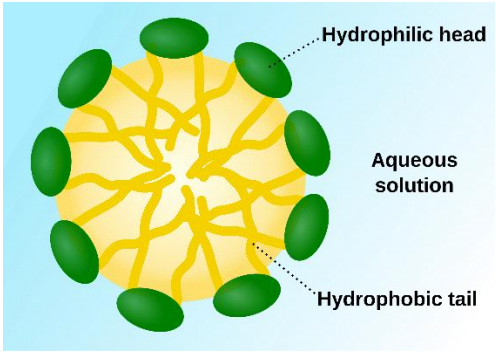


Figure 3.11 Schematic of surfactant compositions. Reproduced from Reference [93].

Figure 3.12 shows the design of the surfactant self-assembling system published in Stupp's group's paper [9]. The peptide molecule consists of 5 regions, and each region plays different roles in the self-assembly. Region 1 is a long alkyl tail that offers hydrophobicity to the molecule. Region 2 is composed of 4 cysteine residues. Disulphide bonds can from by oxidation in this region, and they can polymerise the peptide structure, which can facilitate the self-assembly. Region 3 consists of three glycine residues, and they can convey hydrophilic characters to the molecule. The last two regions are bioactive, where phosphorylated serine

residue in region 4 is designed to react with calcium ions and mineralisation, and the final section is made up of the cell-adhesion motif RGD (R: arginine, G: glycine, and D: aspartic acid). As a result, Hartgerink *et al.* [9] found that the self-assembling fibre has the hydrophobic lipid core, and outer hydrophilic surface form β-sheet secondary structures.

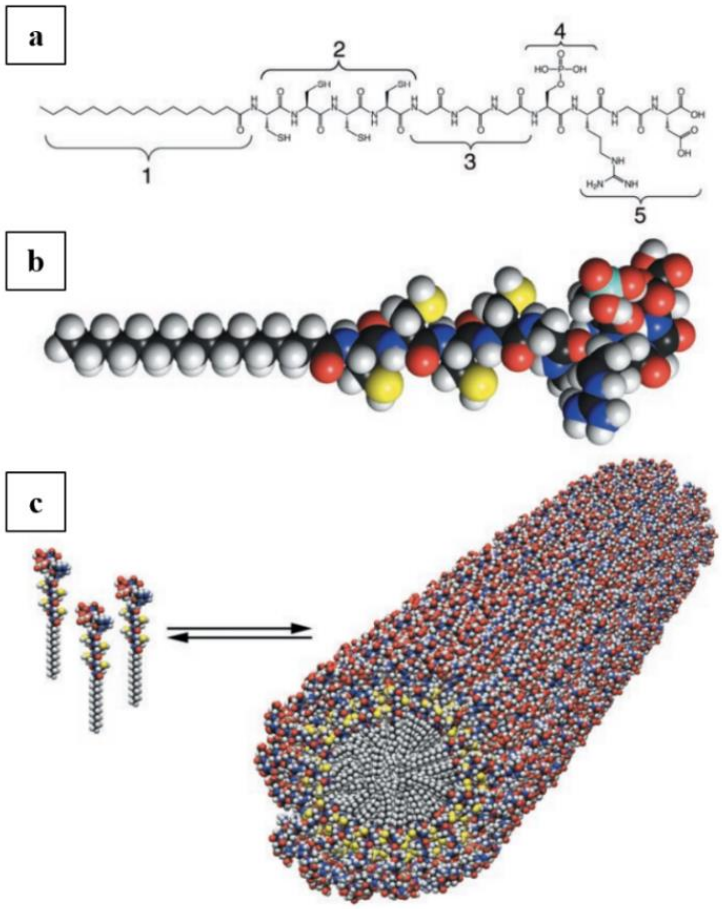


Figure 3.12 Structures of a surfactant self-assembling system designed by Stupp's group. Reprinted from their paper published in 2001 [9]. (a). Chemical structure of the peptide amphiphile, incorporating motifs with different natures. Region 1: a long hydrophobic tail. Region 2: residues with disulphide bonds that can facilitate the self-assembly. Region 3: hydrophilic head group. Region 4: bioactive residues with calcium ions. Region 5: bioactive residues for cell adhesion. (b) Molecular model of the PA. (c) The self-assembly

to PA fibres, with hydrophobic lipid core, and outer hydrophilic surface formed by β-sheet secondary structures.

Inspired by the above research, many more surfactant peptide systems have been designed, and this type of system has shown promising potential for tissue engineering and drug delivery applications [10][95][96].

3.3.2.2 Coiled-coil Systems

A coiled coil is a structural motif in which several (normally from 2 to 7, but the most prevalent kinds are dimers and trimers) alpha-helices are coiled together like rope strands [97]. The coiled-coil systems are built on heptad repeats, which consist of a repeating pattern of seven amino acids, HPPHCPC (sometimes also presented as *abcdefg*), where H refers to hydrophobic residues, P stands for the polar and hydrophilic segments, and C represents charged sequences [98][99]. Figure 3.13 shows the mechanism of the coiled-coil self-assembly. As shown in Figure 3.13(a), two helices associate through hydrophobic amino acids in positions a and d, and complementary charged interactions between their e and g residues can also help to stabilise the dimers [99][100]. For the connection along the longitudinal fibre axis, as shown in Figure 3.13(b), Papapostolou *et al.* [100] suggested that complementary ionic interactions in locations e and g in Figure 3.13(a) assist the dimers stacking along the fibre width axis. Figure 3.13(c) concludes the process from α helixes to helical dimers, and finally to form coiled-coil fibrils. Sharp *et al.* [101] manged to observe the coiled-coil self-assembling fibres using cryo-TEM (shown in Figures 3.13(d) and (e)). Coiled-coil peptide hydrogels have been demonstrated to have application potentials in tissue engineering and drug delivery [102][103].

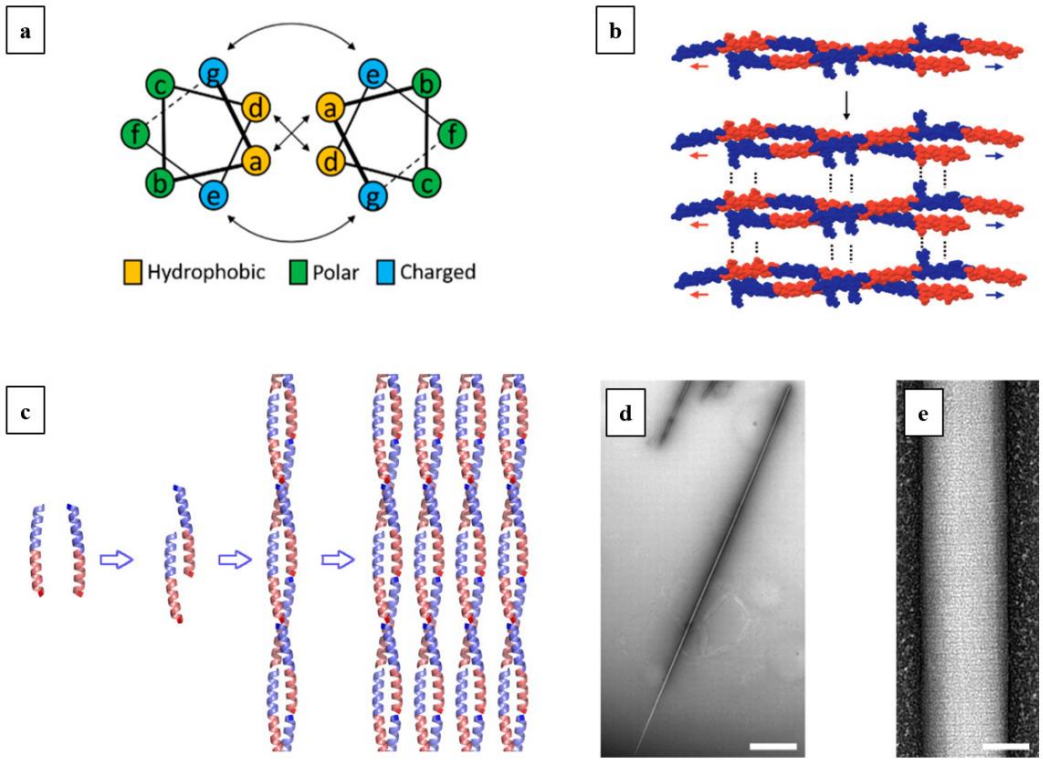


Figure 3.13 Schematic of a coiled-coil self-assembling system. Reproduced from references [99]-[101]. (a). Self-assembly of alpha-helical dimmers, based on heptad helical wheels. (b) Coiled-coil dimers stack along the longitudinal fibre axis. Complementary charged interactions can enhance the self-assembly. (c) Process from α helixes to helical dimers, and finally to form coiled-coil fibrils. (d) A cryo-TEM images of coiled-coil fibrils. (e) A cryo-TEM image of a fibril at a high magnification.

3.3.2.3 π-π stacking Systems

A variety of research [104]-[107] suggests that π-π stacking interactions play vital roles in PA β-sheet self-assembly into peptide fibres. As shown in Figure 3.14(a), Wychowaniec *et al.* [104] proposed the π-π stacking self-assembling models for peptides with two phenylalanine (F) side groups. The modulation of peptide fibres has been demonstrated by changes in pH [104]. Besides, our peptide provider, Saiani's group proposed a self-assembling model for F8 (presented in

Figure 3.14(b)) [69]. They suggest that π-π stacking is the main motivation that contributes to the structure shown in Figure 3.14(b) along the beta-sheet-layer axis (the y axis in Figure 3.6) [69]. This can be a useful reference of the electron ptychographic study on F8, and even for F9 and FP, as they have similar natures of F8. However, the mechanism from 1.5-nm fibrils to thick fibres with diameters of dozens of nanometres were not covered by the reference [69]. It is expected that electron ptychography can bring a new understanding of the pattern how π-π stacking self-assembling units form peptide fibres.

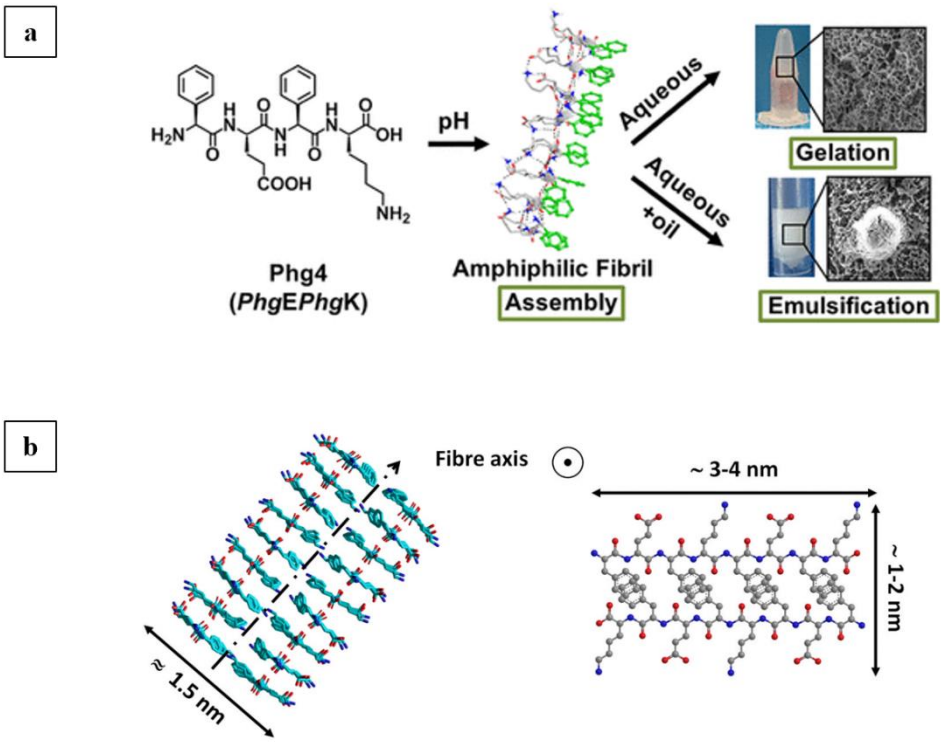


Figure 3.14 Schematic of a π-π stacking self-assembling system. (a). Process of the π-π stacking self-assembly with confirmation of microscopic images. Reproduced from reference [104]. (b) A π-π stacking self-assembling system based on F8 molecules. Proposed by Wychowaniec *et al.* This figure is reproduced from reference [69].

In addition, a slightly different model from the above one was developed Smith *et al.* [105], in which they suggest that the hydrophobicity of aromatic rings is an important factor influencing the self-assembly. Based on this point, they built the "sawtooth" structure shown in Figure 3.15(a) and suggest that peptide fibres can be formed by multiple "sawtooth" residues (shown in Figure 3.15(b)) [105]. This "sawtooth" model to form fibres contributed by both hydrophobicity and π-π stacking can be the most related reference to understand and study how PAs in this thesis form their peptide fibres.

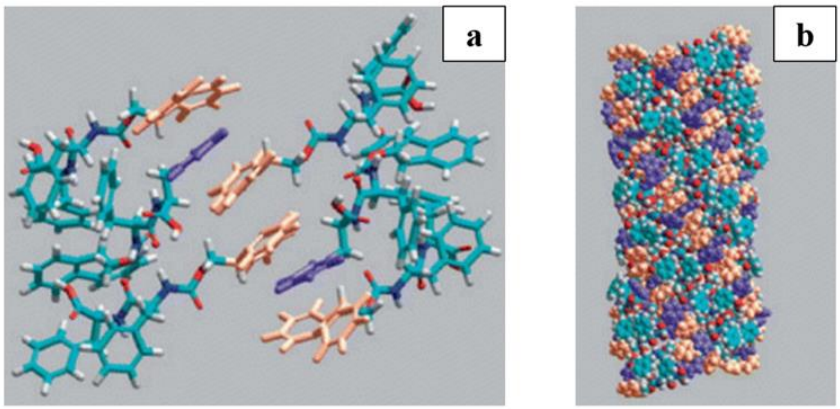


Figure 3.15 Previous peptide fibre models developed by Smith *et al.*, in view of π-π stacking systems. Reproduced from reference [105]. (a) A self-assembling pair of molecules. Presented as the "sawtooth" structure. (b) A fibre consisting of self-assembling molecules.

3.3.3 Parameters Influencing the Self-assembly

3.3.3.1 Amino Acid Sequence

As discussed previously, a self-assembled system is built with the involvement of a number of non-covalent interactions, including hydrogen bonding, hydrophobicity, ionic interactions, π-

π stacking, van der Waal force, *etc*. Researchers therefore have been attempted to control and modulate the self-assembly for different desirable scenarios by changing these interactions via alerting the peptide milieu or the peptide itself. Herein, the most straightforward strategy is to change the amino acid sequence that makes up the peptide. Previous studies [91][108]-[110] have demonstrated that the amino acid sequence can influence on both secondary and tertiary structures.

A classic instance can be found in the paper published by Hong *et al.* [108] in 2003, where they found that peptide with different amino acid sequences form different morphologies. EAK16-II and EAK16-IV were used for the study in Hong *et al.*'s paper, and their structures can be found in Figures 3.16(a) and (b). EAK16-II has alternative positively and negatively charged sections, whereas EAK16-IV has two isolated positively and negatively charged sections. As shown in Figure 3.16, the peptide EAK16-IV forms globular assemblies at neutral pH conditions, whereas EAK16-II has fibrillar assemblies. Hong *et al.* then attributed the morphological difference from the change in electrostatic interactions with the alter in amino acid sequence [109].

M. López De La Paz *et al.* [110] reported another example on how the amino acid sequence influences the self-assembling secondary structures. They studied the self-assembly of three different peptides KTVIIE, KTVLIE and KTVIYE. The overall sequences of them are almost the same except for a single amino acid residue, where KTVIIE has isoleucine, KTVLIE owns leucine, and KTVIYE possesses tyrosine. Finally at pH 2.6, only KTVIIE formed β-sheet structures. They concluded the reason to be the positive effect of the hydrophobicity and the negative effect of π-π stacking to the formation of β-sheet structures in their system.

Moreover, previous studies [39][40] in our group also show that F8, F9, FAFA and F2A2 present different morphologies with the same conditions in pH, peptide concentration and substrates.

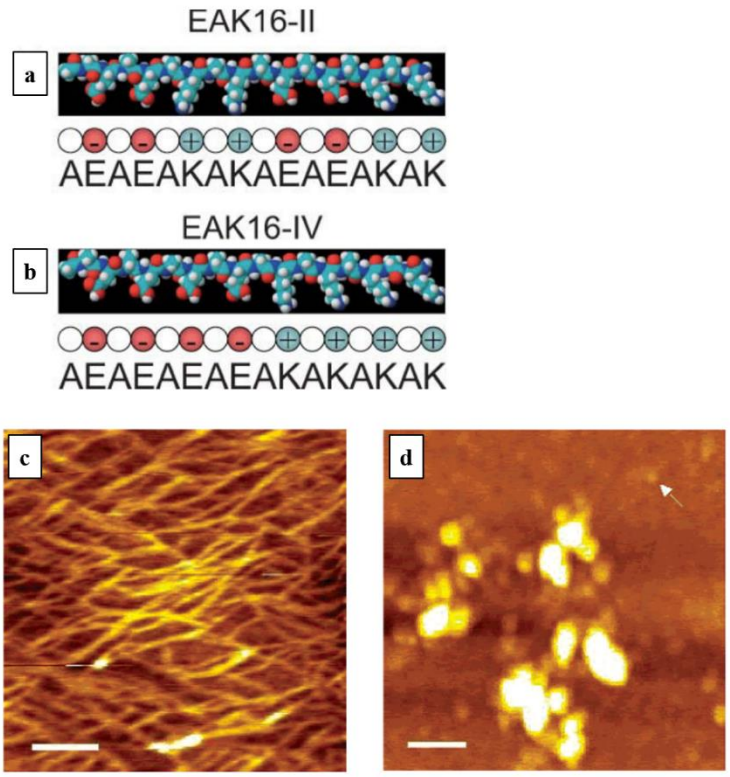


Figure 3.16 Structure and self-assembling morphologies of EAK16-II and EAK16-IV. Reproduced from references [108] and [109]. (a) The molecular model of EAK16-II. (b) The molecular model of EAK16-IV. (c) An AFM image of self-assembling EAK16-II. (d) An AFM image of self-assembling EAK16-IV.

3.3.3.2 Peptide Concentration

A number of previous [111]-[116] studies also suggest that peptide concentration plays an important role in peptide self-assembly, especially for the conformation of peptide fibres and hydrogels. Taking the EAK16-II peptide mentioned in the last section as the example, as shown in Figure 3.17, EAK16-II formed well-defined fibrils (nanofibers) at low peptide

concentrations and dense fibre-networks at high peptide concentrations, according to Hong *et al.* [111].

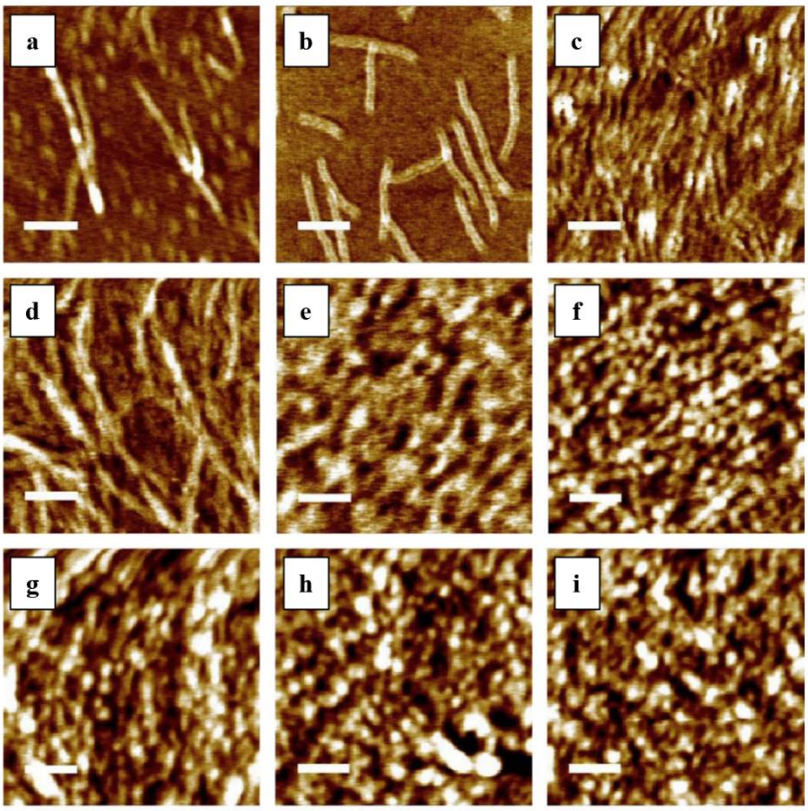


Figure 3.17 AFM images of EAK16-II in pure water at various peptide concentrations: (a) 0.01; (b) 0.05; (c) 0.075; (d) 0.1; (e) 0.2; (f) 0.4; (g) 0.5; (h) 0.75; and (I) 1 mg/mL. Reproduced from reference [111].

In another Hong *et al.* 's paper [115], they proposed a conception, critical assembly concentration (CAC) for the peptide EAK16-I. As shown in Figure 3.18, there are no peptide fibres found at low concentrations (lower than 0.05 mg/mL).

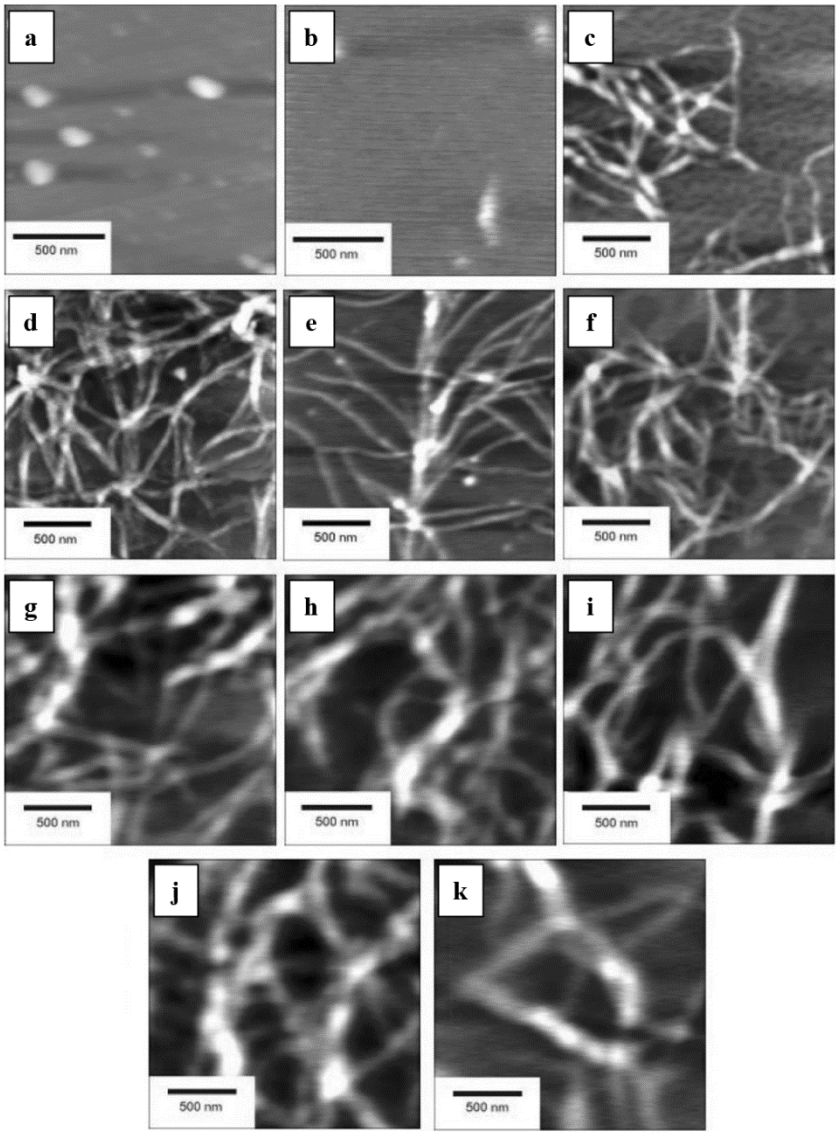


Figure 3.18 AFM images of EAK16-I assemblies at various peptide concentrations: (a) 0.01, (b) 0.025, (c) 0.05, (d) 0.075, (e) 0.1, (f) 0.2, (g) 0.3, (h) 0.5, (i) 0.8, (j) 1.0, and (k) 2.0 mg/mL. Reproduced from reference [115].

Turning to the peptides in this thesis, previous studies [39][40] suggest for F8 and F9, peptide concentration increases do not obviously change the width of fibres, but the density of fibres (number of fibres in a certain area) rises with the increase of peptide concentration [39][40]. Also, no CAC were found for F8 and F9, which indicates peptide concentration cannot determine whether fibres are formed or not [39][40].

3.3.3.3 pH

The effect of pH is also regarded as one the most important parameters that can control peptide self-assembling systems [111],[117]-[120]. Here, the concept of the isoelectric point (pI), needs to be introduced first for later discussions on pH effects. The isoelectric point of an amino acid is the pH value at which the amino acid has no net electrical charge. Since every amino acid includes at least one pair of acid-base groups, pI is a significant characteristic for amino acids that can determine their structures and therefore, affect many properties. The pI concept is then extended to peptides and proteins, which is the pH at which the net charge on the molecular ensemble is zero [121]. Isoelectric point is a crucial factor when researchers design the pH-responsive peptide self-assembling systems [122]-[125].

In the literature [108] mentioned in section 3.3.3.1, Hong *et al.* also found pH can influence the morphology of peptide EAK16-IV. As shown in Figure 3.19, at the pH around the pI of EAK16-IV (pH=7), peptides undergo a fibrillar-globular-fibrillar transition. They then attributed this phenomenon to the electrostatic repulsion straightening change with the change of pH values.

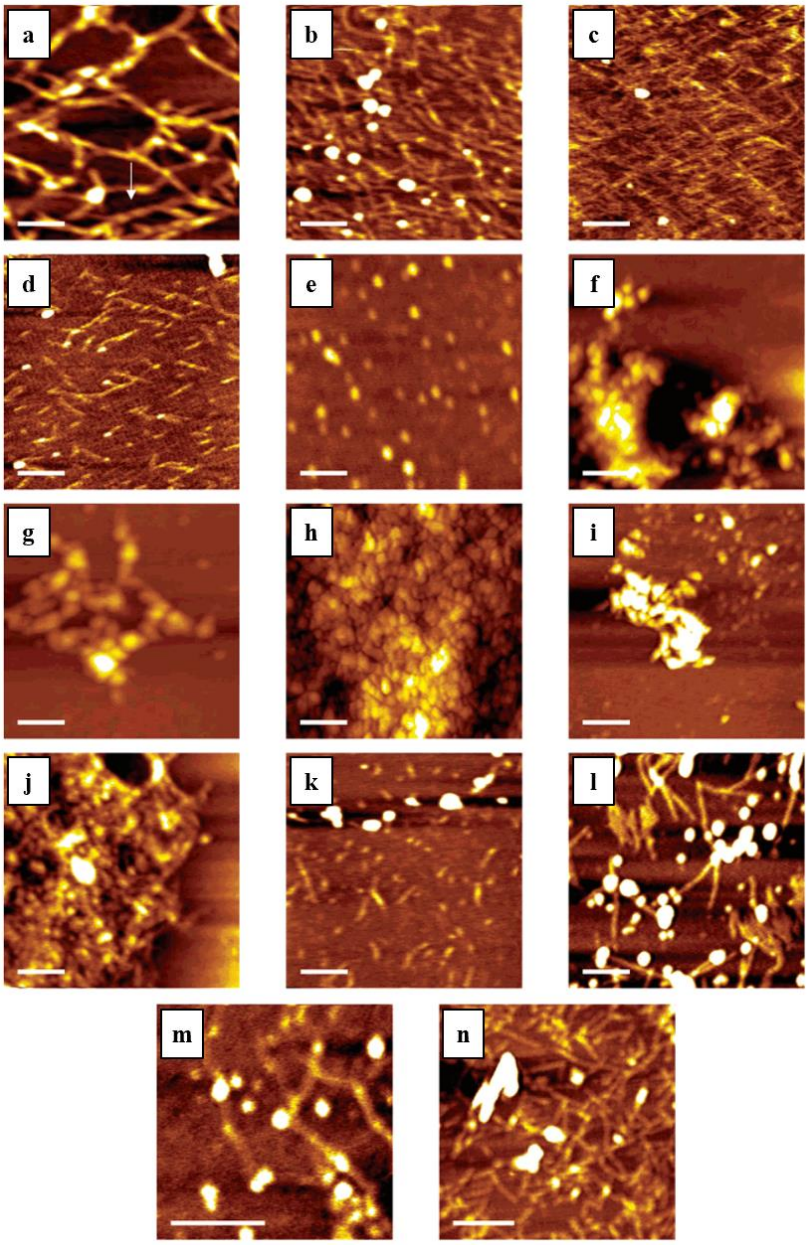


Figure 3.19 AFM images of EAK16-IV at various pH values. (A) pH 4, (B) pH 6.25, (C) pH 6.40, (D) pH 6.55, (E) pH 6.70, (F) pH 6.85, (G) pH 7.00, (H) pH 7.15, (I) pH 7.30, (J) pH 7.45, (K) pH 7.60, (L) pH 7.90, (M) pH 8.50, and (N) pH 11. Reproduced from reference [108].

In addition, Schneider *et al.* [118] successfully designed a pH-responsive self-assembling system for the MAX1 peptide. A reversible transition from random coils at pH 5.5 to β-sheet structures at pH 9 was observed. For peptides in this work, Wang's results [40] suggest

that F8 and F9 have the widest fibres at their isoelectric points, while the density of fibres at their minimum at the pI.

3.3.3.4 Other Parameters

There are some studies suggest that parameters including salt (ionic) concentration, temperature, substrate for peptide self-assembling systems, *etc.* can also affect the self-assembly for some systems.

Caplan *et al.* [126] suggest that salts impact self-assembly because of their charge screening abilities, which occur when a charged particle is surrounded by ions [127]. This screens any charge-charge contacts between two peptides, decreasing the effect of the interactions in the self-assembling systems.

Temperature has been shown to influence the structure of some self-assembled peptides. Structures in certain systems may be denatured at high temperatures [128], whereas assemblies in others may be activated at higher temperatures [129]. Temperature has also been seen to induce conformational changes in self-assembling peptide structures [120].

Substrate can also be another factor influence the self-assembly of peptides. Wang [40] found that F8 and F9 present different morphologies on mica and polystyrene (PS) substrates. The difference was concluded to the charge of surface, which may alter interactions for the self-assembly [40]. However, there have not been any publications reported salt and temperature (within the variation range of room temperature) can make significant differences on the self-assemblies of peptides used in this work.

3.4 Main Applications of Peptide Amphiphiles

3.4.1 Tissue Engineering

Compared to other hydrogels, PA hydrogels constructed by self-assembling fibres have tremendous capability to absorb and release water, where hydrogels can be made to take up from 0% to more than 99% water content [130][131]. This means that the volume, mass and relevant properties of hydrogels can be transformed in a wide range, which is promising for applications such as tissue engineering (hydrogels need to be tuned for catering to various cells) and drug delivery (hydrogels need to readily responsive, and the amplitude of change are detectable).

PA hydrogels are mostly used as the extracellular matrix (ECM) in tissue engineering areas. ECM is a three-dimensional network consisting of extracellular macromolecules which can provide structural and biochemical support to surrounding cells [132]. Working as the bone ECM, Amosi *et al.* [133] constructed hydrogels from β-sheet peptide amphiphiles high in aspartic amino acids and tricalcium phosphate. The hydrogels were discovered to be effective for depositing calcium ions for bone growth. Meanwhile, this system has outstanding performance in osteoblast differentiation and bone regeneration [133]. Moreover, peptide hydrogels have found great potential as cell scaffolding ECMs. Song *et al.* [134] prepared hydrogels using self-assembling IKVAV-containing peptide amphiphiles (RADA-1). They found that neural progenitor cells (NPCs) were incubated in these hydrogels [134]. This research implies that these hydrogels could serve as a cell scaffold for nerve tissue engineering.

In addition, a number of other previous studies [135]-[137] also support the potential of self-assembling PA hydrogels in tissue engineering applications.

3.4.2 Drug Delivery

Drugs are essential for therapies, however there are some natural challenges for drug transport. Firstly, some biological barriers such as cell membranes can hinder drugs being delivered the target point [138]. Solubility is another problem, as lots of drugs are hydrophobic [138]. Finally, to prevent disintegration of the drug by reaction with enzymes *in vivo* is another factor which needs to be considered for drug transport [138]. Hence, effective drug delivery systems are crucial for treatments.

A number of properties, such as, biocompatibility, nontoxicity, controlled biodegradability, and responsiveness to environmental stimuli make PA hydrogels ideal material for drug delivery [139]. What is more, its amphiphilicity provides the ability to deliver and release both hydrophilic and hydrophobic drugs [139].

For example, Liu *et al.* [140] developed an injectable hydrogel based on the self-assembling peptide RADA16 for the controlled release of the hydrophobic anticancer medication paclitaxel (PTX). They found that the RADA16 hydrogel extended the inhibitory impact of PTX on breast cancer cell proliferation *in vitro* [140]. Additionally, Mocanu *et al.* [141] prepared cationic dextran hydrogels and investigated their interactions different drugs, including α-tocopherol, bovine serum albumin protein and tetanus toxoid. Their results suggest that these hydrogels functioned well in controlled drug release of above drugs and have the potential to be employed as vaccine adjuvants [141].

Other studies also confirmed that PA hydrogels can be used for delivering drugs including pindolol [142], vitamin B1 [143], dexamethasone [144], doxorubicin hydrochloride [145], *etc*.

3.4.3 Other Applications

Self-assembled PA have demonstrated potentials for uses as antibiotic agents [146], biosensors [147], *etc*. For instance, according to Riess's research [146], A9K2 hydrogels have demonstrated a strong antibacterial activity against both Gram-negative and Gram-positive bacterial stains while causing minor damage in mammalian cells. Bhattacharya *et al.* [147] developed ascorbic acid-based hydrogel-encapsulated luminous amphiphilic carbon-dots (C-dots), which are capable of detecting reactive oxygen species (ROS).

Although PAs have great potential in the above applications, as Sun *et al.* [148] suggest the lack of structural understanding, including PA crystallinity, how specifically different interactions work in each kind of self-assembling system, and supramolecular conjugations in self-assembling structures are the main challenge to tailor these applications in real industries.

3.5 Why Studying Crystallinity of Peptide Amphiphiles Matters

To date, no study has yet clearly demonstrated the mechanism of self-assembling protofibrils formation from secondary structures, instead, it is concluded as the coeffect of "a multitude of non-covalent interactions" [149]. Although there are some well-acknowledged self-assembling systems and models constructed by different calculation methods, these models have still not been proven by direct observation, and therefore, cannot provide direct information to understand the self-assembling structure. Hence, a microscopic technique which is capable of direct imaging of ordered PA crystals can be helpful to understand self-assembling peptides and may be also useful to modify their self-assembling structures.

Extending the importance to applications, here cell scaffolding is taken as an example. For sustaining cells, cell scaffolds require appropriate mechanical properties [131][136][148]. As introduced in Section 2.4, crystallinity is related to mechanical properties of materials, particularly for organics [64]. This implies that a better understanding of PA crystals is important to design and produce PA cell scaffolds. In addition, according to Galler *et al.* [150], scaffold stiffness and morphology has been shown to be important in determining cell interactions and differentiation. For this reason, it is also significant to study how PA self-assembling scaffolds form and explore by which means the self-assembly can be desirably controlled.

Hence, a better knowledge on PA self-assembling crystals, structures or mechanisms is meaningful for PA system designers, biomedical scientists, and tissue engineers in this field.

3.6 Design of Using Electron Ptychography to Image Peptide Amphiphiles

As introduced previously in this chapter, peptide crystallisation is believed to have a strong correlation to peptide protofibril and fibre formation. Meanwhile, the PA crystallography (both α-helix and β-sheet) is not well established. Therefore, the study will start with the morphology of fibres by using AFM and TEM. By studying at what conditions, such as pH and peptide concentration, widest fibres (in theory, aggregated by most ordered PA crystals) can be formed.

Then, within these fibres, how crystals are transferred to protofibrils, and fibres can be investigated using HRTEM. If the link between PA fibres and PA crystals are not clear, freeze-thawing will be used as a spare method for increasing the degree of crystallinity of PA samples. It should be noted that annealing is not appropriate for crystallising PA samples, since most peptides and proteins can be denatured at high temperatures [128]. Besides, because there are more existing studies on β-sheet crystals than α-helix crystals, the primary goal in this project is to study self-assembling PA β-sheet crystals.

The next step in this project is to use FTIR to study secondary structures of PA samples, as previous studies demonstrate that different secondary structures have different wavenumbers presented in the spectroscopy [36]-[40][151]. After confirming the secondary structures of PAs, the overall crystallinity of as-cast and/or freeze-thawed samples is then detected by XRD.

Similarly to PVA, the basic local information of PA crystals will be explored by HRTEM. At this step, some typical d-spacings are expected, for instance, the d-spacing at 0.44 - 0.47 nm for β-sheet crystals. After that, several crystallites with typical d-spacings will be imaged by STEM and electron ptychography for a more informative and detailed characterisation.

Finally, a better understanding of PA crystals is expected. Note that at the end of this project, it is extremely challenging to rebuild precise PA models and do image simulations on them. This is attributed to very limited knowledge on PA crystals at the moment. However, data interpretation work will also be done by comparing microscopic data to existing models, and some reasonable new models might be raised based on microscopic data.

3.7 References

[1] Block, R. J. (1956). *Amino acid handbook*. Charles C Thomas Publishers.

[2] Dehsorkhi, A., Castelletto, V., & Hamley, I. W. (2014). Self-assembling amphiphilic peptides. *Journal of Peptide Science*, 20(7), 453-467.

[3] Akram, M., Asif, H. M., Uzair, M., Akhtar, N., Madni, A., Shah, S. A., Hasan, Z., & Ullah, A. (2011). Amino acids: A review article. *Journal of medicinal plants research*, *5*(17), 3997-4000.

[4] Latham, M. C. (1997). *Human nutrition in the developing world* (No. 29). Food & Agriculture Org.

[5] Ikehara, K. (2005). Possible steps to the emergence of life: The [GADV]-protein world hypothesis. *The Chemical Record*, *5*(2), 107-118.

[6] Pascal, R., & Boiteau, L. (2007). Origins of Life: Emergence of Amino Acids. *Wiley Encyclopedia of Chemical Biology*, 1-7.

[7] Hamley, I. W. (2020). *Introduction to peptide science*. John Wiley & Sons.

[8] Hamley, I. W. (2011). Self-assembly of amphiphilic peptides. *Soft Matter*, *7*(9), 4122-4138.

[9] Hartgerink, J. D., Beniash, E., & Stupp, S. I. (2001). Self-assembly and mineralization of peptide-amphiphile nanofibers. *Science*, *294*(5547), 1684-1688.

[10] Hartgerink, J. D., Beniash, E., & Stupp, S. I. (2002). Peptide-amphiphile nanofibers: a versatile scaffold for the preparation of self-assembling materials. *Proceedings of the National Academy of Sciences*, *99*(8), 5133-5138.

[11] Zealand Pharma. https://web.archive.org/web/20190429200629/https://www.zealandpharma.com/what-are-peptides.

Accessed February 2, 2023.

[12] Fischer, G., & Wawra, S. (2006). Polypeptide binding proteins: what remains to be discovered? *Molecular microbiology*, *61*(6), 1388-1396.

[13] Alberts, B., Johnson, A., Lewis, J., Raff, M., Roberts, K., & Walter, P. (2002). The shape and structure of proteins. In *Molecular Biology of the Cell. 4th edition*. Garland Science.

[14] Bio Ninja.

https://ib.bioninja.com.au/higher-level/topic-7-nucleic-acids/73-translation/protein-structure.html.

Accessed February 4, 2023.

[15] Piez, K. A. (1976). Primary structure. *Biochemistry of collagen*, 1-44.

[16] Yanofsky, C., Carlton, B. C., Guest, J. R., Helinski, D. R., & Henning, U. (1964). On the colinearity of gene structure and protein structure. *Proceedings of the National Academy of Sciences*, *51*(2), 266-272.

[17] Allen, G. (2011). *Sequencing of proteins and peptides*. Elsevier.

[18] Dasgupta, A., & Das, D. (2019). Designer peptide amphiphiles: self-assembly to applications. *Langmuir*, *35*(33), 10704-10724.

[19] Molday, R. S., Englander, S. W., & Kallen, R. G. (1972). Primary structure effects on peptide group hydrogen exchange. *Biochemistry*, *11*(2), 150-158.

[20] Bai, Y., Milne, J. S., Mayne, L., & Englander, S. W. (1993). Primary structure effects on peptide group hydrogen exchange. *Proteins: Structure, Function, and Bioinformatics*, *17*(1), 75-86.

[21] Sun, P. D., Foster, C. E., & Boyington, J. C. (2004). Overview of protein structural and functional folds. *Current protocols in protein science*, *35*(1), 17-1.

[22] Hubbard, R. E., & Haider, M. K. (2010). Hydrogen bonds in proteins: role and strength. *eLS*.

[23] Sheridan, R. P., Lee, R. H., Peters, N., & Allen, L. C. (1979). Hydrogen-bond cooperativity in protein secondary structure. *Biopolymers: Original Research on Biomolecules*, *18*(10), 2451-2458.

[24] Li, M. S. (2007). Secondary structure, mechanical stability, and location of transition state of proteins. *Biophysical journal*, *93*(8), 2644-2654.

[25] Suat, K., & Jois, S. D. (2003). Design of β-turn based therapeutic agents. *Current pharmaceutical design*, *9*(15), 1209-1224.

[26] Sarabu, R., Lovey, K., Madison, V. S., Fry, D. C., Greeley, D. N., Cook, C. M., & Olson, G. L. (1993). Design, synthesis, and three-dimensional structural characterization of a constrained Ω-loop excised from interleukin-1α. *Tetrahedron*, *49*(17), 3629-3640.

[27] Sawada, T., Inomata, Y., Yamagami, M., & Fujita, M. (2017). Self-assembly of a peptide 2-catenane through Ω-loop folding. *Chemistry Letters*, *46*(8), 1119-1121.

[28] Bajaj, M., & Blundell, T. (1984). Evolution and the tertiary structure of proteins. *Annual review of biophysics and bioengineering*, *13*(1), 453-492.

[29] Ball, K. A., Phillips, A. H., Nerenberg, P. S., Fawzi, N. L., Wemmer, D. E., & Head-Gordon, T. (2011). Homogeneous and heterogeneous tertiary structure ensembles of amyloid-β peptides. *Biochemistry*, *50*(35), 7612-7628.

[30] Cheng, R. P., Gellman, S. H., & DeGrado, W. F. (2001). β-Peptides: from structure to function. *Chemical reviews*, *101*(10), 3219-3232.

[31] Kyte, J. (1995). Structure in Protein Chemistry Garland Publishing. *Inc., New York, and London*, *201*.

[32] Marciano, S., Dey, D., Listov, D., Fleishman, S. J., Sonn-Segev, A., Mertens, H., Busch, F., Kim, Y., Harvey, S. R., Wysocki, V. H., & Schreiber, G. (2022). Protein quaternary structures in solution are a mixture of multiple forms. *Chemical Science*, *13*(39), 11680-11695.

[33] Hu, X., Kaplan, D., & Cebe, P. (2006). Determining beta-sheet crystallinity in fibrous proteins by thermal analysis and infrared spectroscopy. *Macromolecules*, *39*(18), 6161-6170.

[34] Shenoy, B., Wang, Y., Shan, W., & Margolin, A. L. (2001). Stability of crystalline proteins. *Biotechnology and bioengineering*, *73*(5), 358-369.

[35] Schiffer, M., Chang, C. H., & Stevens, F. J. (1985). Formation of an infinite β-sheet arrangement dominates the crystallization behaviour of λ-type antibody light chains. *Journal of molecular biology*, *186*(2), 475-478.

[36] Chiesa, I., Ligorio, C., Bonatti, A. F., De Acutis, A., Smith, A. M., Saiani, A., Vozzi, G., & De Maria, C. (2020). Modelling the three-dimensional bioprinting process of β-sheet self-assembling peptide hydrogel scaffolds. *Frontiers in Medical Technology*, *2*, 571626.

[37] Wychowaniec, J. K., Smith, A. M., Ligorio, C., Mykhaylyk, O. O., Miller, A. F., & Saiani, A. (2020). Role of sheet-edge interactions in β-sheet self-assembling peptide hydrogels. *Biomacromolecules*, *21*(6), 2285-2297.

[38] Ligorio, C., Vijayaraghavan, A., Hoyland, J. A., & Saiani, A. (2022). Acidic and basic self-assembling peptide and peptide-graphene oxide hydrogels: Characterisation and effect on encapsulated nucleus pulposus cells. *Acta Biomaterialia*, *143*, 145-158.

[39] Botwright, S. (2017). *Self-assembly of Peptides on Surfaces* (Master dissertation, University of Oxford).

[40] Wang, Z. (2018). *Self-assembly of Peptides on Surfaces* (Master dissertation, University of Oxford).

[41] MacArthur, M. W., & Thornton, J. M. (1991). Influence of proline residues on protein conformation. *Journal of molecular biology*, *218*(2), 397-412.

[42] Doerfel, L. K., Wohlgemuth, I., Kubyshkin, V., Starosta, A. L., Wilson, D. N., Budisa, N., & Rodnina, M. V. (2015). Entropic contribution of elongation factor P to proline positioning

at the catalytic center of the ribosome. *Journal of the American Chemical Society*, *137*(40), 12997-13006.

[43] Ceruso, M. A., & Weinstein, H. (2002). Structural mimicry of proline kinks: tertiary packing interactions support local structural distortions. *Journal of molecular biology*, *318*(5), 1237-1249.

[44] Egli, M., & Zhang, S. (2022). How the α-helix got its name. *Nature Reviews Molecular Cell Biology*, *23*(3), 165-165.

[45] Aurora, R., Creamer, T. P., Srinivasan, R., & Rose, G. D. (1997). Local interactions in protein folding: lessons from the α-helix. *Journal of Biological Chemistry*, *272*(3), 1413-1416.

[46] Pauling, L., & Corey, R. B. (1950). Two hydrogen-bonded spiral configurations of the polypeptide chain. *Journal of the American Chemical Society*, *72*(11), 5349-5349.

[47] Pauling, L., Corey, R. B., & Branson, H. R. (1951). The structure of proteins: two hydrogen-bonded helical configurations of the polypeptide chain. Proceedings of the National Academy of Sciences, 37(4), 205-211.

[48] Jayatunga, M. K., Thompson, S., & Hamilton, A. D. (2014). α-Helix mimetics: outwards and upwards. *Bioorganic & Medicinal Chemistry Letters*, *24*(3), 717-724.

[49] Levels of Protein Organization.
https://comis.med.uvm.edu/VIC/coursefiles/MD540/MD540-Protein_Organization_10400_574581210/Protein-org/Protein_Organization3.html
Accessed February 21, 2023.

[50] Perutz, M. F. (1951). The 1.5-A. Reflexion from proteins and polypeptides. *Nature*, *168*, 653-654.

[51] Biophysical Methods.
http://www.chemistry.uoguelph.ca/educmat/phy456/456lec01.htm.
Accessed February 21, 2023.

[52] Pace, C. N., & Scholtz, J. M. (1998). A helix propensity scale based on experimental studies of peptides and proteins. *Biophysical journal*, *75*(1), 422-427.

[53] Bowerman, C. J., & Nilsson, B. L. (2012). Review self-assembly of amphipathic β-sheet peptides: insights and applications. *Peptide Science*, *98*(3), 169-184.

[54] Astbury, W. T. (1933). Some problems in the X-ray analysis of the structure of animal hairs and other protein fibres. *Transactions of the Faraday Society*, *29*(140), 193-205.

[55] Pauling, L., & Corey, R. B. (1951). Molecular modelling of proteins and mathematical prediction of protein structure. *Proc. Natl. Acad. Sci*, *37*, 729-740.

[56] Guenther, E. L., Cao, Q., Trinh, H., Lu, J., Sawaya, M. R., Cascio, D., Boyer, D. R., Rodriguez, J. A., Hughes, M. P., & Eisenberg, D. S. (2018). Atomic structures of TDP-43 LCD segments and insights into reversible or pathogenic aggregation. *Nature structural & molecular biology*, 25(6), 463-471.

[57] Mondal, S., Jacoby, G., Sawaya, M. R., Arnon, Z. A., Adler-Abramovich, L., Rehak, P., Vuković, L., Shimon, L. J. W., Král, P., Beck, R., & Gazit, E. (2018). Transition of metastable cross-α crystals into cross-β fibrils by β-turn flipping. *Journal of the American Chemical Society*, 141(1), 363-369.

[58] Fabiola, G. F., Krishnaswamy, S., Nagarajan, V., & Pattabhi, V. (1997). C—H··· O Hydrogen Bonds in β-sheets. *Acta Crystallographica Section D: Biological Crystallography*, *53*(3), 316-320.

[59] Cheng, P. N., Pham, J. D., & Nowick, J. S. (2013). The supramolecular chemistry of β-sheets. *Journal of the American Chemical Society*, *135*(15), 5477-5492.

[60] Maji, S. K., Drew, M. G., & Banerjee, A. (2001). First crystallographic signature of amyloid-like fibril forming β-sheet assemblage from a tripeptide with non-coded amino acids. *Chemical Communications*, (19), 1946-1947.

[61] Serpell, L. C. (2000). Alzheimer's amyloid fibrils: structure and assembly. *Biochimica et Biophysica Acta (BBA)-Molecular Basis of Disease*, *1502*(1), 16-30.

[62] Rapaport, H., Kjaer, K., Jensen, T. R., Leiserowitz, L., & Tirrell, D. A. (2000). Two-dimensional order in β-sheet peptide monolayers. *Journal of the American Chemical Society*, *122*(50), 12523-12529.

[63] Weaver, L., Stagsted, J., Behnke, O., Matthews, B. W., & Olsson, L. (1996). β-Sheet models for the ordered filamentous structure formed by a peptide that enhances the action of insulin. *Journal of structural biology*, *117*(3), 165-172.

[64] Tycko, R., Sciarretta, K. L., Orgel, J. P., & Meredith, S. C. (2009). Evidence for novel β-sheet structures in Iowa mutant β-amyloid fibrils. *Biochemistry*, *48*(26), 6072-6084.

[65] Isenberg, H., Kjaer, K., & Rapaport, H. (2006). Elasticity of crystalline β-sheet monolayers. *Journal of the American Chemical Society*, *128*(38), 12468-12472.

[66] Rabotyagova, O. S., Cebe, P., & Kaplan, D. L. (2010). Role of polyalanine domains in β-sheet formation in spider silk block copolymers. *Macromolecular bioscience*, *10*(1), 49-59.

[67] Sikorski, P., Atkins, E. D., & Serpell, L. C. (2003). Structure and texture of fibrous crystals formed by Alzheimer's Aβ (11–25) peptide fragment. *Structure*, *11*(8), 915-926.

[68] Ligorio, C., Hoyland, J. A., & Saiani, A. (2022). Self-assembling peptide hydrogels as functional tools to tackle intervertebral disc degeneration. *Gels*, *8*(4), 211.

[69] Wychowaniec, J. K., Moffat, J., & Saiani, A. (2021). Quantitative nanomechanical properties evaluation of a family of β-sheet peptide fibres using rapid bimodal AFM. *Journal of the mechanical behavior of biomedical materials*, *124*, 104776.

[70] Morris, O., Elsawy, M. A., Fairclough, M., Williams, K. J., McMahon, A., Grigg, J., Forster, D., Miller, A.F., Saiani, A., & Prenant, C. (2017). In vivo characterisation of a therapeutically relevant self-assembling 18F-labelled β-sheet forming peptide and its hydrogel

using positron emission tomography. *Journal of Labelled Compounds and Radiopharmaceuticals*, *60*(10), 481-488.

[71] Elsawy, M. A., Smith, A. M., Hodson, N., Squires, A., Miller, A. F., & Saiani, A. (2016). Modification of β-sheet forming peptide hydrophobic face: effect on self-assembly and gelation. *Langmuir*, *32*(19), 4917-4923.

[72] Lewis, P. N., Momany, F. A., & Scheraga, H. A. (1973). Chain reversals in proteins. *Biochimica et Biophysica Acta (BBA)-Protein Structure*, *303*(2), 211-229.

[73] Rose, G. D., Glerasch, L. M., & Smith, J. A. (1985). Turns in peptides and proteins. *Advances in protein chemistry*, *37*, 1-109.

[74] Beta Turns: Prediction of beta-turn types.

https://webs.iiitd.edu.in/raghava/betaturns/turn.html.

Accessed February 25, 2023.

[75] Beta-Hairpin Turns.

https://www.cryst.bbk.ac.uk/PPS95/course/3_geometry/hairpin.html.

Accessed February 25, 2023.

[76] Foundations of Clinical Sciences.

https://comis.med.uvm.edu/VIC/coursefiles/MD540/MD540-Protein_Organization_10400_574581210/Protein-org/Protein_Organization5.html.

Accessed February 25, 2023.

[77] Smith, L. J., Fiebig, K. M., Schwalbe, H., & Dobson, C. M. (1996). The concept of a random coil: Residual structure in peptides and denatured proteins. *Folding and Design*, *1*(5), R95-R106.

[78] Lara, J. M. (2009). Intracellular management of information: from DNA to proteins. *tripleC: Communication, Capitalism & Critique. Open Access Journal for a Global Sustainable Information Society*, *7*(2), 376-385.

[79] Yadav, S., Sharma, A. K., & Kumar, P. (2020). Nanoscale self-assembly for therapeutic delivery. *Frontiers in Bioengineering and Biotechnology*, *8*, 127.

[80] Ding, X., & Wang, Y. (2017). Weak bond-based injectable and stimuli responsive hydrogels for biomedical applications. *Journal of Materials Chemistry B*, *5*(5), 887-906.

[81] Rodriguez, L. M. D. L., Hemar, Y., Cornish, J., & Brimble, M. A. (2016). Structure–mechanical property correlations of hydrogel forming β-sheet peptides. *Chemical society reviews*, *45*(17), 4797-4824.

[82] Kisiday, J., Jin, M., Kurz, B., Hung, H., Semino, C., Zhang, S., & Grodzinsky, A. J. (2002). Self-assembling peptide hydrogel fosters chondrocyte extracellular matrix production and cell division: implications for cartilage tissue repair. *Proceedings of the National Academy of Sciences*, *99*(15), 9996-10001.

[83] Roberts, D., Rochas, C., Saiani, A., & Miller, A. F. (2012). Effect of peptide and guest charge on the structural, mechanical and release properties of β-sheet forming peptides. *Langmuir*, *28*(46), 16196-16206.

[84] Boothroyd, S., Saiani, A., & Miller, A. F. (2014). Controlling network topology and mechanical properties of co-assembling peptide hydrogels. *Biopolymers*, *101*(6), 669-680.

[85] Hamley, I. W. (2007). Peptide fibrillization. *Angewandte Chemie International Edition*, *46*(43), 8128-8147.

[86] Bonduelle C. Secondary structures of synthetic polypeptide polymers. *Polymer Chemistry*. 2018;9(13):1517-29.

[87] Lomakin, A., Chung, D. S., Benedek, G. B., Kirschner, D. A., & Teplow, D. B. (1996). On the nucleation and growth of amyloid beta-protein fibrils: detection of nuclei and quantitation of rate constants. *Proceedings of the National Academy of Sciences*, *93*(3), 1125-1129.

[88] Caplan, M. R., Moore, P. N., Zhang, S., Kamm, R. D., & Lauffenburger, D. A. (2000). Self-assembly of a β-sheet protein governed by relief of electrostatic repulsion relative to van der Waals attraction. *Biomacromolecules*, *1*(4), 627-631.

[89] Boothroyd, S. (2012). *Peptide Self-assembly: Controlling Conformation and Mechanical Properties*. The University of Manchester (United Kingdom).

[90] Han, S., Cao, S., Wang, Y., Wang, J., Xia, D., Xu, H., Zhao, X., & Lu, J. R. (2011). Self-assembly of short peptide amphiphiles: the cooperative effect of hydrophobic interaction and hydrogen bonding. *Chemistry–A European Journal*, *17*(46), 13095-13102.

[91] Lee, N. R., Bowerman, C. J., & Nilsson, B. L. (2013). Effects of varied sequence pattern on the self-assembly of amphipathic peptides. *Biomacromolecules*, *14*(9), 3267-3277.

[92] Fung, S. Y., Keyes, C., Duhamel, J., & Chen, P. (2003). Concentration effect on the aggregation of a self-assembling oligopeptide. *Biophysical journal*, *85*(1), 537-548.

[93] Wikipedia_ Surfactant.

https://en.wikipedia.org/wiki/File:A_lipid_micelle.png.

Accessed February 27, 2023.

[94] Furse, S. (2010). Bubbles, bubbles, everywhere, but not a drop to drink. *The lipid cronicles*.

[95] Webber, M. J., Newcomb, C. J., Bitton, R., & Stupp, S. I. (2011). Switching of self-assembly in a peptide nanostructure with a specific enzyme. *Soft Matter*, *7*(20), 9665-9672.

[96] Stupp, S. I. (2010). Self-assembly and biomaterials. *Nano letters*, *10*(12), 4783-4786. [97] Liu, J., Zheng, Q., Deng, Y., Cheng, C. S., Kallenbach, N. R., & Lu, M. (2006). A seven-helix coiled coil. *Proceedings of the National Academy of Sciences*, *103*(42), 15457-15462.

[98] Mason, J. M., & Arndt, K. M. (2004). Coiled coil domains: stability, specificity, and biological implications. *ChemBioChem*, *5*(2), 170-176.

[99] Park, W. M. (2020). Coiled-coils: The molecular zippers that self-assemble protein nanostructures. *International Journal of Molecular Sciences*, *21*(10), 3584.

[100] Papapostolou, D., Smith, A. M., Atkins, E. D., Oliver, S. J., Ryadnov, M. G., Serpell, L. C., & Woolfson, D. N. (2007). Engineering nanoscale order into a designed protein fiber. *Proceedings of the National Academy of Sciences*, *104*(26), 10853-10858.

[101] Sharp, T. H., Bruning, M., Mantell, J., Sessions, R. B., Thomson, A. R., Zaccai, N. R., Brady, R. L., Verkade, P., & Woolfson, D. N. (2012). Cryo-transmission electron microscopy structure of a gigadalton peptide fibre of de novo design. *Proceedings of the National Academy of Sciences*, *109*(33), 13266-13271.

[102] Woolfson, D. N. (2010). Building fibrous biomaterials from α-helical and collagen-like coiled-coil peptides. *Peptide Science: Original Research on Biomolecules*, *94*(1), 118-127.

[103] McFarlane, A. A., Orriss, G. L., & Stetefeld, J. (2009). The use of coiled-coil proteins in drug delivery systems. *European journal of pharmacology*, *625*(1-3), 101-107.

[104] Wychowaniec, J. K., Patel, R., Leach, J., Mathomes, R., Chhabria, V., Patil-Sen, Y., Hidalgo-Bastida, A., Forbes, R. T., Hayes, J. M., & Elsawy, M. A. (2020). Aromatic stacking facilitated self-assembly of ultrashort ionic complementary peptide sequence: β-sheet nanofibers with remarkable gelation and interfacial properties. *Biomacromolecules*, *21*(7), 2670-2680.

[105] Smith, A. M., Williams, R. J., Tang, C., Coppo, P., Collins, R. F., Turner, M. L., Saiani, A., & Ulijn, R. V. (2008). Fmoc-diphenylalanine self assembles to a hydrogel via a novel architecture based on π–π interlocked β-sheets. *Advanced Materials*, *20*(1), 37-41.

[106] Bowerman, C. J., Liyanage, W., Federation, A. J., & Nilsson, B. L. (2011). Tuning β-sheet peptide self-assembly and hydrogelation behaviour by modification of sequence hydrophobicity and aromaticity. *Biomacromolecules*, *12*(7), 2735-2745.

[107] Zhao, Y., Tanaka, M., Kinoshita, T., Higuchi, M., & Tan, T. (2010). Self-assembling peptide nanofiber scaffolds for controlled release governed by gelator design and guest size. *Journal of controlled release*, *147*(3), 392-399.

[108] Hong, Y., Legge, R. L., Zhang, S., & Chen, P. (2003). Effect of amino acid sequence and pH on nanofiber formation of self-assembling peptides EAK16-II and EAK16-IV. *Biomacromolecules*, *4*(5), 1433-1442.

[109] Jun, S., Hong, Y., Imamura, H., Ha, B. Y., Bechhoefer, J., & Chen, P. (2004). Self-assembly of the ionic peptide EAK16: the effect of charge distributions on self-assembly. *Biophysical journal*, *87*(2), 1249-1259.

[110] López de la Paz, M., Goldie, K., Zurdo, J., Lacroix, E., Dobson, C. M., Hoenger, A., & Serrano, L. (2002). De novo designed peptide-based amyloid fibrils. *Proceedings of the National Academy of Sciences*, *99*(25), 16052-16057.

[111] Hong, Y., Pritzker, M. D., Legge, R. L., & Chen, P. (2005). Effect of NaCl and peptide concentration on the self-assembly of an ionic-complementary peptide EAK16-II. *Colloids and Surfaces B: Biointerfaces*, *46*(3), 152-161.

[112] Aggeli, A., Nyrkova, I. A., Bell, M., Harding, R., Carrick, L., McLeish, T. C., Semenov, & A. N., Boden, N. (2001). Hierarchical self-assembly of chiral rod-like molecules as a model for peptide β-sheet tapes, ribbons, fibrils, and fibres. *Proceedings of the National Academy of Sciences*, *98*(21), 11857-11862.

[113] Bowerman, C. J., & Nilsson, B. L. (2010). A reductive trigger for peptide self-assembly and hydrogelation. *Journal of the American Chemical Society*, *132*(28), 9526-9527.

[114] Cui, H., Muraoka, T., Cheetham, A. G., & Stupp, S. I. (2009). Self-assembly of giant peptide nanobelts. *Nano letters*, *9*(3), 945-951.

[115] Hong, Y., Lau, L. S., Legge, R. L., & Chen, P. (2004). Critical self-assembly concentration of an ionic-complementary peptide EAK16-I. *The Journal of Adhesion*, *80*(10-11), 913-931.

[116] Fung, S. Y., Keyes, C., Duhamel, J., & Chen, P. (2003). Concentration effect on the aggregation of a self-assembling oligopeptide. *Biophysical journal*, *85*(1), 537-548.

[117] Rajagopal, K., Lamm, M. S., Haines-Butterick, L. A., Pochan, D. J., & Schneider, J. P. (2009). Tuning the pH responsiveness of β-hairpin peptide folding, self-assembly, and hydrogel material formation. *Biomacromolecules*, *10*(9), 2619-2625.

[118] Schneider, J. P., Pochan, D. J., Ozbas, B., Rajagopal, K., Pakstis, L., & Kretsinger, J. (2002). Responsive hydrogels from the intramolecular folding and self-assembly of a designed peptide. *Journal of the American Chemical Society*, *124*(50), 15030-15037.

[119] Aggeli, A., Bell, M., Carrick, L. M., Fishwick, C. W., Harding, R., Mawer, P. J., Radford, S. E., Strong, A. E., & Boden, N. (2003). pH as a trigger of peptide β-sheet self-assembly and reversible switching between nematic and isotropic phases. *Journal of the American Chemical Society*, *125*(32), 9619-9628.

[120] Altman, M., Lee, P., Rich, A., & Zhang, S. (2000). Conformational behavior of ionic self-complementary peptides. *Protein Science*, *9*(6), 1095-1105.

[121] Bjerrum, E. J., Jensen, J. H., & Tolborg, J. L. (2017). pICalculax: improved prediction of isoelectric point for modified peptides. *Journal of chemical information and modeling*, *57*(8), 1723-1727.

[122] Kumaraswamy, P., Lakshmanan, R., Sethuraman, S., & Krishnan, U. M. (2011). Self-assembly of peptides: influence of substrate, pH and medium on the formation of supramolecular assemblies. *Soft Matter*, *7*(6), 2744-2754.

[123] Sun, Y., Zhang, Y., Tian, L., Zhao, Y., Wu, D., Xue, W., Ramakrishna, S., Wu, W., & He, L. (2016). Self-assembly behaviors of molecular designer functional RADA16-I peptides: influence of motifs, pH, and assembly time. *Biomedical Materials*, *12*(1), 015007.

[124] Conejero-Muriel, M., Contreras-Montoya, R., Díaz-Mochón, J. J., de Cienfuegos, L. Á., & Gavira, J. A. (2015). Protein crystallization in short-peptide supramolecular hydrogels: A versatile strategy towards biotechnological composite materials. *CrystEngComm*, *17*(42), 8072-8078.

[125] Canaves, J. M., Page, R., Wilson, I. A., & Stevens, R. C. (2004). Protein biophysical properties that correlate with crystallization success in Thermotoga maritima: maximum clustering strategy for structural genomics. *Journal of molecular biology*, *344*(4), 977-991.

[126] Caplan, M. R., Schwartzfarb, E. M., Zhang, S., Kamm, R. D., & Lauffenburger, D. A. (2002). Control of self-assembling oligopeptide matrix formation through systematic variation of amino acid sequence. *Biomaterials*, *23*(1), 219-227.

[127] Lockhart, D. J., & Kim, P. S. (1993). Electrostatic screening of charge and dipole interactions with the helix backbone. *Science*, *260*(5105), 198-202.

[128] Petka, W. A., Harden, J. L., McGrath, K. P., Wirtz, D., & Tirrell, D. A. (1998). Reversible hydrogels from self-assembling artificial proteins. *Science*, *281*(5375), 389-392.

[129] Pochan, D. J., Schneider, J. P., Kretsinger, J., Ozbas, B., Rajagopal, K., & Haines, L. (2003). Thermally reversible hydrogels via intramolecular folding and consequent self-assembly of a de novo designed peptide. *Journal of the American Chemical Society*, *125*(39), 11802-11803.

[130] Banwell, E. F., Abelardo, E. S., Adams, D. J., Birchall, M. A., Corrigan, A., Donald, A. M., Kirkland, M., Serpell, L. C., Butler, M. F., & Woolfson, D. N. (2009). Rational design and application of responsive α-helical peptide hydrogels. *Nature materials*, *8*(7), 596-600.

[131] Genové, E., Shen, C., Zhang, S., & Semino, C. E. (2005). The effect of functionalized self-assembling peptide scaffolds on human aortic endothelial cell function. *Biomaterials*, *26*(16), 3341-3351.

[132] Theocharis, A. D., Skandalis, S. S., Gialeli, C., & Karamanos, N. K. (2016). Extracellular matrix structure. *Advanced drug delivery reviews*, *97*, 4-27.

[133] Amosi, N., Zarzhitsky, S., Gilsohn, E., Salnikov, O., Monsonego-Ornan, E., Shahar, R., & Rapaport, H. (2012). Acidic peptide hydrogel scaffolds enhance calcium phosphate mineral turnover into bone tissue. *Acta biomaterialia*, *8*(7), 2466-2475.

[134] Song, Y., Li, Y., Zheng, Q., Wu, K., Guo, X., Wu, Y., Yin, M., Wu, Q., & Fu, X. (2011). Neural progenitor cells survival and neuronal differentiation in peptide-based hydrogels. *Journal of Biomaterials Science, Polymer Edition*, *22*(4-6), 475-487.

[135] Solaro, R., Alderighi, M., Barsotti, M. C., Battisti, A., Cifelli, M., Losi, P., Di Stefano, R., Ghezzi, L., & Tiné, M. R. (2013). Chemical–physical and in vivo evaluations of a self-assembling amphiphilic peptide as an injectable hydrogel scaffold for biomedical applications. *Journal of bioactive and compatible polymers*, *28*(1), 3-15.

[136] Horii, A., Wang, X., Gelain, F., & Zhang, S. (2007). Biological designer self-assembling peptide nanofiber scaffolds significantly enhance osteoblast proliferation, differentiation and 3-D migration. *PloS one*, *2*(2), e190.

[137] Kisiday, J., Jin, M., Kurz, B., Hung, H., Semino, C., Zhang, S., & Grodzinsky, A. J. (2002). Self-assembling peptide hydrogel fosters chondrocyte extracellular matrix production and cell division: implications for cartilage tissue repair. *Proceedings of the National Academy of Sciences*, *99*(15), 9996-10001.

[138] Chen, P. (2005). Self-assembly of ionic-complementary peptides: a physicochemical viewpoint. *Colloids and Surfaces A: Physicochemical and Engineering Aspects*, *261*(1-3), 3-24.

[139] Chang, H., Li, C., Huang, R., Su, R., Qi, W., & He, Z. (2019). Amphiphilic hydrogels for biomedical applications. *Journal of Materials Chemistry B*, *7*(18), 2899-2910.

[140] Liu, J., Zhang, L., Yang, Z., & Zhao, X. (2011). Controlled release of paclitaxel from a self-assembling peptide hydrogel formed in situ and antitumor study in vitro. *International journal of Nanomedicine*, 2143-2153.

[141] Mocanu, G., Nichifor, M., Picton, L., About-Jaudet, E., & Le Cerf, D. (2014). Preparation and characterization of anionic pullulan thermoassociative nanoparticles for drug delivery. *Carbohydrate polymers*, *111*, 892-900.

[142] Barclay, T. G., Constantopoulos, K., & Matisons, J. (2014). Nanotubes self-assembled from amphiphilic molecules via helical intermediates. *Chemical Reviews*, *114*(20), 10217-10291.

[143] Qin, L., Duan, P., Xie, F., Zhang, L., & Liu, M. (2013). A metal ion triggered shrinkable supramolecular hydrogel and controlled release by an amphiphilic peptide dendron. *Chemical Communications*, *49*(92), 10823-10825.

[144] Petta, D., Fussell, G., Hughes, L., Buechter, D. D., Sprecher, C. M., Alini, M., Eglin, D., & D'Este, M. (2016). Calcium phosphate/thermos-responsive hyaluronan hydrogel composite delivering hydrophilic and hydrophobic drugs. *Journal of orthopaedic translation*, *5*, 57-68.

[145] Zhao, L., Zhu, L., Liu, F., Liu, C., Wang, Q., Zhang, C., Li, J., Liu, J., Qu, X., & Yang, Z. (2011). pH triggered injectable amphiphilic hydrogel containing doxorubicin and paclitaxel. *International journal of pharmaceutics*, *410*(1-2), 83-91.

[146] Riess, J. G. (2009). Highly fluorinated amphiphilic molecules and self-assemblies with biomedical potential. *Current opinion in colloid & interface science*, *14*(5), 294-304.

[147] Bhattacharya, S., Sarkar, R., Nandi, S., Porgador, A., & Jelinek, R. (2017). Detection of reactive oxygen species by a carbon-dot–ascorbic acid hydrogel. *Analytical chemistry*, *89*(1), 830-836.

[148] Sun, W., Gregory, D. A., & Zhao, X. (2023). Designed peptide amphiphiles as scaffolds for tissue engineering. *Advances in Colloid and Interface Science*, 102866.

[149] De Santis, E., & Ryadnov, M. G. (2015). Peptide self-assembly for nanomaterials: the old new kid on the block. *Chemical Society Reviews*, *44*(22), 8288-8300.

[150] Galler, K. M., D'souza, R. N., Hartgerink, J. D., & Schmalz, G. (2011). Scaffolds for dental pulp tissue engineering. *Advances in Dental Research*, *23*(3), 333-339.

[151] Zou, Y., Li, Y., Hao, W., Hu, X., & Ma, G. (2013). Parallel β-sheet fibril and antiparallel β-sheet oligomer: new insights into amyloid formation of hen egg white lysozyme under heat

and acidic condition from FTIR spectroscopy. *The Journal of Physical Chemistry B*, *117*(15), 4003-4013.

Chapter 4. Materials and Methods

4.1 Materials

Polyvinyl alcohol (PVA) (99%, Mw 31,000 - 50,000, 98-99% hydrolysed), hydrochloric acid (HCl) (37%wt in H_2O) and sodium hydroxide (NaOH) (≥98%, pellets, anhydrous) were purchased from Sigma-Aldrich.

All peptides in this work were provided by Saiani's group from the University of Manchester. The peptides were synthesised in the laboratory by solid phase peptide synthesis (SPPS) in a ChemTech ACT 90 peptide synthesizer (Advance ChemTech Ltd., UK).

Deionised (DI) water was produced with the aid of DI water filter in our lab.

A CHECKER1 pH Meter was purchased from Hanna Instruments, with ± 0.2 pH accuracy and 0.01 pH resolution.

TEM grids (copper with lacey/holey carbon films support, 400 mesh) were purchased from Agar Scientific.

4.2 Preparing Polyvinyl Alcohol and Peptide Solutions

PVA was dissolved in deionised water at between 80 and 90 °C with 30-minute continuous stirring to achieve a 10 wt% PVA solution.

A series of solutions with pH varying from 1 to 14 was firstly prepared by adding HCl or NaOH into DI water. The final solutions were tested using the pH meter. Then, all types of peptides were dissolved in above solutions at room temperature with 30-minute continuous stirring to get 0.5, 1, 2, 5, 10 and 20 mg/mL solutions with different pH values.

4.3 Sample Preparation Methods

4.3.1 Spin-coating

A H6-23 Spin Coater (Laurell Technologies Corporation) was used for the spin-coating process. Several drops of PVA or peptide solutions were firstly dropped onto a certain substrate (for instance, for a TEM sample, the substrate was a TEM grid. For a XRD sample, the substrate was a Si thin wafer). Then, the solution was spin-coated for 30 or 60 seconds with spinning rates at either 1500 or 2500 rpm.

4.3.2 Dip-casting

A substrate, such as, a TEM grid or a Si wafer was held with a pair of tweezers, and then immersed into different solutions for 20 seconds. The dip-cast sample was then air-dried for 30 minutes. The immersion and drying process were then conducted for three cycles to coat enough sample material onto the substrate.

4.3.3 Drop-casting

Several drops of PVA or peptide solutions were dropped onto a substrate and air-dried for over 30 minutes.

4.4 Increasing Crystallinity of Samples

4.4.1 Freeze-thawing

Prepared by the three methods outlined in the last section, the next step was to increase the crystallinity of samples. Freeze-thawing and annealing were used for further crystallise samples. The freeze-thawing process consisted of three cycles, and each cycle contained 20-hour freezing at 25 ℃ and 4-hour thawing at room temperature. After three cycles, the freeze-thawed samples were air-dried overnight at room temperature.

4.4.2 Annealing

Annealing was carried out at different temperatures between 160 ℃ to 250 ℃. Before annealing, PVA samples prepared by methods in Section 4.3 were air-dried overnight at room temperature. Then, samples were placed onto a hot plate. Referring to previous studies [18], the annealing time was decreased with the increase in temperature, where 160 ℃ for 20 minutes, 190 ℃ for 15 minutes, 220 ℃ for 10 minutes and 250 ℃ for 5 minutes. After annealing, the samples were cooled rapidly on a steel block.

4.5 Transmission Electron Microscopy

4.5.1 Experimental Procedures and Fibre Width Measurement Using Line Profiles

Peptide and PVA aqueous solutions were dip-casted directly onto TEM grids. TEM samples were then prepared using the annealing (at 250 ℃, for PVA) or freeze-thawing (for all peptides) methods introduced in Section 4.4.

Held by the single-tilt holder (± 25°), the sample features and crystallinity were characterised by a high vacuum JEOL 3000F analytical TEM under 200 kV connected to a 4K Gatan Ultrascan filtered camera.

TEM data were processed and analysed using Gatan Digital Micrograph software. Peptide fibre width was measured by using line profiles, and an example is shown in Figure 4.1. A line profile was drawn vertically to the fibre direction, and an integration width of 30 pixels (in this case 4.50 nm) was applied for more accurate results. As shown in Figure 4.1(c), the distance that equals the fibre width was finally measured to be 21.172 nm in this case. The error range of the peptide fibre width was determined by taking 5 measurements from different areas of the image. With calculation of errors, the F8 fibre width at pH=7 and 0.5 mg/mL ranges from 20 to 38 nm.

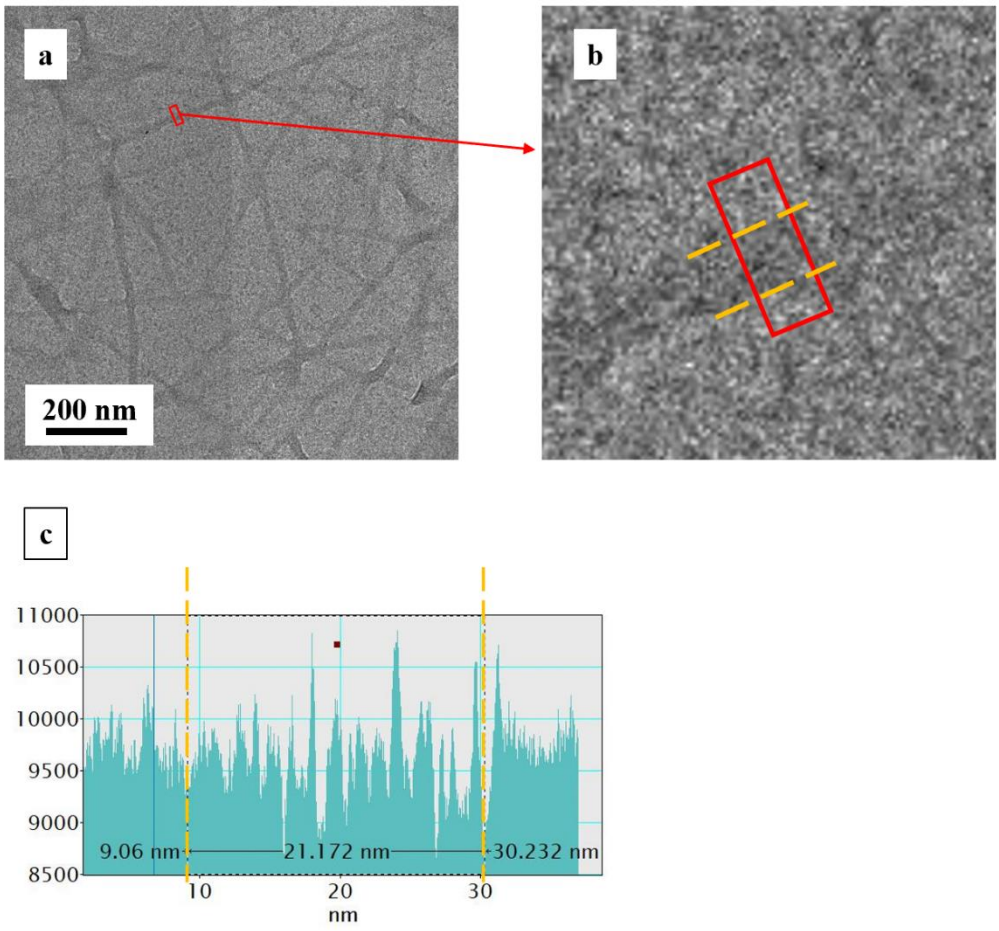


Figure 4.1 Schematic of the measurement of the peptide fibre width using line profiles in a TEM image. (a) A TEM image of a F8 sample at pH=7, 0.5 mg/mL. The red square is the line profile vertical to the fibre direction. (b) A magnified area of (a), where the red square is the line profile in (a), and the spacing between two orange dash lines is the fibre width being measured. (c) The histogram of the line profile, where the fibre width was measured to be 21.172 nm without calculating errors.

4.5.2 High-resolution Transmission Electron Microscopy

HRTEM data were also processed and analysed using Gatan Digital Micrograph software. The pixel sizes of different magnifications were calibrated using the platinum (111) sample, and the calibration errors will not be discussed later. D-spacings were calculated by line profiles

from 5 or 10 different spacings. For instance, as shown in Figure 4.2(a), a line profile was drawn parallel to the *d* (d-spacing were being measured) direction. An integration width of 10 pixels (0.15 nm in this case) was applied for the more accurate results. From the histogram of the line profile shown in Figure 4.2(b), 10 spacings of *d* was measured. On average, *d* was measured to be 0.40 nm. Figure 4.2(c) shows how the margin of error of the d-spacing was acquired. Every spacing within the 10 spacings shown in Figure 4.2(b) were then measured. For instance, the d-spacing in the purple square in Figure 4.2(c) was measured to be 0.390 nm. From left to right within the 10-spacing range, the d-spacings are 0.390, 0.390, 0.405, 0.390, 0.390, 0.390, 0.405, 0.390, 0.405 and 0.405 nm respectively. Accordingly, with the error, *d* in this case was measured to be 0.40 ± 0.01 nm. It should be noted that the errors of the HRTEM and later FFT, STEM and electron ptychographic d-spacings are mainly measurement errors. To be more specific, normally at least errors of ± 2 pixels can occur when measuring the d-spacings. Moreover, statistical errors also exist. For instance, measuring the 10 spacings of *d* shown in Figure 4.2 for 5 times, figures at 3.962, 3.962, 3.947, 3.992 and 3.962 nm were acquired. However, statistical errors can be neglected, as the standard deviation (0.0015 nm for a spacing of *d*) is much smaller than the measurement error (± 0.015 nm for a spacing of *d*).

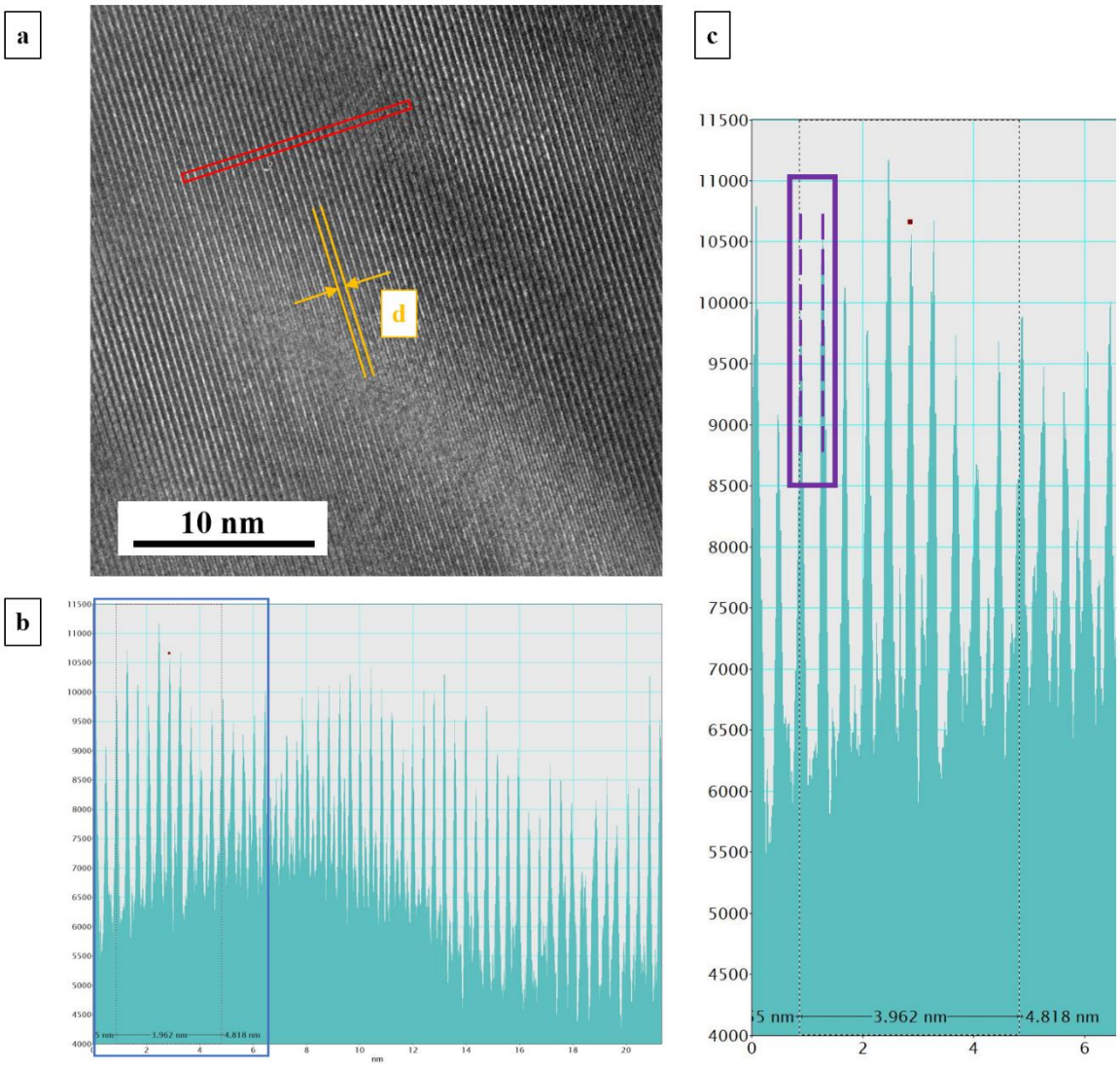


Figure 4.2 Schematic of the measurement of a d-spacing using line profiles in a HRTEM image. (a) The original HRTEM image. *d* is the d-spacing being measured; The red square is the line profile parallel to the *d* direction, where the integration width was 10 for the line profile. (b) The histogram of the line profile, where 10 spacings of *d* was measured to be 3.962 nm. (c) Magnified image of the area in the blue square in (b). The d-spacing in the purple square was measured to be 0.390 nm.

4.5.3 Fast Fourier Transform Analysis

As introduced in Section 1.3.1.1, FFT can be helpful for the analysis of HRTEM images. FFT images were operated by Gatan Digital Micrograph software. The d-spacings indicated by FFT images were also calculated by line profiles. As shown in Figure 4.3(a), *d'* is the d-spacing were being measured. A line profile was drawn in the reciprocal FFT image along the *1/d'* direction. The *1/d'* was then measured by the histogram shown in Figure 4.3(b), and the average *d'* was calculated to be 0.40 nm. After each spacing of *1/d'* was measured at 2.479 and 2.547 1/nm in Figure 4.3(c), *d'* was then fixed to 0.40 ± 0.01 nm with the error.

All line profiles for measuring d-spacings in this thesis are presented in Appendix.

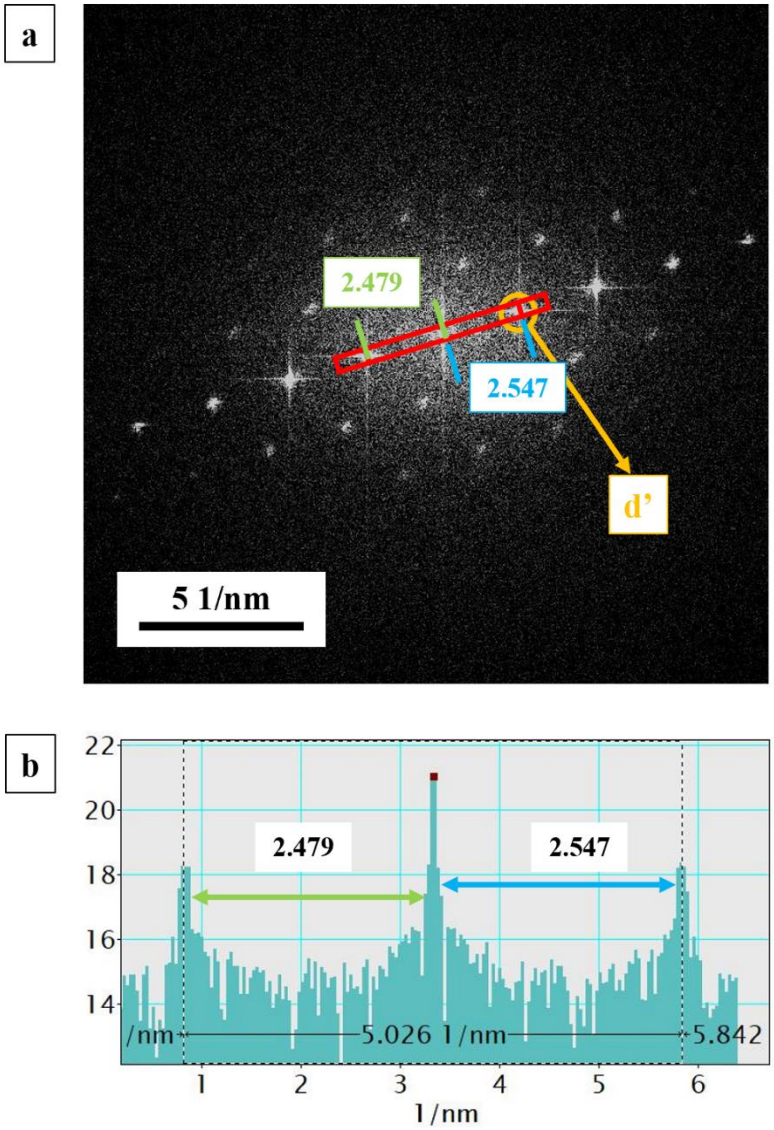


Figure 4.3 Schematic of the measurement of a d-spacing using line profiles in the FFT of Figure 4.1(a). (a) The original FFT image. *d'* is the d-spacing being measured; The red square is the line profile parallel to the *1/d'* direction, where the integration width was 10 for the line profile. (b) The histogram of the line profile, with double spacings of 1/d' measured to be 5.026 1/nm and individual spacings of 2.479 and 2.547 1/nm, respectively.

4.6 Fourier Transform Infrared Spectroscopy

PVA and peptide aqueous solutions were dip-casted onto microscope slides. FTIR samples were then prepared by the aforementioned freeze-thawing or annealing methods.

FTIR spectra were recorded using a Varian Excalibur FTS 3500 FTIR spectrometer (4 cm^{-1} wavenumber resolution) in ATR mode (using the golden gate diamond ATR crystal) with attenuated total reflection in the IR range from 2000 to 1000 cm^{-1}, obtaining 64 scans for co-averaged results. The system was equipped with a Parker FTIR purge gas generator that was run for 5 min before each scan to remove water vapor and carbon dioxide. Before scanning samples, a spectrum obtained without a sample is used for the background spectrum. The spectra in this thesis are obtained by subtracting the background intensity from the actual spectral intensity using the Agilent Cary 630 software. The FTIR data were finally analysed using the Agilent Cary 630 software with the reference of previous studies on PVA and PAs [13]-[18].

4.7 Atomic Force Microscopy

Peptide aqueous solutions were dip-casted on a glass substrate. Samples were then further processed by the freeze-thawing method.

Peptide fibres were characterised by an Agilent 5400 atomic force microscopy (AFM) using NCHV-A AFM tips (Bruker Ltd.) at the tapping mode over different locations within samples. AFM images were processed (flattened and smoothed) using WSxM 5.0 Develop software [1]. Line profiles were used to measure peptide fibre width, which is similar to the method described in Section 4.5.1. As shown in Figure 4.4, by drawing a line profile vertical to the fibre direction, the fibre width was measured to be 41 nm in this case. The error range of the peptide fibre width derived from 5 different measurements using line profiles from different areas of the image.

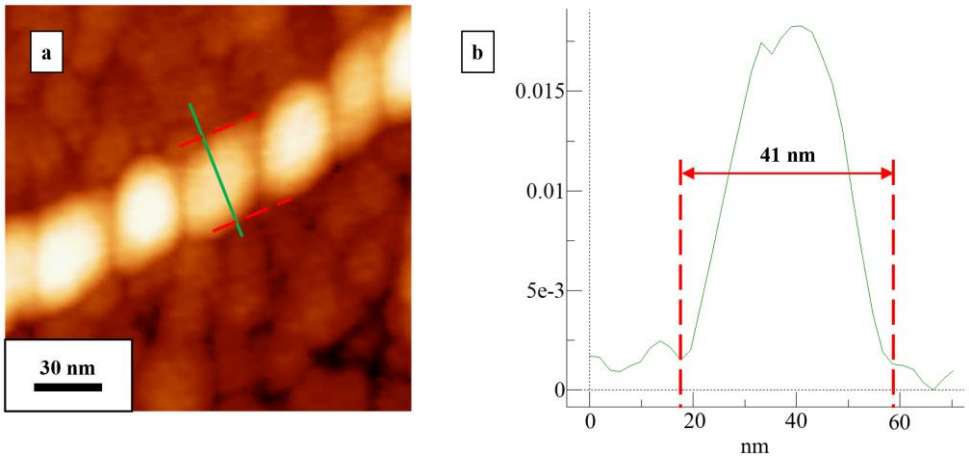


Figure 4.4 Schematic of the measurement of the peptide fibre width using line profiles in an AFM image. (a) An AFM image of a FP sample at pH=5, 0.5 mg/mL. The green line is the line profile vertical to the fibre direction, and the spacing between two red dash lines is the fibre width being measured. (b) The histogram of the line profile, where the fibre width was measured to be 41 nm.

4.8 X-ray Diffraction

Peptide and PVA aqueous solutions were dip-casted onto silicon wafers. Samples were then prepared using the annealing (at 250 ℃, for PVA) or freeze-thawing (for all peptides) methods introduced in Section 4.4.

X-ray Diffraction (XRD) analysis was conducted VIA Rigaku Miniflex diffractometer with a Cu Kα radiation at $\lambda = 0.154$ nm under 40 mA and 40 kV. The 2θ range is $10° – 60°$, with a step size of 0.007°. XRD data were processed using X'Pert Highscore software.

4.9 Scanning Transmission Electron Microscopy and Electron Ptychography

4.9.1 Experimental Procedures and Parameters Used for Images

The same samples of TEM introduced in Section 4.5 were used for the Scanning Transmission Electron Microscopy (STEM) and electron ptychography.

An aberration-corrected JEOL ARM200F electron microscope operated at 200 kV was used for the electron microscopy study. The camera length for all images was 8 cm, and the spot size was 8C. Convergence angles were 14 mrad for the PVA [010] image and 22.5 mrad for all the rest of the high-angle annular dark field (HAADF) STEM and electron ptychographic images. These convergence angles were selected based on the real space sampling of images and d-spacings that were being investigated. To be more specific, at the above convergence angles, the resolutions (at 0.098 nm for 14 mrad and 0.061 nm for 22.5 mrad) were sufficient for imaging the d-spacings of samples (all of which are greater than 0.2 nm) while also providing sufficient sampling for the scan size (0.013 nm for the PVA [$\bar{1}$10] image, and 0.027 nm for all the rest). Reference [2] contains more information on the convergence angle selection for STEM. The above spatial resolutions for the different convergence angles are approximated by the below equation [19], where δ is the resolution, λ is the wavelength of the electron beam (0.025 Å at 200 kV [20]), and α is the convergence semi-angle of the electron probe.

$$\delta \approx \frac{0.61\,\lambda}{\alpha} \tag{4.1}$$

The probe currents were 57 pA for the [010] image and 16 pA for all the other HAADF-STEM and electron ptychographic images. Above probe currents are calculated using normalised coefficients per 1uA of emission current with different spot sizes and condenser apertures. The normalised coefficients were calibrated by pervious users in January 2020 and presented on the ARM wiki website [21]. In the 4D STEM dataset recording, a focused STEM probe was used and the 2D CBED pattern at each probe position was recorded using a JEOL 4Dcanvas pixelated detector mounted on the ARM200F. Through pixel binning by 4-fold by binning fast mode (dwell time is 133μs for each pixel), 4D datasets were recorded. The aberration-corrected ADF images were recorded simultaneously using the JEOL ADF detector with the collection of 2D diffraction patterns. Data were processed and reconstructed by MATLAB scripts using Single-Side Band (SSB) or Wigner Distribution Deconvolution (WDD) methods. Details of the electron ptychographic reconstructions can be found in some previous papers published by our group [3]-[8].

d-spacings acquired from HAADF-STEM and electron ptychographic images were calculated using line profiles with the same method introduced in Section 4.5.2. All line profiles will be presented in Appendix.

4.9.2 Dose and Beam Damage

The dose used for PAs and PVA (will be presented in Sections 7.2 and 8.2) was higher than used for other typical beam-sensitive materials, such as perovskites [9] and zeolites [10]. The equation to calculate the dose is shown below, where *I* refers to the probe current; *t* is the dwell time per pixel, and *S* is the pixel area, which equals the square of the pixel size.

$$\text{Dose} = \frac{\text{I} \times \text{t}}{\text{S}} \tag{4.2}$$

In this project, the dwell time was quite high at 133 μs due to the limited pnCCD camera speed. Also, a relatively high probe current and smaller pixel size (because of the high magnification) were applied for phase-contrast images focused on the small local area. As introduced in Chapter 2, the observation of local information is significant because the extent of macromolecular and polymer crystals can be on a short range. All above factors give rise to the relatively high dose in this project.

Being conscious of the higher dose used for polymers and macromolecules, the first work in both Chapters 7 and 8 was to study the beam damage. It is confirmed that the crystallinity detected in PVA and PA systems was from the material nature, rather than formed through damage by electrons. Although a long-term exposure in electrons can cause mass loss and amorphization on the samples, the first-round acquisition is most likely to bring the clearest image and deliver the most precise information of the area. Therefore, all electron ptychographic images discussed in this thesis were selected from the first-round acquisitions to minimise the effects of the beam damage.

4.10 Model Modification and Image Simulation

The visualisation of all PA and PVA crystal models in the work was achieved by using the CrystalMaker software [11]. The whole PVA and peptide model modification processes presented in Chapters 7 and 8 were achieved using MATLAB scripts.

All image simulation work in this thesis was performed by Zhiyuan Ding in our group. 4D-STEM simulations of the PVA new model (shown in Section 8.5) in [010] and [$\bar{1}$10] directions were carried out using MULTEM [12] and customised MATLAB scripts. A complete static lattice was simulated which is reasonable given that quantitative intensities are not required. The simulated 4D-STEM datasets were used for ptychography reconstruction and integration for virtual ADF images. An acceleration voltage of 200 kV was applied for the simulations as in experiments. Convergence angles used were 14 mrad for the PVA [010] direction and 22.5 mrad for the PVA [$\bar{1}$10] direction. A perfect probe without aberrations was used in simulations. Simulated pixel size of scanning was 0.27 Å with 128×128 diffraction patterns (the [010] direction) and 0.13 Å with 175×175 diffraction patterns (the [$\bar{1}$10] direction). The scanning coordinates were meanwhile collected. The simulated pixelated detector had 256×256 pixels with a pixel size of 1 mrad. Spot sizes of 1.25 Å and 0.65 Å were applied for the [010] direction and the [$\bar{1}$10] direction, respectively. The sample thickness was set at 40 Å, and with the top surface of sample placed at the focal plane.

After simulation for 4D-STEM datasets, Poisson noise corresponding to electron dose was used to simulate a dose condition that is similar to experiments. The virtual ADF images were then integrated from collection angle higher than 72 mrad for both directions. Ptychography phase images were finally reconstructed using SSB and WDD methods [3]-[8].

4.11 References

[1] Horcas, I., Fernández, R., Gomez-Rodriguez, J. M., Colchero, J. W. S. X., Gómez-Herrero, J. W. S. X. M., & Baro, A. M. (2007). WSXM: A software for scanning probe microscopy and a tool for nanotechnology. *Review of scientific instruments*, *78*(1), 013705.

[2] Weyland, M., & Muller, D. A. (2020). Tuning the convergence angle for optimum STEM performance. *arXiv preprint arXiv:2008.12870*.

[3] Nellist, P. D., McCallum, B. C., & Rodenburg, J. M. (1995). Resolution beyond the 'information limit' in transmission electron microscopy. *Nature*, 374(6523), 630-632.

[4] Jesson, D. E., & Pennycook, S. J. (1995). Incoherent imaging of crystals using thermally scattered electrons. *Proceedings of the Royal Society of London. Series A: Mathematical and Physical Sciences*, *449*(1936), 273-293.

[5] Nellist, P. D., & Pennycook, S. J. (2000). The principles and interpretation of annular dark-field Z-contrast imaging. In *Advances in imaging and electron physics* (Vol. 113, pp. 147-203). Elsevier.

[6] Yang, H., MacLaren, I., Jones, L., Martinez, G. T., Simson, M., Huth, M., Ryll, H., Soltau, H., Sagawa, R., Kondo, Y., Ophus, C., Ercius, P., Jin, L., Kovács, A., & Nellist, P. D. (2017). Electron ptychographic phase imaging of light elements in crystalline materials using Wigner distribution deconvolution. Ultramicroscopy, 180, 173-179.

[7] Nellist, P. D., McCallum, B. C., & Rodenburg, J. M. (1995). Resolution beyond the 'information limit' in transmission electron microscopy. *Nature*, 374(6523), 630-632.

[8] O'Leary, C. M., Martinez, G. T., Liberti, E., Humphry, M. J., Kirkland, A. I., & Nellist, P. D. (2021). Contrast transfer and noise considerations in focused-probe electron ptychography. *Ultramicroscopy*, 221, 113189.

[9] Rothmann, M. U., Kim, J. S., Borchert, J., Lohmann, K. B., O'Leary, C. M., Sheader, A. A., … & Herz, L. M. (2020). Atomic-scale microstructure of metal halide perovskite. *Science*, *370*(6516), eabb5940.

[10] Dong, Z., Zhang, E., Jiang, Y., Zhang, Q., Mayoral, A., Jiang, H., & Ma, Y. (2023). Atomic-Level Imaging of Zeolite Local Structures Using Electron Ptychography. *Journal of the American Chemical Society*.

[11] Palmer, D. C. (2015). Visualization and analysis of crystal structures using CrystalMaker software. *Zeitschrift für Kristallographie-Crystalline Materials*, *230*(9-10), 559-572.

[12] Lobato, I., & Van Dyck, D. (2015). MULTEM: A new multislice program to perform accurate and fast electron diffraction and imaging simulations using Graphics Processing Units with CUDA. *Ultramicroscopy*, 156, 9-17.

[13] Wychowaniec, J. K., Smith, A. M., Ligorio, C., Mykhaylyk, O. O., Miller, A. F., & Saiani, A. (2020). Role of sheet-edge interactions in β-sheet self-assembling peptide hydrogels. *Biomacromolecules*, *21*(6), 2285-2297.

[14] Elsawy, M. A., Smith, A. M., Hodson, N., Squires, A., Miller, A. F., & Saiani, A. (2016). Modification of β-sheet forming peptide hydrophobic face: effect on self-assembly and gelation. *Langmuir*, *32*(19), 4917-4923.

[15] Wang, Z. (2018). *Self-assembly of Peptides on Surfaces* (Master dissertation, University of Oxford).

[16] Botwright, S. (2017). *Self-assembly of Peptides on Surfaces* (Master dissertation, University of Oxford).

[17] Zou, Y., Li, Y., Hao, W., Hu, X., & Ma, G. (2013). Parallel β-sheet fibril and antiparallel β-sheet oligomer: new insights into amyloid formation of hen egg white lysozyme under heat and acidic condition from FTIR spectroscopy. *The Journal of Physical Chemistry B*, *117*(15), 4003-4013.

[18] Mansur, H. S., Sadahira, C. M., Souza, A. N., & Mansur, A. A. (2008). FTIR spectroscopy characterization of poly (vinyl alcohol) hydrogel with different hydrolysis degree and chemically crosslinked with glutaraldehyde. *Materials Science and Engineering: C*, *28*(4), 539-548.

[19] Williams, D. B., & Carter, C. B. (1996). *The transmission electron microscope* (pp. 3-17). Springer Us.

[20] Ke, X., Bittencourt, C., & Van Tendeloo, G. (2015). Possibilities and limitations of advanced transmission electron microscopy for carbon-based nanomaterials. *Beilstein journal of nanotechnology*, *6*(1), 1541-1557.

[21] ARM wiki.

https://sites.google.com/view/oxfordarmwiki/home.

Accessed August 16, 2023.

Chapter 5. Morphological Study of Peptide Amphiphiles

5.1 Introduction

As introduced in Chapter 3, some previous papers suggest a strong connection between peptide fibre and peptide crystal morphologies [1]-[9]. Hence, studying peptide fibres using conventional transmission electron microscopy (CTEM) is an appropriate start of this project to gain an overview of the morphology before using high-resolution electron microscopic techniques to study the detailed structure of the PA β-sheet crystals. For the work discussed in this chapter, different sample preparation methods were first attempted to obtain the most appropriate peptide samples for the later microscopic studies. Then, this chapter also reports the morphology of three different peptides, F8, F9 and FP, and explores how parameters including amino acid sequence, peptide concentration and pH influence the morphology of the above peptides. Finally, HRTEM was used to explore the relationship between peptide fibres and the crystallinity of peptide fibres.

5.2 Results

5.2.1 Transmission Electron Microscopic Images of Samples Prepared by Different Methods

The investigation of sample preparation methods for peptide samples is the first step in this project. Spin-coating is a mature method for preparing thin-film peptide samples containing peptide fibres, according to previous dissertations from our group [3][4] that considered spin coating onto mica, glass and polymer substrates. Naturally, spin-coating was firstly tried to prepare thin-film peptide samples, and peptide fibres are expected to be seen under TEM. The spin-coating rotational speed and spinning time used for this work (as elaborated in Chapter 4) were the same as in the previous dissertations. Figure 5.1 shows TEM images of spin-coated F8 samples. In general, spin-coated peptide samples exhibit transparent films attached to the supporting carbon films of TEM grids rather than fibre-like structures. When comparing Figures 5.1(a) to 5.1(b) and 5.1(c) to 5.1(d), the increase in rotational speed causes holes and breaches in the transparent films. Figure 5.1 (comparing Figure 5.1(c) to 5.1(a) and 5.1(d) to 5.1(c)) also shows that a shorter spinning time at a given rotational speed produces samples with more material observable in the field of view. However, because the TEM images in Figure 5.1 appear not to be forming peptide fibres when spun directly onto TEM grids, other sample preparation methods should be considered at this stage.

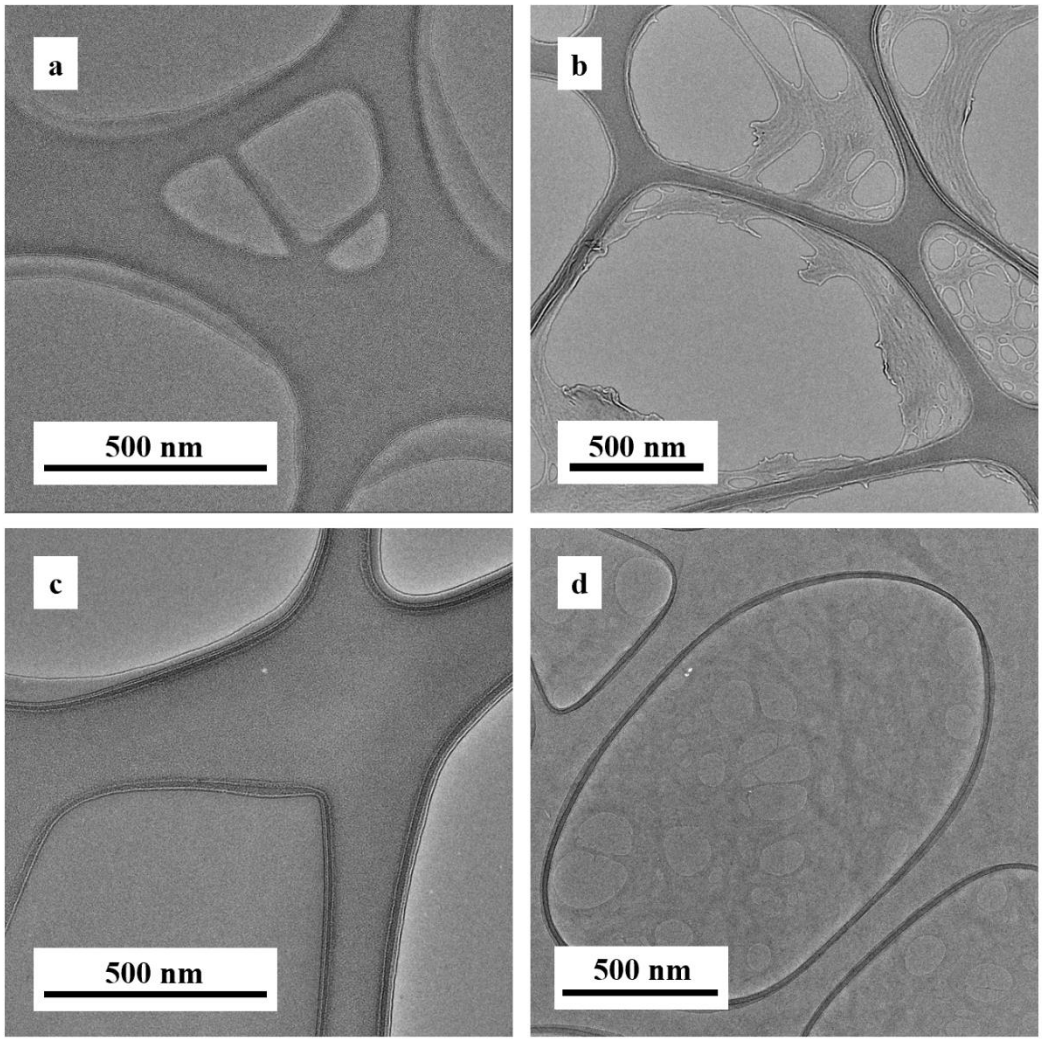


Figure 5.1 TEM images of spin-coated F8 samples (pH=7, 0.5 mg/mL). (a) Spinning at1500 rpm for 60 seconds. (b) Spinning at 2500 rpm for 60 seconds. (c) Spinning at1500 rpm for 30 seconds. (d) Spinning at 2500 rpm for 30 seconds.

Wang also mentioned in her dissertation [3] that dip-casting and drop-casting methods could be used to prepare thin-film peptide samples. Figure 5.2 displays TEM images of samples with the same conditions (peptide type, concentration, and pH) but prepared using different methods. Figure 5.2(b) shows that the drop-casted samples have peptide covering almost the entire field of view. However, it appears that an excessive amount of material has been attached to the TEM grid, and peptide fibres have been buried and cannot be found under TEM. Peptide fibres, on the other hand, can be clearly seen on the dip-cast sample shown in Figure 5.2(c). Based on

this result, dip-casting was selected to be the sample preparation method for thin-film samples in future research.

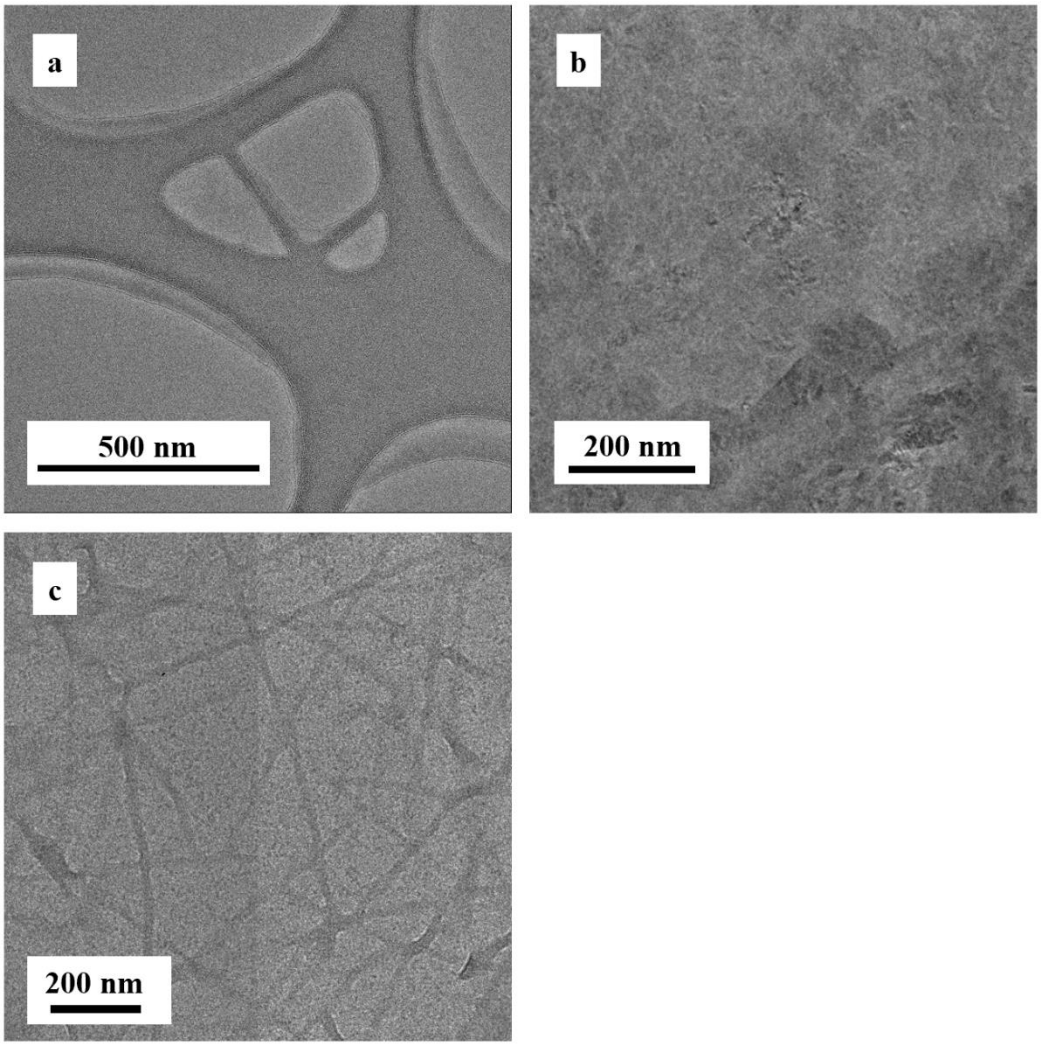


Figure 5.2 TEM images of F8 samples (pH=7, 0.5 mg/mL) by different sample preparation methods. (a) Spin-coating. (b) Drop-casting. (c) Dip-casting.

5.2.2 Study on Critical pH Values for Peptide Fibres

As stated in Section 3.3.3.3, pH is an important factor that influences peptide self-assembly and, as a result, peptide morphology. Previous research [3][4] shows that F8 and F9 only self-assemble to fibres at a specific range of pH values, which varies depending on the surface of

the substrate. Because the substrate of TEM grids with carbon supporting films has not been thoroughly studied, the critical pH values for forming peptide fibres should be investigated before specifically studying how fibre morphology varies with pH.

Previous research [3][4] and results in this work (presented in the following sections) confirm that peptide concentration has no effect on fibre formation, and the observations of pH values that do not form peptide fibres are shown in Figures 5.3 and 5.4, comparing TEM and AFM results. Fibres were found for F8 samples with pH ranging from 3 to 11. By contrast, rather than peptide fibres, other morphologies occurred at pH 2 and 12. Dendritic structures can be found in F8 samples at pH 2, as shown in Figures 5.3(a) using TEM and 5.4(a) using AFM. This kind of structure was also found in previous studies [3][4], and it was thought to be another formation of self-assembling peptide. Turning to F8 at pH 12, aggregated round features can be seen in both TEM image (Figure 5.3(b)) and AFM image (Figure 5.4(b)).

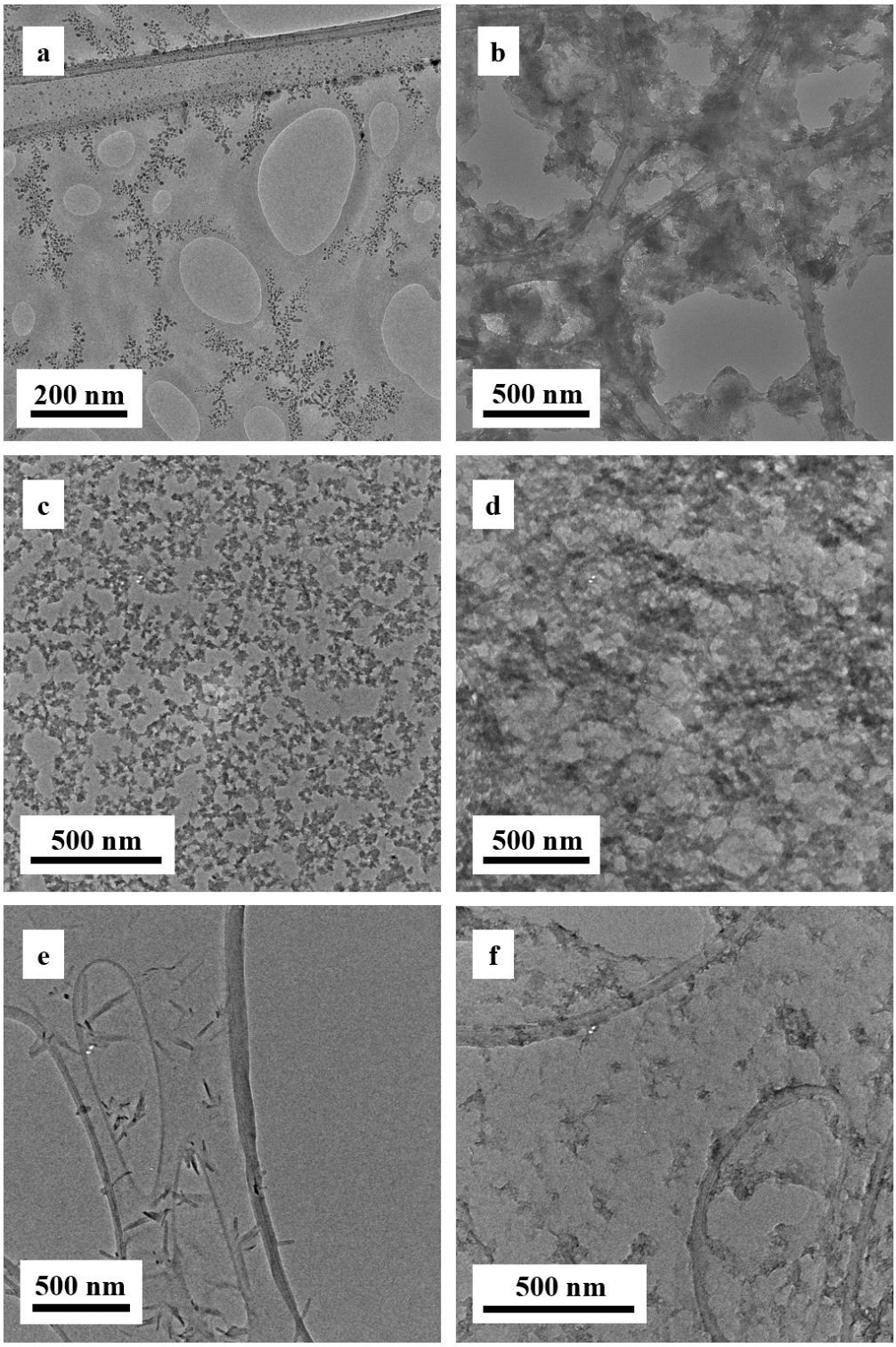


Figure 5.3 TEM images of peptide samples at critical pH values with no fibres (a) F8 at pH = 2. (b) F8 at pH = 12. (c) F9 at pH = 3. (d) F9 at pH = 13. (e) FP at pH = 3. (f) FP at pH = 12.

As for F9, as shown in Figures 5.3(c) and 5.4(c), samples prepared at pH 3 contain evenly distributed small features. At pH 13, indicated by Figure 5.3(d) and 5.4 (d), F9 fibres are transformed into dense peptide networks. In the case of FP, needles form at pH 3 (as shown in Figures 5.3(e) and 5.4(e)). These needles can also be viewed as short and straight fibres, indicating that starting at pH 3, FP molecules self-assemble into fibres with increasing pH until pH 12, at which point FP forms small dots, as shown in Figures 5.3(f) and 5.4(f).

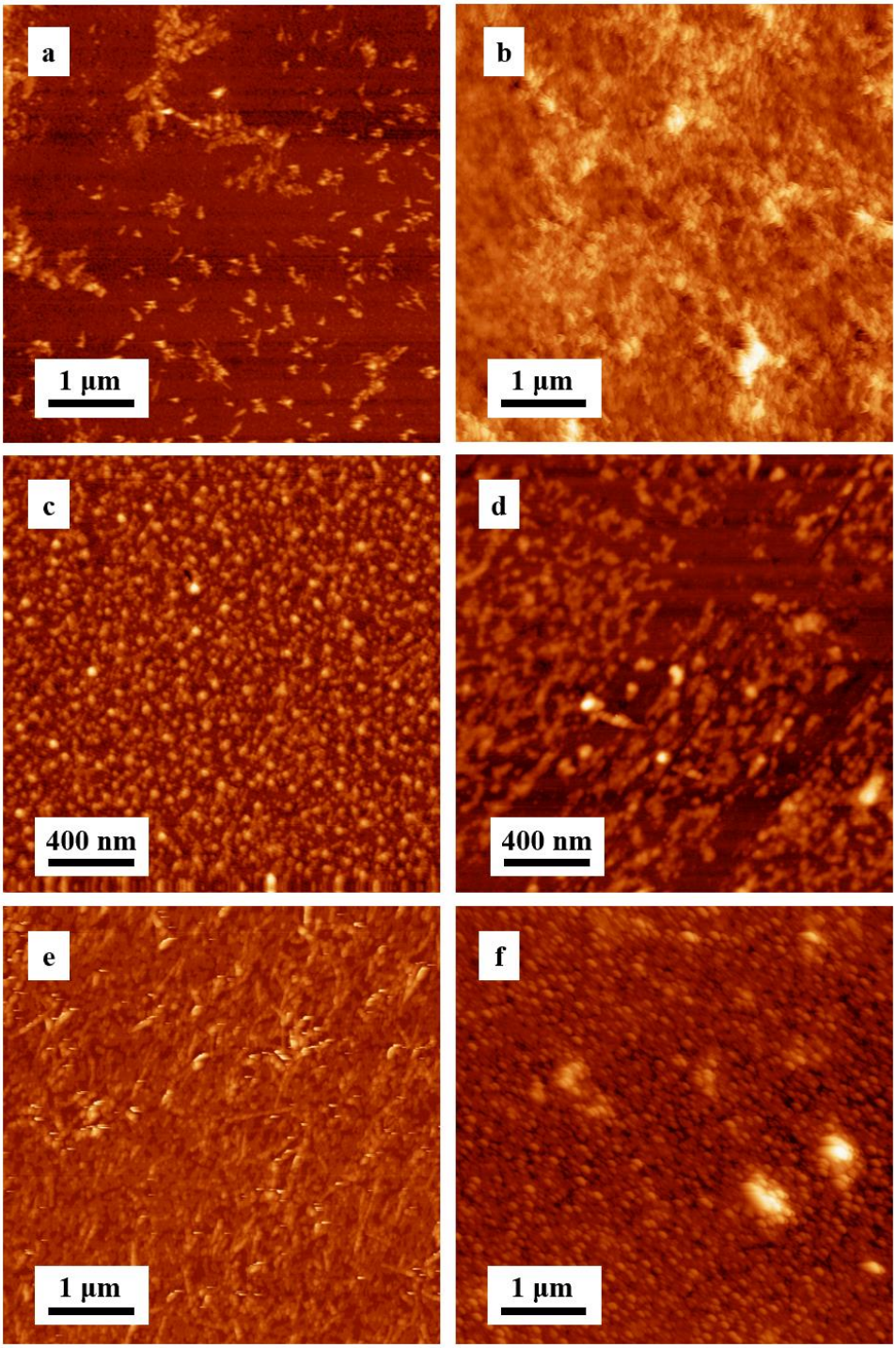


Figure 5.4 AFM images of peptide samples at critical pH values with no fibres (a) F8 at pH = 2. (b) F8 at pH = 12. (c) F9 at pH = 3. (d) F9 at pH = 13. (e) FP at pH = 3. (f) FP at pH = 12.

5.2.3 Microscopic Images of F8

5.2.3.1 Transmission Electron Microscopic Images of Samples with Different Peptide Concentration

Peptide concentration is another factor besides pH that may influence the peptide morphology [3],[4],[10]-[14]. For all three kinds of peptides, pH was fixed at their isoelectric points to study how morphology changes only with peptide concentration. The isoelectric point for F8 is pH 7, here pure water was chosen rather than neutral salt solutions to dissolve F8. This not only controls the pH at a constant number but also eliminates the influence of ionic concentration.

Figure 5.5 shows TEM images of F8 samples at pH 7 with varying peptide concentrations. Peptide fibres can be found in all six images in Figure 5.5. The width and density of fibres are normally two key factors to evaluate morphology [2][7], as these two factors primarily determine the mechanical properties of peptide hydrogels. As introduced in Section 4.5.1, line profiles from 5 different measurements were used to estimate the width and density of fibres in each image and all relevant information is summarised in Table 5.1. It is notable that as peptide concentration increases, fibre width does not change, whereas peptide density increases dramatically. Section 5.3.4.2 will discuss the possible reasons of the phenomenon.

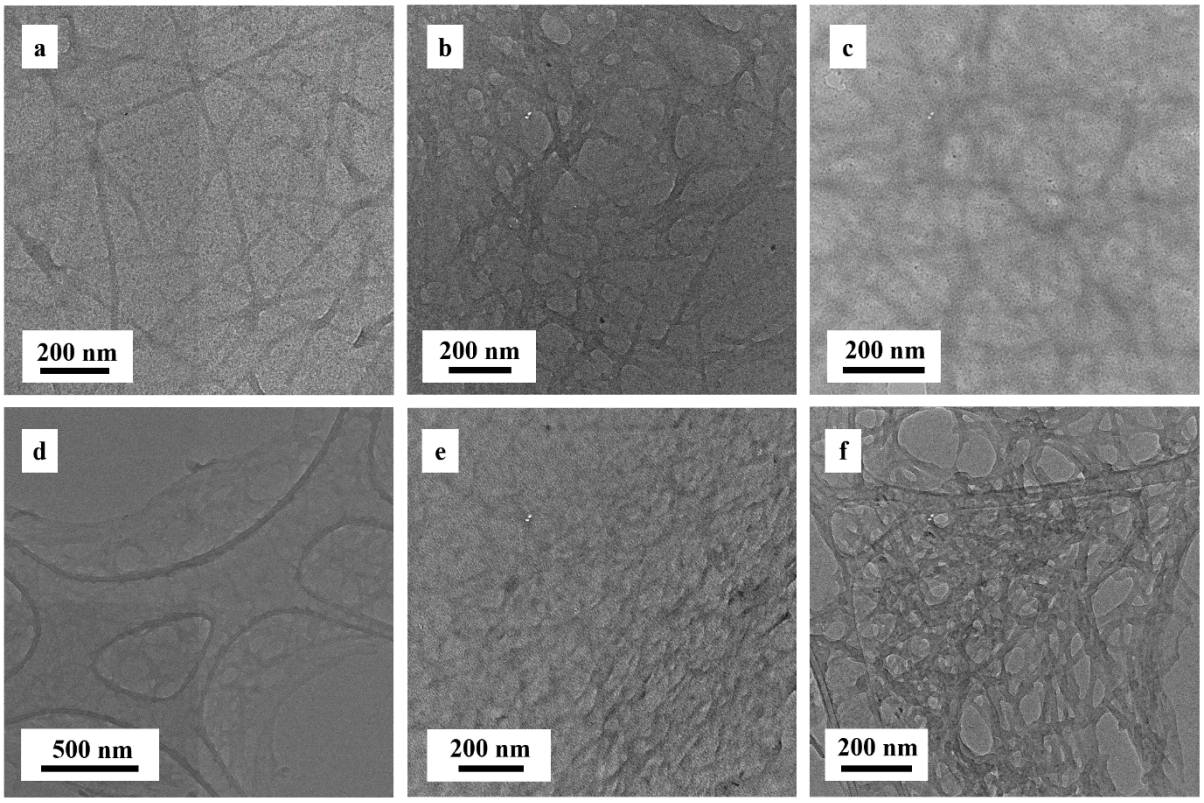


Figure 5.5 TEM images of F8 samples at pH=7, with different peptide concentrations. (a) 0.5 mg/mL. (b) 1 mg/mL. (c) 2 mg/mL. (d) 5 mg/mL. (e) 10 mg/mL. (f) 20 mg/mL.

Table 5.1 Summary of fibre information from F8 TEM images at pH 7 with different peptide concentrations.

Peptide Concentration (mg/mL)	Fibre width (nm)	Number of fibres per 200×200 $(nm)^2$
0.5	20 - 38	3 - 5
1	18 - 41	4 - 8
2	28 - 45	4 - 10
5	25 - 46	5 - 12
10	22 - 51	13 - 22
20	27 - 39	14 - 31

5.2.3.2 Transmission Electron Microscopic Images of Samples with Different pH

Following the exploration of the critical pH to form fibres for each type of peptide in Section 5.2.2, peptide fibre morphologies are studied.

First, F8 samples are examined at various integer pH values ranging from 3 to 11. TEM images are shown in Figure 5.6, and information about fibre width and density in all images in Figure 5.6 is listed in Table 5.2. F8 fibres can be found in all nine images in Figure 5.6. It can also be concluded from Figure 5.6 and Table 5.2 that at its isoelectric point, F8 has the widest but loosest fibre formation. With increasing pH values from 3 to 7, fibres become longer and wider. In terms of the fibre density, it starts with loose fibres, and the density reaches its maximum at pH 5. Similarly, from pH 7 to 11, F8 fibres become thinner as the pH increases. The highest density of peptide fibres is found at pH 9 between pH 7 and 11. Furthermore, aggregated nodes are clearly visible in samples prepared at pH 10 and 11, as shown in Figures 5.6(h) and 5.6(i). Section 5.3.4.3 will analyse and discuss the aforementioned trends.

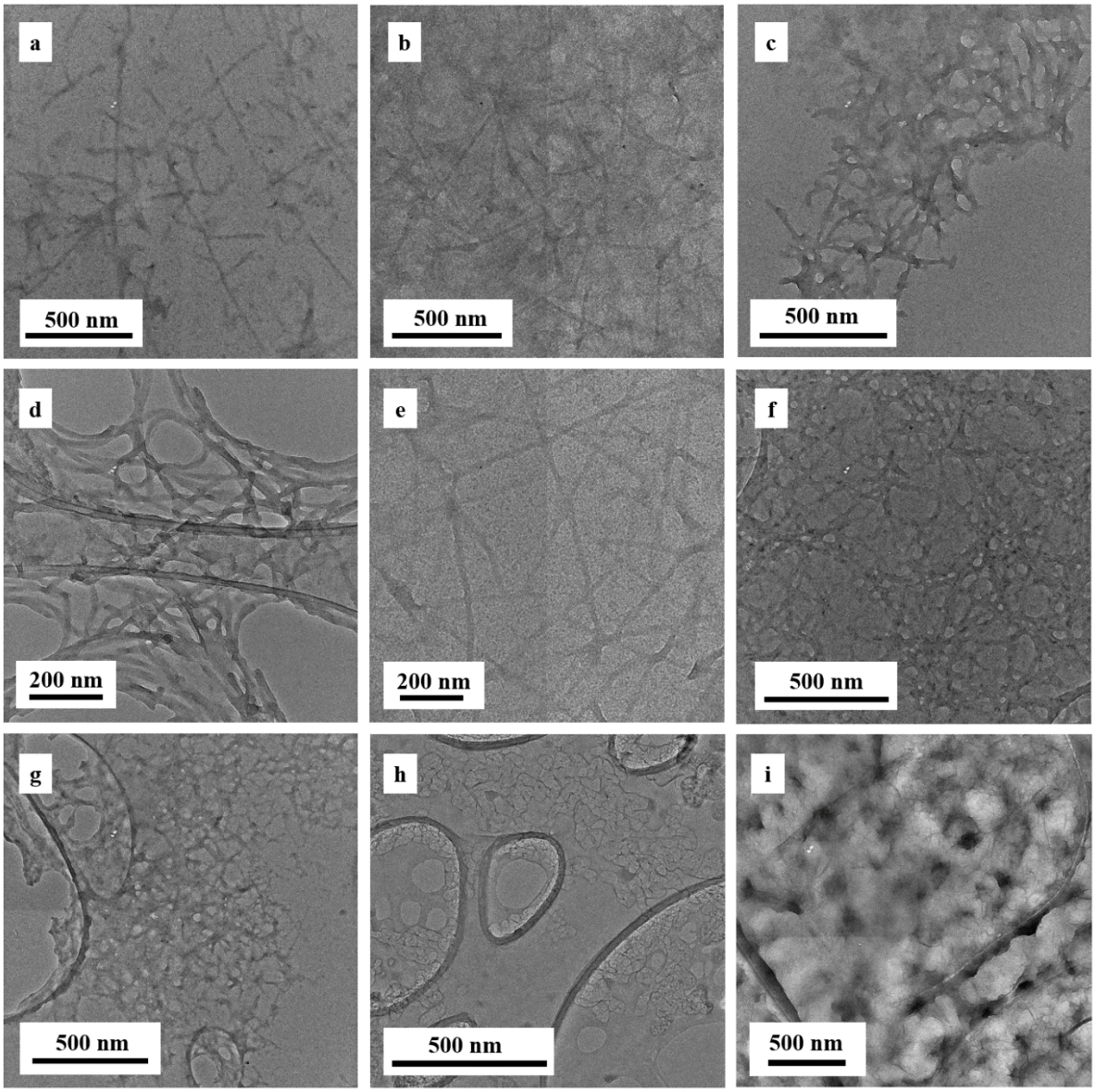


Figure 5.6 TEM images of F8 samples at 0.5 mg/mL, with different pH values. (a) pH=3. (b) pH=4. (c) pH=5. (d) pH=6. (e) pH=7, isoelectric point of F8. (f) pH=8. (g) pH=9. (h) pH=10. (i) pH=11.

Table 5.2 Summary of fibre information from F8 TEM images at 0.5 mg/mL with different pH values.

pH	Fibre width (nm)	Number of fibres per 200×200 $(nm)^2$
3	12 - 22	2 - 4
4	11 - 27	2 - 6
5	15 - 31	8 - 15
6	18 - 29	6 - 9
7	20 - 38	3 - 5
8	16 - 25	11 - 17
9	11 - 30	13 - 21
10	7 - 16	12 - 18
11	12 - 19	9 - 19

5.2.3.3 Atomic Force Microscopic Images

Because most previous studies used AFM to study morphology, AFM was also used to further characterise the peptide fibres in this study. Figure 5.7 depicts AFM images of F8 fibres, and Table 5.3 summarises the data obtained from Figure 5.7. As introduced in Section 4.7, fibre width and density in each after AFM image was calculated using line profiles derived from 5 different measurements.

The morphologies in AFM data mostly agree with the TEM results, with thin and straight fibres at pH 4 (shown in Figure 5.7(a)), aggregated nodes at pH 10 (shown in Figure 5.7(c)), loose and wide fibres at pH 7 (shown in Figure 5.7(b)), and denser fibres at pH 7 with a higher concentration at 20 mg/mL (shown in Figure 5.7(d)). However, AFM data (including later AFM data of F9 and FP) show a significant difference in fibre size, which will be discussed in Section 5.3.2.

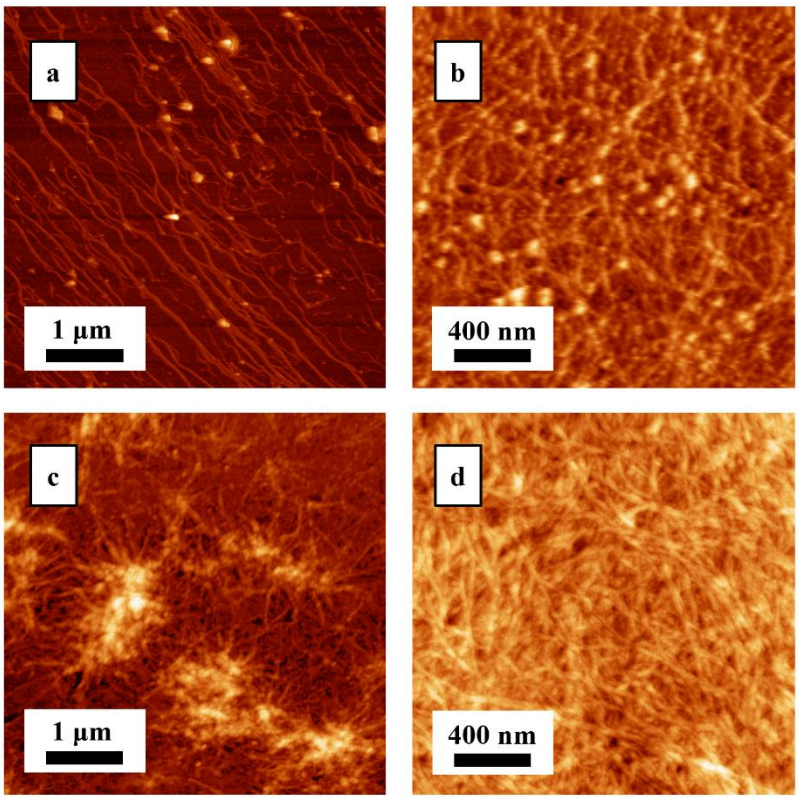


Figure 5.7 AFM images of F8 samples. (a) pH=4, 0.5 mg/mL. (b) pH=7, 0.5 mg/mL. (c) pH=10, 0.5 mg/mL. (d) pH=7, 20 mg/mL.

Table 5.3 Summary of fibre information from F8 AFM images shown in Figure 5.7.

pH	Peptide Concentration (mg/mL)	Fibre width (nm)	Number of fibres per 200×200 $(nm)^2$
4	0.5	21 - 31	2 - 5
7	0.5	19 - 36	3 - 7
10	0.5	15 - 28	4 - 10
7	20	22 - 38	6 - 15

5.2.4 Microscopic Images of F9

5.2.4.1 Transmission Electron Microscopic Images of Samples with Different Peptide Concentration

Similarly to F8, the effect of peptide concentration on fibre width and density is firstly investigated on F9. Figure 5.8 shows TEM images of F9 samples at the same pH (at the isoelectric point of F9, pH = 9.5) with different peptide concentrations, and Table 5.4 summarises the information on fibre width and density in Figure 5.8. F9 follows the same trend as F8, in that increasing peptide concentration increases fibre density dramatically but does not contribute to an increase in fibre width.

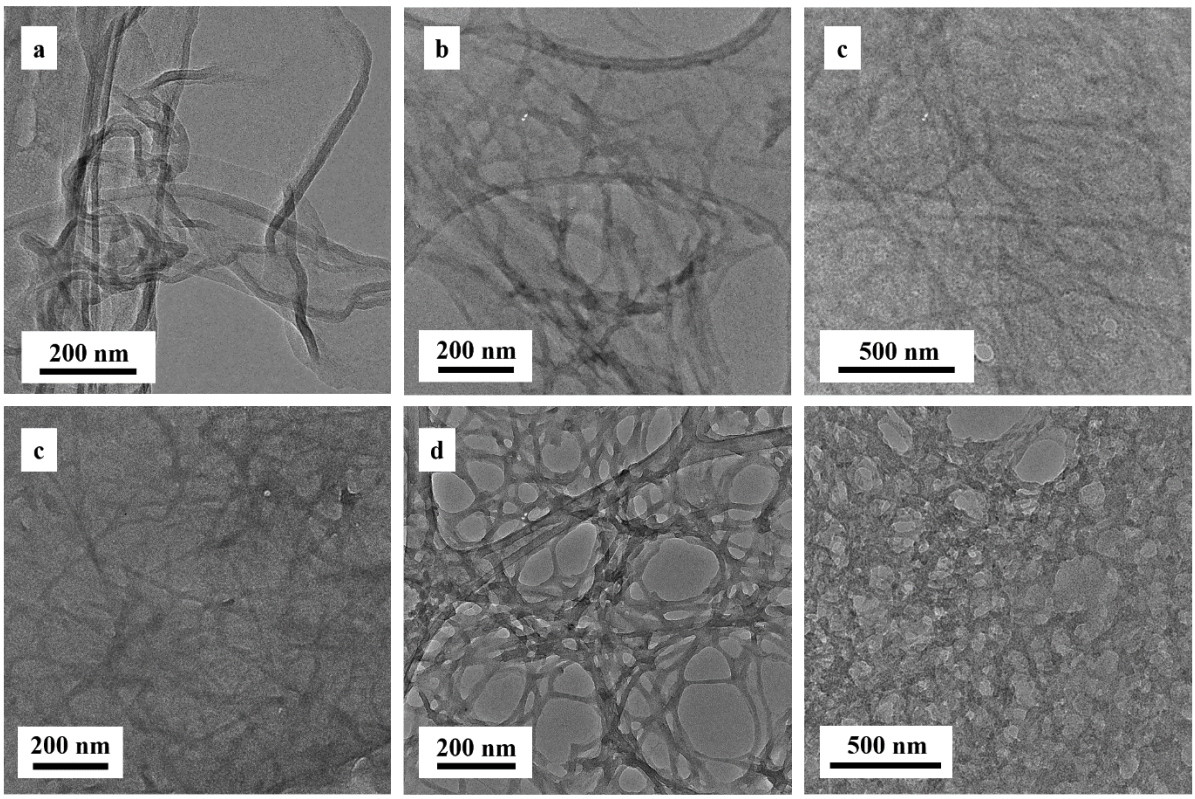


Figure 5.8 TEM images of F9 samples at pH=9.5, with different peptide concentrations. (a) 0.5 mg/mL. (b) 1 mg/mL. (c) 2 mg/mL. (d) 5 mg/mL. (e) 10 mg/mL. (f) 20 mg/mL.

Table 5.4 Summary of fibre information from F9 TEM images at pH 9.5 with different peptide concentrations.

Peptide Concentration (nm)	Fibre width (nm)	Number of fibres per 200×200 $(nm)^2$
0.5	28 - 37	5 - 11
1	21 - 35	8 - 17
2	22 - 35	11 - 19
5	25 - 41	13 - 18
10	20 - 35	14 - 21
20	27 - 38	16 - 25

5.2.4.2 Transmission Electron Microscopic Images of Samples with Different pH

Then, F9 samples of the same concentration but at different pHs were characterised. Figure 5.9 depicts their results from pH 4 to 12, and Table 5.5 lists the information obtained from these images. In a similar manner to F8, F9 has the widest but loosest fibres at its isoelectric points. Figures 5.9(a) to (f) show that as the pH increases, short fibres develop into longer and wider ones, and reaching their maximum density at pH 6. After surpassing through the isoelectric point, fibres become denser but thinner. As shown in Figures 5.9(h) and (i), F9 fibres also have the tendency to aggregate to nodes.

The results of F9 are essentially the same as those of F8, including how peptide concentration and pH influence peptide morphology.

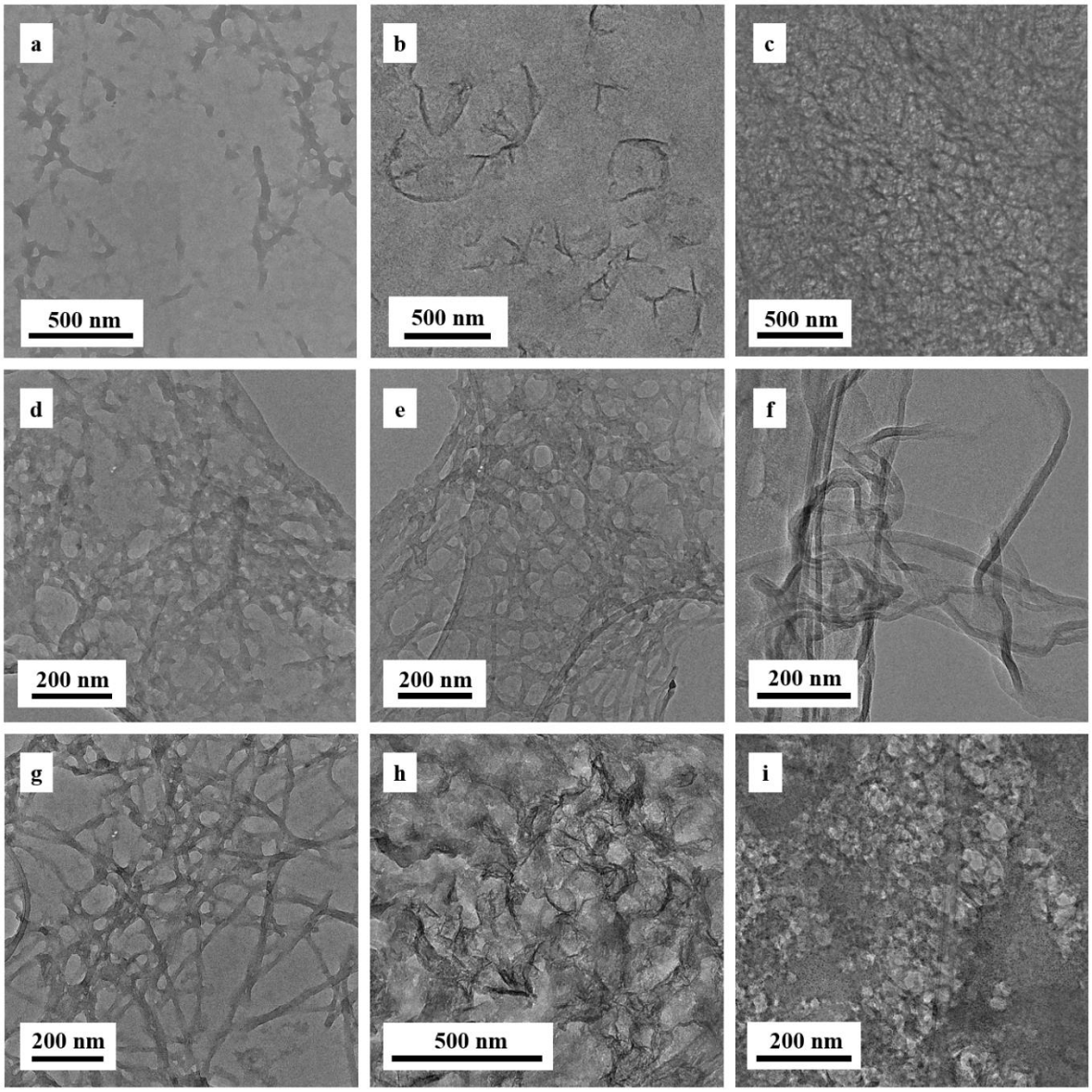


Figure 5.9 TEM images of F9 samples at 0.5 mg/mL, with different pH values. (a) pH=4. (b) pH=5. (c) pH=6. (d) pH=7. (e) pH=8. (f) pH=9.5, isoelectric point of F8. (g) pH=10. (h) pH=11. (i) pH=12.

Table 5.5 Summary of fibre information from F9 TEM images at 0.5 mg/mL with different pH values.

pH	Fibre width (nm)	Number of fibres per 200×200 $(nm)^2$
4	15 - 28	6 - 12
5	18 - 29	3 - 9
6	21 - 32	18 - 26
7	22 - 32	16 - 25
8	25 - 35	13 - 20
9.5	28 - 37	5 - 11
10	22 - 31	6 - 17
11	16 - 28	10 - 18
12	15 - 24	22 - 39

5.2.4.3 Atomic Force Microscopic Images

AFM images of F9 are presented in Figure 5.10 and information from this Figure is concluded in Table 5.6. According to these figure and tables, the above conclusions are also supported by the AFM images of F9. High-concentration samples in Figures 5.10(d) and (e) have much denser fibres, whereas samples at the isoelectric points of F9 have the widest and loosest structure.

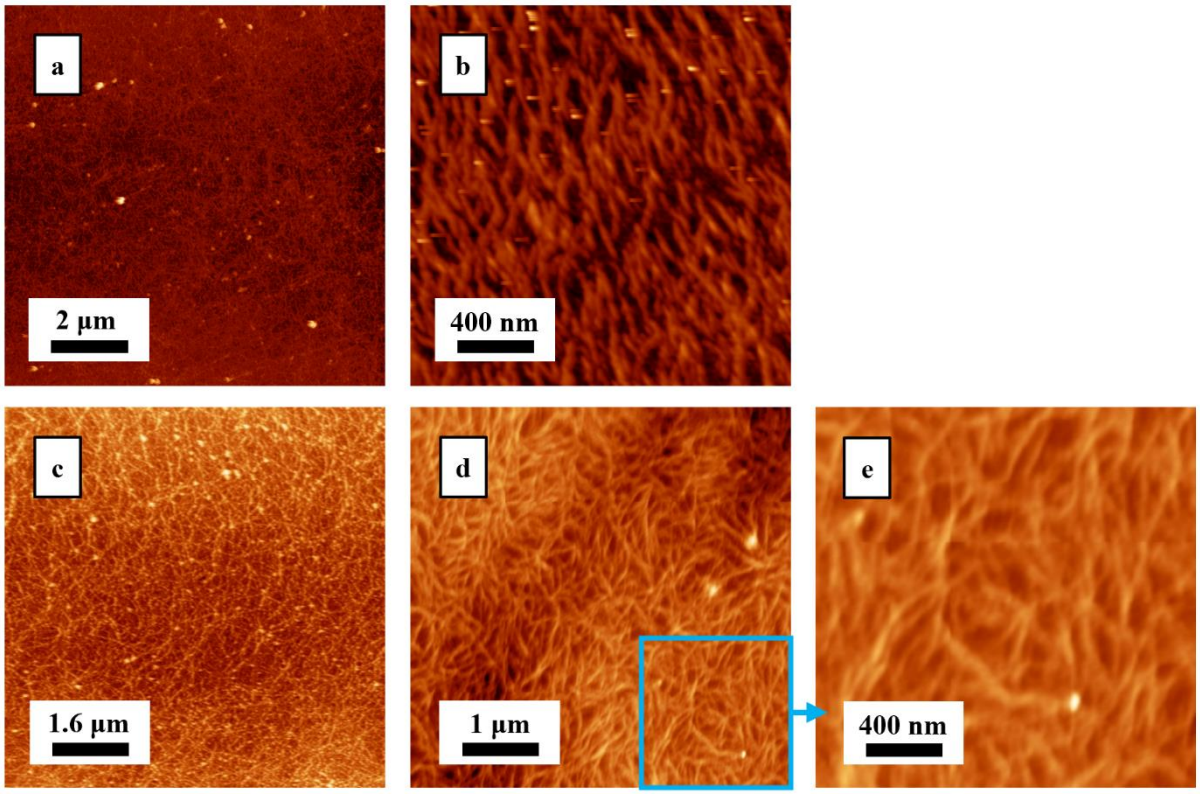


Figure 5.10 AFM images of F9 samples. (a) pH=6, 0.5 mg/mL. (b) pH=9.5, 0.5 mg/mL. (c) pH=12, 0.5 mg/mL. (d) pH=9.5, 20 mg/mL. (e) Magnified image of the area in the blue square in (d).

Table 5.6 Summary of fibre information from F9 AFM images shown in Figure 5.10.

pH	Peptide Concentration (mg/mL)	Fibre width (nm)	Number of fibres per 200×200 $(nm)^2$
6	0.5	28 - 45	9 - 12
9.5	0.5	36 - 52	3 - 6
12	0.5	31 - 50	5 - 9
9.5	20	33 - 58	8 - 12

5.2.5 Microscopic Images of FP

5.2.5.1 Transmission Electron Microscopic Images of Samples with Different Peptide Concentration

In this section, the morphology of FP is studied. The study sequence is similar to that of F8 and F9, but in section 5.2.5.4, the level of twisting of fibres will be investigated further.

Figure 5.1 and Table 5.7 show the results of research on how peptide concentrations influence the morphology of FP peptides. Twisting fibres can be seen in all four images of Figure 5.11, which successfully fulfil the design of inserting proline mid ring the FP molecule [15]-[17]. High-concentration FP samples have a denser fibre system, with no apparent changes in fibre width with peptide concentration, which is similar to F8 and F9.

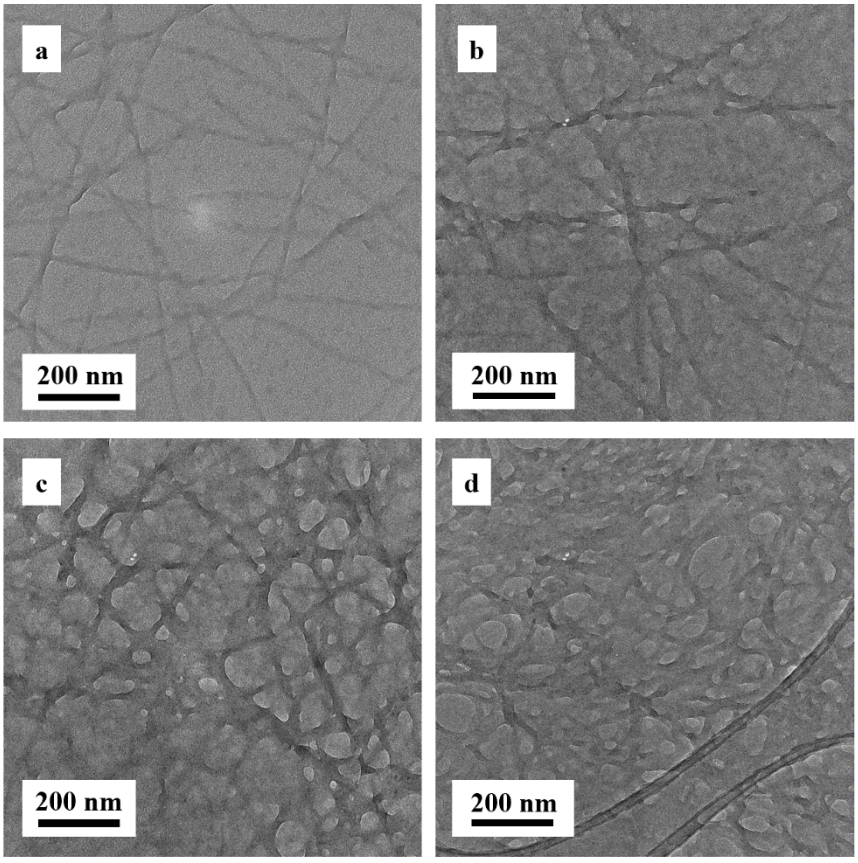


Figure 5.11 TEM images of FP samples at pH=7, with different peptide concentrations. (a) 0.5 mg/mL. (b) 2 mg/mL. (c) 5 mg/mL. (d) 20 mg/mL.

Table 5.7 Summary of fibre information from FP TEM images at pH 7 with different peptide concentrations.

Peptide Concentration (nm)	Fibre width (nm)	Number of fibres per 200×200 $(nm)^2$
0.5	22 - 29	7 - 11
2	20 - 27	8 - 13
5	16 - 26	11 - 16
20	21 - 26	15 - 21

5.2.5.2 Transmission Electron Microscopic Images of Samples with Different pH

Figure 5.12 illustrates FP samples at the same concentration but with varying pH values. In terms of fibre width and density (as shown in Table 5.8), FP follows the same trend as F8 and F9. However, pH changes, on the other hand, have a significant impact on the FP twisting structure. Twisting fibres can be found in Figure 5.12(b), whereas fibres are more likely to be "bobbed" than "twisted" in samples with pH 5 and 9. Furthermore, at pH 11, fibres stack together to form a larger bundle. Accordingly, the study on how pH influences the level of twisting of FP fibres can be interesting. Section 5.2.4.4 will show the findings in this area.

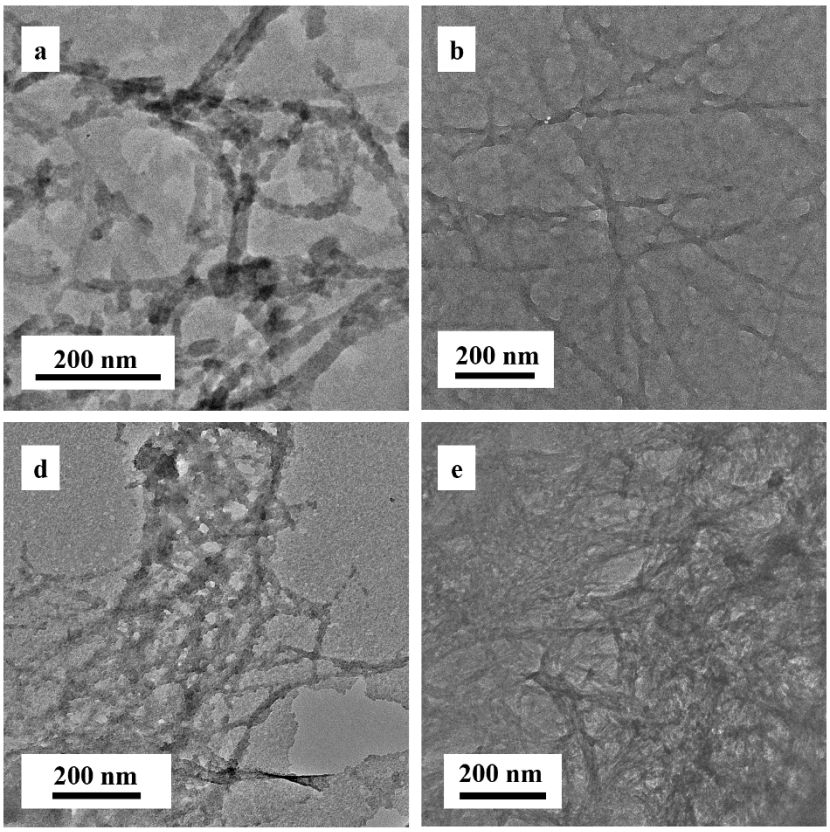


Figure 5.12 TEM images of FP samples at 0.5 mg/mL, with different pH values. (a) pH=5. (b) pH=7, isoelectric point of FP. (c) pH=9. (d) pH=11.

Table 5.8 Summary of fibre information from FP TEM images at 0.5 mg/mL with different pH values.

pH	Fibre width (nm)	Number of fibres per 200×200 $(nm)^2$
5	19 - 28	8 - 13
7	22 - 29	7 - 11
9	15 - 26	12 - 19
11	13 - 19	17 - 22

5.2.5.3 Atomic Force Microscopic Images

AFM images of FP are shown in Figure 5.13. The trend of width and density with the changes of pH and concentration is consistent to what TEM images suggest in the last two sections.

More importantly, AFM images show a better contrast of the fibre twisting. Because peptides are made up of light atoms, the contrast in TEM images can be relatively weak [18][19]. It should be noted that stacking fibres can also be found using AFM at pH 11, as shown in Figure 5.13(d). This demonstrates that FP fibres tend to stack together at high pH (at least higher than 11).

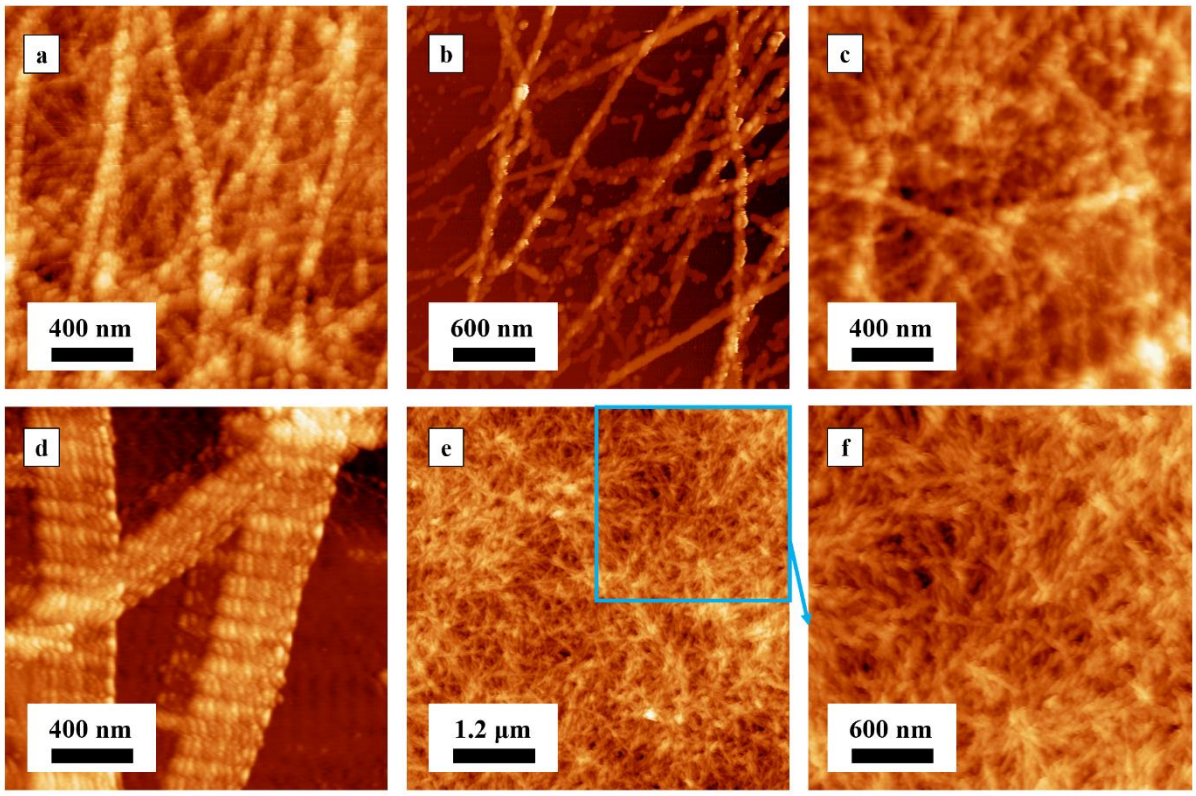


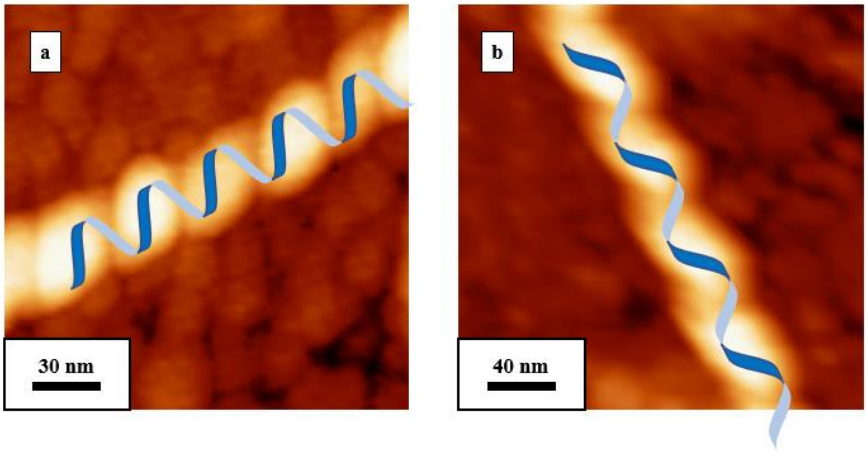
Figure 5.13 AFM images of FP samples. (a) pH=5, 0.5 mg/mL. (b) pH=7, 0.5 mg/mL. (c) pH=9, 0.5 mg/mL. (d) pH=11, 0.5 mg/mL. (e) pH=7, 20 mg/mL. (f) Magnified image of the area in the blue square in (e).

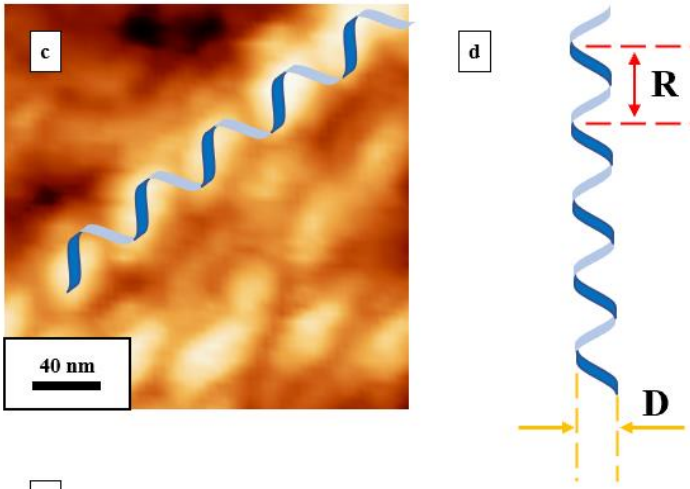
Table 5.9 Summary of fibre information from FP AFM images shown in Figure 5.13.

pH	Peptide Concentration (mg/mL)	Fibre width (nm)	Number of fibres per 200×200 $(nm)^2$
5	0.5	35 - 59	6 - 11
7	0.5	36 - 58	3 - 6
9	0.5	27 - 36	5 - 8
11	0.5	N/A	N/A
7	20	41 - 54	9 - 12

5.2.5.4 High-magnification Atomic Force Microscopic Images of Twisting Fibres

As previously stated, FP is intended to form twisting fibres by introducing proline mid-groups [20]. According to the results of the last two sections, pH appears to be able to change the twisting of the fibres. This section investigates how pH values affect the level of twisting of fibres. As mentioned in the previous section, AFM images can provide better contrast in the twisting of fibres than TEM images. Therefore, this section describes AFM investigations of the fibre twisting. Figure 5.14(a), (b), and (c) show high-magnification AFM images of twisting fibres at pH 5, 7, and 9. After checking the selected fibres are horizontal to the viewing plane using WSxM 5.0 Develop software (where the thickness of the fibre is consistent), the value R/D is used to assess the level of twisting, where R represents the unit repeat distance of the twist along the fibre axis and D represents the diameter of the fibre. The greater the R/D ratio, the lower the level of twisting. According to Figure 5.14(e), fibres at pH 7 (the isoelectric point of FP) twist the least. The potential reason will be discussed in section 5.3.3.





e

Figure	pH	R (the unit repeat distance of the twist along the fibre axis) / nm	D (diameter of the fibre) / nm	Average R/D
a	5	34 ± 3	41 ± 2	0.83
b	7	72 ± 2	40 ± 3	1.80
c	9	48 ± 2	31 ± 3	1.55

Figure 5.14 AFM images of FP twisting fibres at high magnification at 0.5 mg/mL, with different pH values. (a) pH=5. (b) pH=7. (c) pH=9. (d) Scheme of a twisting fibre. R stands for the unit repeat distance of the twist along the fibre axis. D represents the diameter of the fibre. The ratio of R over D can reflex the level of twisting, where the level increases with the ratio decreases. (e) Summary of R/D ratios of (a), (b) and (c).

5.2.6 High-resolution Transmission Electron Microscopic Images of Peptide Fibres

Finally, because there is a suggested link between peptide fibres and peptide crystals, HRTEM is used in this section to image peptide fibres, and regular fringes indicating peptide crystals are expected to be detected using HRTEM.

HRTEM images of F8, F9, and FP fibres are shown in Figure 5.15. Surprisingly, as shown in Figure 5.15(b), (c), and (e), F8 and F9 fibres have very small areas of crystalline materials in the sample when magnified. Furthermore, as illustrated in Figure 5.15(c), the crystalline part is not locked within F8 fibres, but are observed outside the fibres. Besides this, for the FP fibres shown in Figure 5.15(f), the selected area electron diffraction results in Figure 5.15(g) demonstrate that the FP fibres in (f) are amorphous. The findings in this chapter suggest that peptide crystals do not have a strong relationship with peptide fibres.

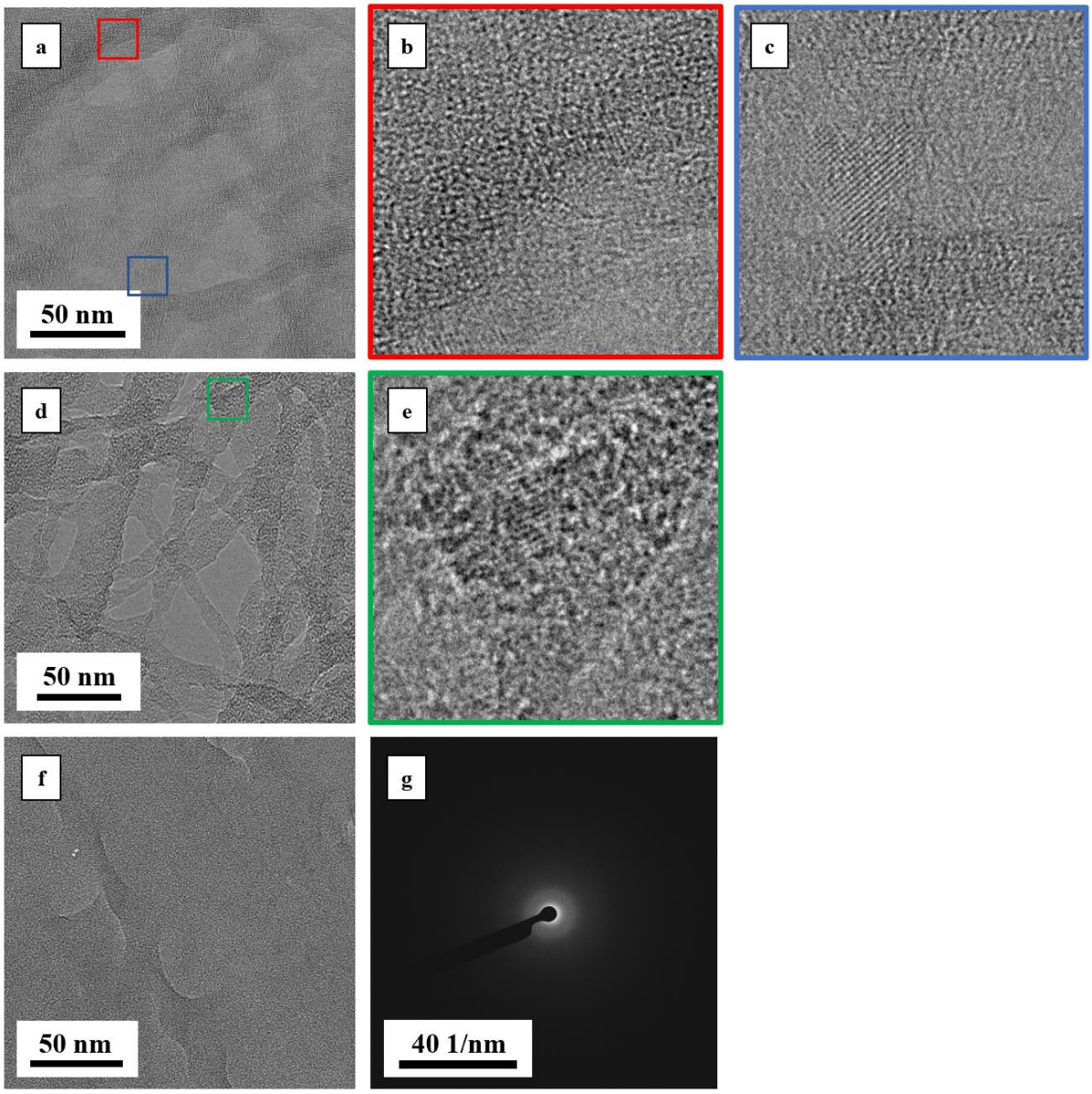


Figure 5.15 HRTEM and FFT images of peptide fibres. (a) F8 fibres. (b) Magnified image of the area in the red square in (a). (c) Magnified image of the area in the blue square in (a). (d) F9 fibres. (e) Magnified image of the area in the green square in (d). (f) FP fibres. (g) SAED of (f).

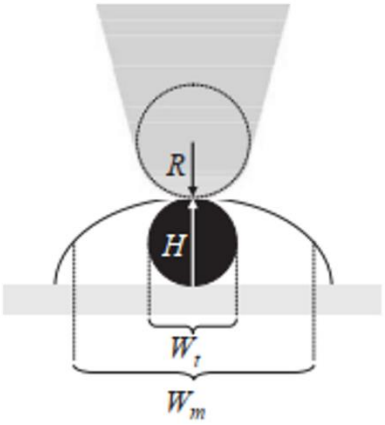
5.3 Discussion

5.3.1 Methods of Sample Preparation

The preparation of samples is a critical first step in the entire project. It was found (Section 5.2.1) that dip-casting is the most appropriate method to prepare thin-film peptide TEM samples. Then, it is worthwhile to discuss why previous studies [3][4] managed to make decent AFM samples using spin-coating, while it was unable to be achieved on TEM grids. Wang [3] discovered that peptide morphology is substrate-dependent in her master's dissertation. She chose mica and glass sheets as substrates for AFM samples, while carbon supported copper grids were used for TEM samples. Dip-casting can probably place peptide samples on TEM grids better than spin-coating and drop-casting. Dip-casting were selected to prepare all subsequent peptide samples based on above results.

5.3.2 Differences between Transmission Electron Microscopic and Atomic Force Microscopic Images

Although TEM and AFM images show the same trends in how concentrations and pH affect fibre morphology, AFM images exhibit a significant difference in fibre size when compared to TEM images. Sherratt *et al.* [21] previously investigated this problem on biological cylindrical samples. They suggest that AFM data can have errors due to the radius of the AFM probes, as shown in Figure 5.16. Figure 5.16 also depicts the relationship between the measured width (W_m) and the true width (W_t).



$$W_m = 2 \times \sqrt{R \times W_t + \frac{W_t^2}{4}}$$

Figure 5.16 Explanation of AFM size errors resulted from the radius of the AFM probes. Proposed by Sherratt *et al.* [21]. W_m is the measured width of the cylindrical sample, and W_t is the true width of the cylindrical sample.

Widths measured by AFM in this chapter are then calibrated using the equation in Figure 5.16. Tables 5.10 and 11 present the calibrated results of F8 and F9 fibres. Although the calibration brings AFM measurements closer to those of TEM, there are still major differences between them. The results for fibre density are also significantly different, with peptide fibres being denser under TEM than AFM. As mentioned in the Section 3.3.3.4, peptide fibres are substrate sensitive. It is likely that these differences can also be attributed to different substrates.

Table 5.10 Summary of fibre information from F8 TEM images and calibrated AFM images.

Calibrated Fibre width measured by AFM (nm)	Fibre width measured by TEM (nm)	Number of fibres per 200×200 $(nm)^2$ measured by AFM	Number of fibres per 200×200 $(nm)^2$ measured by TEM
9 - 17	11 - 27	2 - 5	2 - 6
8 - 21	20 - 38	3 - 7	3 - 5
5 - 14	7 - 16	4 - 10	12 - 18
10 - 23	27 - 39	6 - 15	14 - 31

Table 5.11 Summary of fibre information from F9 TEM images and calibrated AFM images.

Calibrated Fibre width measured by AFM (nm)	Fibre width measured by TEM (nm)	Number of fibres per 200×200 $(nm)^2$ measured by AFM	Number of fibres per 200×200 $(nm)^2$ measured by TEM
15 - 29	21 - 32	9 - 12	18 - 26
21 - 36	28 - 37	3 - 6	5 - 11
17 - 34	15 - 24	5 - 9	22 - 39
19 - 41	27 - 38	8 - 12	16 - 25

5.3.3 Twisting Fibres of FP

Next, how factors such as pH affect the molecular structure of peptides should be considered, which then influences peptide fibre morphologies.

Figure 5.17 (duplicate of Figure 3.15 for data interpretation in this section) shows a typical peptide fibre molecular model proposed by Smith *et al.* [22], from which it can be seen that PA molecules tend to self-assemble into a "sawtooth" structure (introduced in section 3.2.5), owing to the hydrophobicity of the side groups. Then, after a large number of pairs stack together, fibres are formed as suggested in Figure 5.17 (b). It should be noted that the mechanism for transforming from Figure 5.17(a) to (b) has not been thoroughly investigated, but the model shown in (b) can still be used to interpret above results.

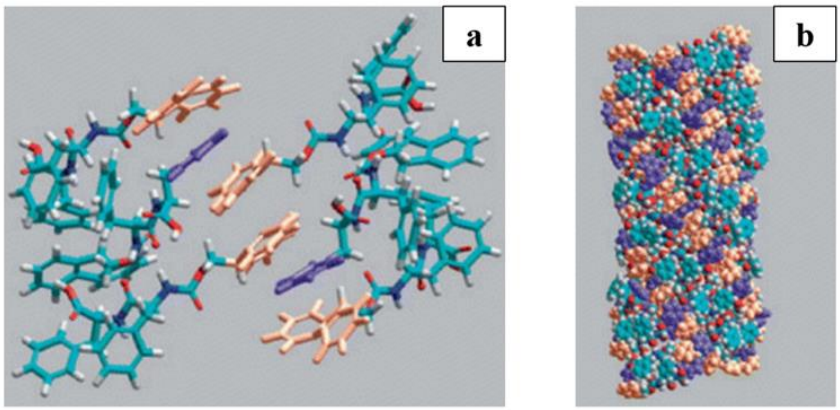


Figure 5.17 Previous peptide fibre models developed by Smith *et al.* [22]. Duplicate of Figure 3.15 for data interpretation in this section. (a) A self-assembling pair of molecules. Presented as the "sawtooth" structure. (b) A fibre consisting of self-assembling molecules.

The first question is how pH affects the twisting of FP fibres. Based on Figure 17(b), the FP models shown in Figure 5.18 are constructed. There are electrostatic interactions between these hydrophilic side groups belonging to the neighbouring molecules. At the isoelectric point of FP, adjacent hydrophilic chains in neighbouring molecules can have the most repulsive interactions, allowing the distance between adjacent molecules to reach its maximum. As the pH changes away from the isoelectric point dissociative ions in the system, tend to be attracted by charged side groups. This, however, reduces original repulsive interactions between hydrophilic side groups of neighbouring chains, and as a result, the distance between adjacent molecules is decreased. As introduced in Sections 3.1.4 and 3.3.3.1, FP is thought to form the twisting fibres mainly due to the steric effect of proline [17]. Since chains are further apart at FP's isoelectric point, the steric effect of proline can be impaired. And therefore, it is more difficult to form the twisting structure at pH 7. By contrast, compact twisting FP fibres with higher levels of twisting are formed at pH 5 and pH 9.

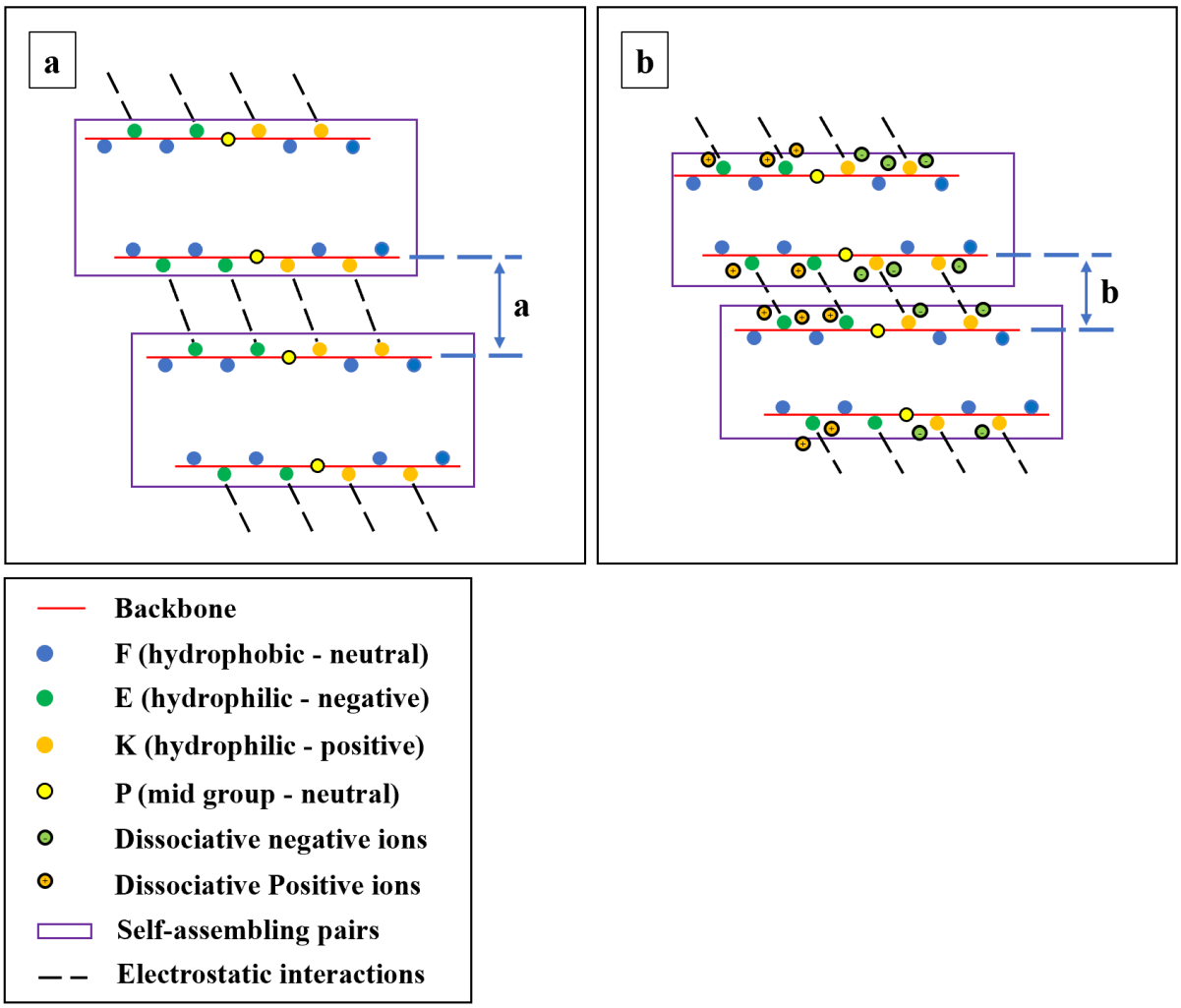


Figure 5.18 FP models constructed following the model shown in Figure 5.18(b). (a) FP at its isoelectric point, no ions in the system. The spacing "a" represents the distance of adjacent molecules along the fibre length direction. (b) FP not at its isoelectric point, ions are involved in the system. The spacing "b" represents the distance of adjacent molecules along the fibre length direction. Spacings comparison, a > b.

5.3.4 How Different Factors Influence PA Morphologies

5.3.4.1 Peptide Sequence

This section begins to discuss in theory how parameters such as peptide sequence, peptide concentration, and pH influence peptide morphology. The peptide sequence is the first factor to be discussed. Table 5.12 summarises fibre information obtained from TEM images of three peptides. To avoid the pH effect, discussion will only focus on peptides at their own isoelectric points here. Table 5.12 shows that, in most cases, at the same peptide concentration, F9 has wider and denser fibres than F8 and FP.

Table 5.12 Summary of fibre information of three peptides acquired from TEM images. All pH values are at their isoelectric points, with different concentrations.

	Peptide concentration at its isoelectric point	Fibre width (nm)	Number of fibres per 200×200 $(nm)^2$
F8	0.5	20 - 38	3 - 5
	2	28 - 45	4 - 10
	5	25 - 46	5 - 12
	20	27 - 39	14 - 31
F9	0.5	28 - 37	5 - 11
	2	22 - 35	11 - 19
	5	25 - 41	13 - 18
	20	27 - 38	16 - 25
FP	0.5	22 - 29	7 - 11
	2	20 - 27	8 - 13
	5	16 - 26	11 - 16
	20	21 - 26	15 - 21

Figure 5.19 illustrates the reason for this. The key factor here is still electrostatic interactions. The difference of the F9 molecules is that F9 has one more charged side groups than F8 and FP. This difference, as shown in Figure 5.19(c), can contribute to a stronger repulsive

interaction between adjacent molecules along the chain axis, namely along the fibre width direction. The molecules are then more separated in the direction of the fibre width, as a result, the width of the fibre can be increased. In contrast, the density of fibres can be determined by inter-fibre electrostatic interactions rather than intra-fibre electrostatic interactions. Charged end groups in the fibre, as indicated by the red squares in Figure 5.19, can attract negatively charged end groups of other fibres, and therefore, increase the fibre density locally. End groups belonging to F9 have a higher number of charges, so a single F9 fibre can attract more neighbouring fibres, resulting in a denser fibre system than F8 and FP.

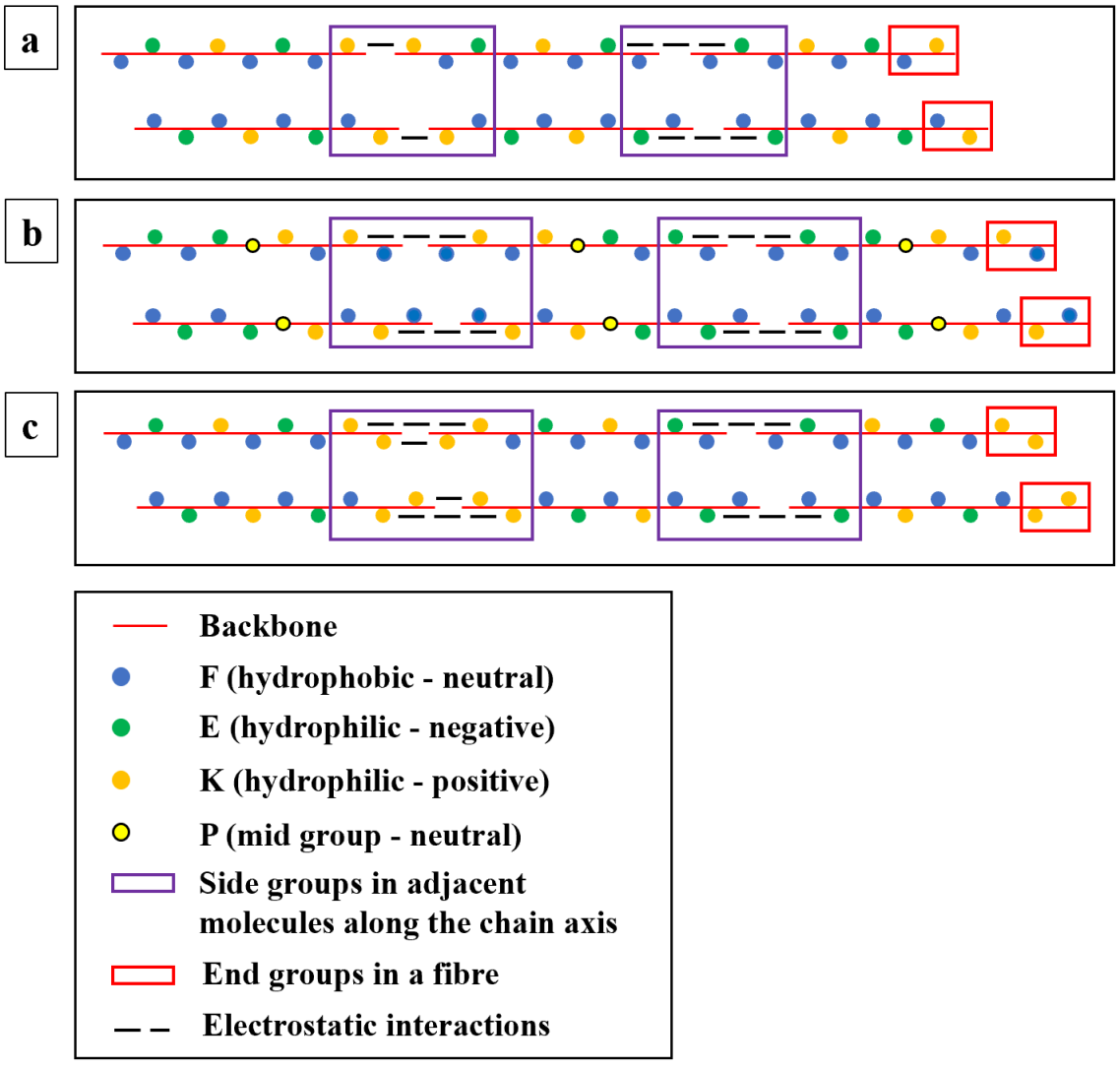


Figure 5.19 Peptide models (a) F8. (b) F9. (c) FP.

5.3.4.2 Peptide Concentration

In terms of peptide concentration and pH, F8, F9, and FP were found to follow the same trend, so F8 models will be used to explain all three PAs.

The mechanism of peptide concentration altering morphology may be simple. As discussed in the previous section, intra-fibre electrostatic interactions control fibre width. Because an increase in peptide concentration has no effect on these kinds of interactions, the peptide width does not change significantly. In terms of density, increasing peptide concentration means increasing the density of peptides in a specific area. As a result, fibre density naturally increases.

5.3.4.3 pH

The final parameter to be discussed is pH. Firstly, the pH ranges for three different types of peptides spun on TEM grids in order to form fibres was investigated. The range for F8 is 3 to 11, and the lowest and highest bounds for F9 are pH 4 and pH 12. It is debatable whether FP molecules begin to form fibres at pH 3 or pH 4. However, at pH 12, FP fibres begin to collapse.

Previous results [3][4] also show that, within the pH ranges that peptides can form fibres, all three types of peptides form the widest but loosest fibres at their isoelectric points. Figure 5.20 is used to explain this phenomenon. Using F8 as an example, as shown in Figure 5.20(a), repulsive forces between adjacent molecules along the chain axis (the fibre width direction) reach their maximum at its isoelectric point. Changes in pH, as discussed in section 5.3.3, can also be interpreted as an increase in ionic concentration in the system. When extra ions are

present, repulsive interactions between neighbouring chains along the fibre width direction tend to be reduced, and the distance between adjacent molecules along the chain axis can be reduced as well. As a result, the isoelectric point produces the widest fibres. On the contrary, as for the density, dissociative ions near the end charged groups are also capable of attracting other molecules, causing several fibres to congregate locally. Consequently, fibres have a higher density than at the isoelectric point. This could also be why, when the pH rises above 11, FP twisting fibres tend to stack together to form a larger peptide bundle.

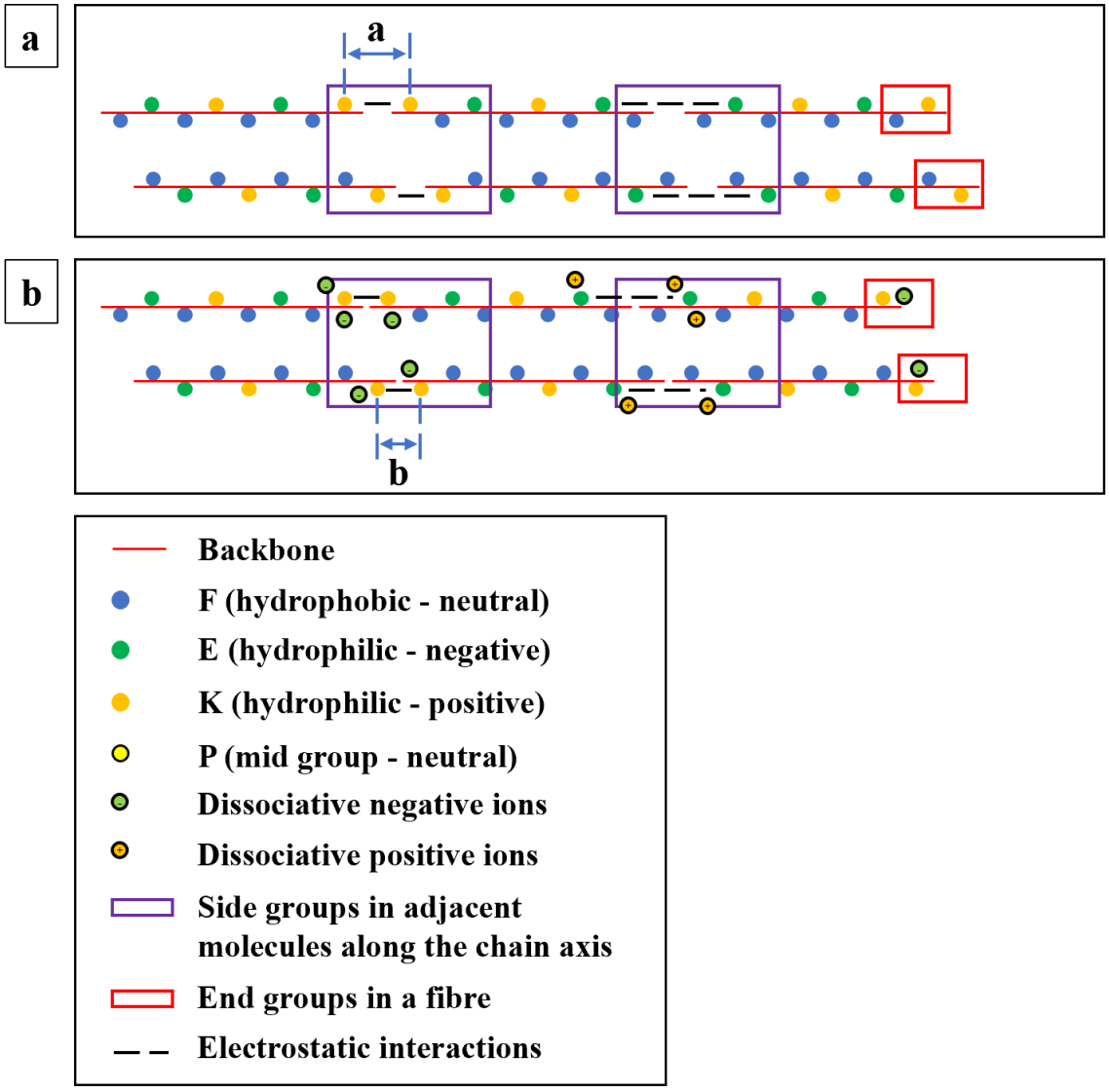


Figure 5.20 F8 models. (a) F8 at its isoelectric point, no ions in the system. The spacing "a" represents the distance of adjacent molecules along the chain axis (the fibre width

direction). (b) F8 not at its isoelectric point, ions are involved in the system. The spacing "b" represents the distance of adjacent molecules along the chain axis (the fibre width direction). Spacings comparison, a > b.

5.3.5 Relationship Between Peptide Morphology and Peptide Crystallisation

Figure 5.16 shows that the findings presented here do not support a strong correlation between peptide fibres and peptide crystals. However, because the principles of electromagnetic interactions still hold, even without the regular ordering required for crystals, the changes in fibre morphologies are still explainable. It is possible that fibres still contain oriented molecules, but the order is insufficient to lock into crystals. In other words, fibres can be driven by free energy rather than crystallisation *per se*. At this point, because the primary goal in the project is to use electron ptychography to study PA-sheet crystallisation, future work will not be related specifically to peptide fibres. In the following chapter, another sample processing method, freeze-thawing, will be introduced to prepare more crystallised PA samples.

Based on the findings in this chapter, the concentration of PA samples used in Chapters 6 and 7 will be 20 mg/mL, which was the highest concentration used for the morphological study in this chapter. Although there is no correlation between peptide concentration and fibre width, which may be related to ordered structures, a higher concentration can contribute to a denser fibre network, potentially resulting in more crystallites in a local area. This is useful for identifying crystal regions for future electron microscopy work. In terms of pH, all PA samples for Chapters 6 and 7 will be prepared at their isoelectric points. There are two reasons for the selection of pH values. Firstly, at the isoelectric point, fibres are the widest and can contain the most oriented molecules, which might be helpful for the electron microscopic study on PA

crystals. Also, PA samples at the isoelectric point can be simply prepared by dissolving materials in pure water, removing the effect of salts on PA crystals. This ensures that the crystals being studied are in their natural states.

5.4 Conclusions

In this chapter, peptide fibres are studied using TEM and AFM. To begin, it was confirmed that dip-casting is superior to traditional peptide sample preparation methods such as spin-coating and drop-casting. Following on from previous research, how pH and peptide concentration affect peptide morphology was explored. This chapter investigates two factors that are critical to the mechanical properties of peptide products: peptide fibre width and fibre density. Critical pH values for each peptide are then investigated prior to specific exploration. Finally, the pH ranges of fibre formation for each peptide were confirmed using TEM and AFM: pH 3 to 11 for F8, pH 4 to 12 for F9, and pH 4 to 11 for FP.

Peptide fibres are then imaged using TEM and AFM. AFM measures a greater peptide width than TEM, which can be attributed to the errors resulting from AFM probes and fibres' sensitivity to different substrates. From the TEM and AFM images, it can be found that F8 and F9 can form relatively straight fibres, whereas FP forms twisting fibres. At their own isoelectric points with the same peptide concentration, F9 possesses the widest and densest fibres. This is because F9 has the most powerful intra-fibre repulsive forces to increase the width of the fibre and the strongest inter-fibre attractive forces to attract more fibres locally.

Then, using three different materials, how pH and peptide concentration affect fibre morphology was studied. All three materials reach nearly identical conclusions. At a constant pH, as peptide concentration increases, peptide fibres become denser, but there is no discernible change in peptide width. Peptide concentration is increased to increase the density of peptides in a specific area. As a result, fibre density naturally increases. The intra-fibre electrostatic interactions are thought to control fibre width, according to the peptide fibre models introduced

in Section 5.3.4.1. Because an increase in peptide concentration has no effect on electrostatic interactions, peptide width does not change dramatically.

Another factor affecting the peptide morphology is pH. Peptide fibres are the widest but loosest at their relevant isoelectric points for all F8, F9, and FP. Furthermore, when the pH exceeds 11, the twisting fibres in FP stack together. These trends are due to the effect of intra and inter-fibre electrostatic interactions. Repulsive forces between adjacent molecules along the fibre width direction are at their peak at the isoelectric point. Changes in pH, on the other hand, increase the external ionic strength of fibres, which reduces repulsive interactions along the fibre width direction, allowing the fibre width to be reduced. The charges around end groups on the surface of fibres can be linked to fibre density. Dissociative ions can be attracted to fibres that are not at the isoelectric point, resulting in a local high-density fibre. Furthermore, at their isoelectric point, FP fibres have the lowest level of twisting. This is because enhanced repulsive forces increase the intermolecular distance of FP chains at the isoelectric point, and this makes fibre twisting more difficult.

Finally, HRTEM is used to investigate the connection between peptide fibres and peptide crystals. Surprisingly, no direct link between them was found. At this point, it can be attributed that while molecules remain ordered (e.g., aligned) in fibres, the driving force behind fibre formation could be free energy rather than crystallisation *per se*. More importantly, this finding demonstrates that a new method is required to generate more crystalline samples for the upcoming electron microscopic crystallographic study.

In summary, this chapter investigates F8, F9, and FP fibre morphology, but it does not significantly advance future electron ptychographic work. Crystallographic analysis especially increasing the crystallinity of samples must be completed later.

5.5 References

[1] Dehsorkhi, A., Castelletto, V., & Hamley, I. W. (2014). Self-assembling amphiphilic peptides. *Journal of Peptide Science*, 20(7), 453-467.

[2] Boothroyd, S. (2012). *Peptide Self-assembly: Controlling Conformation and Mechanical Properties*. The University of Manchester (United Kingdom).

[3] Wang, Z. (2018). *Self-assembly of Peptides on Surfaces* (Master dissertation, University of Oxford).

[4] Botwright, S. (2017). *Self-assembly of Peptides on Surfaces* (Master dissertation, University of Oxford).

[5] Bowerman, C. J., & Nilsson, B. L. (2012). Review self-assembly of amphipathic β-sheet peptides: insights and applications. *Peptide Science*, *98*(3), 169-184.

[6] Rodriguez, L. M. D. L., Hemar, Y., Cornish, J., & Brimble, M. A. (2016). Structure–mechanical property correlations of hydrogel forming β-sheet peptides. *Chemical society reviews*, *45*(17), 4797-4824.

[7] Boothroyd, S., Saiani, A., & Miller, A. F. (2014). Controlling network topology and mechanical properties of co-assembling peptide hydrogels. *Biopolymers*, *101*(6), 669-680.

[8] Hamley, I. W. (2007). Peptide fibrillization. *Angewandte Chemie International Edition*, *46*(43), 8128-8147.

[9] Bonduelle C. Secondary structures of synthetic polypeptide polymers. *Polymer Chemistry*. 2018;9(13):1517-29.

[10] Hong, Y., Pritzker, M. D., Legge, R. L., & Chen, P. (2005). Effect of NaCl and peptide concentration on the self-assembly of an ionic-complementary peptide EAK16-II. *Colloids and Surfaces B: Biointerfaces*, *46*(3), 152-161.

[11] Aggeli, A., Nyrkova, I. A., Bell, M., Harding, R., Carrick, L., McLeish, T. C., Semenov, & A. N., Boden, N. (2001). Hierarchical self-assembly of chiral rod-like molecules as a model for peptide β-sheet tapes, ribbons, fibrils, and fibres. *Proceedings of the National Academy of Sciences*, *98*(21), 11857-11862.

[12] Cui, H., Muraoka, T., Cheetham, A. G., & Stupp, S. I. (2009). Self-assembly of giant peptide nanobelts. *Nano letters*, *9*(3), 945-951.

[13] Hong, Y., Lau, L. S., Legge, R. L., & Chen, P. (2004). Critical self-assembly concentration of an ionic-complementary peptide EAK16-I. *The Journal of Adhesion*, *80*(10-11), 913-931.

[14] Fung, S. Y., Keyes, C., Duhamel, J., & Chen, P. (2003). Concentration effect on the aggregation of a self-assembling oligopeptide. *Biophysical journal*, *85*(1), 537-548.

[15] MacArthur, M. W., & Thornton, J. M. (1991). Influence of proline residues on protein conformation. *Journal of molecular biology*, *218*(2), 397-412.

[16] Doerfel, L. K., Wohlgemuth, I., Kubyshkin, V., Starosta, A. L., Wilson, D. N., Budisa, N., & Rodnina, M. V. (2015). Entropic contribution of elongation factor P to proline positioning at the catalytic center of the ribosome. *Journal of the American Chemical Society*, *137*(40), 12997-13006.

[17] Ceruso, M. A., & Weinstein, H. (2002). Structural mimicry of proline kinks: tertiary packing interactions support local structural distortions. *Journal of molecular biology*, *318*(5), 1237-1249.

[18] Sawyer, L., Grubb, D. T., & Meyers, G. F. (2008). *Polymer microscopy*. Springer Science & Business Media.

[19] Tang, C. Y., & Yang, Z. (2017). Transmission electron microscopy (TEM) In *Membrane characterization* (pp. 145-159). Elsevier.

[20] Lorusso, M., Pepe, A., Ibris, N., & Bochicchio, B. (2011). Molecular and supramolecular studies on polyglycine and poly-L-proline. *Soft Matter*, *7*(13), 6327-6336.

[21] Sherratt, M. J., Bax, D. V., Chaudhry, S. S., Hodson, N., Lu, J. R., Saravanapavan, P., & Kielty, C. M. (2005). Substrate chemistry influences the morphology and biological function of adsorbed extracellular matrix assemblies. *Biomaterials, 26*(34), 7192-7206.

[22] Smith, A. M., Williams, R. J., Tang, C., Coppo, P., Collins, R. F., Turner, M. L., Saiani, A., & Ulijn, R. V. (2008). Fmoc-diphenylalanine self assembles to a hydrogel via a novel architecture based on π–π interlocked β-sheets. *Advanced Materials*, *20*(1), 37-41.

Chapter 6. Basic Structural and Crystallographic Study on Polyvinyl Alcohol and Peptide Amphiphiles

6.1 Introduction

After discovering that peptide crystals have no direct relationship to peptide fibres in Section 5.2.6, a method was required for crystallising peptide samples. Besides, the crystallinity of PVA, another material in this thesis, may also need to be increased for later electron ptychographic study. Overall, this chapter investigates the effects of crystallising methods and studies the basic crystallinity information of the two types of materials in this thesis, PVA and PAs. Annealing was used to increase the crystallinity of PVA, and HRTEM images of annealed samples show some key d-spacings of PVA. In the case of PAs, freeze-thawing was used to increase the crystallinity. The β-sheet d-spacings of F8, F9 and FP (d_1 introduced in Chapter 3) were observed in XRD and HRTEM data. HRTEM was also used in this project to detect the potentially α-helix peptides, F2A2 and FAFA. As a result, HRTEM obtained a d-spacing equal to the typical α-helix repeat distance introduced in Section 3.2.1. This indicates that helical pitch can have a correlation to the α-helix crystal unit cell. Furthermore, the β-sheet d-spacing were also acquired from the HRTEM images. This reveals the potential coexistence of α-helix and β-sheet structures in F2A2 and FAFA.

6.2 Results and Discussion

6.2.1 Fourier-transform Infrared Spectroscopy

6.2.1.1 β-sheet Peptide Amphiphiles

Before studying the crystallinity of PVA and peptides, the confirmation of some key features is required, for instance, hydrogen bonding of PVA and β-sheet secondary structures of peptides, because they have significant influence on the crystallisation [1]-[5]. FTIR is therefore used for the preliminary study of PVA and PAs in this sector.

The FTIR spectra of three PAs are shown in Figure 6.1. The results of F8 and F9 are consistent with previous studies [6]-[9], and there are also two peaks with similar positions at around 1625 and 1695 cm $^{-1}$ for FP. According to Zou *et al.* [10], these two peaks confirm the existence of anti-parallel β-sheet structures and indicate a possible coexistence of parallel and anti-parallel β-sheet structures [10]. The findings here can be served as the foundation for all subsequent microscopic studies of all three PAs.

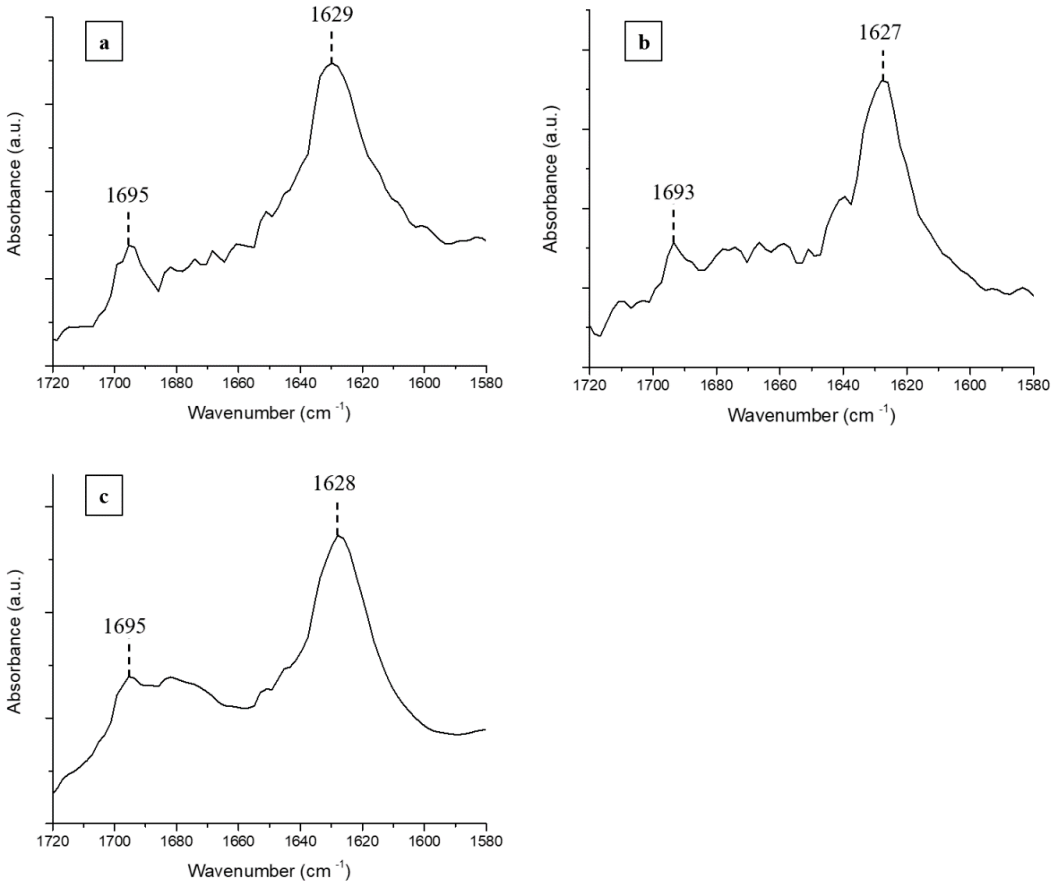
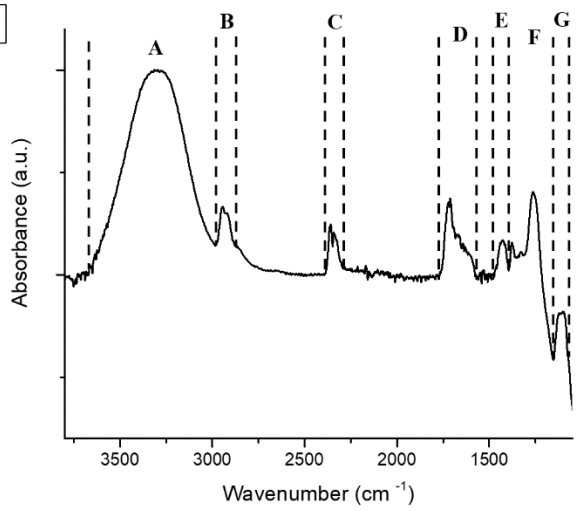


Figure 6.1 FTIR spectrum of peptides. (a) F8. (b) F9. (c) FP.

6.2.1.2 Polyvinyl Alcohol

Figure 6.2(a) depicts the FTIR spectrum of PVA. The previous study by Mansur *et al.* [11] were used as the reference to interpret the data, and the interpretated results are shown Figure 6.2(b). FTIR results of the PVA sample in this project accord with Mansur *et al.*'s study [11], where there are seven zones in the spectrum. Herein, the broad and high peak in Zone A in Figure 6.2(a) from around 3800 to 3000 cm $^{-1}$ confirms the intermolecular and intramolecular hydrogen bonds in PVA. These hydrogen bonds could have varying orientations [1][2], potentially increasing the complexity of PVA crystals. In Chapter 8, the orientations of hydrogen bonding will be thoroughly discussed.

a



b

Zone	Suggested Structures
A	Stretched O–H from the intermolecular and intramolecular hydrogen bonds
B	C–H from alkyl groups
C	Stretched O=C=O from carbon dioxide in the background
D	Stretched C=O from unhydrolysed carboxylic acid and aliphatic ketone
E	Bent C–H from methyl groups
F	Bent O–H from hydroxyl groups
G	Stretched C–O from secondary alcohol

Figure 6.2 FTIR analysis of PVA. (a) FTIR spectrum of PVA. (b) Interpretation of (a) based on the information from the previous study by Mansur *et al.*

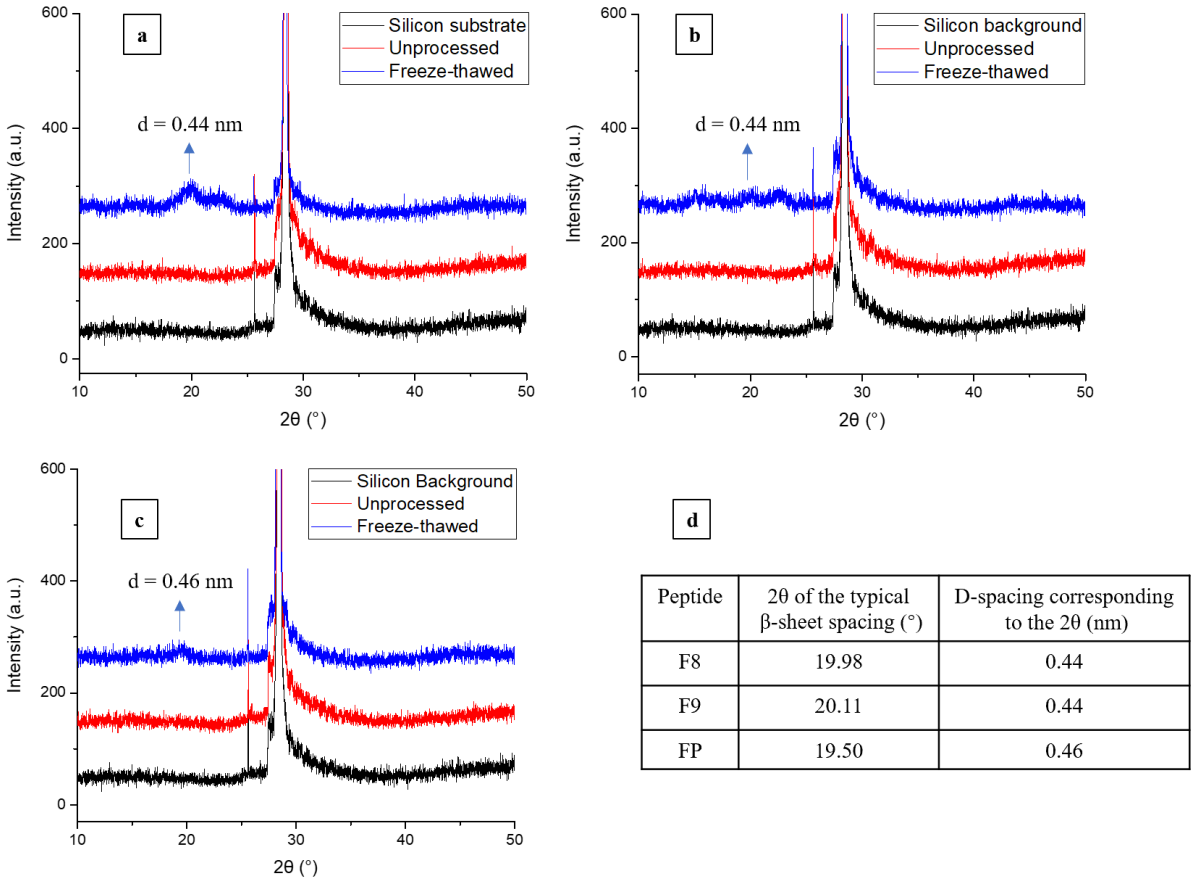
6.2.2 X-ray Thin-film Diffraction

6.2.2.1 β-sheet Peptide Amphiphiles

After confirming the key structures of PVA and PAs using FTIR, X-ray diffraction (XRD) was utilised to study the basic crystal information of PVA and PAs.

A thin-film PA sample with a good degree of crystallinity is necessary for electron microscopic study. Inspired by previous findings on gluten protein [12] and polyvinyl alcohol [13], freeze-thawing was used to achieve a higher degree of crystallinity. The effect of freeze-thawing was investigated using XRD.

As shown in Figure 6.3, XRD traces (middle lines in red) confirmed solution-cast thin-films of three PAs show little or no crystallinity. In contrast, the freeze-thawed PA samples (shown by the top lines in blue) begin to show some crystallinity, as indicated by small peaks near 20ᵒ 2θ. These peaks suggest that PA crystals have the d-spacing with the range of 0.44 to 0.46 nm, indicating their β-sheet structures [14]-[16]. Based on the XRD results, freeze-thawing was confirmed to be an appropriate sample preparation method of PAs in the following microscopy work.



Peptide	2θ of the typical β-sheet spacing (°)	D-spacing corresponding to the 2θ (nm)
F8	19.98	0.44
F9	20.11	0.44
FP	19.50	0.46

Figure 6.3 XRD patterns of peptide thin-film samples showing in each case the trace from: the Si substrate material (lower), as-cast peptide on Si (middle), and freeze-thawed peptide on Si (upper trace). (a) F8. (b) F9. (c) FP. (d) Summary of the crystal peak of the

three peptides. The large peaks at around 29 degrees 2θ are due to signal from the underlying Si substrate, as can be seen from the Si background traces.

6.2.2.2 Polyvinyl Alcohol

Similar to the PAs, a thin-film PVA sample with a good degree of crystallinity is also necessary for the electron microscopy study, and the work in this area started with a study on increasing the crystallinity of solution-cast PVA. Inspired by results of PAs in the previous section and previous findings [17] on PVA, freeze-thawing and annealing were conducted as methods to achieve a greater degree of crystallinity. XRD was utilised to test the effects of these two methods. As shown in Figure 6.4, in the XRD trace (lowest line) confirmed unprocessed solution cast thin-film of PVA shows little or no crystallinity. In contrast, the freeze-thawed PVA sample starts to show greater crystallinity as indicated by the small peak close to 20̊ 2θ. Furthermore, the annealed samples have the highest crystallinity among these three methods, and a higher annealing temperature contributes to a higher degree of crystallinity, ultimately showing multiple, sharp peaks in the XRD trace arising from the polymer crystals. XRD results here bring the general crystal information of the PVA crystal, and the results accord with the previous studies [17]. The XRD data can be used as a reference for future local studies on the PVA crystal using electron microscopy. Also, based on the XRD results, annealing at 250 ℃ was chosen as the sample preparation method of PVA in the following microscopy work.

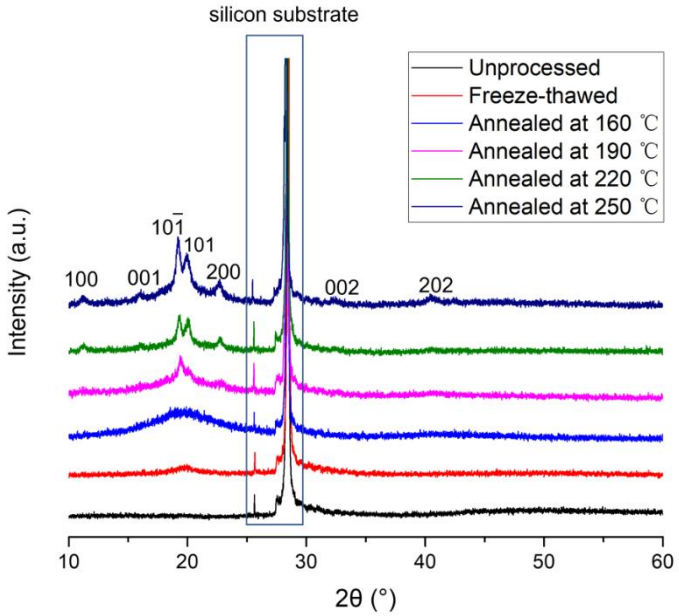


Figure 6.4 XRD patterns of PVA thin-film samples including unprocessed one, freeze-thawed one and a series of samples after annealing at temperatures between 160 °C and 250 °C for 20min.

6.2.3 High-resolution Transmission Electron Microscopy

6.2.3.1 Polyvinyl Alcohol

Following the results shown in the last section, high-resolution transmission electron microscopy (HRTEM) was used in this chapter to study the local crystal information of the materials. Firstly, annealed PVA samples were imaged by HRTEM.

According to Figures 6.5 and 6.6, following using annealing it was possible to image single-crystal regions of samples, and clear fringes can be observed in the HRTEM images. Calculating the d-spacings via line profiles from measuring 10 different spacings as introduced in Section 4.5.2, a 0.40 ± 0.01 nm d-spacing was measured from the HRTEM image shown in

Figure 6.5(a), and the FFT of the image in Figure 6.5(b) also shows some other d-spacings at 0.45 (± 0.02) nm, 0.26 (± 0.01) nm and so on. Based on previous studies [17], d-spacings at 0.40, 0.45 and 0.26 nm accord with the d-spacings of the (200), (101), and (002) planes of PVA. This crystallite will be used for the electron ptychographic imaging, and detailed analysis of above d-spacings can be found in Sections 8.2.2 and 8.3.1.

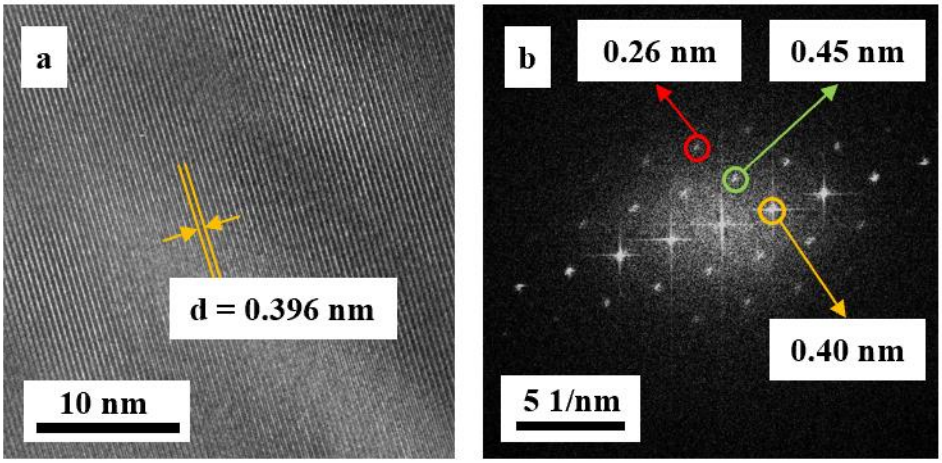


Figure 6.5 Electron microscopic images of a single-crystal PVA thin-film sample. (a) HRTEM. (b) FFT of (a).

Another PVA crystal was also imaged by HRTEM, and its image is shown in Figure 6.6(a). A d-spacing at 0.55 ± 0.01 nm was found. From its FFT image shown in Figure 6.6(b), other d-spacings including 0.23 ± 0.01 nm can be also observed. These two d-spacings are in accord with the d-spacings of the (001) and (110) planes of PVA [17]. More details of the-spacings will be discussed in Sections 8.2.2 and 8.3.1.

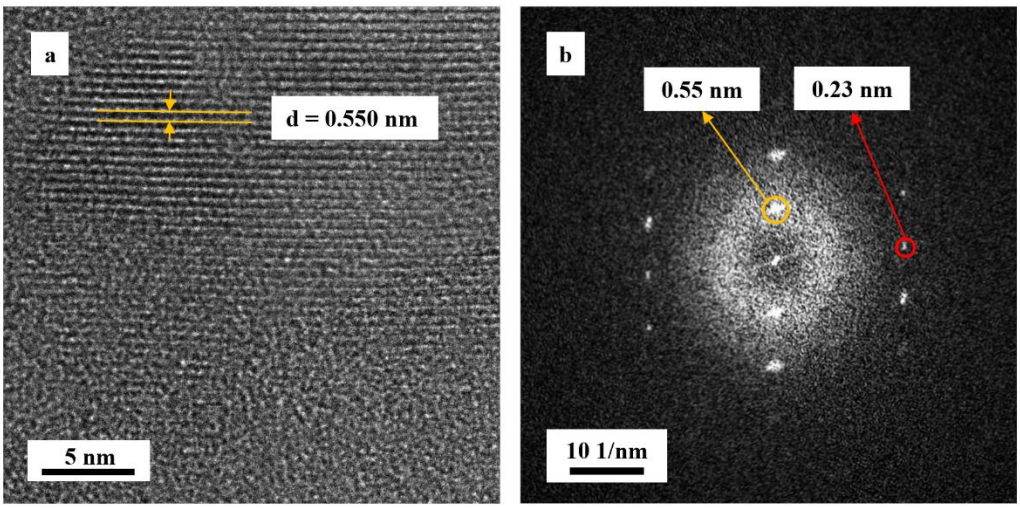


Figure 6.6 Electron microscopic images another single-crystal PVA thin-film sample. (a) HRTEM. (b) FFT of (a). (c) Line profile of the d-spacing marked in (a).

Electron ptychography was used on the two single-PVA crystallites mentioned above to obtain more detailed information about the PVA crystal, and their ptychographic images and crystallographic analysis will be presented and discussed in Chapter 8.

6.2.3.2 β-sheet Peptide Amphiphiles

PA freeze-thawed samples were then imaged using HRTEM. Figures 6.7(a), (b) and (c) show the HRTEM images of F8, F9 and FP, respectively. Single-crystal regions of the samples were imaged as a result of the freeze-thawing process, and clear fringes indicating the crystal structures of PAs can be seen in the HRTEM images. Three d-spacings at 0.46 ± 0.02 nm, 0.47 ± 0.03 and 0.45 ± 0.01 nm were obtained from HRTEM images for F8, F9 and FP, respectively. These d-spacings match the d_1 introduced in Section 3.2.2 and are consistent with the previous XRD data shown in Section 6.2.2.1. HRTEM results suggest the three PAs in this work possess β-sheet structures [14]-[16], which is the first time the β-sheet structure has been detected by HRTEM.

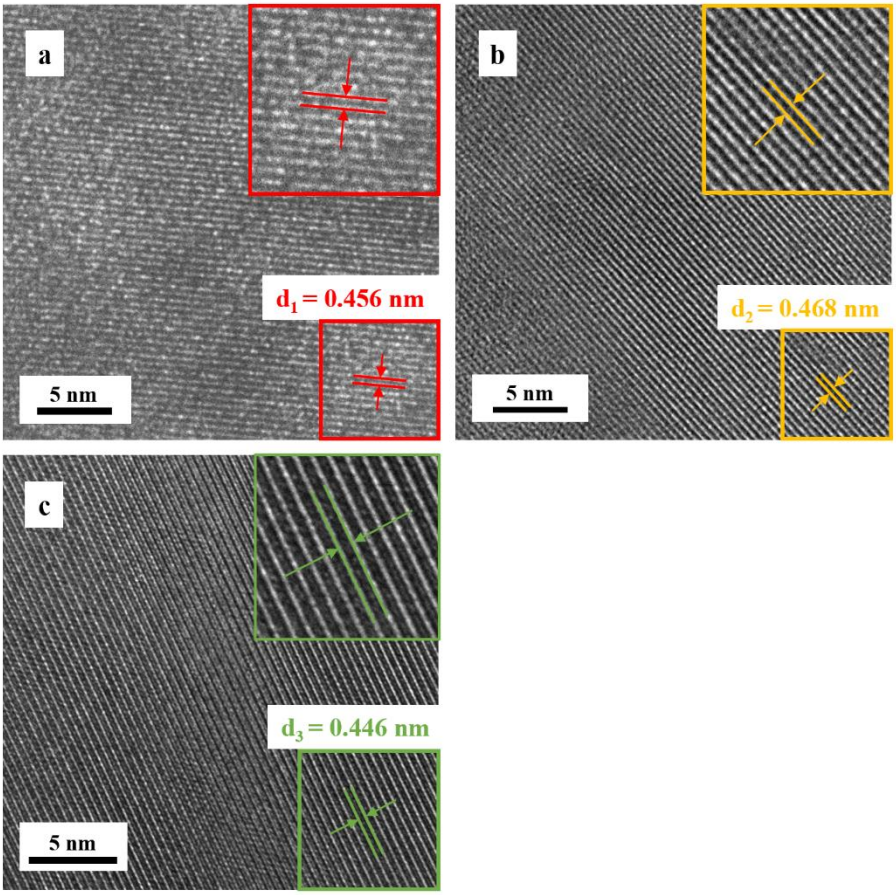


Figure 6.7 HRTEM images of freeze-thawed single-crystal peptide thin-film samples. Peptide concentration is 20 mg/mL, and pH are at their corresponding isoelectric points for each sample. (a) F8. (b) F9. (c) FP.

As with the PVA in the last section, these three PA single-crystal samples were used in the electron ptychographic study for a deeper understanding of their fine β-sheet structures, and their ptychographic images and analysis on their crystallography will be presented and discussed in Chapter 7.

6.2.3.3 Potential α-helix Peptide Amphiphiles

As introduced in the Section 3.1.2 and 3.2.2, Botwright [9] found that F2A2 and FAFA have α-helix secondary structures, but meanwhile, β-sheet structures may also coexist [9]. As demonstrated in the previous section, HRTEM can be an effective characterisation method for PA crystals. In this section, besides PVA and β-sheet PAs, the crystallinity of F2A2 and FAFA is investigated by HRTEM.

Figures 6.8 and 6.9 show HRTEM images of F2A2 and FAFA, respectively. As introduced in Section 3.2.1, the pitch of the alpha-helix (the vertical distance between consecutive turns of the helix) is around 0.54 nm [18]. Here, 0.54 nm is acquired in the form of d-spacings of F2A2 and FAFA from Figures 6.8 and 6.9. The d-spacing acquired from the HRTEM images indicates that helical pitch may have a correlation to the α-helix crystal unit cell of FAFA and F2A2. However, because no study has yet reported α-helix PA's crystallography, this point needs to be further confirmed by future research.

In addition, d-spacings at 0.46 ± 0.02 nm and 0.46 ± 0.01 were also acquired for F2A2 and FAFA in the same samples from which the 0.54-nm d-spacing was acquired. These d-spacings are consistent with β-sheet d-spacings, and these findings here can potentially support Botwright's previous studies [9] that α-helix and β-sheet structures can coexist in F2A2 and FAFA. However, the lack of basic understanding of α-helix crystallography makes it hard for the electron ptychographic study. Therefore, these two PAs were not studied using electron ptychography in this thesis. As the knowledge of α-helix crystallography advances in the future, studying their fine structures using electron ptychography will form part of the future work for this thesis.

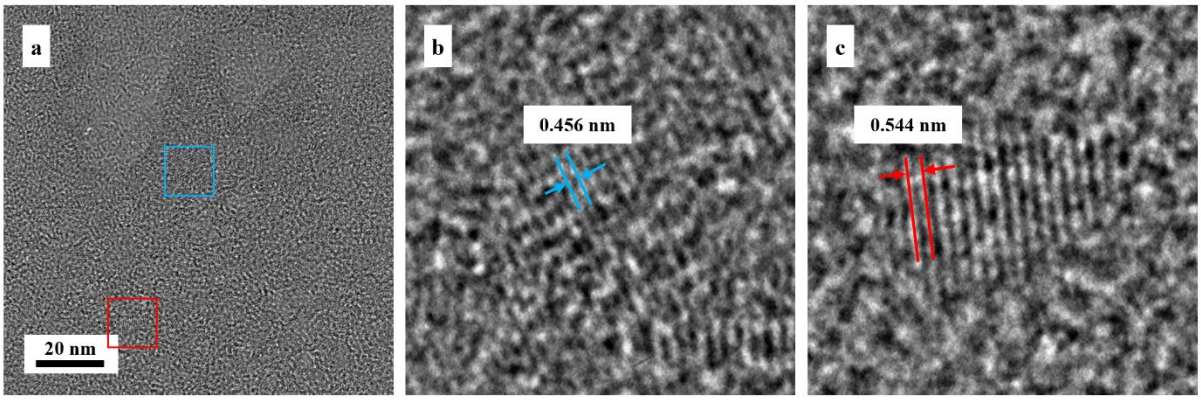


Figure 6.8 Electron microscopic images of a F2A2 thin-film sample, pH=7, 20 mg/mL. (a) HRTEM. (b) Magnified image of the area in the red square in (a). (c) Magnified image of the area in the blue square in (a).

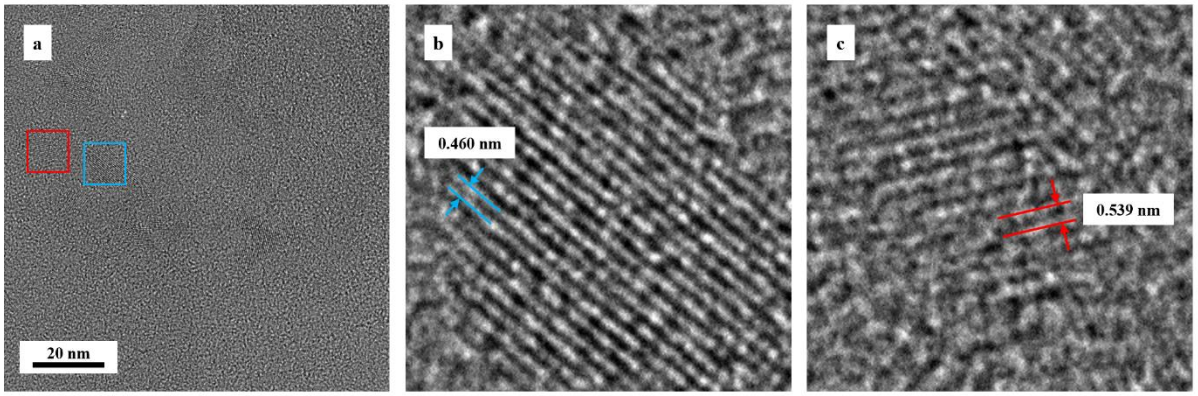


Figure 6.9 Electron microscopic images of a FAFA thin-film sample, pH=7, 20 mg/mL. (a) HRTEM. (b) Magnified image of the area in the red square in (a). (c) Magnified image of the area in the blue square in (a).

6.3 Unassigned d-spacings of the Above Materials

Aside from aforementioned d-spacings, there are some more d-spacings of F8, F9 and FP acquired by using HRTEM. These d-spacings cannot be properly assigned at the moment because the PA β-sheet crystallography has not been thoroughly established. When the study of PA β-sheet crystals progress, the d-spacing presented in this section may be useful for further exploring PA β-sheet structure. From Figure 6.10 to Figure 6.15, there are six more sets of images of F8, F9 and FP, and they will be discussed in this section later.

Figures 6.10 and 6.11 show two more sets of F8 HRTEM images. A d-spacing at 0.46 (± 0.01) nm is found in these two figures, which further supports the existence of β-sheet structure in F8. Besides, d-spacings at 0.28 (± 0.02) nm and 0.32 (± 0.01) nm are also found in Figure 6.10 and 11, respectively.

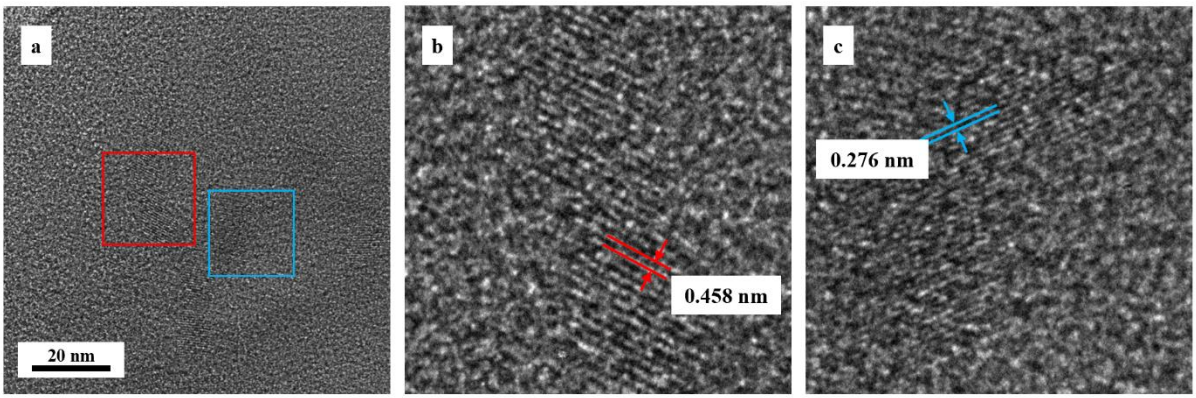


Figure 6.10 Electron microscopic images of a F8 thin-film sample, pH=7, 20 mg/mL. (a) HRTEM. (b) Magnified image of the area in the red square in (a). (c) Magnified image of the area in the blue square in (a).

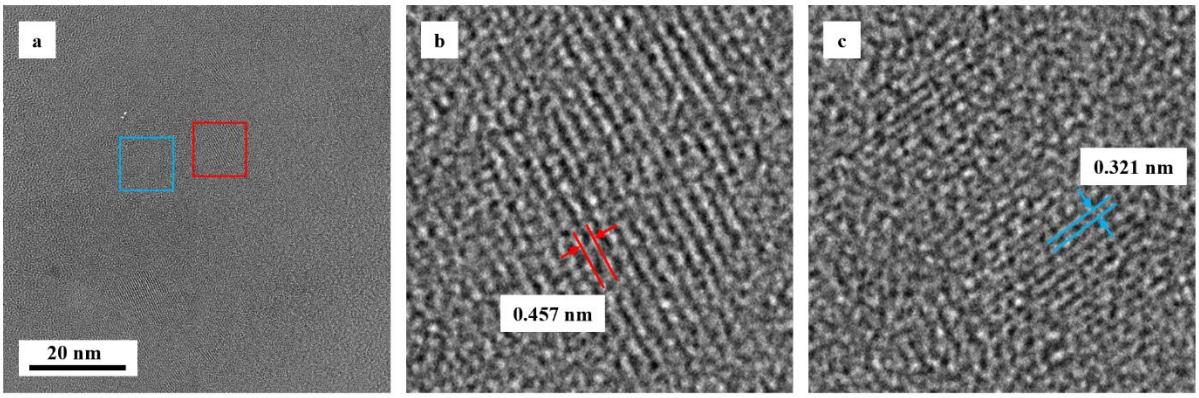


Figure 6.11 Electron microscopic images of a F8 thin-film sample, pH=7, 20 mg/mL. (a) HRTEM. (b) Magnified image of the area in the red square in (a). (c) Magnified image of the area in the blue square in (a).

Moving on to F9, there are 6 more unassigned d-spacings obtained from the three sets of F9 HRTEM images shown in Figures 6.12 to 6.14. In Figures 6.12 and 6.13, 0.58 (± 0.02) nm, 0.50 (± 0.02) nm and 0.28 (± 0.01) are observed. d-spacings at 0.44 (± 0.02) and 0.46 nm (± 0.02) are found in Figures 6.13 and 6.14. Although these d-spacings differ slightly from those obtained in Figure 6.7(b), they are still in the 0.44 to 0.47 nm range and thus can be regarded as d_1-equivalent β-sheet d-spacings. In addition, d-spacings at 0.41 (± 0.02), 0.37 (± 0.02) and 0.35 (± 0.01) can be found in above two figures.

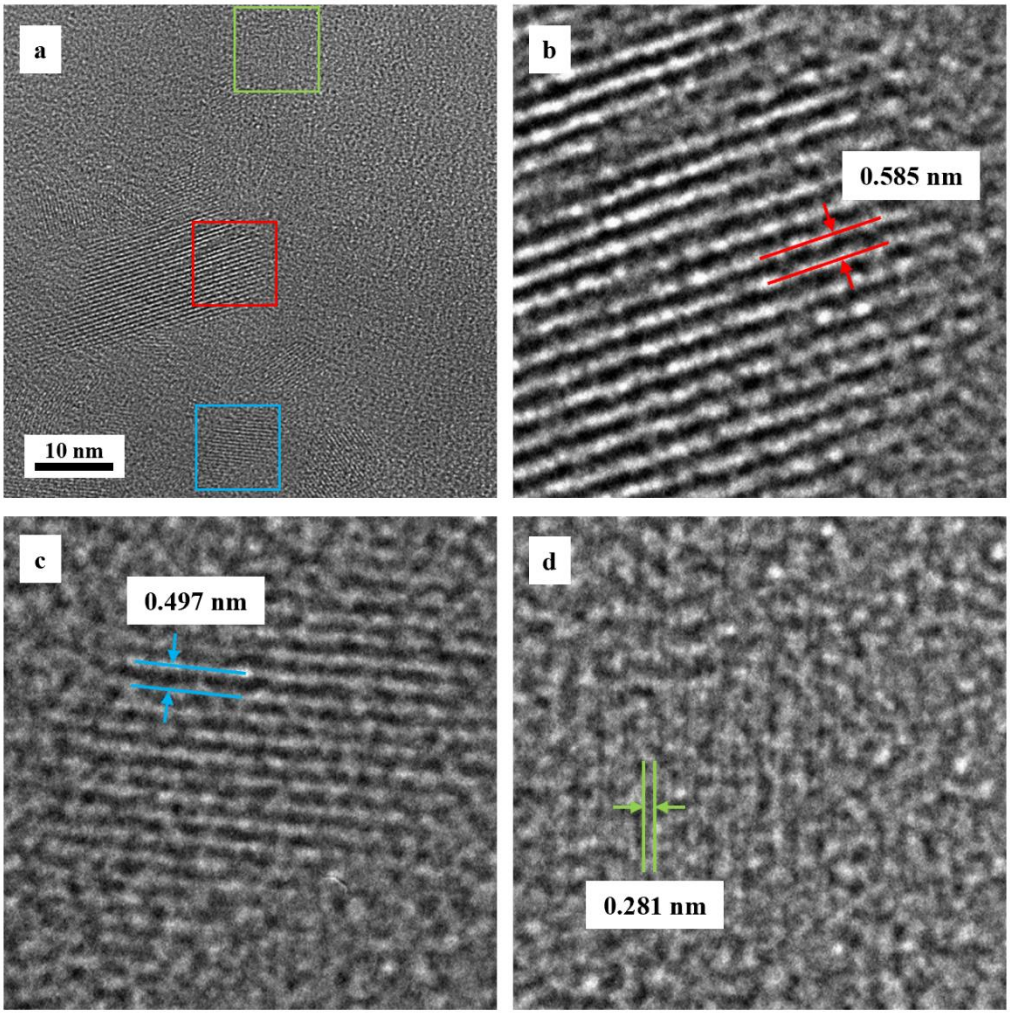


Figure 6.12 Electron microscopic images of a F9 thin-film sample, pH=9.5, 20 mg/mL. (a) HRTEM. (b) Magnified image of the area in the red square in (a). (c) Magnified image of the area in the blue square in (a). (d) Magnified image of the area in the blue square in (a).

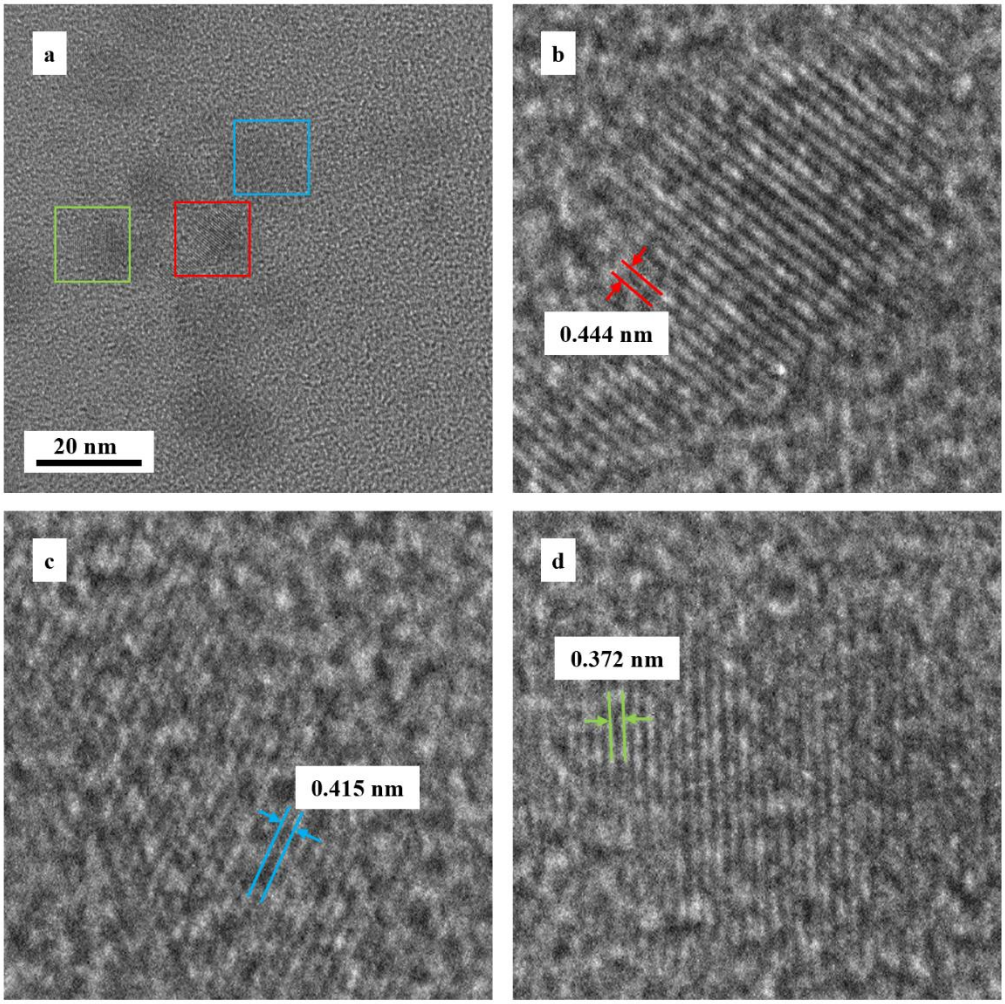


Figure 6.13 Electron microscopic images of a F9 thin-film sample, pH=9.5, 20 mg/mL. (a) HRTEM. (b) Magnified image of the area in the red square in (a). (c) Magnified image of the area in the blue square in (a). (d) Magnified image of the area in the blue square in (a).

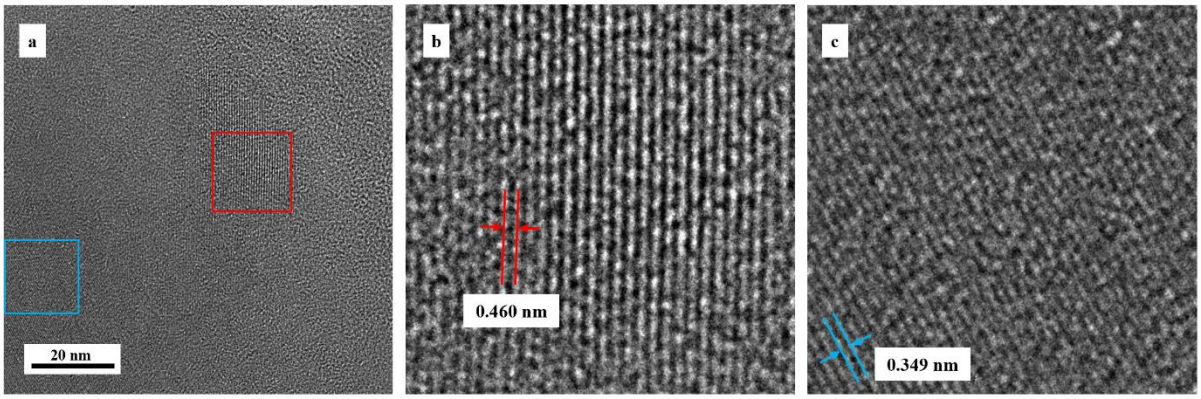


Figure 6.14 Electron microscopic images of a F9 thin-film sample, pH=9.5, 20 mg/mL. (a) HRTEM. (b) Magnified image of the area in the red square in (a). (c) Magnified image of the area in the blue square in (a).

Finally, Figure 6.15 is another set of HRTEM image of FP a d-spacing at 0.25 (± 0.01) nm can be observed.

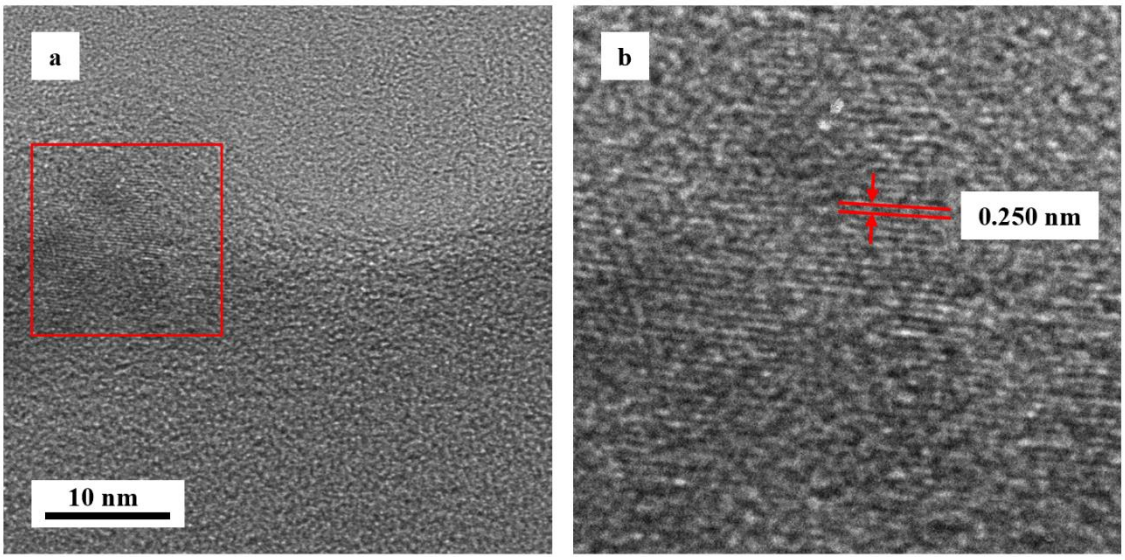


Figure 6.15 Electron microscopic images of a FP thin-film sample, pH=7, 20 mg/mL. (a) HRTEM. (b) Magnified image of the area in the red square in (a).

Table 6.1 summarises all d-spacings of F8, F9, and FP obtained from HRTEM. It is anticipated that future electron ptychography images will be able to interpret some of these d-spacings. Even if electron ptychography cannot assign them, they can also be useful for further exploring the PA β-sheet structure as research into PA β-sheet crystals advances.

Table 6.1 Summary of all d-spacings of F8, F9 and FP acquired from HRTEM.

Materials	D-spacings (nm)
F8	0.28, 0.32, 0.46
F9	0.28, 0.35, 0.37, 0.41, 0.44/0.46/0.47, 0.50, 0.58
FP	0.25, 0.45

6.4 Conclusions

To summarise, this chapter aims to increase the crystallinities of PVA and PAs and to study some basic structural and crystallographic information on these materials using FTIR, XRD and HRTEM.

As β-sheet secondary structures and hydrogen bonds have a significant impact on PA and PVA crystals, FTIR was firstly used to demonstrate their existence. As a result, the broad and high peak in the PVA FTIR spectrum ranging from around 3800 to 3000 cm^{-1} indicates that PVA samples contain a large number of hydrogen bonds. Also, two peaks near 1695 cm^{-1} and 1625 cm^{-1} suggest the β-sheet secondary structures of F8, F9 and FP.

Then, as confirmed by XRD, both thin-film unprocessed samples have a low degree of crystallinity, making it difficult to image crystals using electron microscopy. Inspired by previous studies on other organic materials, freeze-thawing was used to endeavour to further crystallise PA crystals. The XRD results show that freeze-thawing can indeed increase the crystallinities of the three PAs to a certain level, and the peaks around 2θ demonstrate PA crystals have the d-spacing with the range of 0.44 to 0.47nm, indicating their β-sheet structures. In the case of PVA, XRD results suggest that both freeze-thawing and annealing can increase the crystallinity of PVA, but annealing has a better effect then freeze-thawing. Additionally, in the range of 160 to 250 ℃, crystallinity is increased with the rise of annealing temperature. Based on the XRD results, freeze-thawing and annealing at 250 ℃ were chosen as the processing methods for PA and PVA electron microscopic samples respectively with higher crystallinities.

HRTEM was then employed in the investigation of the local crystal information of PVA and PAs. Two single-crystal PVA samples were firstly imaged. Two d-spacings at around 0.40 nm and 0.55 nm are acquired, and they are consistent with the (200) and (001) spacings of PVA. These samples will be studied using electron ptychography in Chapter 8, and the crystallinity of PVA will also be discussed then. HRTEM images of freeze-thawed PAs also show regions of crystallinity, and fringes with d-spacings in the range of 0.44 to 0.47 nm are found in HRTEM images. This is the first time HRTEM has been used to demonstrate the PA's β-sheet secondary structures. These three single-crystal samples, like PVA, will be used for electron ptychographic studies, and their crystallinities will be analysed using electron ptychographic images in Chapter 7.

In addition, two other PAs, FAFA and F2A2 were also characterised by HRTEM. According to previous research, these two PAs have α-helix structures and probably have the coexisting β-sheet structures. From their HRTEM images, d-spacings around 0.54 nm suggests the potential correlation between helical pitches to the α-helix crystals, and this d-spacing can potentially be evidence that FAFA and F2A2 form α-helix crystalline structures. Simultaneously, typical β-sheet d-spacings at approximately 0.46 nm are found in their HRTEM images. This can potentially support the coexistence of α-helix and β-sheet structures in FAFA and F2A2, but further research is required to confirm this point here.

Finally, in their HRTEM images, some additional d-spacings of F8, F9, and FP were observed. Although these d-spacings cannot be properly allocated in this chapter, they can still be useful for the future electron ptychographic work and further investigations of their PA β-sheet crystals.

In summary, this chapter completes preparatory steps including increasing the crystallinity of materials and studying the basic structures of PAs and PVA to provide a foundation for the electron ptychography work.

6.5 References

[1] Bunn, C. W. (1948). Crystal structure of polyvinyl alcohol. *Nature*, *161*(4102), 929-930.

[2] Sakurada, I., Fuchino, K., & Okada, N. (1950). Crystal structure of polyvinyl alcohol. *Bull. Inst. Chem. Res., Kyoto Univ.*, 1950, 23, 78-79.

[3] Fabiola, G. F., Krishnaswamy, S., Nagarajan, V., & Pattabhi, V. (1997). C—H··· O Hydrogen Bonds in β-sheets. *Acta Crystallographica Section D: Biological Crystallography*, *53*(3), 316-320.

[4] Cheng, P. N., Pham, J. D., & Nowick, J. S. (2013). The supramolecular chemistry of β-sheets. *Journal of the American Chemical Society*, *135*(15), 5477-5492.

[5] Han, S., Cao, S., Wang, Y., Wang, J., Xia, D., Xu, H., Zhao, X., & Lu, J. R. (2011). Self-assembly of short peptide amphiphiles: the cooperative effect of hydrophobic interaction and hydrogen bonding. *Chemistry–A European Journal*, *17*(46), 13095-13102.

[6] Wychowaniec, J. K., Smith, A. M., Ligorio, C., Mykhaylyk, O. O., Miller, A. F., & Saiani, A. (2020). Role of sheet-edge interactions in β-sheet self-assembling peptide hydrogels. *Biomacromolecules*, *21*(6), 2285-2297.

[7] Elsawy, M. A., Smith, A. M., Hodson, N., Squires, A., Miller, A. F., & Saiani, A. (2016). Modification of β-sheet forming peptide hydrophobic face: effect on self-assembly and gelation. *Langmuir*, *32*(19), 4917-4923.

[8] Wang, Z. (2018). *Self-assembly of Peptides on Surfaces* (Master dissertation, University of Oxford).

[9] Botwright, S. (2017). *Self-assembly of Peptides on Surfaces* (Master dissertation, University of Oxford).

[10] Zou, Y., Li, Y., Hao, W., Hu, X., & Ma, G. (2013). Parallel β-sheet fibril and antiparallel β-sheet oligomer: new insights into amyloid formation of hen egg white lysozyme under heat

and acidic condition from FTIR spectroscopy. *The Journal of Physical Chemistry B*, *117*(15), 4003-4013.

[11] Mansur, H. S., Sadahira, C. M., Souza, A. N., & Mansur, A. A. (2008). FTIR spectroscopy characterization of poly (vinyl alcohol) hydrogel with different hydrolysis degree and chemically crosslinked with glutaraldehyde. *Materials Science and Engineering: C*, *28*(4), 539-548.

[12] Meziani, S., Jasniewski, J., Gaiani, C., Ioannou, I., Muller, J. M., Ghoul, M., & Desobry, S. (2011). Effects of freezing treatments on viscoelastic and structural behavior of frozen sweet dough. *Journal of Food Engineering*, *107*(3-4), 358-365.

[13] Chee, B. S., de Lima, G. G., Devine, D. M., & Nugent, M. J. (2018). Investigation of the effects of orientation on freeze/thawed Polyvinyl alcohol hydrogel properties. *Materials Today Communications*, *17*, 82-93.

[14] Rapaport, H., Kjaer, K., Jensen, T. R., Leiserowitz, L., & Tirrell, D. A. (2000). Two-dimensional order in β-sheet peptide monolayers. *Journal of the American Chemical Society*, *122*(50), 12523-12529.

[15] Weaver, L., Stagsted, J., Behnke, O., Matthews, B. W., & Olsson, L. (1996). β-Sheet models for the ordered filamentous structure formed by a peptide that enhances the action of insulin. *Journal of structural biology*, *117*(3), 165-172.

[16] Tycko, R., Sciarretta, K. L., Orgel, J. P., & Meredith, S. C. (2009). Evidence for novel β-sheet structures in Iowa mutant β-amyloid fibrils. *Biochemistry*, *48*(26), 6072-6084.

[17] Assender, H. E., & Windle, A. H. (1998). Crystallinity in poly (vinyl alcohol). 1. An X-ray diffraction study of atactic PVOH. *Polymer*, 39(18), 4295-4302.

[18] Talbot, J. A., & Hodges, R. S. (1982). Tropomyosin: a model protein for studying coiled-coil and. alpha-helix stabilization. *Accounts of Chemical Research*, *15*(7), 224-230.

Chapter 7. Electron Ptychographic Imaging of Peptide Amphiphiles

7.1 Introduction

In the last chapter, it was confirmed that freeze-thawing can be used to generate isolated crystals in the amorphous matrix within a field of view of the electron ptychographic study. After further confirming the β-sheet structure by using FTIR and XRD, and studying the basic crystallography of F8, F9 and FP by using HRTEM in the last chapter, this chapter uses electron ptychography to investigate the fine structure of PA β-sheet crystals. High-resolution electron ptychographic imaging is expected to improve current understanding of PA β-sheet crystals.

7.2 Results

7.2.1 Beam Damage Study on Peptides

As introduced in Section 1.3.1, peptides are beam-sensitive materials under electron microscopy [1][2] and introduced electrons can change the structure of the sample, which may make the information acquired from electron microscopy unprecise [2][3]. Therefore, the first topic in this chapter is to study how electrons influence the crystal structure of PAs. Evidence of beam damage can be seen after excessive electron exposure of the PA samples. Figure 7.1 depicts a set of F8 images that illustrate the beam damage. Figures 7.1(a) and 7.1(b) show the first scan of an F8 sample with a dose of 7.8×10^3 ($e^-/Å^2$). Figure 7.1(c) shows the second scan on the same F8 crystallite, with a dose of 1.7×10^4 ($e^-/Å^2$) used to acquire this image. When looking at Figures 7.1(a) and 7.1(b), electrons begin to damage the right side of the field of vision. In contrast, as the sample is exposed to electrons for a longer period of time and at a higher dose, more areas on the right side of Figure 8c become amorphous. Figures 7.2 and 7.3 also show examples of beam damage to F9 and FP. The dose used for Figures 7.2(a) and 7.2(b) is 1.9×10^4 ($e^-/Å^2$), and the dose used for Figures 7.3(a) and 7.3(b) is 5.2×10^3 ($e^-/Å^2$). Electrons were damaging the left side of the F9 crystal in this field of view and the right side of the FP crystal in this field of view. Similarly to F8, these images show that on the F9 and FP samples, the process of damage is also amorphization, indicating that the crystallinity observed is not due to beam effects. In addition, as shown in Figure 7.4, mass loss of materials was observed in the high-resolution HAADF-STEM and electron ptychography work. This means that on top of the amorphization process, PA materials can be removed by the incident electrons of the electron microscope, and imaging these PA crystals may require a lower dose and a shorter acquisition time to avoid the mass loss.

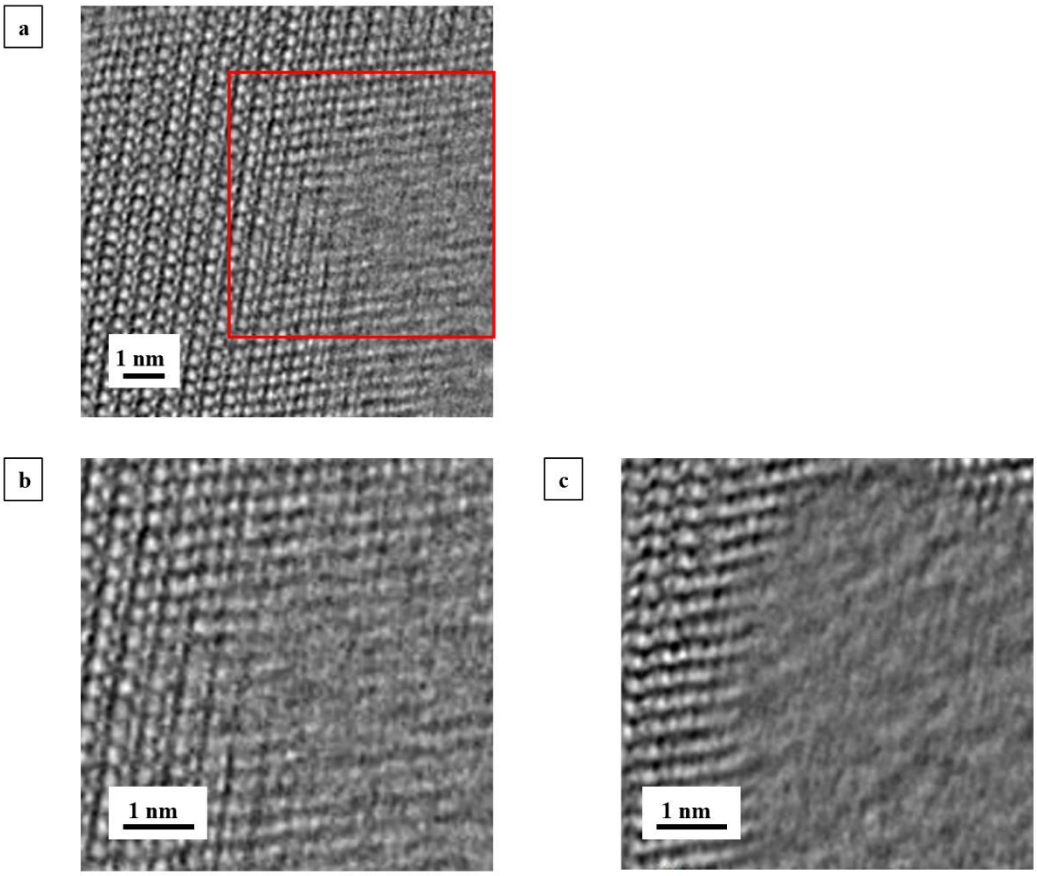


Figure 7.1 Two sequential SSB scans of the F8 sample. (a) First scan of the F8 sample. (b) Enlargement of the area in the red square in (a). (c) Second scan of the F8 sample with the same crystal of (a), with a larger magnification.

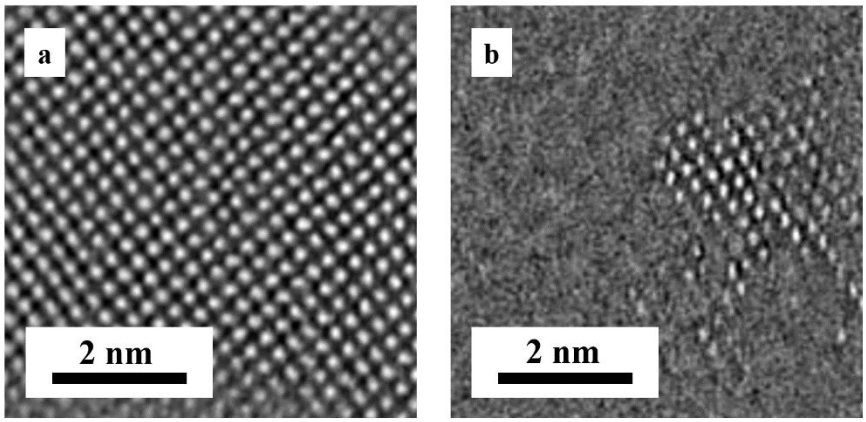


Figure 7.2 Two sequential SSB scans of the F9 sample. (a) First scan of the F9 sample. (b) Second scan of the F9 sample with the same crystal of (a), with the magnification and dose.

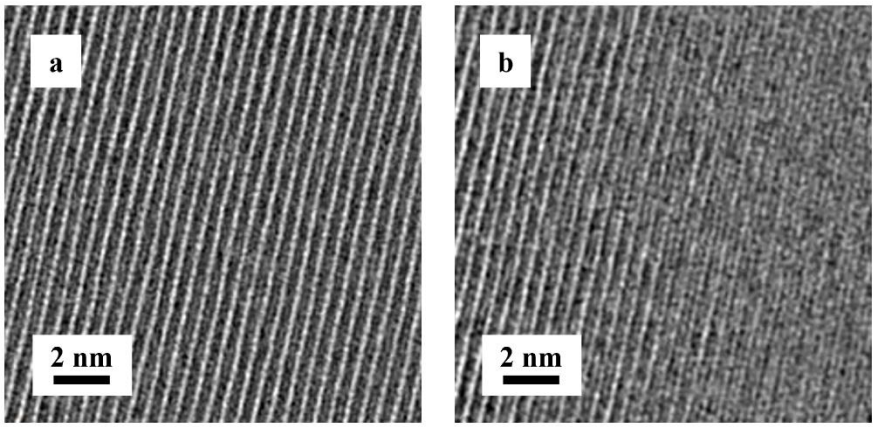


Figure 7.3 Two sequential SSB scans of the FP sample. (a) First scan of the FP sample. (b) Second scan of the FP sample with the same crystal of (a), with the magnification and dose.

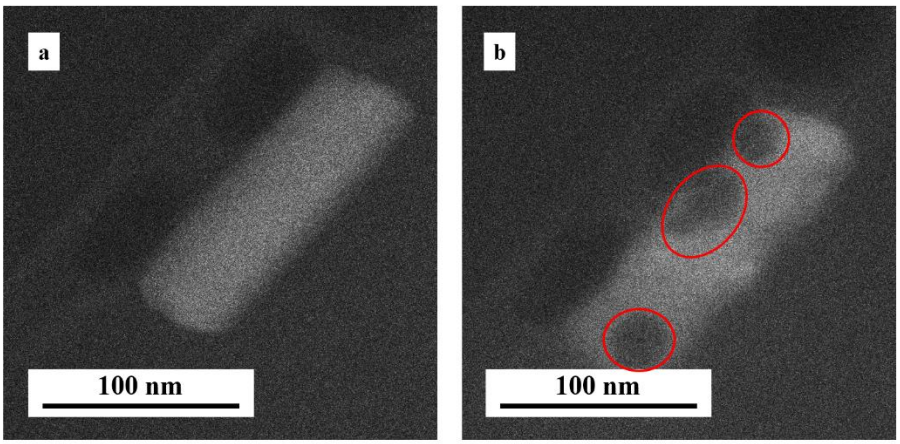


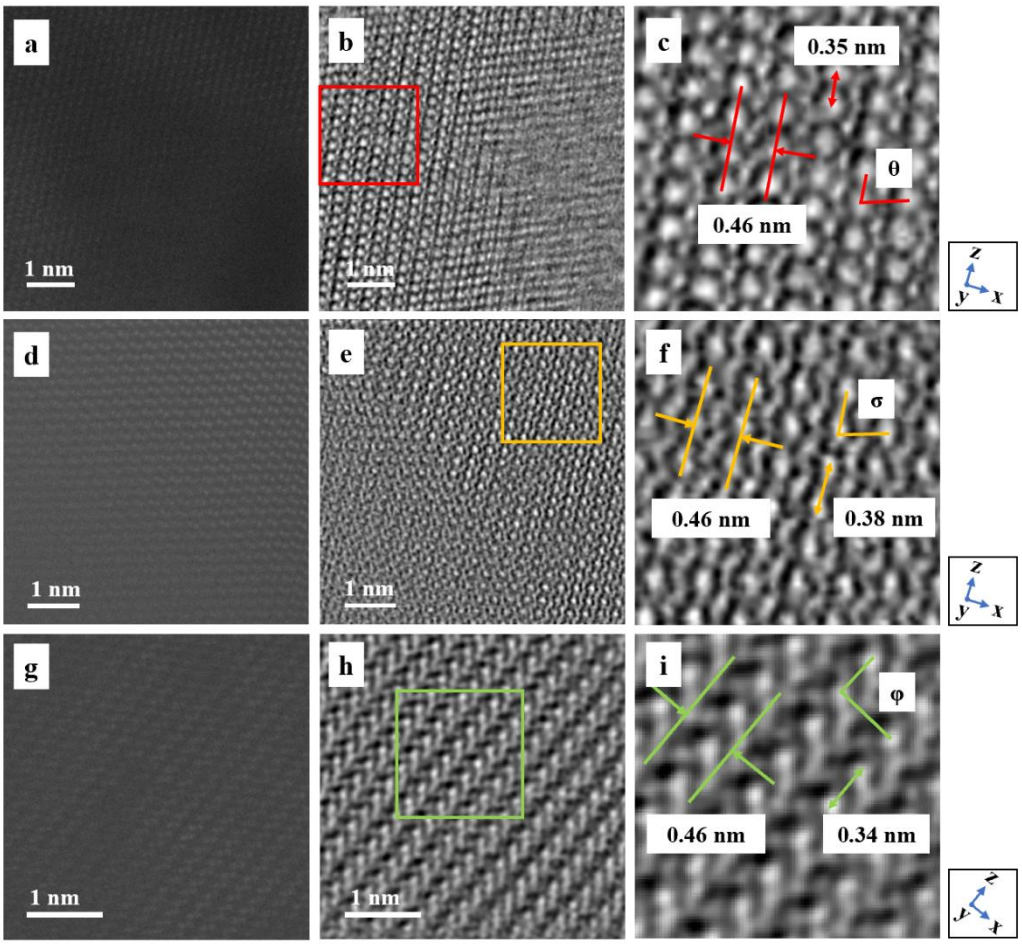
Figure 7.4 HAADF-STEM images of the same crystallite of an F9 before and after the high-resolution HAADF-STEM and electron ptychography work. (a) Before HAADF-STEM and electron ptychography acquisitions. (b) After HAADF-STEM and electron ptychography acquisitions.

7.2.2 High-angle Annular Dark Field-Scanning Transmission Electron Microscopy and Electron Ptychography

Section 6.2.2.1 showed how freeze-thawing can be used to generate areas in the sample with isolated single-crystals within an amorphous matrix, suitable for imaging. Single-crystals shown in Figure 6.7 where β-sheet d-spacings were acquired are used here for a deeper understanding of their fine β-sheet structures. In this chapter, the study proceeds to use electron ptychography and its simultaneous HAADF-STEM to image the crystals of the three PA types. The dose applied for F8 and F9 is 7.8×10^3 ($e^-/Å^2$), and the dose used for FP is 1.7×10^4 ($e^-/Å^2$). Reconstructed SSB-phase ptychographic images are shown in 7.5(b), 7.5(e) and 7.5(h), and their simultaneous HAADF-STEM images are shown in Figures 7.5(a), 7.5d and 7.5(g). Plane d-spacings and repeat distances acquired from Figures 7.5 (a) to (i) are summarised in Table 7.5(j). For all three PAs, a d-spacing at around 0.46 nm was acquired. This d-spacing is consistent with the β-sheet d-spacing. In addition, another repeat distance at around 0.35 nm is obtained for the three PAs from reconstructed ptychographic images. This distance is around the length of the amino acid repeat unit, which is half of what previous research defines as the repeat distance [4][5]. Given these two key spacings acquired are relevant to d_1 and repeat distance suggested by previous studies, it can be inferred that, these images project the structure in the xz plane, where the β-sheets are lying in this plane. Another noticeable result from Figure 7.5 is that no obvious repeat features relevant to the whole molecular chain, namely the length of 8 or 9 amino acids, can be detected.

Figures 7.5(c), 7.5(f), and 7.5(i) show magnified ptychographic images with dots and zigzag lines. The symmetry of the dots differs between the three PA-types' β-sheet crystals. The angle

between FP's neighbouring dots (as indicated on the image) is 88°, *i.e.*, close to 90°, whereas the angles for F8 and F9 are 74° and 78°, respectively. Angles are calculated by averaging 5 measurements from 5 different positions in each image. When the HAADF-STEM and electron ptychographic images are compared, electron ptychography provides more information on the structure, and electron ptychographic images can give information on how peptide backbones and side groups are ordered in the material.



j

Peptide	β-sheet spacing (nm)	Amino acid spacing along the chain axis (nm)	Angle marked in each image (°)
F8	0.46 ± 0.04	0.35 ± 0.02	θ = 74.0 ± 2.0
F9	0.46 ± 0.04	0.38 ± 0.04	σ = 78.0 ± 2.0
FP	0.46 ± 0.04	0.34 ± 0.02	φ = 88.0 ± 1.0

Figure 7.5 Electron microscopic images of peptides. (a) HAADF-STEM image of F8. (b) Electron ptychography SSB phase image of F8. (c) Enlarged SSB phase image of the

marked area in (b), with marked spacings and an angle. (d) HAADF-STEM image of F9. (e) Electron ptychography SSB phase image of F9. (f) Enlarged SSB phase image of the marked area in (e), with marked spacings and an angle. (g) HAADF-STEM image of FP. (h) Electron ptychography SSB phase image of FP. (i) Enlarged SSB phase image of the marked area in (h), with marked spacings and an angle. (j) Summary of spacings and angles acquired from above electron ptychographic images.

7.3 Discussion

7.3.1 β-sheet Structural Study

Within the allowable range of error, β-sheet spacings acquired from the above six electron ptychographic and their simultaneous HAADF-STEM images accord with the ones obtained from the HRTEM images and XRD results. The details of the spacings are displayed in Table 7.1. This characteristic d-spacing of the β-sheet structure suggests that PA β-sheet crystals have been visualised. However, because there is no evidence to distinguish the orientation of each molecular strand, even with electron ptychography data, it is still unable to be determined whether the PA-sheet crystals are parallel or anti-parallel.

Table 7.1 Summary of all potential d_1-equivalent d-spacings acquired from XRD, HRTEM and HAADF-STEM/electron ptychography.

Peptide	D-spacings acquired from XRD (nm)	D-spacings acquired from HRTEM (nm)	D-spacings acquired from HAADF-STEM and electron ptychography (nm)
F8	0.44	0.46	0.46
F9	0.44	0.46	0.46
FP	0.46	0.45	0.46

7.3.2 Repeat Distance Study and New Understandings of Peptide Amphiphilic β-sheet Crystals

Here the “sawtooth” structure is introduced to demonstrate the repeat distance at around 0.35 nm. Several previous studies [6]-[9] suggest that, due to the hydrophobicity, molecules tend to minimise unfavourable interactions with the aqueous environment by exposing the hydrophilic domains while shielding the hydrophobic moieties, and therefore, forming the self-

assembling “sawtooth” structure. For PAs which have aromatic side groups, π–π stacking is another factor that contributes to the “sawtooth” structure A schematic representation of this sawtooth phenomenon using F8 molecules can be found in Figure 7.6.

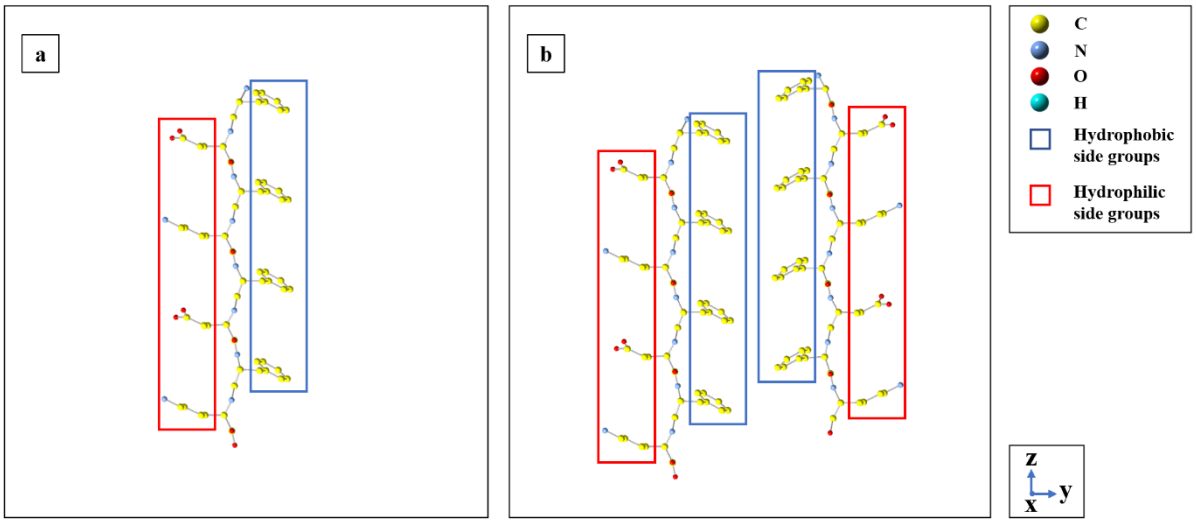


Figure 7.6 Schematic of PA self-assembly due to the hydrophobicity, taking F8 molecules as the example. (a) A F8 single molecule. (b) A pair of self-assembling F8 molecules.

To further interpret the repeat distance shown in electron ptychographic images, Figure 7.7 depicts a possible PA-sheet crystal model derived from ptychographic images. As introduced above in Figure 7.6, pairs of β-sheets (occupying the xz plane, projecting into the page) are arranged such that the side groups lie with the hydrophobic groups facing one another on adjacent sheets, and the hydrophilic groups face one another in the next inter-sheet interaction. The microscopy images a projection of the average electron density as viewed along a particular direction. In this case, viewing along the [010] direction would lead to a repeat distance equal to the length of the amino acid (half of what previous research defined [4][5]10][11]) along the [001] direction, as is observed in Figure 7.5(c), (f) and (i).

Figure 7.7 further explains the differences between two forms of PA β-sheet crystals in the yz plane. As shown in Figure 7.7(a), previous studies [10][11] suggest that PA β-sheet molecules order neatly along the z axis, with a d_3 (equal to the length of two amino acids) repeat distance. By contrast, Figure 7.7(b) is constructed based on the "sawtooth" structure with the hydrophobic or hydrophilic groups facing one another, and the side groups 'interleaved'. The repeat distance along the molecular chain is 0.5 d_3 according to the periodicity in this case.

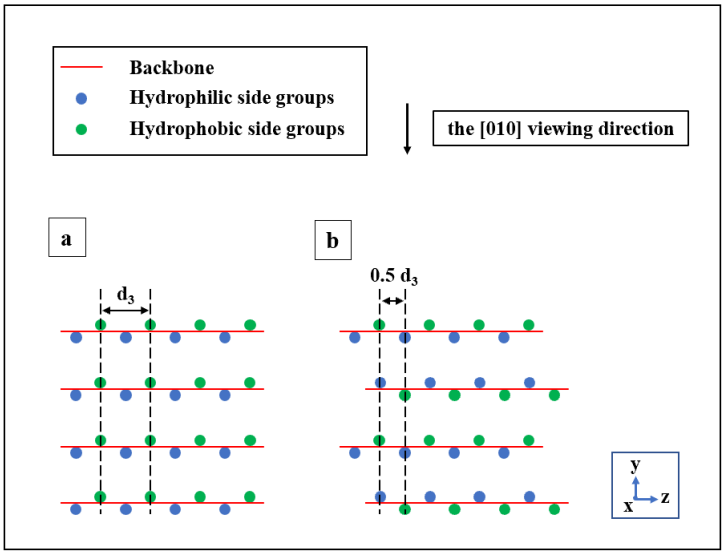


Figure 7.7 Schematic of two F8 crystal models in the yz plane. (a) Models built based on information taken from references [4] and [5], with no "sawtooth" structure involved. Scientists treat the length between two adjacent same side groups (d_3) as the repeat distance. (b) Models built with the consideration of the "sawtooth" structure. According to the periodicity of the molecules, the repeat distance is 0.5 d_3 in this model.

Furthermore, if all the chain ends aligned with one another along the [010] as is indicated in Figure 7.8(a), taking F8 as an example, evidence of a repeat distance of at least 4.5 d_3 (for an 8 amino acid chain) associated with the chain ends (and the P unit in FP) is expected. No such long repeat is observed in the FFT images, suggesting that there is not a strong correlation of

end groups in PA crystals, and the chain ends are not completely aligned along the y axis in the [001] direction, as illustrated in Figure 7.8(b). Nevertheless, it cannot be precisely determined whether the chain terminations are random within a single β-sheet or in successive β-sheets. The results in this study accord with the previous model proposed by Zhang *et al.* [12][13] for the PA EAK16. They believed the "staggered" model is the coeffect of the hydrophobicity from hydrophobic side groups and electrostatic interactions from hydrophilic side groups. The staggered structure of PA crystals would contribute to stability in the direction along the molecules [12][13].

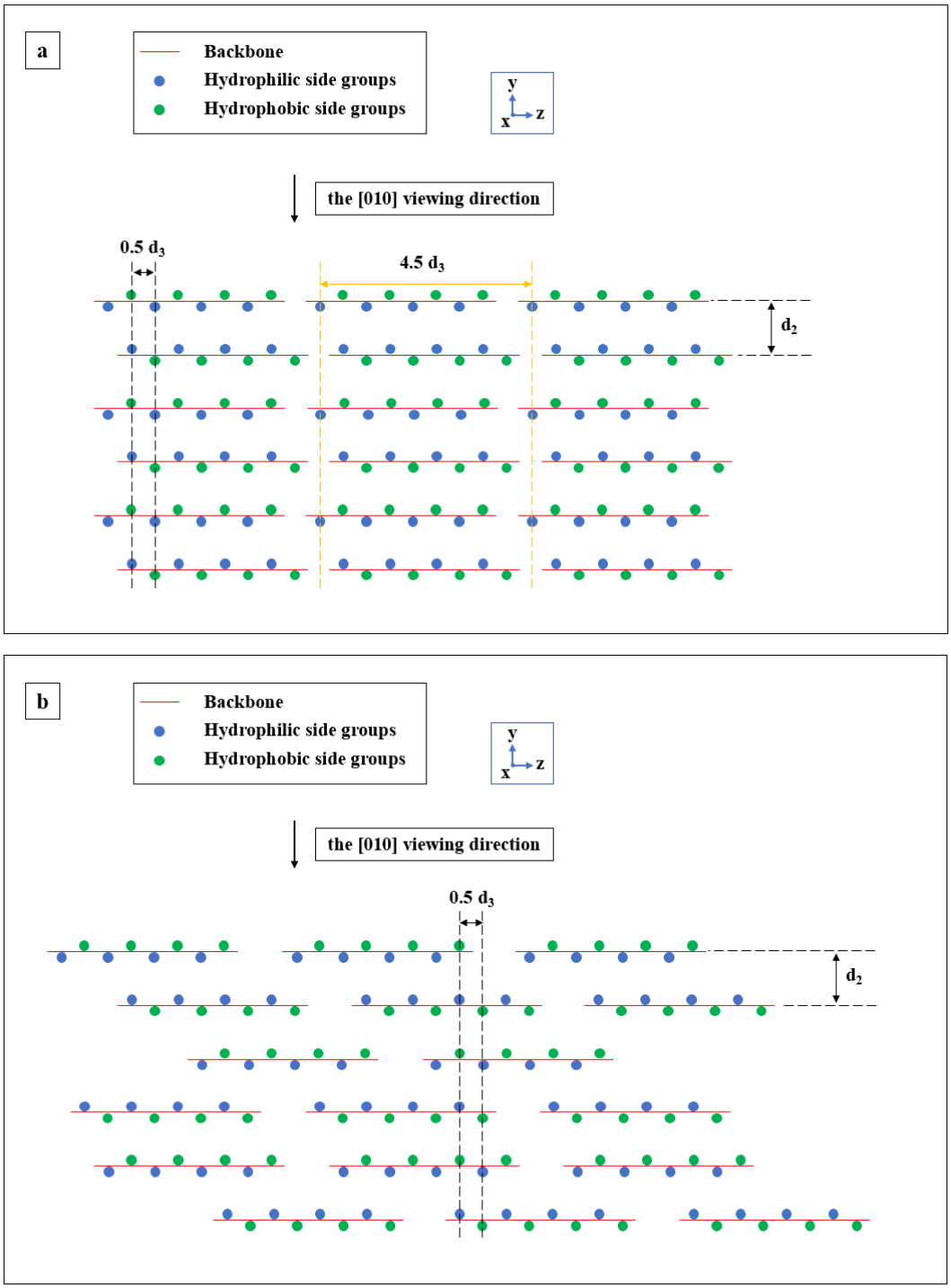


Figure 7.8 (a) A F8 crystal model in the yz plane, with all the chain ends aligning with one another along the [010] direction. A notable repeat distance at 4.5 d_3 is expected. (b) A F8 crystal model in the yz plane, with and the chain ends are rather randomly distributed in the [001] direction. No repeat distance at 4.5 d_3 is expected.

7.3.3 Symmetrical Differences Between Three Peptide Amphiphiles

Having rationalised the ptychographic images with the basic ordering of the peptide chains in β-sheets, the differences observed between the various peptide molecules can be further examined. Although elaborating on the precise crystal structures of each PA is challenging, here some rationale for the difference in angles and repeat distances can still be given. First, as concluded in Figure 7.5(j), F9 has a slightly larger repeat distance along the molecular axis than that of F8 and FP. This can be attributed to the sequence of amino acids of F9. As shown in Figure 7.9, in black squares, two positively charged side groups K, are adjacent at the end of each F9 molecule. Due to this unfavourable electrostatic interaction, these two groups tend to be further apart, and the neighbouring chains can stretch to accommodate this. Similarly, along the chain axis, there are two K groups that adjacently face one another at the chain ends and outsets of neighbouring chains. This may also elongate the chain, and as a result, increase the repeat distance of F9. The exact way of F9 stretches or elongates is not clear at present. It could be achieved by increasing C-C bond length, opening out of the primary chain zigzags of carbon atoms in the β-sheet plane, or opening out of zigzags of chains out of the β-sheet plane. Future computational work is required to explore the exact way that the F9 molecule stretches.

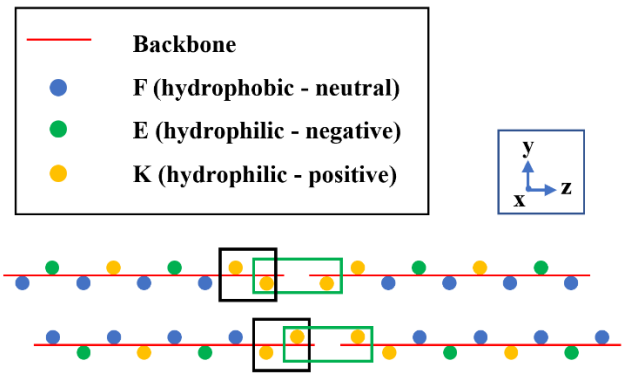


Figure 7.9 An F9 crystal model in the yz plane, with two K groups locate adjacently at the end of each F9 molecule and two K groups face one to another at the chain ends and outsets of neighbouring chains.

Moreover, according to Table 7.5(j), F8 and F9 have a different symmetry than FP. The angles F8 and F9 are close, but neither is orthogonal, whereas the angle FP is close to 90°. This may be caused by relative offsets of adjacent C-C chains in F8 and F9 β-sheet crystals. Schmidt *et al*. [14] proposed, through cryo-EM studies, that peptides have a "dimer" structure, in which a molecular chain can have an offset relative to neighbouring chains along the molecular axis. To further explain the molecular offsets of F8 and F9, several models are generated, as shown in Figure 7.10. Figures 7.10(b) and 7.10(d) depict parallel and anti-parallel models using F8 as the example, with each chain offset by 0.13nm along the molecular axis from its left chain. Chain offsets produce a 74° angle between adjacent chains, which corresponds to the electron ptychographic images. Except for the directions of hydrogen bonding, the hydrogen bonding in the offset models of F8 does not differ significantly from hydrogen bonding in non-offset models of FP. As a result, it is anticipated that the offset models can be structurally and energetically rational. This offset structure could be the result of a variety of interactions, including van der Waals force, steric effects, and π- π stacking.

In contrast, FP has a unique middle ring located central to the molecular chain, which can increase the energy cost of chain offsets. In other words, there should be an anticipated energetic favourability of the middle rings of FP lining up adjacent to one another along the [100] direction, as shown in the orange squares in Figure 7.10(a) and 7.10(c). Accordingly, FP molecules have a different molecular symmetry to that of F8 and F9. As previously stated, no repeat distance for the length of 9 amino acids is detected in electron ptychographic images,

indicating that middle rings do not have a strong correlation along the viewing direction. Because it is expected that the middle rings do align in an orderly fashion within the β-sheet to avoid energy cost of chain offsets, middle rings then should be rather randomly ordered in successive β-sheet layers.

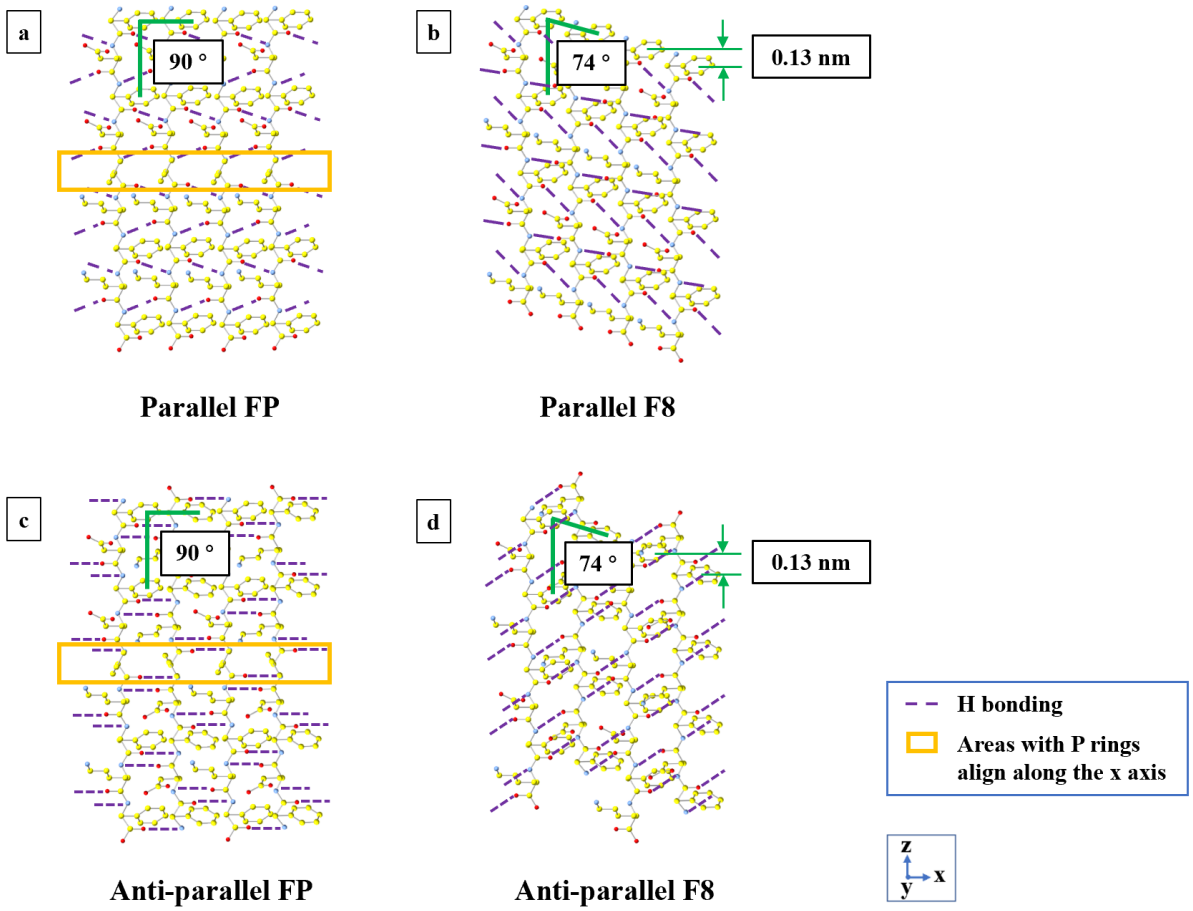


Figure 7.10 Parallel and anti-parallel F8 and FP models in the xz plane. (a) Parallel FP model, with no chain offset. (b) Parallel F8 model, with a 0.13 nm offset along the molecular axis between neighbouring molecular chains, forming a 74° angle between adjacent chains. (c) Anti-parallel FP model, with no chain offset. (d) Anti-parallel F8 model, with a 0.13 nm offset along the molecular axis between neighbouring molecular chains, forming a 74° angle between adjacent chains.

These four models in Figure 7.10 are then compared to the electron ptychographic images. As shown in Figure 7.11, when overlaying the parallel and anti-parallel models on the electron ptychography image, the overall symmetries, periodicities and spacings match properly despite some minor differences, such as the size of aromatic rings or the spots in the electron ptychographic images (this comes from the uncertainty of the positions of side groups). This means that models shown in the Figure 7.10 essentially work well on the PAs.

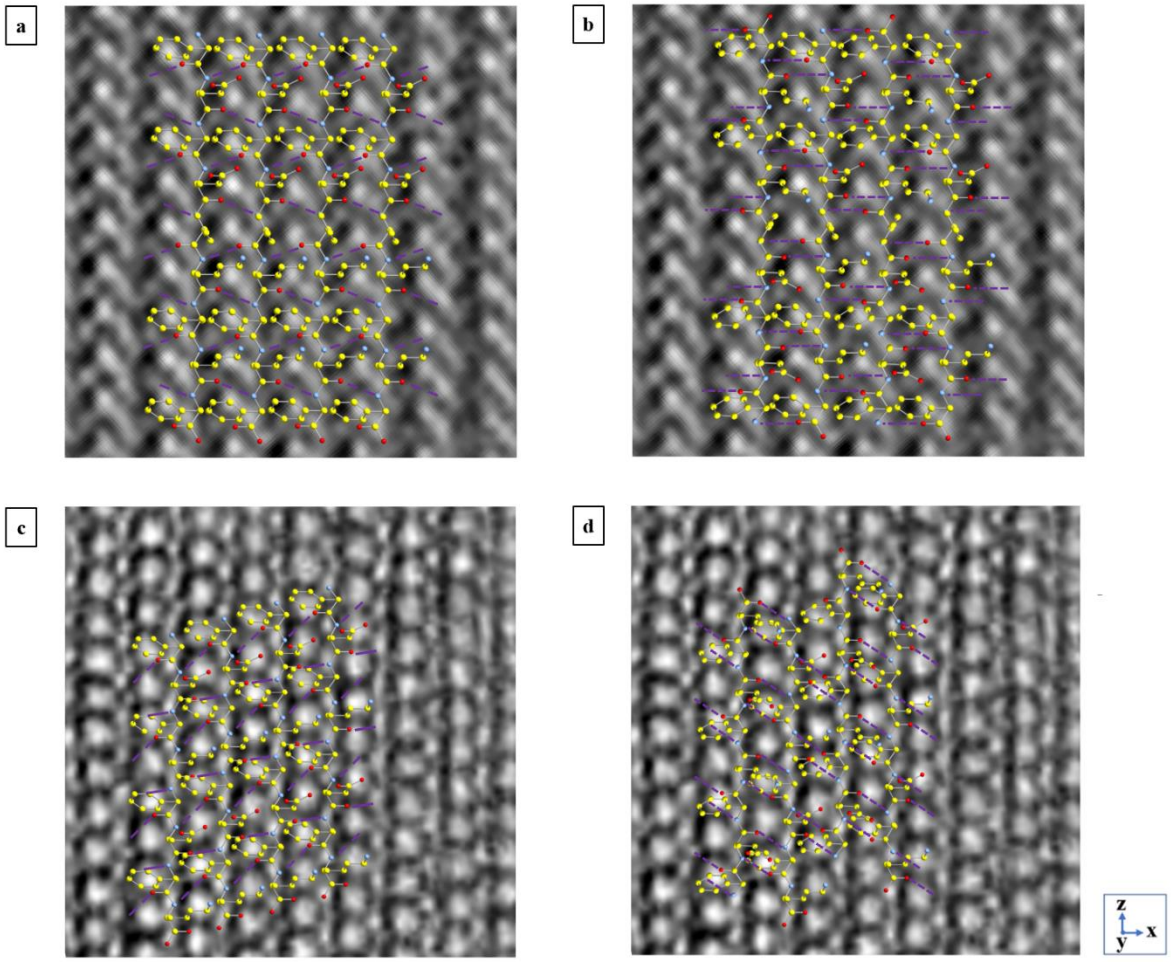


Figure 7.11 Parallel and anti-parallel F8 and FP models overlaying in their electron ptychographic images. (a) Parallel FP model on its electron ptychographic image. (b) Anti-parallel FP model on its electron ptychographic image. (c) Parallel F8 model on its

electron ptychographic image. (b) Anti-parallel F8 model on its electron ptychographic image.

7.3.4 Possible Interpretation of the Contrast in the Electron Ptychographic Images

Based on the single-layer models shown above, multilayer models can be constructed to interpret the contrast in the electron ptychographic images. As presented in Figure 7.6 and discussed above, adjacent layers along the y axis should follow the "sawtooth" structure. Figure 7.12(a) shows the view of the "sawtooth" structure in the [010] direction. Following this pattern, Figure 7.12(b), (c), (d) and (e) illustrates the multilayer parallel and anti-parallel F8 and FP models. However, it is noticeable that for the two F8 models, as projected along [010] the side groups are not evenly distributed along the molecular axis, which is different to what the F8 electron ptychographic image suggests. To accurately match the image, as shown in Figure 7.13, the F8 multilayer parallel and anti-parallel models are modified by shifting the top layer along the z axis to make the side groups evenly distributed along the molecular axis. This even distribution may be the result of a combination of several interactions, such as π-π stacking of aromatic side groups and electrostatic interactions of hydrophilic side groups.

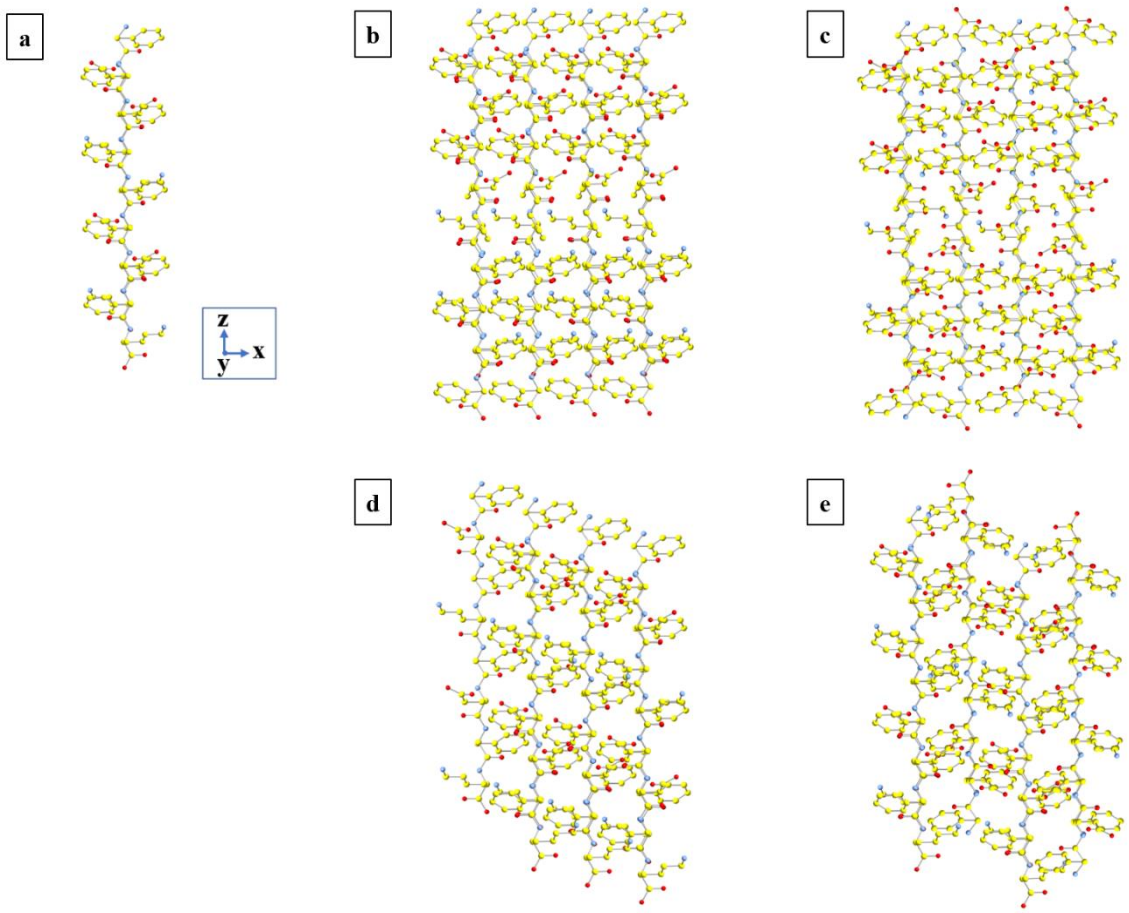


Figure 7.12 Multilayer parallel and anti-parallel F8 and FP models. Based on the models shown in Figure 7.7(b), another layer is added along the y axis onto the single-layer models shown in Figure 7.11. (a) View of the self-assembling "sawtooth" structure shown in Figure 7.7(b) in the [010] direction. (b) Multilayer parallel FP model. (c) Multilayer anti-parallel FP model. (d) Multilayer parallel F8 model. (e) Multilayer anti-parallel F8 model.

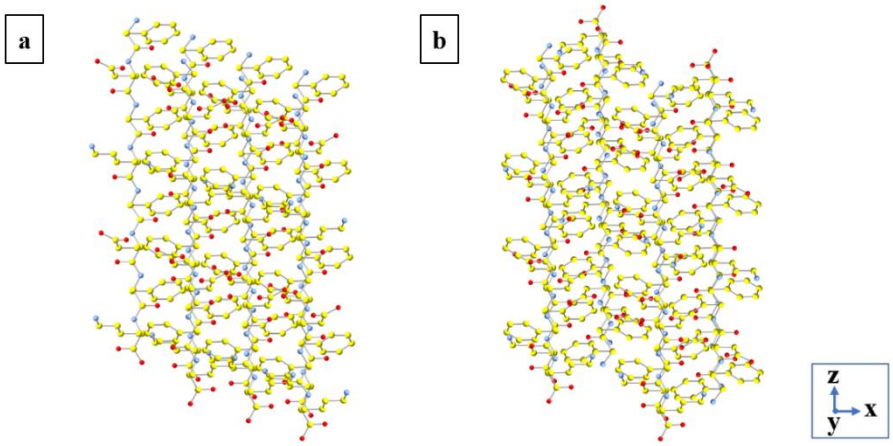


Figure 7.13 Modified multilayer F8 models. (a) Modified multilayer parallel F8 model. (b) Modified multilayer anti-parallel F8 model.

Finally, as shown in Figures 7.14 and 7.15, the multilayer FP models and the modified multilayer F8 models are compared to the electron ptychographic images. As shown in Figure 7.14, the symmetries and the spacings of both parallel and anti-parallel models essentially match the FP ptychography image. The mid rings of the FP molecules can give rise to "uncovered" positions of the side groups shown in the green squares in Figure 7.14. Nevertheless, considering several more layers stacked along the y axis as the method suggested in Figure 7.8(b), those "uncovered" positions can finally be filled. Turning to the F8 models, both parallel and anti-parallel models also basically match the symmetries and the spacings presented in the F8 ptychographic image despite some minor malposition.

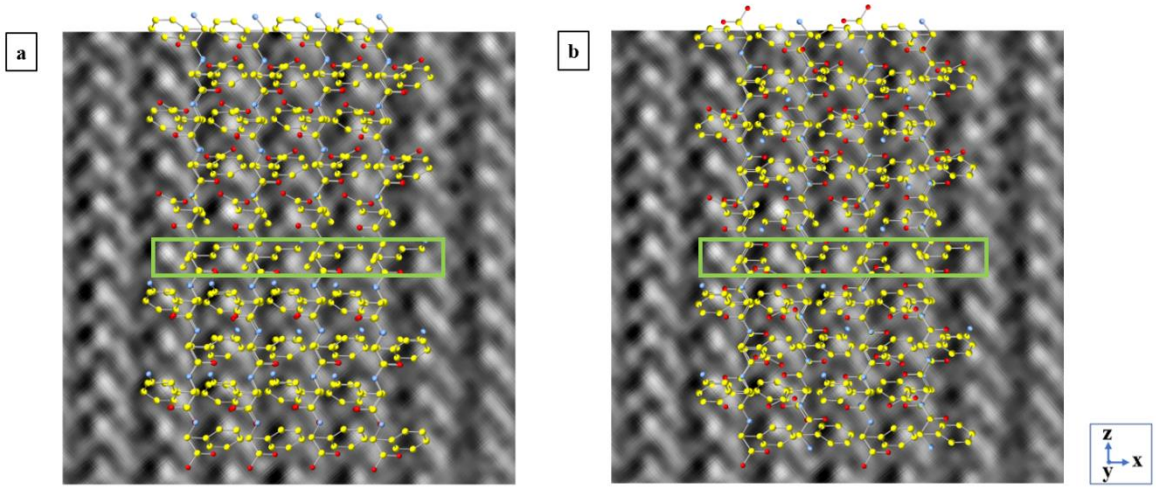


Figure 7.14 Modified multilayer parallel and anti-parallel FP models overlaying in its electron ptychographic images. (a) Modified multilayer parallel FP model on its electron ptychographic image. (b) Modified multilayer anti-parallel FP model on its electron ptychographic image.

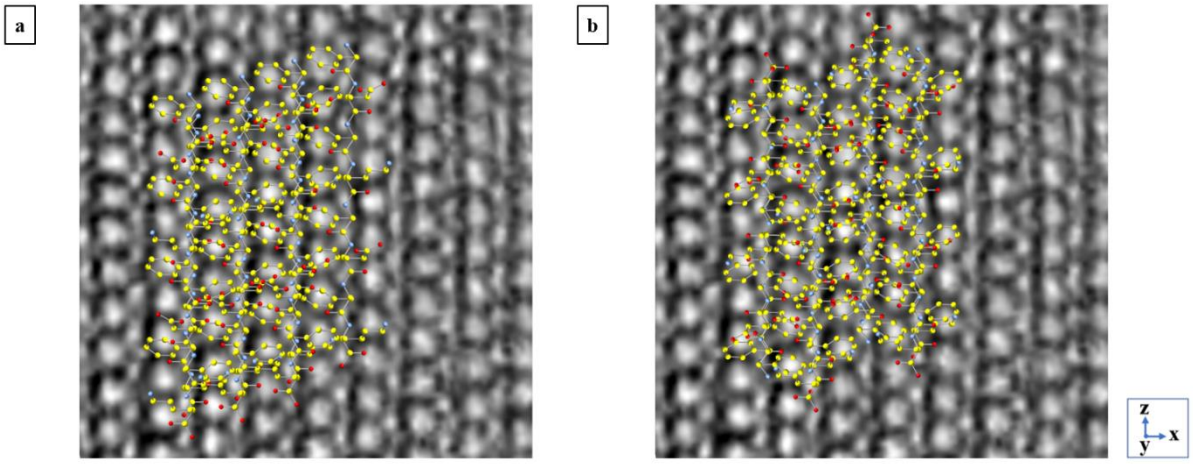


Figure 7.15 Modified multilayer parallel and anti-parallel F8 models overlaying in its electron ptychographic images. (a) Modified multilayer parallel F8 model on its electron ptychographic image. (b) Modified multilayer anti-parallel F8 model on its electron ptychographic image.

The preceding discussion only offers one interpretation of the contrast in electron ptychographic images. Image simulations on the precise PA β-sheet crystals are required for an accurate interpretation. However, due to the lack of the basic knowledge of these PA β-sheet crystals, image simulations will not be performed in this thesis. When there are some advances in the study of PA β-sheet crystallography by other methods, for instance, calculation and modelling of the crystals, the electron ptychographic images can be further interpreted in the future.

7.4 Unassigned d-spacings of the Above Materials

In addition to above d-spacings and repeat distances, some more d-spacings of the three kinds of PAs are acquired by using HAADF-STEM and electron ptychography. Because the PA β-sheet crystals are not very well studied, these d-spacings cannot be properly assigned at present. Nonetheless, images in this section can also be useful for further exploring PA β-sheet structure when the study of PA β-sheet crystals advances. From Figure 7.16 to Figure 7.19, there are four more sets of images of F8, F9 and FP, and they will be discussed in this section.

Figure 7.16 shows another set of F8 electron microscopic images. The electron ptychographic image in Figure 7.16(b) does not clearly show more information than its simultaneous HAADF-STEM as shown in Figure 7.16(a). Firstly, a repeat distance at 0.35 (± 0.01) nm is found, and this repat distance accords with the result presented in Figure 7.5(a), (b) and (c). Besides, there are three more d-spacings at 0.30 (± 0.02) nm, 0.32 (± 0.02) nm and 0.36 (± 0.02) nm are acquired. Herein, the d-spacing at 0.32 nm is also found by using HRTEM as shown in Section 6.3.

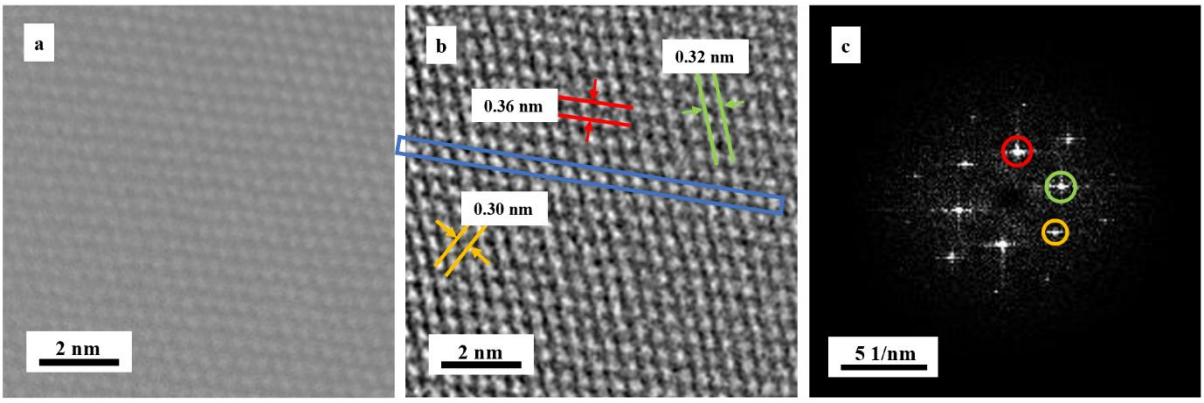


Figure 7.16 Electron microscopic images of F8 in an unassigned viewing direction. (a) HAADF-STEM image. (b) Simultaneous electron ptychography SSB phase image. (c) FFT of (b).

Figures 7.17 and 7.18 present two groups of F9 images. In Figure 7.17(b), the electron ptychographic image brought more information than the HAADF-STEM image shown in Figure 7.17(a), however, the information is not interpretable now due to the lack of knowledge of F9 crystallography. By contrast, in Figure 7.18, electron ptychography does not provide obvious additional information compared to their relative HAADF-STEM images. The 0.38 nm repeat distance can be found in blue squares in both Figure 7.17(b) and 7.18(b). This repeat distance is consistent with the one discussed in Section 7.3.2. Furthermore, d-spacings at 0.20 (± 0.02) nm (the d-spacing in red in Figure 7.18(b)), 0.35 (± 0.03) nm (the d-spacing in green in Figure 7.17(b)), 0.37 (± 0.03) nm (the d-spacing in red in Figure 7.17(b)) and 0.50 (± 0.04) nm (the d-spacing in orange in Figure 7.17(b)) are also obtained. Compared to the HRTEM images in Section 6.3, d-spacings at 0.35, 0.37 and 0.50 nm are also found from the HRTEM.

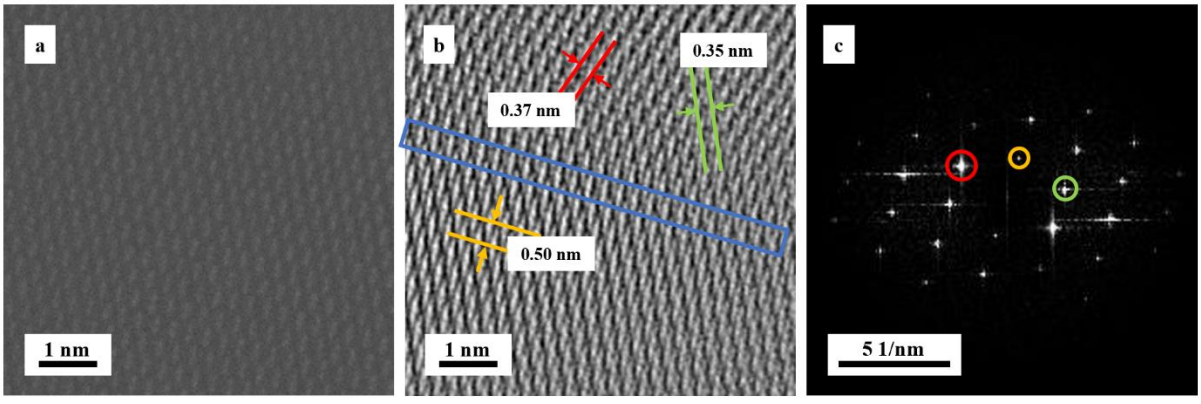


Figure 7.17 Electron microscopic images of F9 in an unassigned viewing direction. (a) HAADF-STEM image. (b) Simultaneous electron ptychography SSB phase image. (c) FFT of (b).

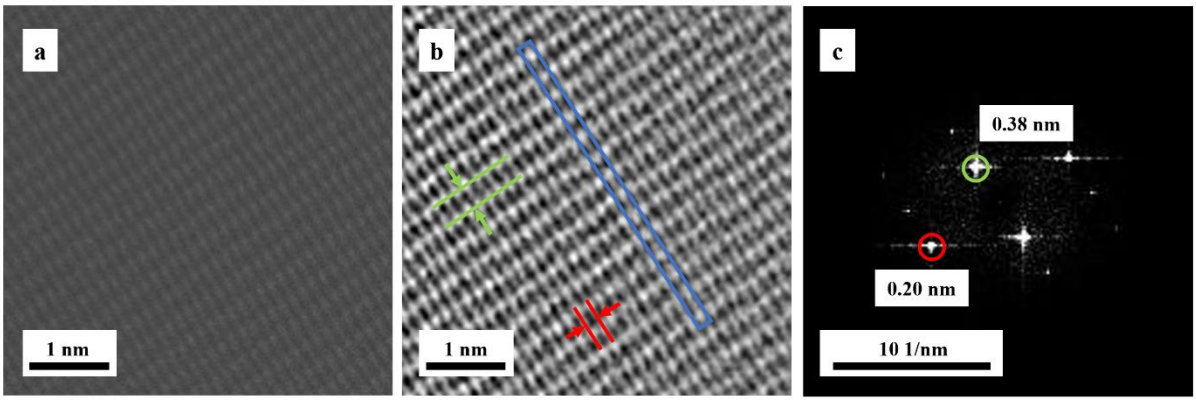


Figure 7.18 Electron microscopic images of F9 in an unassigned viewing direction. (a) HAADF-STEM image. (b) Simultaneous electron ptychography SSB phase image. (c) FFT of (b).

As for FP, the repeat distance at 0.34 (± 0.02) nm is also found in the HAADF-STEM and electron ptychographic images shown in the blue square in Figure 7.19(b). Because the included angle of two d-spacings at 90°, the corresponding d-spacing shares the same number. In addition, previously found in an FP HRTEM image, d-spacing at 0.25 (± 0.02) nm is also found in the FP HAADF-STEM and electron ptychographic images. More importantly, the electron ptychographic image (Figure 7.19(b)) is more informative than the HAADF-STEM shown in Figure 7.19(a). The use of electron ptychography reveals some features between the bright dots, and these features could be useful in understanding the FP crystal structure once the viewing direction of Figure 7.19 can be assigned.

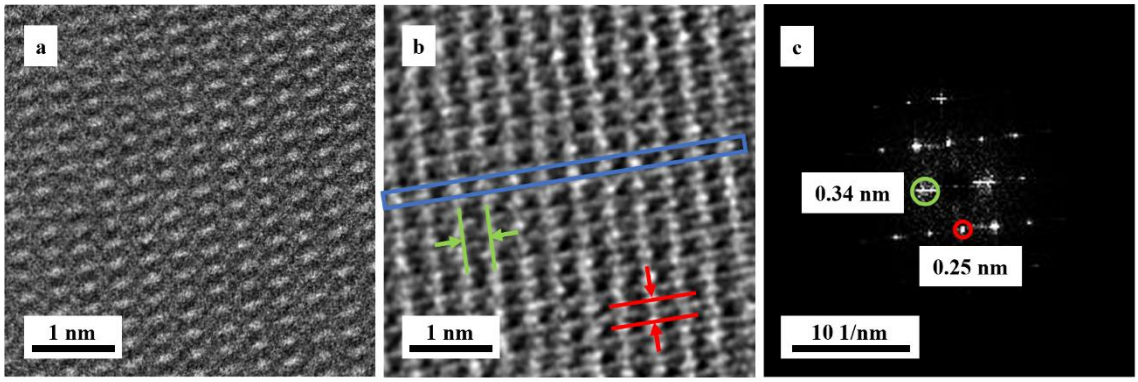


Figure 7.19 Electron microscopic images of FP in an unassigned viewing direction. (a) HAADF-STEM image. (b) Simultaneous electron ptychography SSB phase image. (c) FFT of (b).

Table 7.2 Summary of all d-spacings of F8, F9 and FP acquired from HAADF-STEM/electron ptychography. Numbers in red represent the d-spacings are also found using HRTEM.

Materials	D-spacings (nm)
F8	0.30, 0.32, 0.36, 0.46
F9	0.20, 0.35, 0.37, 0.46, 0.50
FP	0.25, 0.44, 0.46

All d-spacings of three PAs acquired from electron ptychography and HAADF-STEM are summarised in Table 7.2. The interpretation work of them will be resumed when the study of PA β-sheet crystals advances, for example from detailed molecular modelling.

7.5 Conclusions

In this chapter, electron ptychographic data with the simultaneous HAADF-STEM results are acquired to study the fine structures of PA β-sheet crystals. Firstly, it was confirmed that the mechanism of beam damage of PAs is amorphization, and the crystal information acquired here is not due to beam effects. By comparison, electron ptychography brings more detailed information than HAADF-STEM, and the reconstructed ptychographic image shows how PA β-sheet crystals order at the molecular scale. The electron ptychographic images clearly show the β-sheet d-spacings. This demonstrates the existence of β-sheet secondary structures, and for the first time, β-sheet structures are directly visualised using electron microscopy.

Furthermore, electron ptychographic images show a repeat distance around the length of the amino acid repeat unit at 0.35 nm. The repeat distance in the crystal is half of what previous work defined. By constructing brief crystal models of PAs, the repeat distance 0.35 nm can be attributed to the "sawtooth" structure stated in the discussion. Additionally, as no repeat distance representing 8 amino acids or 9 acid acids are acquired, it can be concluded that there is not a strong correlation of end groups, whether that be within or between PA β-sheets.

Differences in symmetry of microscopic images between different peptide molecules can be investigated. F9 has a greater repeat distance than F8 and FP. It can be inferred that the two positively charged side groups at the end of F9 molecules contribute to the stretch and the elongation possibly inter and intra molecular chains along the chain axis. The neighbouring groups or chains also stretch to accommodate this. As a result, the repeat distance for F9 is longer, but the exact manner of stretch or elongation is still unclear.

As for the angles shown in electron ptychographic images, the angles of F8 and F9 are not orthogonal, whereas that of FP is close to 90°. F8 and F9 symmetry can be linked to chain offsets. In FP, on the other hand, chain offsets may be less energetically favourable because its middle rings are likely to align alongside one another to reduce the energy cost. To avoid offsets, FP forms an approximate right angle.

Multilayer models are built to interpret contrast in electron ptychographic images using the chain-offset model and the self-assembling "sawtooth" structure. By superimposing the models on the electron ptychographic images, the symmetries and spacings of the models are found to match the microscopic images correctly, despite some minor and explainable discrepancies. However, as research into PA β-sheet crystals progresses, image simulations on these PAs will be required for a more precise understanding of F8, F9, and FP β-sheet crystals.

Finally, some additional d-spacings of the three PAs are found by using electron ptychography, and these d-spacings can be useful for the further investigation of their PA β-sheet crystals.

In summary, by using electron ptychography, it is possible to directly image the structure within PA β-sheet crystals, which has not previously been achieved by any conventional methods. And with the aid of broad models, the self-assembling “sawtooth” structure model is confirmed, as well as a lack of end group ordering in the crystals. Some rationale for the differences in angles and repeat distances, and contrasts presented in electron ptychographic images can be made, though these conclusions will need to be confirmed by further computational and simulation work. In general, this work brings a new understanding of PA β-sheet crystals, and it is meaningful to explore its applications in many new areas.

7.6 References

[1] Yeh, G. K., Sun, Q., Meneses, C., & Julian, R. R. (2009). Rapid peptide fragmentation without electrons, collisions, infrared radiation, or native chromophores. *Journal of the American Society for Mass Spectrometry*, *20*, 385-393.

[2] Sawyer, L., Grubb, D. T., & Meyers, G. F. (2008). *Polymer microscopy*. Springer Science & Business Media.

[3] Egerton, R. F. (2019). Radiation damage to organic and inorganic specimens in the TEM. *Micron*, *119*, 72-87.

[4] Rapaport, H., Kjaer, K., Jensen, T. R., Leiserowitz, L., & Tirrell, D. A. (2000). Two-dimensional order in β-sheet peptide monolayers. *Journal of the American Chemical Society*, *122*(50), 12523-12529.

[5] Isenberg, H., Kjaer, K., & Rapaport, H. (2006). Elasticity of crystalline β-sheet monolayers. *Journal of the American Chemical Society*, *128*(38), 12468-12472.

[6] Guenther, E. L., Cao, Q., Trinh, H., Lu, J., Sawaya, M. R., Cascio, D., Boyer, D. R., Rodriguez, J. A., Hughes, M. P., & Eisenberg, D. S. (2018). Atomic structures of TDP-43 LCD segments and insights into reversible or pathogenic aggregation. *Nature structural & molecular biology*, 25(6), 463-471.

[7] Löwik, D. W., & van Hest, J. C. (2004). Peptide based amphiphiles. *Chemical Society Reviews*, *33*(4), 234-245.

[8] Sievers, S. A., Karanicolas, J., Chang, H. W., Zhao, A., Jiang, L., Zirafi, O., Stevens, J. T., Münch, J., Baker, D., Eisenberg, D. (2011). Structure-based design of non-natural amino-acid inhibitors of amyloid fibril formation. *Nature*, 475(7354), 96-100.

[9] Cheng, Y., Koh, L. D., Li, D., Ji, B., Han, M. Y., & Zhang, Y. W. (2014). On the strength of β-sheet crystallites of Bombyx mori silk fibroin. *Journal of the Royal Society Interface*, *11*(96), 20140305.

[10] Krejchi, M. T., Cooper, S. J., Deguchi, Y., Atkins, E. D., Fournier, M. J., Mason, T. L., & Tirrell, D. A. (1997). Crystal structures of chain-folded antiparallel β-sheet assemblies from sequence-designed periodic polypeptides. *Macromolecules*, *30*(17), 5012-5024.

[11] Parkhe, A. D., Cooper, S. J., Atkins, E. D., Fournier, M. J., Mason, T. L., & Tirrell, D. A. (1998). Effect of local sequence inversions on the crystalline antiparallel β-sheet lamellar structures of periodic polypeptides: implications for chain-folding. *International journal of biological macromolecules*, *23*(4), 251-258.

[12] Zhang, S., Holmes, T., Lockshin, C., & Rich, A. (1993). Spontaneous assembly of a self-complementary oligopeptide to form a stable macroscopic membrane. *Proceedings of the National Academy of Sciences*, *90*(8), 3334-3338.

[13] Zhang, S., Lockshin, C., Cook, R., & Rich, A. (1994). Unusually stable β-sheet formation in an ionic self-complementary oligopeptide. *Biopolymers: Original Research on Biomolecules*, *34*(5), 663-672.

[14] Schmidt, M., Rohou, A., Lasker, K., Yadav, J. K., Schiene-Fischer, C., Fändrich, M., & Grigorieff, N. (2015). Peptide dimer structure in an Aβ (1–42) fibril visualized with cryo-EM. *Proceedings of the National Academy of Sciences*, *112*(38), 11858-11863.

Chapter 8. Electron Ptychographic Imaging of Polyvinyl Alcohol

8.1 Introduction

Chapter 6 reported that annealing could be used to make samples in which a single-PVA crystallite within the amorphous matrix could be observed within the field of view when imaging. d-spacings at 0.40 and 0.55 nm were acquired via HRTEM. Based on these findings, this chapter utilises the electron ptychography to image the two single-crystallite areas of sample described in Chapter 6 and compares the high-resolution images to the two existing PVA crystal models [1][2]. Image simulations are also performed to help understand the PVA crystal structure. Results in this chapter are expected to bring up a new and deeper understanding of PVA crystal structure.

8.2 Results

8.2.1 Beam Damage Study on Polyvinyl Alcohol

Similarly to the peptides discussed in Chapter 7, PVA is also a beam-sensitive material under electron irradiation, and this chapter first explores how electrons influence the crystal structure of PVA samples.

After excessive electron exposure of the PVA samples, evidence of beam damage can be seen. Figure 8.1 shows the second scan of a PVA sample image after the first scan in this area, with a slight movement of the sample. This movement introduced some fresh material on the left side of the image that had not previously been exposed to the electron beam. The dose applied in this fresh area is 2.9×10^4 (e-/Å^2). From the image, clear patterns were acquired on the left virgin side, while the right side that had previously been exposed has a reduced contrast. This image shows that on the PVA sample, the process of damage is likely to be amorphization. Besides, Figure 8.2 suggests that after a long period where the sample had been exposed to electrons, there was mass loss of PVA samples during the acquisition of electron ptychography and HAADF-STEM images. These results show that a limited dose and a relatively short acquisition time is important for the electron ptychographic study, and normally, the first-round acquisition is most likely to bring the clearest image of the area. This is also important because it means that the crystallinity is being seen is not due to beam effects.

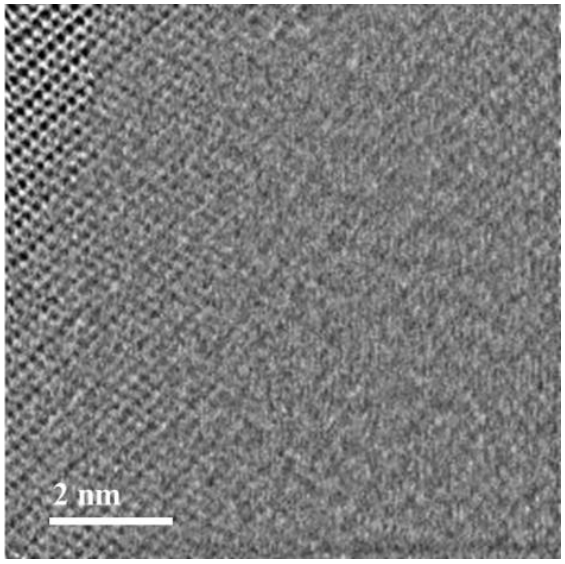


Figure 8.1 Second WDD acquisition with a slight sample move on the PVA sample.

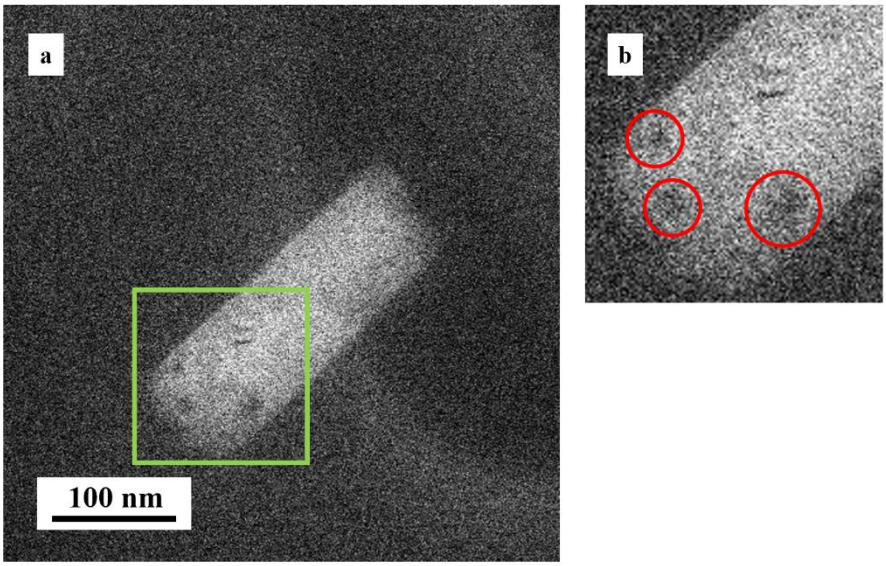


Figure 8.2 HAADF-STEM images of a PVA crystallite after HAADF-STEM and electron ptychography work. (a) A PVA crystallite. (b) Magnified image of the area in the green square in (a). Holes in red circles suggest mass loss of the sample after image acquisitions.

8.2.2 High-angle Annular Dark Field-Scanning Transmission Electron Microscopy and Electron Ptychography

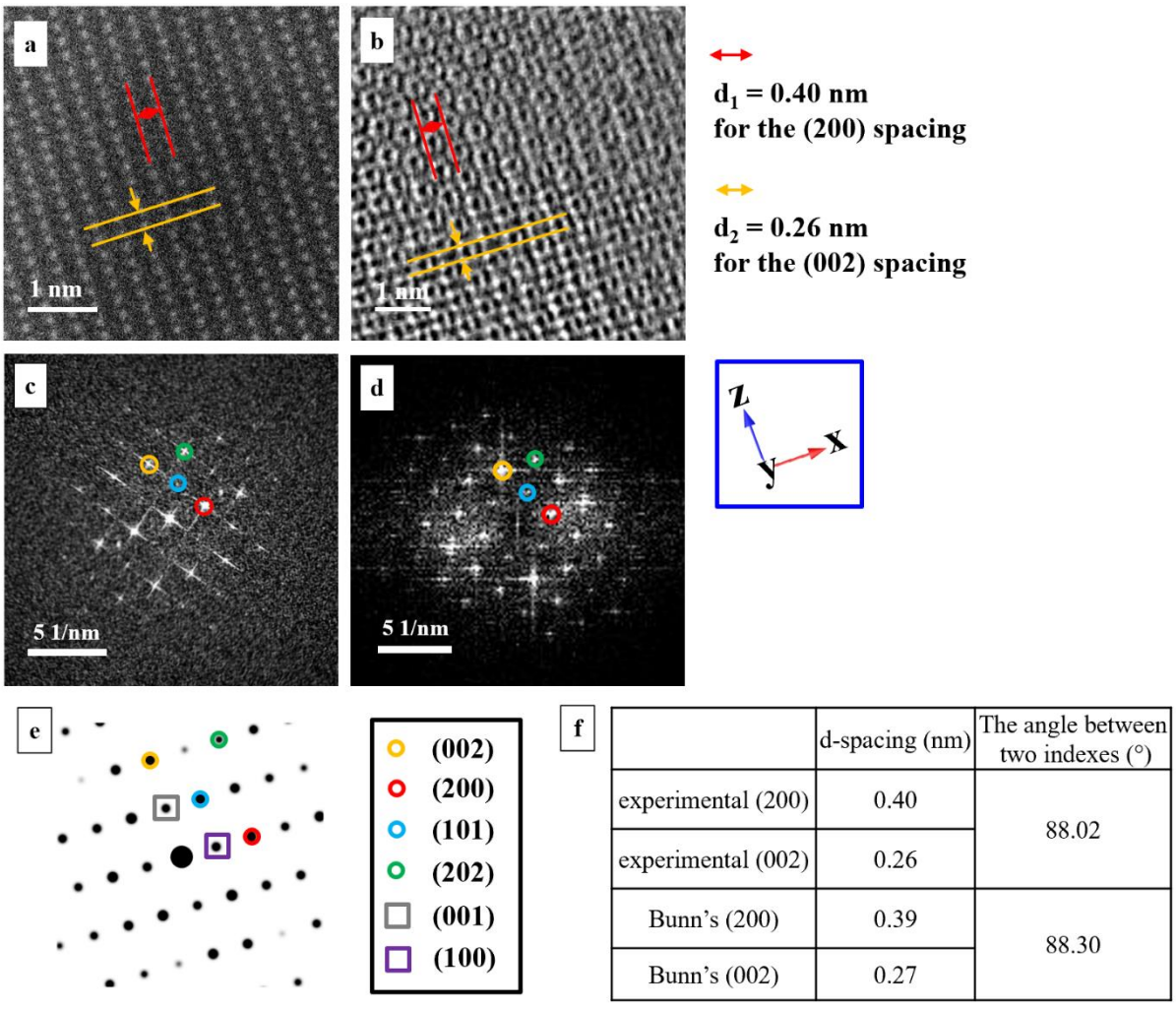
Following the HRTEM work presented in Section 6.2.3.1, the same crystallites of the PVA samples were imaged via electron ptychography and its simultaneous HAADF-STEM in this section.

The same area of the crystallite as the HRTEM image shown in Figure 6.5 was imaged. Collection angles for HAADF-STEM images are from 72 to 271 mrad. The dose here is 6.5×10^4 ($e^-/Å^2$), and no severe beam damage was found during the acquisition. The reconstructed WDD-phase image and the HAADF-STEM image are shown in Figures 8.3(b) and (a), respectively. The d-spacings acquired from Figures 8.3(b) and (a) are consistent with the ones obtained from the HRTEM image shown in Figure 6.5(a), and the d-spacings or the spots representing these d-spacings are marked in Figures 8.3(b), 8.3(a) and their FFT images of Figures 8.3(c) and 8.3(d). Their FFT images also have the same pattern of the FFT of its HRTEM image shown in Figure 6.5(b).

As shown in Figure 8.3, the two d-spacings acquired at 0.40 ± 0.02 nm and 0.26 ± 0.03 nm are close to theoretical d-spacings of the (200) and (002) planes of PVA at 0.39 nm and 0.27 nm. The view direction of the reciprocal lattice is normal to both plane vectors, thus the view direction vector is the cross product of the two plane vectors. Therefore, it can be calculated that the viewing direction of the above images should be [010]. To confirm this point, the single-crystal electron diffraction pattern of the [010] direction of Bunn's PVA model [1] (in Figure 8.3(e)) was also simulated by using the CrystalMaker®/SingleCrystal™ software [3].

All experimental-acquired and simulated d-spacings of the (200), (002), (101) and (202) planes are identified in FFT images as shown in Figures 8.3(c), (d) and (e). As concluded in Figure 8.3 (f), both d-spacings mentioned above and included angle acquired from electron

microscopic images accord with the simulated values of PVA in the [010] direction. This confirms that the images shown in Figure 8.3 were taken from the [010] direction. Comparing the HAADF-STEM and the electron ptychographic image, Figure 8.3(b) shows much more detail than Figure 8.3(a), and thus, electron ptychography brings more information on the structure, and the image shows how the atoms order in the material in the [010] viewing direction.



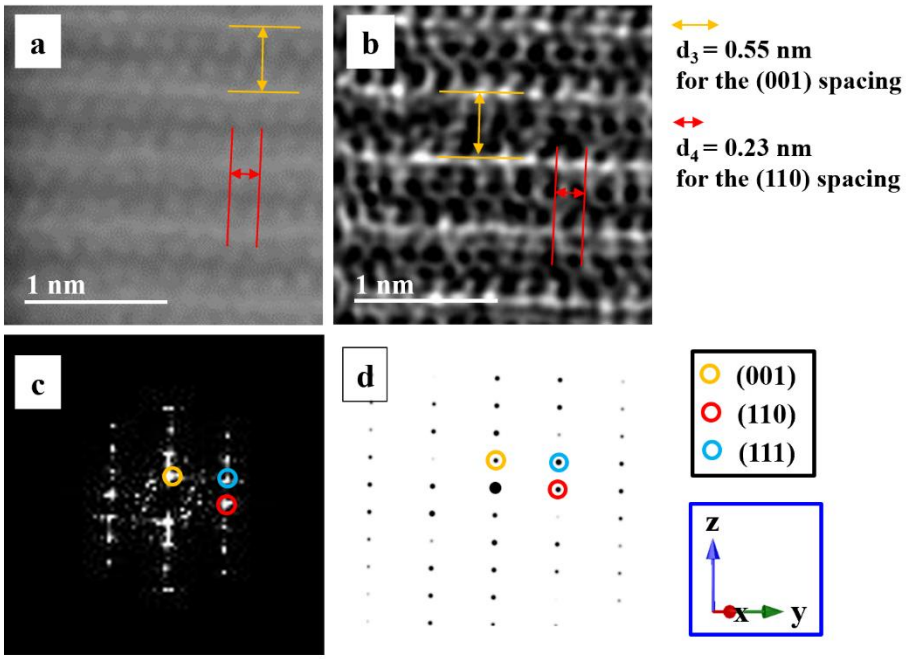
f

	d-spacing (nm)	The angle between two indexes (°)
experimental (200)	0.40	88.02
experimental (002)	0.26	
Bunn's (200)	0.39	88.30
Bunn's (002)	0.27	

Figure 8.3 Electron microscopic and simulated images of PVA orientated in the [010] viewing direction. (a) HAADF-STEM image. (b) Simultaneous electron ptychography WDD phase image. (c) FFT of (a). (d) FFT of (b). (e) Simulated single-crystal electron

diffraction pattern of Bunn's model. (f) Comparison between electron ptychographic data and Bunn's model.

Information from another viewing direction can facilitate understanding of the structure. As shown in Figure 8.4, another series of microscopic images are acquired via HAADF-STEM (Figure 8.4(a)) and electron ptychography (Figure 8.4(b)) from the same crystal imaged by HRTEM and previously shown in Figure 6.6. Collection angles for HAADF-STEM images are from 72 to 271 mrad. The dose here is 7.9×10^4 ($e^-/Å^2$), and no severe beam damage was found during the acquisition. From the images, two d-spacings at 0.55 ± 0.03 nm and 0.23 ± 0.03 nm can be found. Using the same method demonstrated in the last paragraph, it is concluded that [$\bar{1}$10] is the viewing direction here. As shown in Figure 8.4(e), comparing the FFT of the electron ptychographic image (Figure 8.4(c)) and simulated single-crystal electron diffraction pattern (Figure 8.4(d)), 0.55 ± 0.03 nm and 0.23 ± 0.03 nm correspond to the (001) (at 0.55 nm) and (110) (at 0.24 nm) d-spacings of PVA, and the viewing direction is indeed [$\bar{1}$10]. It should be noted that the (001) d-spacing was not observed in the [010] viewing direction (see Figure 8.3), and the reason for this will be discussed in Section 8.5.



e

	d-spacing (nm)	The angle between two indexes (°)
experimental (001)	0.55	91.80
experimental (110)	0.23	
Bunn's (001)	0.55	90.00
Bunn's (110)	0.24	

Figure 8.4 Electron microscopic images of PVA orientated in the [$\bar{1}$10] viewing direction. (a) HAADF-STEM image. (b) Simultaneous electron ptychography WDD phase image. (c) FFT of b. (d) Simulated single-crystal electron diffraction pattern of Bunn's model. (e) Comparison between experimental data and Bunn's model.

8.3 Discussion

8.3.1 d-spacings Acquired from Electron Ptychographic Images

All d-spacings acquired from XRD and electron ptychography are presented in Table 8.1. As shown in Figures 8.3(e), 8.4(e) and Table 8.1, although key spacings found in electron microscopic images are consistent with the XRD (Figure 6.4) and simulated results (Figures 8.3(d) and 8.4(d)), there are still some differences between them. Firstly, the d-spacings of (110) and (111) planes are not clearly found in the XRD data. This can be attributed to the low intensity and overlapping of the signals of the above-mentioned planes to the (202) plane, as their d-spacings and hence 2θ angle detected in XRD (Figure 6.4) are very close. Another important discrepancy is the absence in the [010] electron microscopic image of (100) (purple square in Figure 8.3(e)) and (001) (grey square in Figure 8.3(e)) planes observed in XRD and reproduced in the electron diffraction simulation from Bunn's model. In the simulated electron diffraction pattern, the (100) and (001) signals are relatively weak in the simulated results, which indicates the periodicities of (100) and (001) are weaker than those of (200) and (002). From Bunn's and Sakurada's models shown in Figure 2.5, it is expected to see the (100) and (001) reflexions as the intermediate molecules between these planes do not lie at precisely the half-way point nor in the same orientation. Therefore, the disappearance of (100) and (001) spacings in the microscopic images suggest some structural differences between the detected PVA crystal and old models. Particularly, experimental images suggest a higher symmetry of the structure with half the molecules lying at the midpoints of these planes (will be discussed in Section 8.5 with the aid of Figure 8.10) rendering them forbidden reflections, and this can eliminate the (100) and (001) signals [4][5]. At this stage, some modifications on Bunn's model are necessary to interpret the experimental data. The model modification process will be

introduced later, and then, the disappearance of (100) and (001) spacings will be further discussed with the aid of a new PVA model.

Table 8.1 Summary of d-spacings acquired from XRD, HAADF and electron ptychography.

XRD acquired		HAADF and electron ptychography acquired	
d-spacings (nm)	plane	d-spacings (nm)	plane
0.79	(1 0 0)	0.40	(2 0 0)
0.55	(0 0 1)	0.26	(0 0 2)
0.46	(1 0 $\bar{1}$)	0.45	(1 0 1) and/or (1 0 $\bar{1}$)
0.45	(1 0 1)	0.22	(2 0 2)
0.39	(2 0 0)	0.55	(0 0 1)
0.27	(0 0 2)	0.23	(1 1 0)
0.22	(2 0 2)	0.21	(1 1 1)

acquired from the [010] viewing direction

acquired from the [$\bar{1}$10] viewing direction

8.3.2 Patterns Acquired from the Electron Ptychographic Images

A comparison in terms of patterns between the electron ptychographic image and the previous models can be helpful to further investigate the discrepancy. Electron microscopic images can be regarded as a projection of the detected crystal in a certain direction, so the projections of Bunn's and Sakurada's models [1][2] in the [010] and [$\bar{1}$10] directions will be used for the comparison.

As shown in Figure 8.5, when superposing each of the two extant models on the electron ptychography image, no matter whether Bunn's model (in Figure 8.5(a)) or Sakurada's model (in Figure 8.5(b)) is used, only half of the spots in the electron ptychographic image match each of the two previous models. Considering that (100) and (001) are not present in the FFT of the [010] images, symmetrising the PVA model could be helpful to fit the experimental results. To

be specific, symmetrising means that the central group of atoms is moved to the centre of the blue parallelogram marked in Figure 8.5. The symmetrising step will also be conducted for the PVA model modification in Section 8.4.

Additionally, the presence of elongated features (which may indicate the ordering of oxygens) between the bright spots (which may indicate the ordering of carbons) suggests that the real PVA crystal is more complex than the old models suggest, particularly in terms of oxygen positions. As differences can be found in both microscopic images and FFT results, further modifications to the PVA model are required.

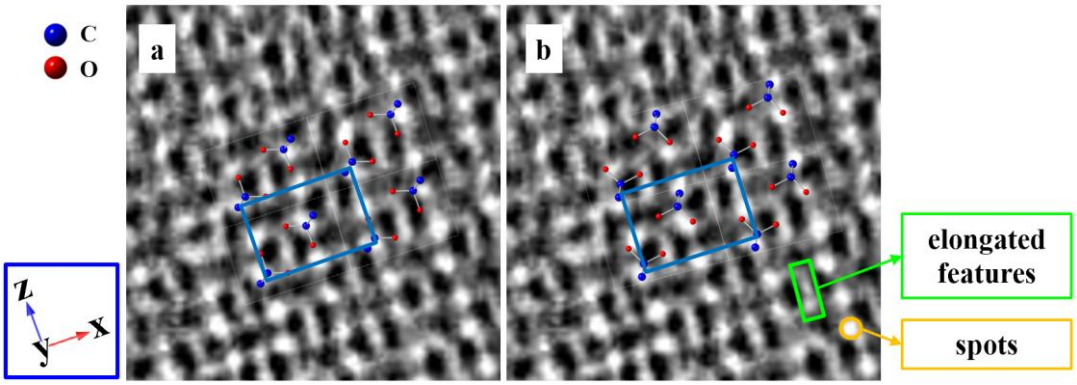


Figure 8.5 Enlarged WDD phase image superposed with previous models orientated in the [010] viewing direction. (a) WDD phase image with Bunn's model. (b) WDD phase image with Sakurada's model.

Similar to the images taken from the [010] viewing direction, electron ptychographic images in the [$\bar{1}$10] direction also bring more information on PVA than HAADF-STEM. To figure out how the atoms order in the viewing direction, previous models are superimposed onto the electron ptychographic image (shown in Figure 8.6). All oxygen sites in Figure 8.6 represent a half-occupancy of oxygen atoms. It can be found that the shapes of the original models look close to the image in the [$\bar{1}$10] viewing direction, but some differences are obvious between

the electron ptycgraphic image to two old models. Taking Bunn's model as the example, in the experimental image, there is a mid layer between two intense layers, but in Bunn's model (in Figure 8.6(a)), all layers (parallel carbon backbones with side oxygens) should have the same electron density, and hence the same contrast in the electron microscopic image. Turning to Sakurada's model, the distance between two adjacent chains in the model along the z axis is uneven, which is different from what the electron ptychography image suggests. Furthermore, all features presented in both models in the [$\bar{1}$10] viewing direction are periodic. By contrast, there is a certain amount of non-periodic structure observable in the electron ptychographic image as one passes along the chain axis. Therefore, a modification of the PVA crystal model based on images taken on [010] and [$\bar{1}$10] directions are required to fit the image well.

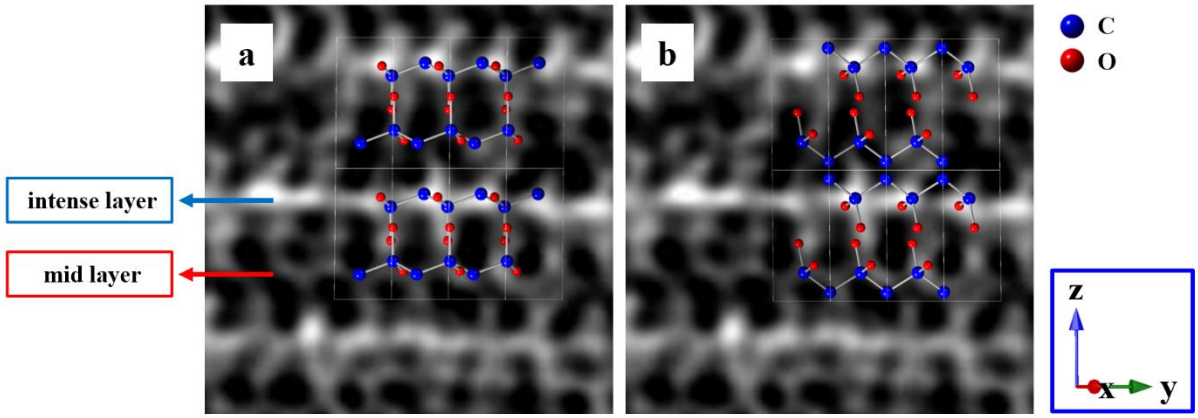


Figure 8.6 Enlarged WDD phase image superposed with previous model orientated in the [$\bar{1}$10] viewing direction. (a) WDD phase image with Bunn's model. (b) WDD phase image with Sakurada's model.

8.4 PVA Model Modification

Given the observed difference between the XRD data and the FFT of the images, and between the experimental images and previous XRD-derived models, a new description of the PVA structure is proposed here which takes into account the possibility that the backbone of the molecule may rotate and shift, allowing for intermolecular H-bonding in many different directions. This may not be the thermodynamically minimum energy structure, but as the crystals form, the more disordered structure may be locked in. The energetics of the local backbone twisting that would be required for such a rotation or a shift has not been modelled here, but rather the consistency of this model with the observed imaging has been considered.

The whole model modification process as observed in the [010] viewing direction is schematically illustrated in Figure 8.7. Based initially on Sakurada's model, the model modification starts by rotating each molecule around the [010] (molecular) axis in 90° steps and then superimposing them on one another along the y (molecular) axis. This step reasonably gives explorable configurations of hydrogen bonding, appealing to the difference between Bunn and Sakurada's models. No account is made here of the connectivity of C-atoms between one rotation and the next, and the positions shown are only approximate. As shown in Figure 8.7(a), "star" groups are produced after step 1. Note that the carbon (and oxygen) atoms shown in this viewing direction show the possible locations of carbon (and oxygen), they do not represent the position of atoms in every unit cell repeat. From the [001] viewing direction shown in Figure 8.7(b), the superimposed model can be understood better. Herein, layer A refers to the original form (it will be marked as 0° in the following), and layer B was generated by rotating 90° clockwise around the [010] (molecular) axis from A (it will be marked as 90° in the following). In the same manner, layer C (180° rotated clockwise from A) and layer D

(270° rotated clockwise from A) can be also developed. After superimposing 0° (A), 90° (B), 180° (C) and 270° (D) along the molecular axis, two "stars" can be viewed from the [010] viewing direction in a PVA crystal unit cell. The rotation angle in this step is close to the PVA unit cell parameter β (91.7 ° in Bunn's model and 87.0 ° in Sakurada's model), which means rotating does not change the crystal structure but just forms different projected patterns (the [010] and [$\bar{1}$10] projected patterns based on the new model are shown in Figures 8.8(c) and 8.9(c) respectively) from the original formation.

After that, step 2, symmetrising, means the central star-shape group of atoms is moved to the centre of the orange parallelogram marked in Figure 8.7(a). The motivation here is to match the experimental data better, and the symmetry would eliminate signals from (100) and (001) planes in the microscopic images by making the associated diffraction reflections forbidden [4][5].

Next, a shift of the whole package of ABCD is operated in Procedure 3 (in Figure 8.7(b)) to half a unit cell along the x axis, then the shifted two stars are rotated 45° clockwise, such that adjacent oxygens face one another to form intermolecular hydrogen bonds. This is done to achieve the spacing of intensities observed in the experimental images. This shift could represent a 'kink' in the chain for example, and once again it represents the possible occupancy of spaces, which when viewed in projection through many unit cells in the microscopy image, will appear as overlapping locations. To distinguish these from the original ABCD layers, here the shifted layers are indicated by A'B'C'D'. The shifted and rotated unit cell is shown in Figure 8.7(b) after Procedure 3. From the [010] viewing direction shown in Figure 8.7(a), four "stars" including two "stars" marked in orange squares from the new layers can be viewed in the middle PVA unit cell. The modification of PVA crystal is now completed, and the whole

process is due to the flexibility of polymer backbones and the influence of hydrogen bonding, and this new structure can make the PVA crystal that forms.

Some additional notes can be made in this part. First, it was clear from the electron ptychographic image taken in the [010] viewing direction, including the elongated features between bright spots (as shown in Figure 8.7(b)), the positions of oxygens are varied arising from various directions of hydrogen bonding, the new model represents the average positions of the atoms in the PVA crystals. Secondly, the 8-layer structure shown in Figure 8.7(b) can be periodic like ABCDA'B'C'D' or more likely random like ACDBB'A'C'D', AACDB'C'C'D' *etc.*, in practice.

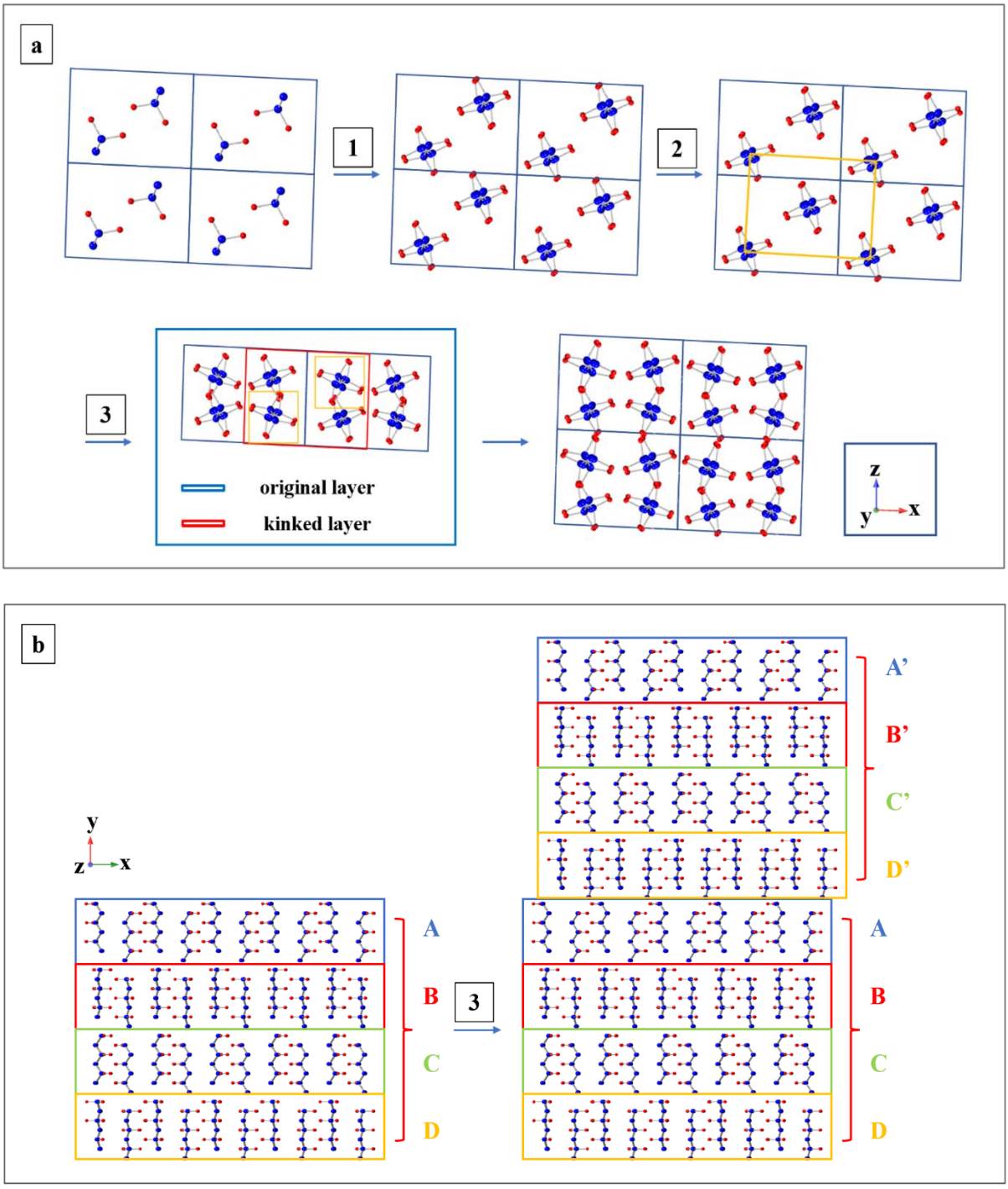


Figure 8.7 Schematic illustration of the model modification process as observed in the [010] viewing direction (all oxygen sites represent half the occupancy of oxygen atoms). (a) The whole process of PVA model modification includes three steps. Note that the carbon (and oxygen) atoms shown in this viewing direction show the possible locations of carbon (and oxygen) they do not represent the position of atoms in every unit cell repeat.

However, all such locations will be represented in the projection of many unit cells along this axis. (b) Explanation of the third step, viewing from the [001] direction.

8.5 Image Simulation

The multislice method [6] enables the simulation of STEM and electron ptychographic images of structural models, and here the multislice method was used to simulate the images based on the new PVA model. Figure 8.8 shows the experimental data, the new crystal model, and the simulated images of the PVA new model as observed in the [010] viewing direction. Simulation results have the same spacings and patterns and contrasts show good agreement with the experimental data, where HAADF images show the orderings of carbon backbones, while electron ptychographic images provide additional information about oxygen positions. This supports the methods used to modify the PVA model.

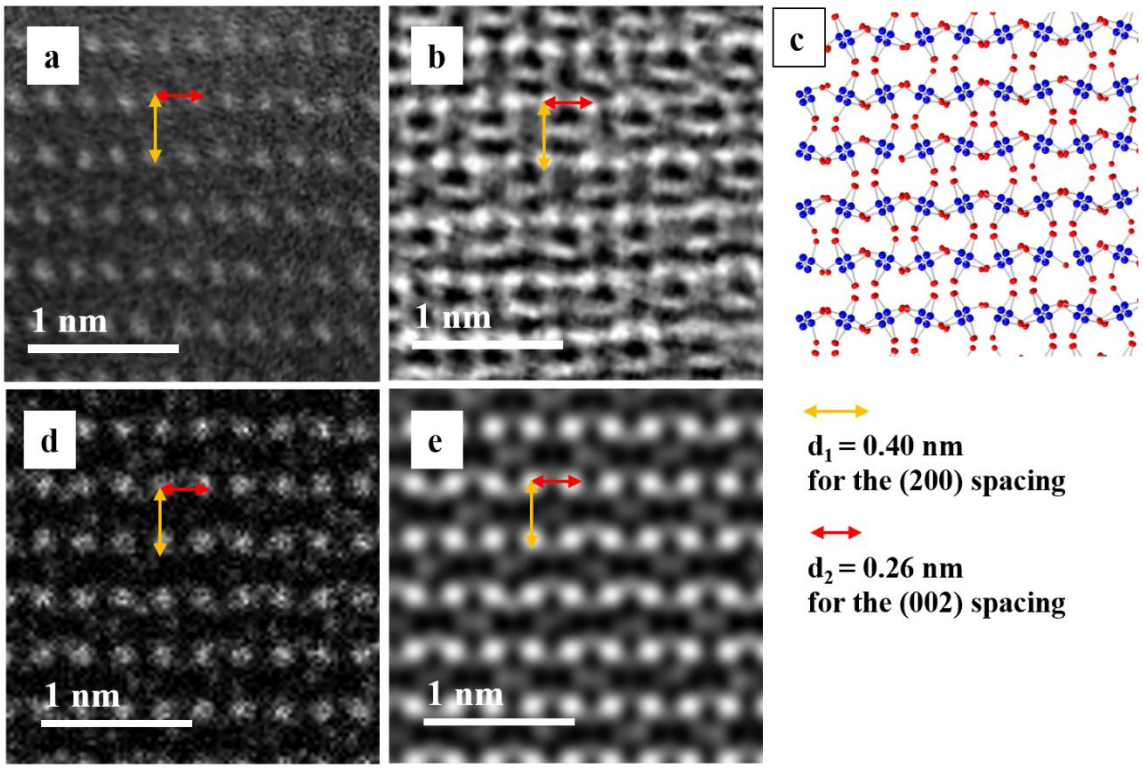


Figure 8.8 Experimental and simulated images of PVA in the [010] viewing direction. (a) Experimental HAADF-STEM image. (b) Experimental electron ptychography WDD

phase image. (c) The modified PVA structure by the method elaborated in Figure 8.7 (all oxygen sites represent half the occupancy of oxygen atoms). (d) Simulated flat HAADF image. (e) Simulated electron ptychographic WDD-phase image.

As for the [$\bar{1}$10] viewing direction, d-spacings are the same in the experimental and simulated results. As shown in Figure 8.9, electron ptychography reasonably closely reproduces the results, although the precise details in the HAADF images are not precisely reproduced. The new model still works on this direction as the symmetry and the periodicity are the same in both sides, but the differences in the details likely arise from the high randomness of the oxygen atoms' locations, depending on their local environment. Future studies on the PVA microstructure can further tune some details.

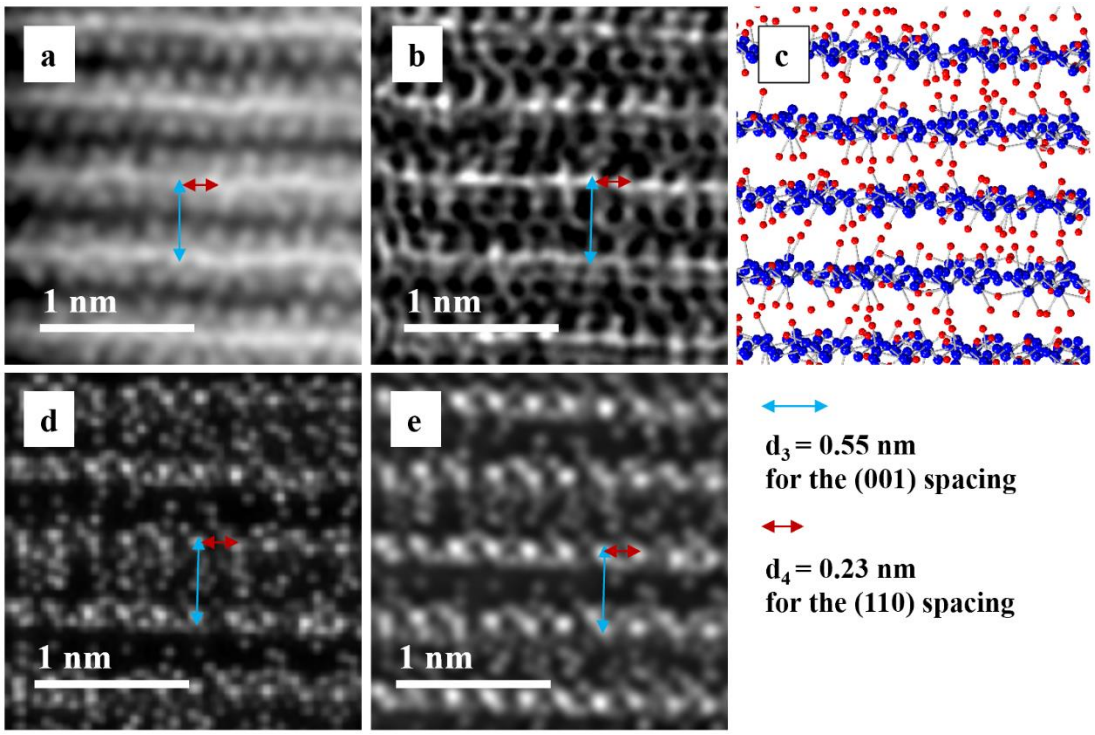


Figure 8.9 Experimental and simulated images of PVA in the [$\bar{1}$10] viewing direction. (a) Experimental HAADF image. (b) Experimental electron ptychography WDD phase image. (c) The modified PVA structure by the method elaborated in Figure 8.7 (all oxygen

sites represent half the occupancy of oxygen atoms). (d) Simulated flat HAADF image. (e) Simulated electron ptychographic WDD-phase image.

As the new model is supported by simulation data along both experimentally determined viewing directions, the model can now be used to illustrate the remaining question as to why the (001) and (100) disappeared from the FFT images viewed from the [010] direction. To answer this question, the difference between XRD and the FFT of images should firstly be discussed. The XRD intensity arises from the overall information of all the local interplanar spacings in the structure. In contrast, the microscopic imaging gives the average positions of the atoms projected through the whole thickness of the image (depth of focus).

Here, Figure 8.10 is utilised to explain this further. For both extant models, as indicated by green arrows in Figure 8.10(a), and blue arrows in Figure 8.10(b), the distances between the backbones can be different. Furthermore, in all cases, the positions of the oxygen atoms with respect to the backbone are different. So locally, driven by the rotation of backbones and the randomness of the hydrogen bonding directions, the (001) and (100) d-spacings can lead to diffraction because the other molecules are not exactly at these plane midpoints, and the intensities can be captured by XRD. If the chain can randomly reorientate along the chain axis as suggested in Section 8.4, the structure can move between Bunn-like and Sakurada-like models. Therefore, the projected average atomic positions will be the average of Bunn's and Sakurada's models. With the averaging, the projected atomic positions on average are more symmetric, and hence, the (100) and (001) d-spacings disappear from the FFT.

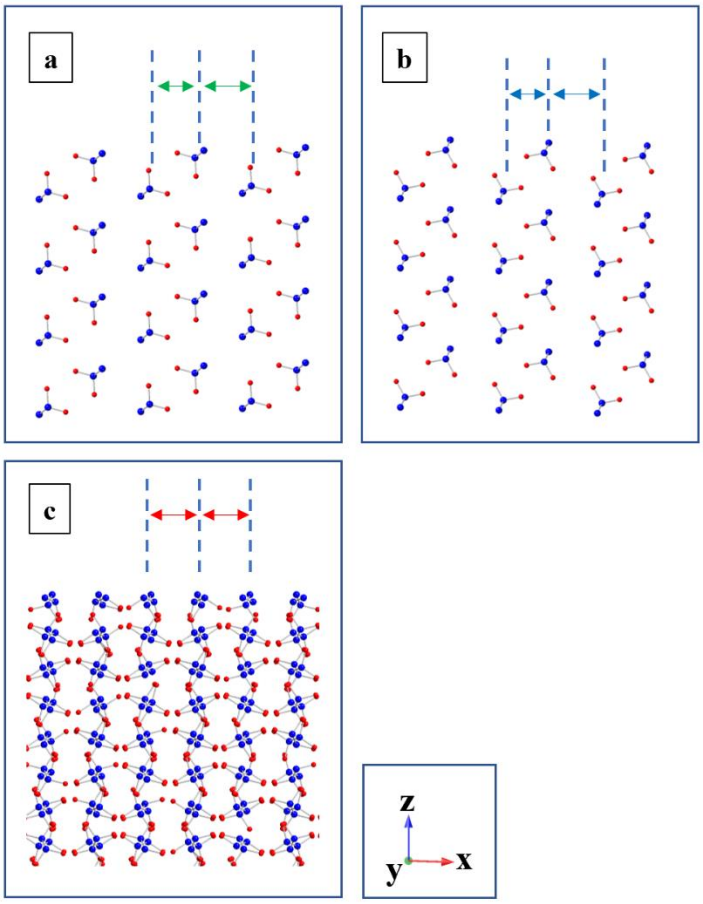


Figure 8.10 PVA model models viewed from the [010] direction (all oxygen sites represent half the occupancy of oxygen atoms). (a) Bunn's model. (b) Sakurada's model. (c) The modified PVA structure by the method elaborated in Figure 8.7.

This example illustrates an important difference between a diffraction pattern and the FFT of a projected image in the case when there is randomness in the structure. The diffraction pattern reflects the average of the periodicity and symmetry of the local interactions, whereas the FFT of the projected image reflects the periodicity of the average positions of the atoms.

8.6 Conclusions

In this chapter, electron ptychographic data with the simultaneous HAADF-STEM results are acquired to study the PVA crystal. Firstly, the mechanism of beam damage of PVA is amorphization, and the crystal information acquired is not due to beam effects. In the [010] viewing direction, the same d-spacings got from HRTEM are detected in both HAADF-STEM and electron ptychographic images, but the spacings for the (100) and (001) planes are still missing. By comparison, electron ptychography brings more information than HAADF-STEM, and the reconstructed ptychographic image shows how the atoms order in the PVA. The ptychographic image shows some agreements with previous models, but deviations from previous models derived from X-ray diffraction are also observed.

Besides [010], images were also acquired along the [$\bar{1}$10] viewing direction. Two d-spacings at 0.55 nm and 0.23 nm can be found, and the simulated single-crystal electron diffraction pattern supports that they are the spacings for the (001) and (110) planes of PVA. Similarly to the [010] direction, electron ptychography also brings a clearer and more informative image than HAADF-STEM. However, both similarities and discrepancies are also found in the direction between the old models and the experimental results. Therefore, [$\bar{1}$10] projections were utilised to tune the PVA crystal model.

Without changing unit cell dimensions, the model modification process is composed of rotating, symmetrising and shifting. Finally, a multilayer PVA crystal model is constructed. The modification process is driven by the flexibility of polymer backbones and the randomness of hydrogen bonding directions. The symmetries of the new PVA model viewed from both directions are the same as their experimental images.

To further interpret the data, image simulations on the new model were performed. The multislice simulation results essentially accord with the experimental data, which supports the hypothesis to modify the model. Finally, the extinction of the (100) and (001) spacings in the [010] viewing direction can be attributed to symmetry of the new model, where the symmetrising step introduced in Section 8.4 leads to the extinction. The projected average atomic positions of the new model can therefore be the average of Bunn's and Sakurada's models. As the FFT of the projected image reflects the periodicity of the average positions of the atoms, the (100) and (001) d-spacings disappear from the FFT. However, XRD reflects the average of the periodicity and symmetry of the local interactions. The rotation of backbones and the randomness of the hydrogen bonding directions give rise to diffractions of the (001) and (100) d-spacings, and their intensities can be captured by XRD.

In summary, by using electron ptychography, the PVA crystal structure could be directly imaged, which has not previously been achieved by any conventional methods. And with the aid of model modification and image simulation, the results bring a new and deeper understanding of the PVA crystal structure. This suggests that the molecular configurations locked into the crystal are far more variable than suggested by the previous models. This can be achieved as there are multiple possible inter- and intramolecular hydrogen bonding directions depending on the nearest neighbour oxygen positions. This methodology can be expanded to other polymeric systems for better microstructural insights.

8.7 References

[1] Bunn, C. W. (1948). Crystal structure of polyvinyl alcohol. *Nature*, *161*(4102), 929-930.

[2] Sakurada, I., Fuchino, K., & Okada, N. (1950). Crystal structure of polyvinyl alcohol. *Bull. Inst. Chem. Res., Kyoto Univ.*, 1950, 23, 78-79.

[3] Palmer, D. C. (2015). Visualization and analysis of crystal structures using CrystalMaker software. *Zeitschrift für Kristallographie-Crystalline Materials*, *230*(9-10), 559-572.

[4] Carra, P., & Thole, B. T. (1994). Anisotropic x-ray anomalous diffraction and forbidden reflections. *Reviews of Modern Physics*, 66(4), 1509.

[5] Dmitrienko, V. E. (1983). Forbidden reflections due to anisotropic X-ray susceptibility of crystals. *Acta Crystallographica Section A: Foundations of Crystallography*, 39(1), 29-35.

[6] Cowley, J. M., & Moodie, A. F. (1957). The scattering of electrons by atoms and crystals. I. A new theoretical approach. *Acta Crystallographica*, *10*(10), 609-619.

Chapter 9. General Conclusions and Future Work

As a new powerful microscopic technique, electron ptychography is used for imaging PVA and self-assembling PA β-sheet systems in this thesis.

For self-assembling PA β-sheet systems, the morphologies of PA fibres were firstly studied. It is found that width and density of F8, F9 and FP fibres and networks follow the same trend with the change of pH and peptide concentration. To be specific, fibres are the widest but loosest at their relevant isoelectric points. Peptide fibres become denser as peptide concentration rises, but there is no discernible change in peptide width. In addition, F8 and F9 can form relatively straight fibres, whereas FP can form twisting fibres. F9 has the widest and densest fibres at their own isoelectric points with the same peptide concentration. These findings show how pH, concentration and peptide sequence influence morphologies of peptides as observed in this thesis. However, unexpectedly, results in this thesis suggest peptide morphology does not have a strong correlation to PA crystals, and peptide fibres can be driven by free energy rather than crystallisation *per se*.

At this stage, freeze-thawing was used to make more crystalline samples for the electron ptychographic study. The effect of freeze-thawing and secondary structures of PA samples were then confirmed by FTIR, XRD and HRTEM. Finally, electron ptychographic images brought a fresh understanding of F8, F9 and FP crystals. According to these images, the "sawtooth" structure firstly was confirmed from the repeat distance at 0.35 nm. Then, the periodicity from images also indicates PA β-sheet strands ends randomly along the molecular chain axis. From the images, there is a difference of symmetry between FP patterns to F8/F9 patterns. This can be attributed to molecular offsets of F8 and F9, whereas in FP such chain

offsets are less energetically favourable due to the presence of the proline units. Some possible models to interpret the contrasts and patterns of PA images were also proposed.

Turning to PVA, freeze-thawing and annealing were firstly each applied to make a more crystalline sample. Annealing was then proven by XRD and HRTEM to be an appropriate way to prepare crystalline PVA samples. Some characteristic spacings related to the [010] and [$\bar{1}$10] directions were found in HRTEM images. Electron ptychography was then used for studying the crystals viewed from each of these two directions. Although key d-spacings and angles were matched, there are discrepancies between the images and each of the two old models. Model modifications of the PVA crystal were then conducted based on electron ptychographic data, and image simulation results support the new PVA model. From above results, it is found that hydrogen bonding and polymeric bonds of PVA have more randomness than the old models expected.

Overall, electron ptychography contributes to new understandings of PVA and PA β-sheet crystals. Based on results from this thesis, future work is suggested to focus on the following areas. For the PA systems, salts can be introduced to the system for a better self-assembling ordering. However, whether salts would drastically change the original self-assembling crystals need to be further studied. Also, α-helix crystals can be studied using electron ptychography. Especially, electron ptychography can be helpful to study molecular changes during the α-helix-β-sheet (α-β) transition. Turning to PVA, besides annealed PVA, commercial PVA products, including PVA packing materials and freeze-thawed PVA hydrogels can be also investigated using electron ptychography. Better understandings of these products may contribute to the improvement of their properties and the reduction in their prices. To

summarise, the methodology used in this thesis can potentially be expanded to other polymeric and macromolecular systems for studying their precise crystal structures.

Appendix

A.1 Line Profiles of High-resolution Transmission Electron Microscopy Images

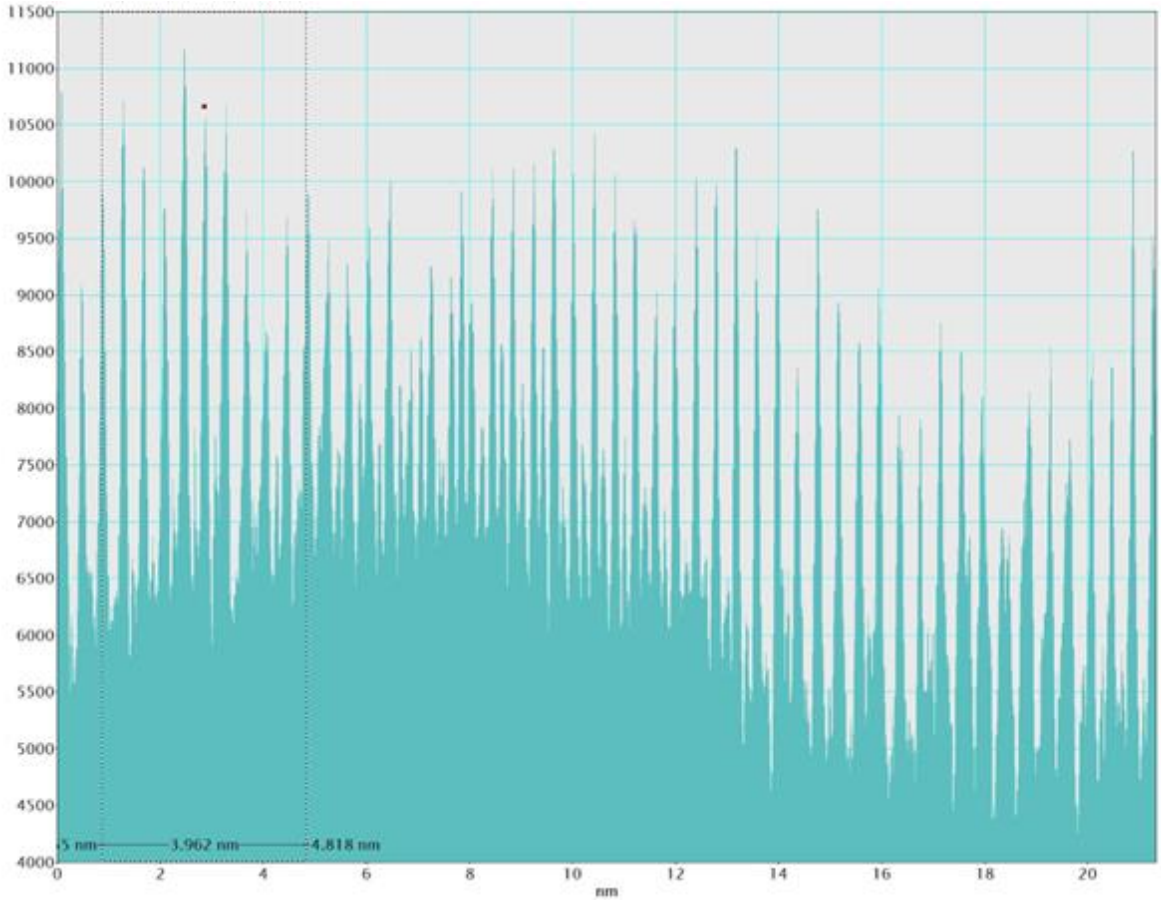


Figure A.1 Line profile of the d-spacing marked in Figure 6.5(a).

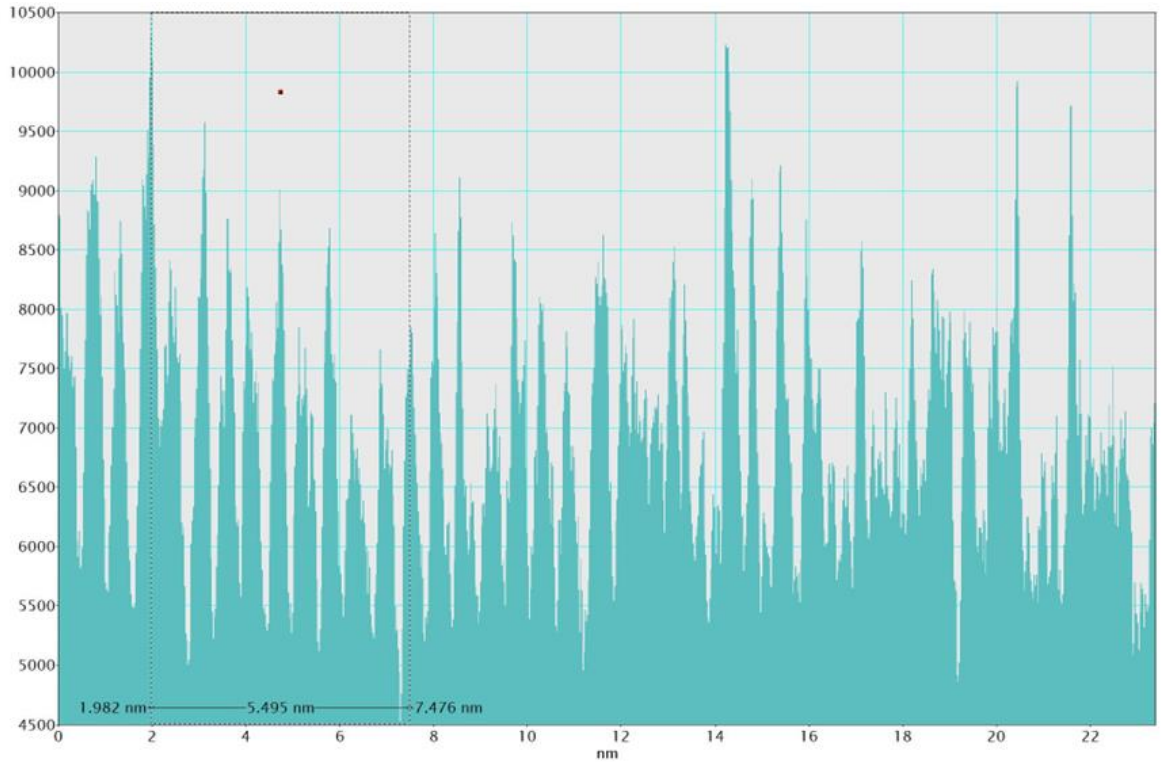
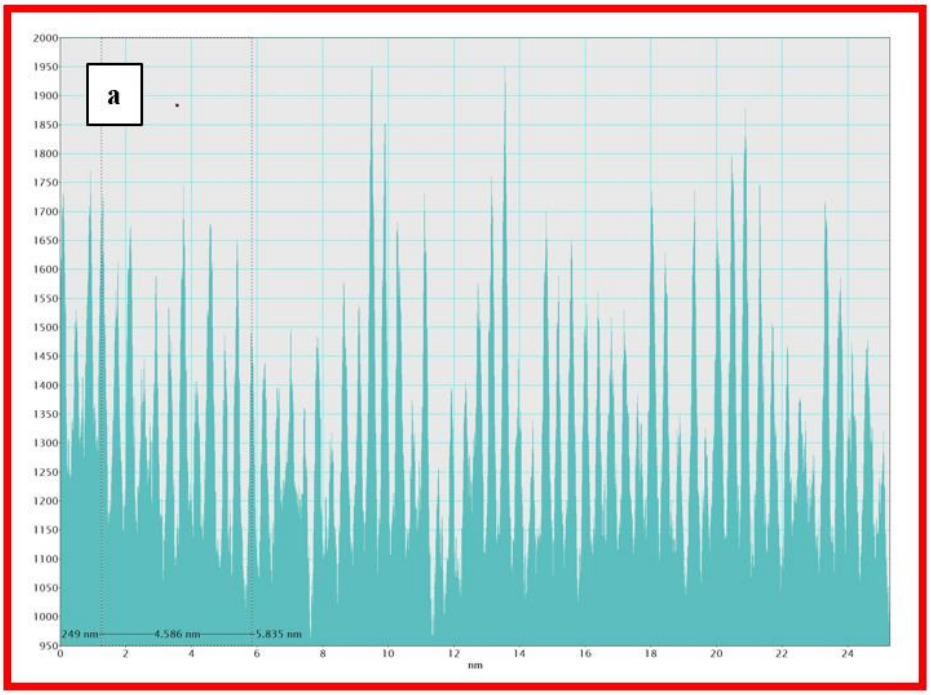
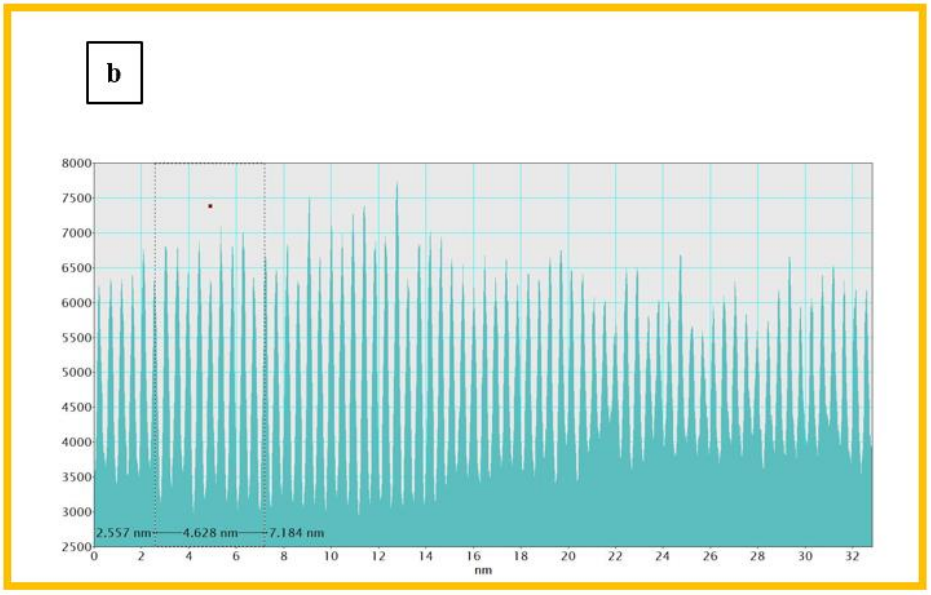


Figure A.2 Line profile of the d-spacing marked in Figure 6.6(a).


a
2000
1950
1900
1850
1800
1750
1700
1650
1600
1550
1500
1450
1400
1350
1300
1250
1200
1150
1100
1050
1000
950
249 nm
4.586 nm
5.835 nm
0
2
4
6
8
10
12
14
16
18
20
22
24
nm


b
8000
7500
7000
6500
6000
5500
5000
4500
4000
3500
3000
2500
2.557 nm
4.628 nm
7.184 nm
0
2
4
6
8
10
12
14
16
18
20
22
24
26
28
30
32
nm

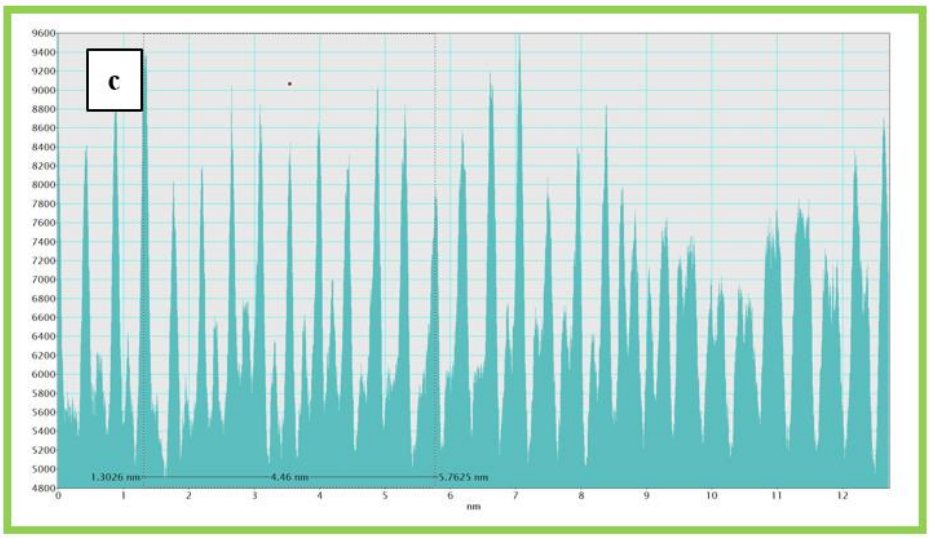

c
9600
9400
9200
9000
8800
8600
8400
8200
8000
7800
7600
7400
7200
7000
6800
6600
6400
6200
6000
5800
5600
5400
5200
5000
4800
1.3026 nm
4.46 nm
5.7625 nm
0
1
2
3
4
5
6
7
8
9
10
11
12
nm

Figure A.3 Line profiles of d-spacings marked in Figure 6.7. (a) Line profile of the d-spacing marked in Figure 6.7(a). (b) Line profile of the d-spacing marked in Figure 6.7(b). (c) Line profile of the d-spacing marked in Figure 6.7(c).

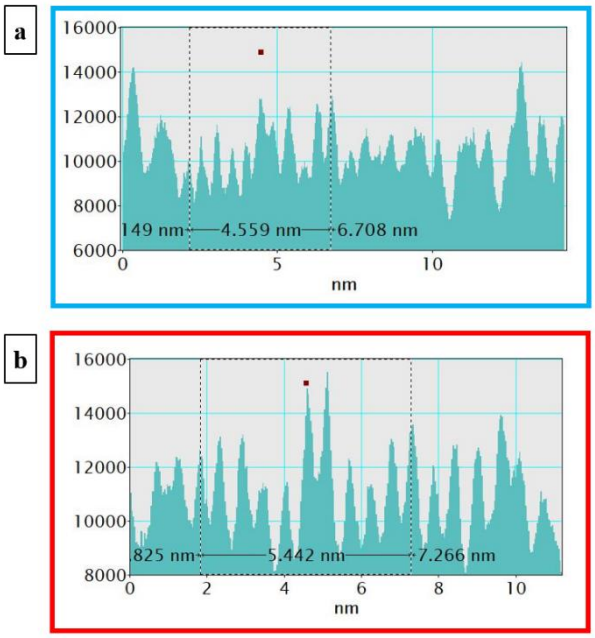


Figure A.4 Line profiles of d-spacings marked in Figure 6.8. (a) Line profile of the d-spacing marked in Figure 6.8(a). (b) Line profile of the d-spacing marked in Figure 6.8(b).

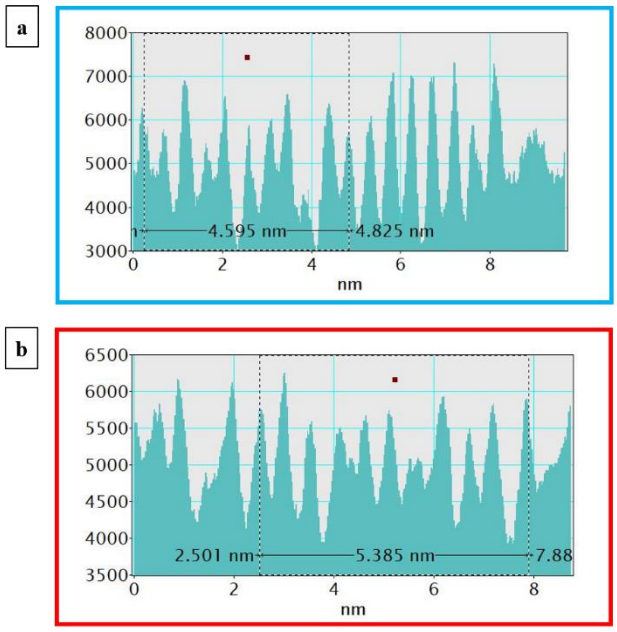


Figure A.5 Line profiles of d-spacings marked in Figure 6.9. (a) Line profile of the d-spacing marked in Figure 6.9(a). (b) Line profile of the d-spacing marked in Figure 6.9(b).

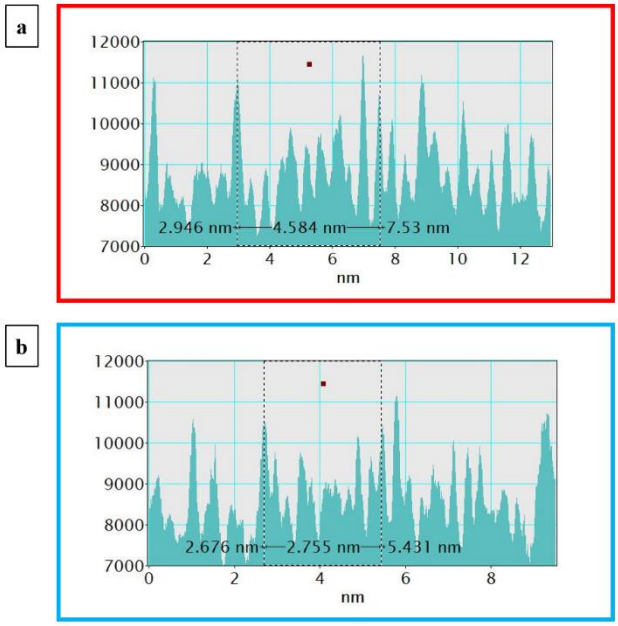


Figure A.6 Line profiles of d-spacings marked in Figure 6.10. (a) Line profile of the d-spacing marked in Figure 6.10(a). (b) Line profile of the d-spacing marked in Figure 6.10(b).

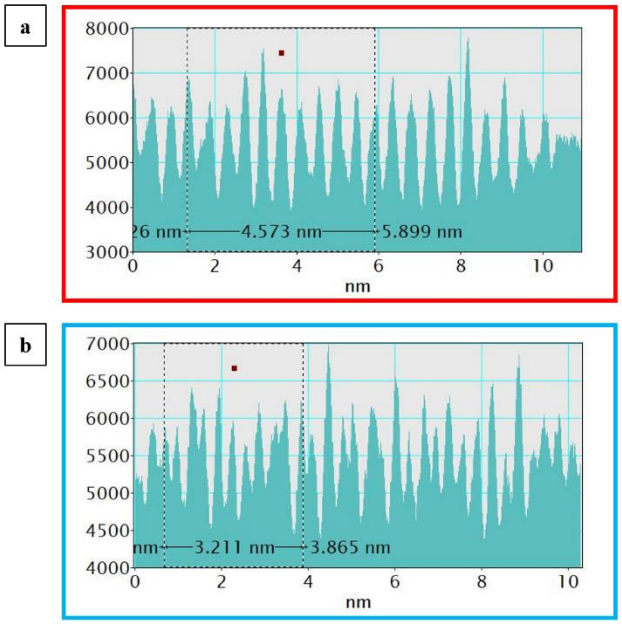


Figure A.7 Line profiles of d-spacings marked in Figure 6.11. (a) Line profile of the d-spacing marked in Figure 6.11(a). (b) Line profile of the d-spacing marked in Figure 6.11(b).

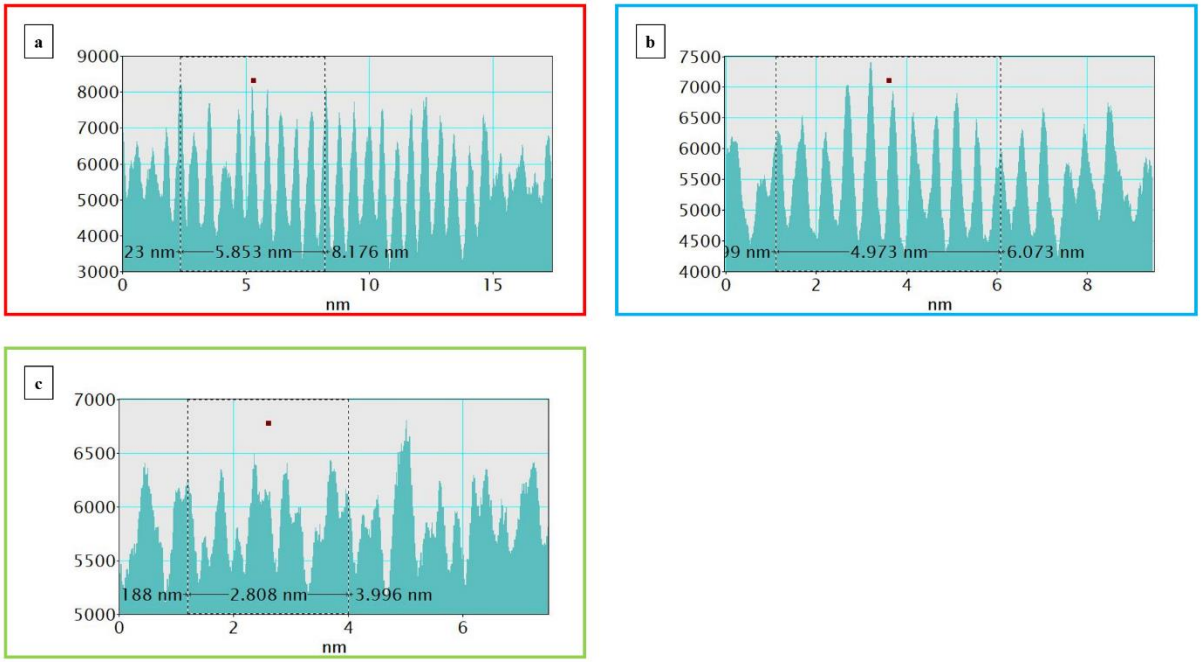


Figure A.8 Line profiles of d-spacings marked in Figure 6.12. (a) Line profile of the d-spacing marked in Figure 6.12(a). (b) Line profile of the d-spacing marked in Figure 6.12(b). (c) Line profile of the d-spacing marked in Figure 6.12(c).

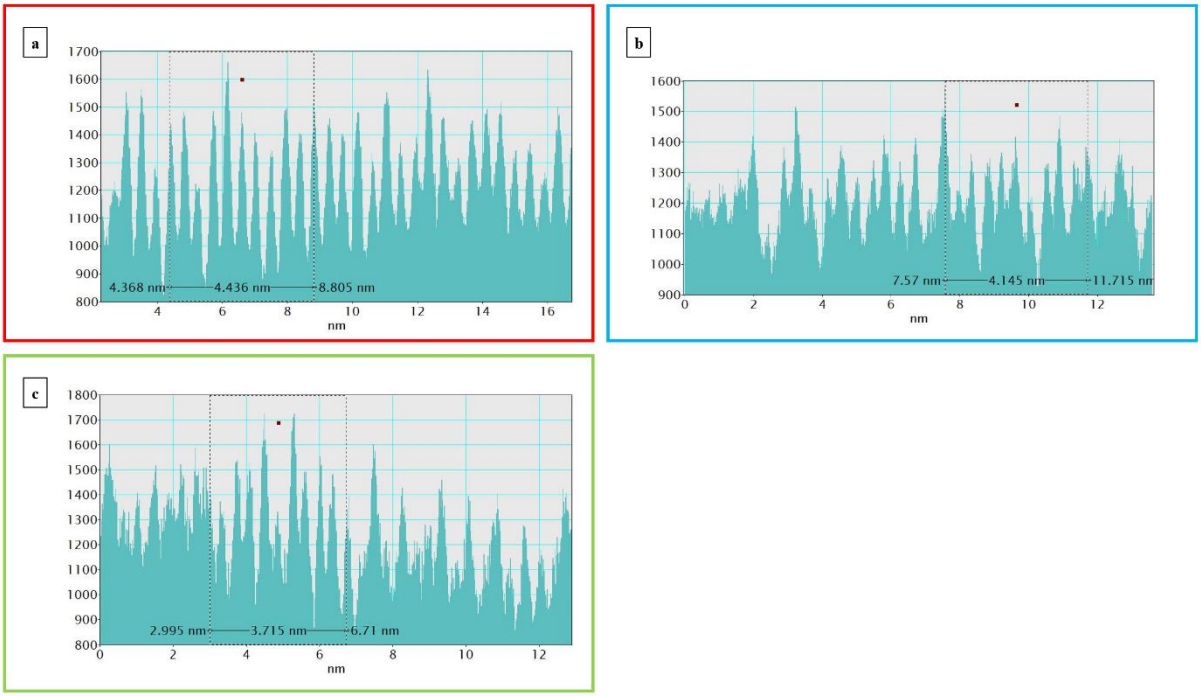


Figure A.9 Line profiles of d-spacings marked in Figure 6.13. (a) Line profile of the d-spacing marked in Figure 6.13(a). (b) Line profile of the d-spacing marked in Figure 6.13(b). (c) Line profile of the d-spacing marked in Figure 6.13(c).

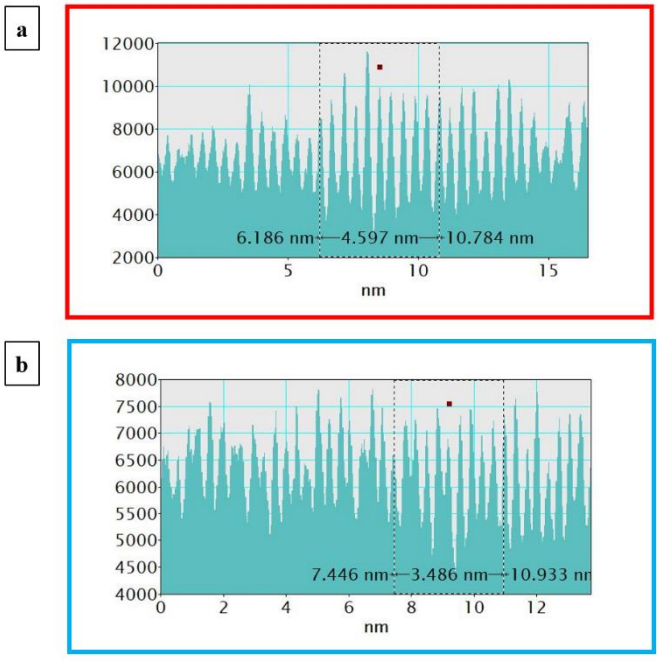


Figure A.10 Line profiles of d-spacings marked in Figure 6.14. (a) Line profile of the d-spacing marked in Figure 6.14(a). (b) Line profile of the d-spacing marked in Figure 6.14(b).

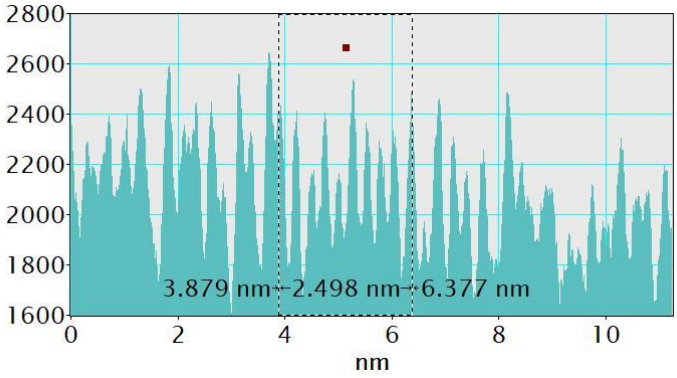


Figure A.11 Line profile of the d-spacing marked in Figure 6.15(b).

A.2 Line Profiles of Fast Fourier Transform Images of High-resolution Transmission Electron Microscopy

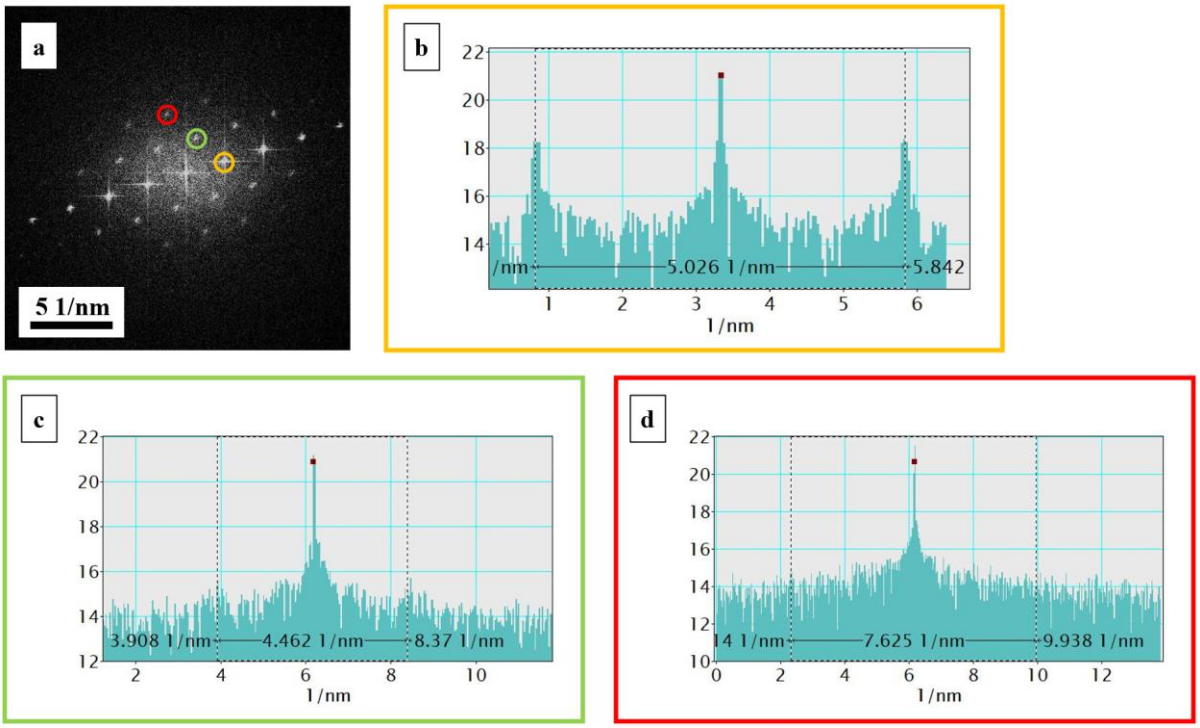


Figure A.12 (a) FFT of Figure 6.5(a). (b) The line profile of the index in the orange circle in (a). (c) The line profile of the index in the green circle in (a). (d) The line profile of the index in the red circle in (a).

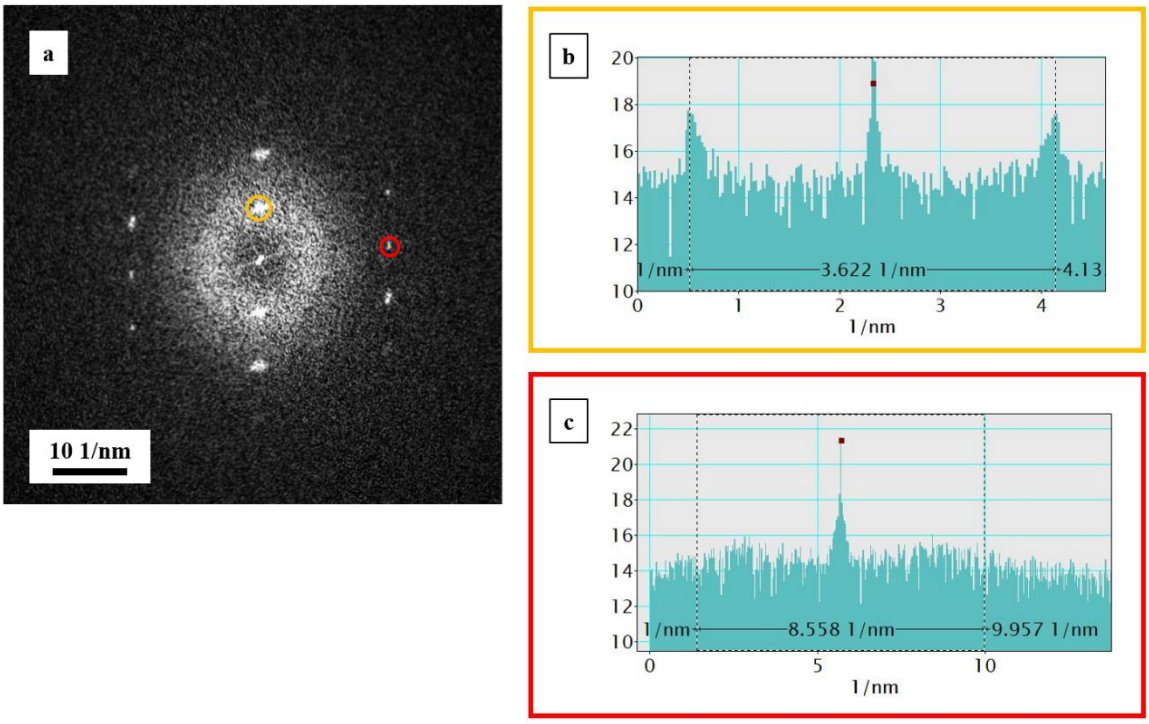


Figure A.13 (a) FFT of Figure 6.6(a). (b) The line profile of the index in the orange circle in (a). (c) The line profile of the index in the red circle in (a).

A.3 Line Profiles of High-angle Annular Dark Field-Scanning Transmission Electron Microscopy and Electron Ptychography Images

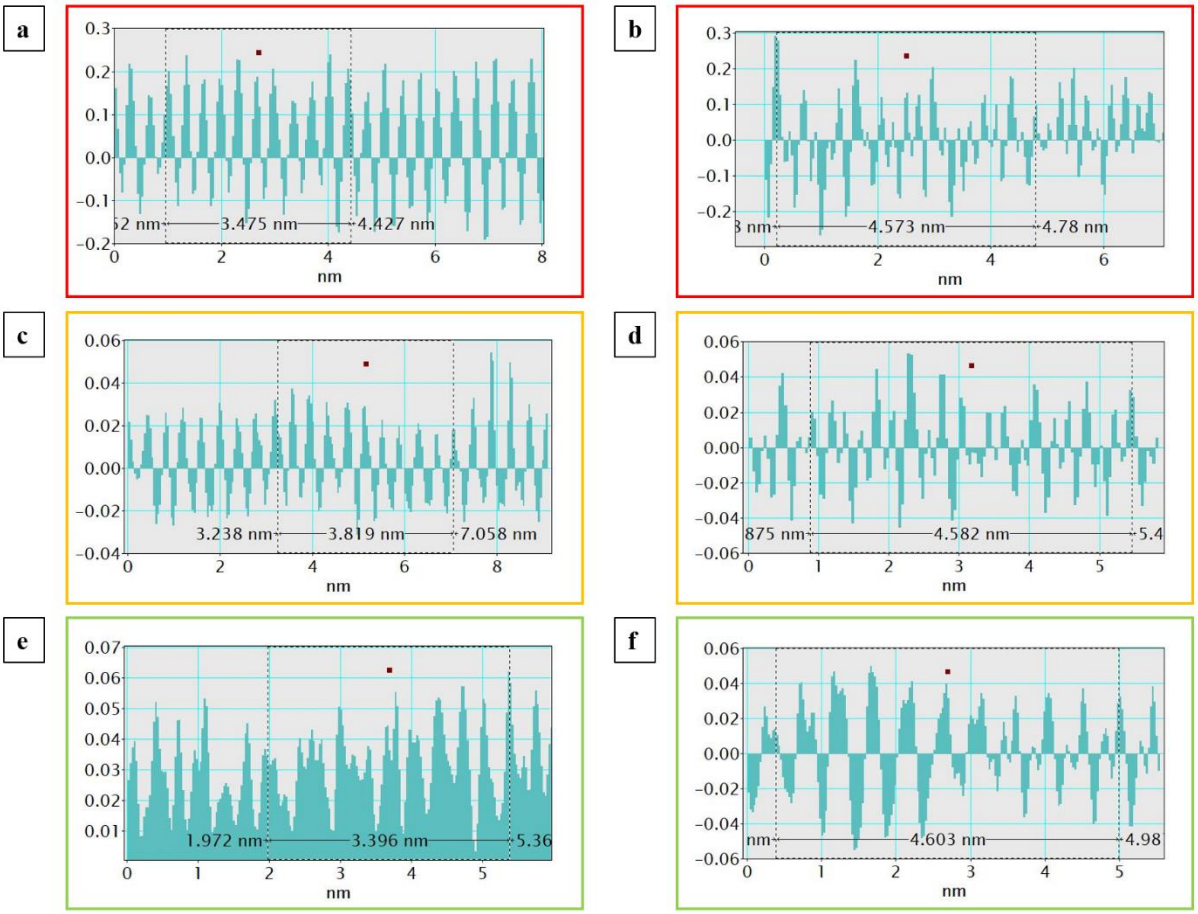


Figure A.14 Line profiles of the d-spacings and repeat distances summarised in Table 7.5j. (a) Repeat distance of F8. (b) The β-sheet d-spacing of F8. (c) Repeat distance of F9. (d) The β-sheet d-spacing of F9. (e) Repeat distance of FP. (f) The β-sheet d-spacing of FP.

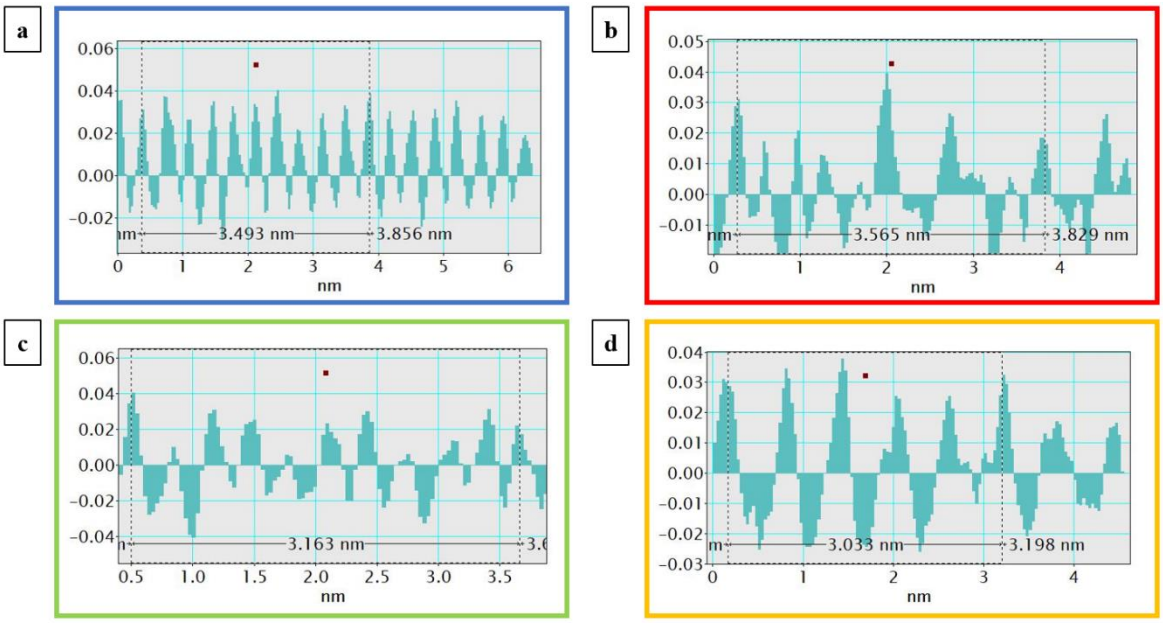


Figure A.15 Line profiles of the repeat distance and d-spacings marked in Figure 7.16. (a) Line profile of the repeat distance in the blue square in Figure 7.16(b). (b) Line profile of the d-spacing marked in red in Figure 7.16(b). (c) Line profile of the d-spacing marked in green in 7.16(b). (d) Line profile of the d-spacing marked in orange in Figure 7.16(b).

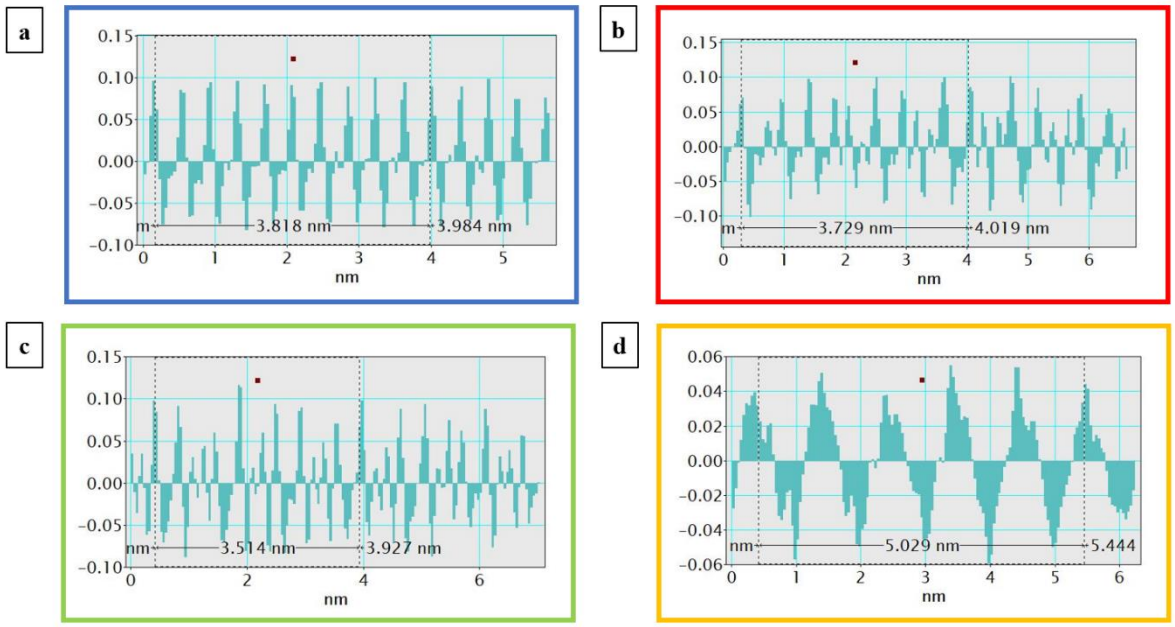


Figure A.16 Line profiles of the repeat distance and d-spacings marked in Figure 7.17. (a) Line profile of the repeat distance in the blue square in Figure 7.17(b). (b) Line profile of

the d-spacing marked in red in Figure 7.17(b). (c) Line profile of the d-spacing marked in green in Figure 7.17(b). (d) Line profile of the d-spacing marked in orange in Figure 7.17(b).

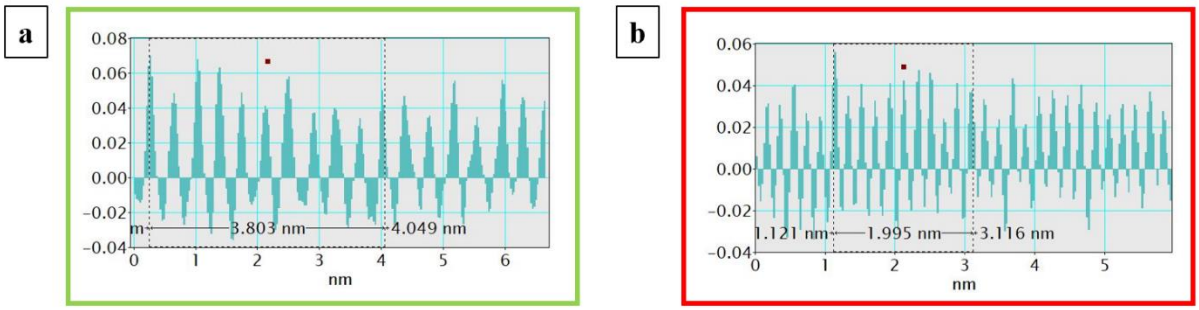


Figure A.17 Line profiles of d-spacings marked in Figure 7.18. (a) Line profile of the d-spacing marked in green in Figure 7.18(b). (b) Line profile of the d-spacing marked in red in Figure 7.18(b).

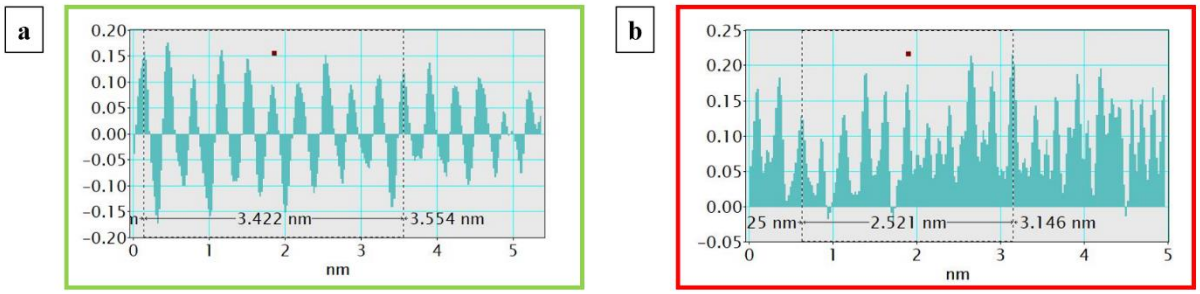


Figure A.18 Line profiles of d-spacings marked in Figure 7.19. (a) Line profile of the d-spacing marked in green in Figure 7.19(b). (b) Line profile of the d-spacing marked in red in Figure 7.19(b).

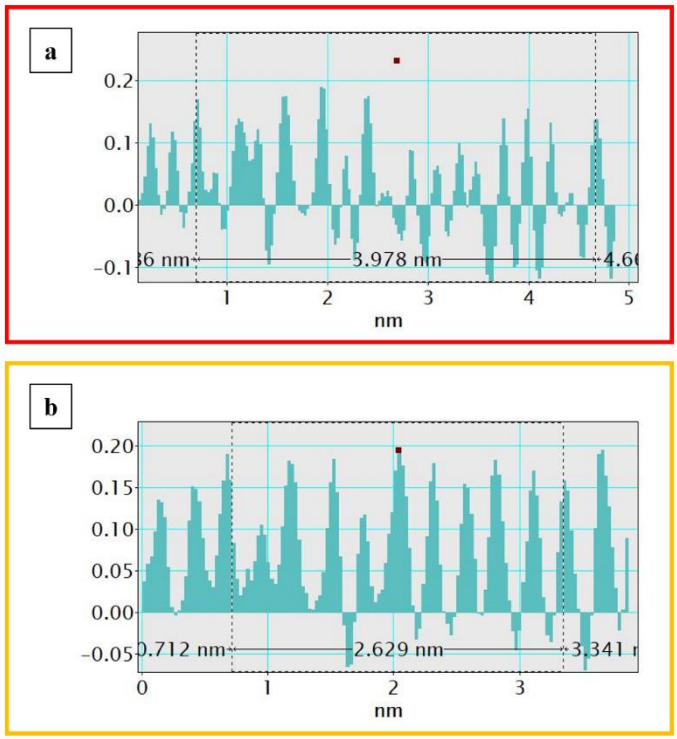


Figure A.19 Line profiles of d-spacings marked in Figure 8.3. (a) Line profile of the d-spacing marked in red in Figure 8.3. (b) Line profile of the d-spacing marked in orange in Figure 8.3.

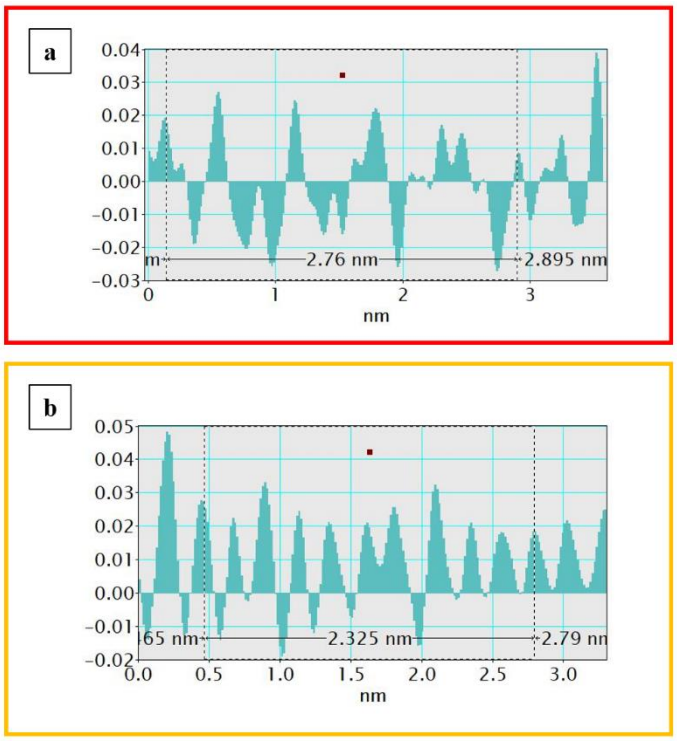


Figure A.20 Line profiles of d-spacings marked in Figure 8.4. (a) Line profile of the d-spacing marked in red in Figure 8.4. (b) Line profile of the d-spacing marked in orange in Figure 8.4.